Vanadium oxides and their derivatives as superb cathodes for aqueous zinc ion batteries

Jianwei Li

A thesis presented for the degree of

Doctor of Philosophy

Supervised by

Professor Ivan P. Parkin

Professor Claire J. Carmalt

Department of Chemistry

Mathematical and Physical Sciences Faculty

University College London

September 2020

Declaration

I, Jianwei Li, confirm that the work presented in this thesis is my own. Where information has been derived from other sources (publications, websites and database), I confirm that this has been indicated in the thesis.

Abstract

Aqueous zinc ion batteries have drawn great attention recently due to remarkable properties compared with conventional batteries systems, which attains benefits from the low-cost and ultra-safe aqueous electrolyte, and the stable metallic zinc anode. However, cathode materials in aqueous zinc ion batteries still require a breakthrough because of relatively slow kinetics and unstable microstructures for Zn^{2+} intercalation/extraction in aqueous zinc salt electrolyte compared with other metal ions batteries. Therefore, this thesis targets on design and development of vanadium-based cathodes and their derivatives to overcome the issues and bring a deep insight into the energy storage mechanism. Step-by step investigations of novel cathode materials were carried out to evaluate their physiochemical properties, electrochemical performance and microstructures/chemical states evolutions upon charge/discharge process. Moreover, Density functional theory (DFT) and 3D-tomorgraphy simulations were adopted to elucidate specific characteristics of as-prepared cathode materials and their corresponding electrodes. Finally, the as-fabricated zinc ion batteries exhibit competitive performance in terms of high energy/power density and long cycling stability compared with reported researches in this area. The details of the work was summarized into three main aspects shown as follows:

(1) Vanadium oxides cathodes are widely utilized as electrode materials in batteries system because of active redox species and various accessible microstructures for ions accommodation. However, conventional vanadium oxides still suffer from poor conductivity, irreversible phase transformation, structure collapse and confined ion migrations channels as cathode in aqueous zinc ion batteries, which results in unfavourable battery performance in previous reported works. Therefore, as vanadium pentoxide analogues, hydrated vanadium bronzes stepped into the spotlight recently because of their special two dimensional microstructures consisting of V_2O_5 matrix, pre-intercalated ions and/or water molecules accommodated within the layer space, which effectively overcome the issues. Here, an investigations of hydrated vanadium bronzes, δ-$Ni_{0.25}V_2O_5{\cdot}nH_2O$ / $Co_{0.25}V_2O_5{\cdot}nH_2O$, was carried to uncover the reaction mechanism and beneficial effects derived from pre-intercalated species. Moreover, different electrochemical behaviours between nickel vanadium bronze and cobalt

vanadium bronze were discussed with a verdict of an importance of choosing competent pre-intercalated species for aqueous zinc ion batteries applications. Rational designed cathode electrode prepared by porous δ-$Ni_{0.25}V_2O_5{\cdot}nH_2O$ micro-ribbons delivered a specific capacity of 402 mAh g^{-1} at current density of 0.2 A g^{-1} and a capacity retention of 98% over 1200 cycles at 5 A g^{-1}, which achieved the uppermost performance compared with the literature. Meanwhile, a versatile design principle for novel vanadium bronzes was suggested for high performance energy storage materials.

(2) Vanadium bronzes cathode materials have exhibited promising capability in aqueous zinc ion batteries. However, researches on improving as-developed vanadium bronzes are rare, which inevitably hinder their practical applications such as grid-scale energy storage system and portable devices. Therefore, higher power/energy density and cycling stability are eagerly needed for such purposes. In this work, a two-pronged approach of oxygen deficiency enriched and water-lubricated ammonium vanadium bronze ($NH_4V_4O_{10}$) cathodes for high performance aqueous zinc ion batteries was exploited by tailored synthetic protocol consisting of induced defects and interlayer-spacing engineering. In particular, the conventional phase of $NH_4V_4O_{10}$ were demonstrated as an adequate Zn^{2+} storage/extraction host with active redox sites in "double-layer" motif of VO_x polyhedra and the introducing hydrogen-bonded NH_4^+ as the "pillar". Oxygen deficiency and lattice water were successfully introduced into $NH_4V_4O_{10}$, which demonstrated significantly improved Zn^{2+} storage properties, such as enhanced specific capacity of 435 mAh g^{-1} at 0.2 A g^{-1} and improved stability (negligible capacity decay after 1500 cycles at 10 A g^{-1}). Combined with widely recognized beneficial pre-intercalated species of water and NH_4^+, the as-developed oxygen deficient $NH_4V_4O_{10}$ illustrated a universal strategy for the design of superior vanadium bronze cathodes in aqueous zinc ion batteries and their broader sphere of applications in other types of aqueous metal-ion batteries.

(3) Prussian blue analogues have been successfully adopted as cathodes materials for aqueous zinc ion batteries with relatively high discharge plateau, but they are limited by extremely low specific capacity (<70 mAh

g^{-1}) and poor cycling stability (self-dissolution in aqueous electrolyte). Moreover, conventional Prussian blue analogues consist of two metal ions coordinated with a cyanide group, which exhibits a rigid cubic crystal structure. The limited tunnel size and artificially introduced defects give rise to unstable electrochemical reactions and slow ion diffusion coefficient upon Zn^{2+} insertion/extraction. Therefore, a new Prussian blue analogues, vanadyl hexacyanoferrate and its defected analogue were proposed in this work. The resulting superb battery performance caused by an unique crystal structure, in which, the oxycation (vanadyl) occupy the ligand of $[Fe(CN)_6]^{4-}$ generating similar cubic crystallography with spontaneously stable vacancy on its facets. Additionally, highly active vanadyl redox reaction between 3^+ to 5^+ and iron cyanide group contribute to a record-high specific capacity of 226 mAh g^{-1} at current density of 0.2 A g^{-1}. Meanwhile, a hydrogel shield strategy was carried out to enhance the stability of the materials which exhibit extraordinarily long-cycling capability and optimized kinetics due to stabilization from surface anchoring polymerization, interfacial hydroxylation and accessible ion channels within the hydrogel. Furthermore, the as-obtained vanadyl hexacyanoferrate was assembled into a flexible quasi-solid state device with superior performance and robust durability under multiple mechanical measurements, demonstrating a promising potential for practical applications.

Impact Statement

This PhD project targets on developing and investigating vanadium-based cathode materials to boost aqueous zinc ion batteries performance. The impact and highlights in this thesis were summarized as below:

1) In the first study, multi-scale characterizations were employed to investigate physiochemical properties and electrochemical performance of two novel vanadium bronzes as cathode materials for aqueous zinc ion batteries. More specifically, structure evolutions and chemical environment changes were discussed in detail to verify an unusual reaction behaviour of each vanadium bronzes with Zn^{2+}. The concluded achievements in this research are listed as follows:

- It first demonstrates that there are many wrong claims in previous reported works on crystal structures of vanadium bronzes for aqueous zinc ion batteries since an inaccurate δ-V_2O_5 framework (should be σ-V_2O_5 in fact) was considered as their crystal phase for further analysis. Therefore, through meticulous investigations, we clarified the crystal phase variations between δ-vanadium bronzes (this work) and σ-vanadium bronzes (majority reported cathode materials). Moreover, varied subtle coordination between "double layer" VO_x polyhedron slabs and pre-intercalated ions such as Ca^{2+}, Zn^{2+}, Mg^{2+} and Ni^{2+}/Co^{2+} were clearly illustrated, which offer a conception of optimal selectivity within varied vanadium bronzes as promising cathode materials.

- In addition to comparison of reported δ-/ σ- pre-intercalated vanadium bronzes, it was expected to understand battery performance variations between Ni and Co ions pre-accommodated vanadium bronzes because of the comparable microstructures. Therefore, control group samples of δ-$Ni_{0.25}V_2O_5{\cdot}nH_2O$ / $Co_{0.25}V_2O_5{\cdot}nH_2O$ were designed for this purpose and their divergent electrochemical behaviours were successfully evaluated by multiple *ex-situ* characterizations. Through comprehensive studies, it is the first time to reveal the importance of choosing pre-intercalated ions in vanadium bronzes even though a same coordination between pre-intercalated ions and host framework was observed in atomic level of microstructures.

- Moreover, the outstanding performance of vanadium bronzes is also validated in a diverse control group of samples (δ-$Ni_{0.25}V_2O_5{\cdot}nH_2O$/$Co_{0.25}V_2O_5{\cdot}nH_2O$ and $V_3O_7{\cdot}H_2O$), where $V_3O_7.H_2O$ was fabricated using the same recipe but without adding transition metal precursors during the preparation process. Interestingly, it possessed same layered vanadyl polyhedron motif compared with the adopted δ-vanadium bronzes in this work. The corresponding results successfully indicate beneficial effects of pre-intercalated ions for stabilizing microstructures and enhancing electrochemical reaction capabilities upon Zn^{2+} (de)intercalation.

- The δ-$Ni_{0.25}V_2O_5{\cdot}nH_2O$//Zn batteries showed remarkable specific capacity of 402 mAh g^{-1} at 0.2 A g^{-1} and a capacity retention of 98% over 1200 cycles at 5 A g^{-1} which are superior than other control group samples and reported works. DFT simulations and 3D tomography indicate potential accommodation sites and migration channels for Zn^{2+} and facilitated electrode configuration of as-fabricated cathode materials printed on porous hydrophilic carbon paper, thus opening up an avenue for material design of vanadium bronzes and its practical applications.

(2) The second study proposed a feasible method on structural engineering of ammonium vanadium bronzes ($NH_4V_4O_{10}$), in terms of constructing expanded interlayer spacing by introduced water molecule and oxygen vacancy defects. Through rational design of reduction reagent proportion and addition of NH_4F in the precursor, the resulting defected $NH_4V_4O_{10}{\cdot}nH_2O$ presented optimized capacitive energy storage characteristic and a faster ionic diffusion coefficient compared with pristine $NH_4V_4O_{10}$. Consequently, the corresponding battery performance of defected $NH_4V_4O_{10}{\cdot}nH_2O$ exhibited a high capacity of 435 mA h g^{-1} at a current density of 0.2 A g^{-1} and excellent stability with 95% capacity retention after 1500 cycles at 10 A g^{-1}. Meanwhile, extraordinary rate performance of 43% capacity retention after a 28-fold increase of current density (from 0.2 to 14 A g^{-1}) was achieved compared with only 19% in untreated $NH_4V_4O_{10}$ with identical conditions. The variation of microstructures, chemical states and electrochemical properties are critically analysed to present a comprehensive understanding of zinc storage mechanism. The impact and highlights of the outcomes are shown as follows:

- The preparation strategy for structural engineered $NH_4V_4O_{10}$ was realized *via* a single step hydrothermal reaction with slight modification of the original recipe for pristine $NH_4V_4O_{10}$. It was seen that the systematically controlled amount of oxalic

acid and NH_4F in the precursor solution can critically adjust the pH value and reduction process for generation of pure phase defected $NH_4V_4O_{10}{\cdot}nH_2O$ cathode material. Moreover, addition of NH_4F can effectively generate porous structures *via* hydrolysis during the reaction, which present 2.8 times increase of BET specific surface area in defected $NH_4V_4O_{10}{\cdot}nH_2O$ compared with untreated control sample. Therefore, a larger interfacial contact area of active material with electrolyte can be expected in this case after modification of microstructures.

- Additionally, performance enhancement was analysed by experimental methods and DFT calculations. It was clearly illustrated that enlarged d-spacing and localized electron around defects can effectively facilitate Zn^{2+} migration reflected with an obviously optimization of ion diffusion coefficient and rate performance. In addition, more liberated electrons formed in oxygen vacancy are easily excited into conduction band from its donor level, which also contribute to conductivity improvement in the as-prepared defective sample. Thus, structural engineering could be considered as a promising strategy for designing advanced cathode materials not only for vanadium bronzes, but for other metal oxides.

(3) The third study of vanadium based cathodes relies on a hypothesis that the diatomic ion**,** vanadyl, can replace conventional single-atom ions (Fe^{3+}, Co^{2+}, Ni^{2+}, Zn^{2+}, Mn^{2+} and Cu^{2+}) in Prussian blue analogues to construct novel analogues with alternated connection of vanadyl and ligand of $[Fe(CN)_6]^{4-}$, which could efficiently promote specific capacity since two electrons reaction ($V^{3+}\leftrightarrow V^{5+}$) during charge/discharge process instead one electron or inert redox active species in conventional Prussian blue analogues. Experimentally this hypothesis was verified by successful synthesis of vanadyl hexacyanoferrate and its defected control sample along with critical characterizations afterward. The corresponding battery performance not only breaks record compared with all reported Prussian blue analogues, but also exhibit inherently higher work voltage and power density compared with other reported cathode materials for aqueous zinc ion batteries. Additionally, hydrogel shielded cathode material strategy was the first time proposed in aqueous zinc ion batteries applications *via* alginate salt self-confined polymerization by consuming vanadyl dissolution from vanadyl hexacyanoferrate. The shielded sample presents remarkable stability and

ultra-high rate performance compared with the pristine sample, in line with expectations. The novelty and significant impacts in this work are concluded as follows:

- By comparison of different precursors of potassium ferricyanide(III) and potassium ferrocyanide(II) reacted with vanadyl ions, the resulting products showed distinct characteristics such as colours, crystallinity, chemical states and composition. Moreover, through structure analysis, spontaneous defects were observed because of saturated spatial occupation of oxygen with vanadium resulting in missing neighbour ferrocyanide group in 3D framework. Consequently, larger cavities within the crystal structure can be expected and further confirmed by characterization of BET specific surface area where a 158 m^2 g^{-1} was attained in vanadyl hexacyanoferrate. It is worth mentioning that the value of specific surface area in this work is 1.5-2 times higher than conventional Prussian blue analogues. Therefore, because of structural benefits and redox-active diatomic ions, a record-high specific capacity of 213 mAh g^{-1} at a current density of 0.2 A g^{-1} was obtained, which is 3-4 times higher than all reported Prussian blue based cathode materials for aqueous zinc ion batteries.

- Although a superior battery performance was observed, the as-prepared vanadyl hexacyanoferrate still face self-dissolution issues like other Prussian blue analogues, which is more serious in aqueous electrolyte due to a strong dipolar interaction of water molecule. Thus, a novel strategy was verified in this work using ionic conductive hydrogel polymerized on surface of vanadyl hexacyanoferrate could stabilize the structures and introduce hydroxylation surface for enhancing the interfacial capability of fast zinc desolvation process. Additionally, a self-confined polymerization formation mechanism of alginate salt with limited self-dissolved vanadyl ions exhibited less adverse impacts on porous structures and other properties. In contrast, a fast polymerization process (few seconds) and simple reaction parameters (directly mixed as-prepared vanadyl hexacyanoferrate powder with sodium alginate aqueous solution) at ambient environment were apparently favourable for scalable production in practical applications. Therefore, the obtained battery performance of hydrogel shielded vanadyl hexacyanoferrate bring even better specific capacity of 226 mAh g^{-1} at a current density o f 0.2 A g^{-1} and 176 mAh g^{-1} at a current density of 5 A g^{-1}. Moreover, rate performance (raised from

62% to 88% after 25 fold increase of current density from 0.2 A g^{-1} to 5 A g^{-1}) and interfacial resistance (reduced from 87.7Ω to 29.6Ω in the initial state of electrode) display a significant improvement compared with pristine vanadyl hexacyanoferrate which further confirmed the beneficial effects discussed above.

- In addition to excellent battery performance, the as-obtained vanadyl hexacyanoferrate was also fabricated into quasi-solid-state flexible cell equipped with poly(acrylamide) as electrolyte. The cell exhibited superior mechanical properties with steadily power output even after bending/twisting/stretching and partial cutting tests, which sufficiently demonstrate its feasibility for practical portable devices.

To sum up, these achievements are believed to promote a step-change on aqueous zinc ion batteries researches and could draw broad interests not only from academics working in field of materials science associated with energy storage techniques, but from a wider community on advanced materials design and practical applications.

Acknowledgements

First and foremost, I would like to express the deep appreciation to my supervisors, Prof. Ivan P. Parkin and Prof. Claire Carmalt. They offered me a most precious opportunity to pursue my academic ambition and enlightened me with wise guidance and massive support during my PhD. Moreover, I am deeply grateful to Dr. Russell Binions, who gave me a chance to continue my dream of research, and always opened up to me with his enthusiasm not only on PhD. projects, but also on our hobbies such as music and sports. With their assistance, I never feel lost and desperate even in disruption of my PhD. studies. Moreover, their attitudes towards science, management and life also inspired me a lot, which will be beneficial my future lifetime.

Then, I would like specially thank to Dr. Guanjie He and Dr. Sanjayan Sathasivam, who taught me the experimental skills and helped me to build up my research project, without whom I could not achieve my current progress in research. Furthermore, I am also grateful to Prof. Min Wang, who offered me great help when I exchanged to the Chinese Academy of Science as a researcher to continue my studies in the period of COVID-19.

Additionally, I would like to thank all my collaborators for their support on my research, including Prof. Dan Brett, Prof. Paul Shearing, Prof. Furio Cora, Prof. Wenyao Li, Dr. Ryan Wang, Dr. Andreas Kafizas, Dr. Guoliang Chai, Dr. Kit McColl, Dr. Xuekun Lu, Mr.Liqun Kang, Miss Ningjing Luo and Miss Feng Wang. Meanwhile, Many thanks to all the group members from Prof. Parkin's, especially Dr. Zhuangnan Li, Mr. Siyu Zhao, Mr. Fangjia Zhao, Mr. Haobo Dong, Mr. Yiding Jiao, Mr. Jian Guo and Mr. Juntao Li, with all your help and companionship. I had a wonderful and meaningful time in UCL. Also thanks to Dr. Steve Firth, Mr. Martin Vickers, Dr. Kristopher Page and Dr. Raul Quesada Cabrera for providing me the equipment training, technical help and project suggestions.

Finally, I would like to express my deepest gratitude to my family for their infinite love and continuous support during my PhD study.

Content

List of Figures

List of Tables

Abbreviation

2D	Two-dimensional
3D	Three-dimensional
AZIBs	Aqueous zinc ion batteries
BET	Brunauer–Emmett–Teller
CD	Charge-discharge curves
C_{lsf}	Element account for the low-frequency surface capacitance
CV	Cyclic voltammetry
CPE	Constant phase element
DFT	Density Functional Theory
DOS	Density of states
E_{mass}	Gravimetric energy density
EDS	Energy dispersive X-ray spectroscopy
EES	Electrochemical energy storage
EIS	Electrochemical impedance spectroscopy
FTIR	Fourier transform infrared spectroscopy
GCD	Gravimetric charge-discharge
GITT	Galvanostatic Intermittent Titration Technique
HCF	Hexacyanoferrate
HRTEM	High-resolution transmission electron microscopy
HPG	Hierarchical porous graphene
LED	light-emitting diode
LIBs	Lithium-ion batteries
micro-CT	X-ray micro-computed tomography

nano-CT	X-ray nano-computed tomography
NVO	Ammonium vanadium bronze ($NH_4V_4O_{10}$)
NEXAFS	Near edge X-ray absorption fine structure
O_d-$NVO{\cdot}nH_2O$	Oxygen deficient ammonium vanadium bronze
PAM	Polyacrylamide
PBAs	Prussian blue analogues
PVDF	Polyvinylidene fluoride
P_{mass}	Gravimetric power density
R_{ct}	Interfacial charge transfer resistance
R_s	Equivalent series resistance
R_{leak}	Leakage resistance at low frequency
SEM	Scanning electron microscope
SSA	Specific surface area
STEM	Scanning transmission electron microscope
TEM	Transmission electron microscope
TGA	Thermogravimetric analysis
W_0	Warburg element
XPS	X-ray photoelectron spectroscopy
XRD	X-ray diffraction
XRF	X-ray fluorescence
$Zn(TFSI)_2$	Zinc bis(trifluoromethanesulfonyl)imide

Chapter 1

Background and Literature Review

1. Introduction

Rechargeable metal-ions batteries have triggered a race to meet rapidly expanded energy consumption market demands over the last decades.[1] Meanwhile, there is greater attention on ultimate performance and parameter restrictions on electrochemical energy storage (EES) apparatus for different purposes and sustainable development, which are a compelling academic community for aggressively exploring various novel battery systems.[2,3,4]

1.1 Lithium-ion batteries

Up to now, there are many types of rechargeable metal-ions batteries that have been successfully invented including alkali metal-ions batteries (Li^+, Na^+, K^+)[5,6,7] and multivalent ions batteries (Ca^{2+}, Mg^{2+}, Al^{3+}, Zn^{2+}).[8,9] Among them, Lithium-ion batteries (LIBs) as a striking example of synergetic development from both marketing and academic interests not only open-up an innovation of powerful EES devices, but also inspire more aggressive researches on battery science. A matured configuration of LIBs with an illustration of "rocking chair" storage mechanism is shown in Figure 1. In doing so, LIBs, first commercialized in the 1990s, was intensively explored in many fields of cathode/anode materials, electrolytes and reaction mechanism to further boost their performance for satisfying applications such as electric vehicles, portable devices and grid-scale stationary EES apparatus.[10] Therefore, it was seen that an overwhelming gravimetric energy density of LIBs with > 240 Wh kg^{-1} was achieved, and further improvement could push ahead with the value to 500 Wh kg^{-1} theoretically.[11,12] Although various breakthroughs on many aspects of LIBs have been witnessed in 30-years development, it currently still suffers critical degradation from both electrodes and electrolyte with performance decays and increases internal pressure within the packaging.[13] This is owing to self-dissolution of cathode materials with transition metal ions presenting in the electrolyte, which can deteriorate solid electrolyte interphase (SEI) formation and further catalyze the decomposition of the electrolyte with oxygen emitted.[14] Moreover, poor ionic conductivity of organic electrolytes equipped in LIBs seriously affect energy efficiency with a compromised penalty of SEI formation and gravimetric power density.[15,16] Additionally, Li metal plating process can be hindered by sluggish kinetics of intercalation/deposition of Li^+ within/on graphite or metallic lithium, which induces formation of dendrites on the anode surface, consequently

resulting in short circuit with conspicuous hazard.[17,18] In addition to safety constraints for practical applications, the natural abundance of lithium resources has also gained considerate public concern since the price of battery-grade lithium carbonate had a rapid increase from less than $3600 per tone to $14000 within 10 years from 2007 to 2017.[19,20] Apart from the inflated price, the treatment of toxic/combustible organic electrolyte and rigorous assemble requirements (strict moisture-free) during LIBs fabrication process also impact not only on environmental perspective, but a high cost for expensive manufacturing facilities and recycling treatment. There is no doubt that the demand of LIBs will continue growing along with more innovations from many aspects such as ionic liquid electrolytes, interfacial modification of metallic lithium anode and cobalt-free cathodes, but the drawbacks currently still critically impede their widespread applications especially on grid-scale stationary EES system and flexible wearable devices. Therefore, other metal ion rechargeable batteries have been proposed contemporaneously.

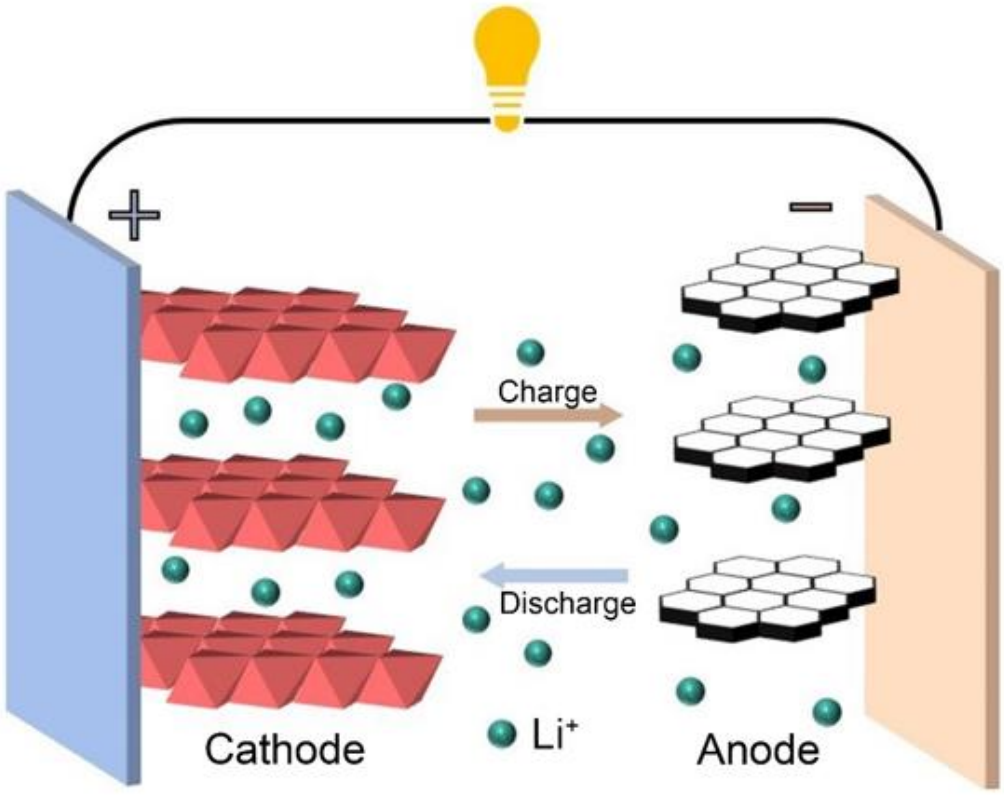

Figure 1.1. LIBs configuration and illustration of charge carrier storage mechanism.

1.2 Sodium-ion batteries

Sodium-ion batteries (SIBs) were suggested initially as promising alternative EES

techniques for competing with LIBs since a lower cost and similar energy storage mechanisms compared with LIBs. [6] Many efforts have been intensively devoted to investigating high-performance crucial components in battery systems including polyanionic-based materials for potential cathodes and red phosphate/metallic tin as promising anodes.[21,22] More specifically, it should be mentioned that the choice of proper anodes are limited so far since conventional graphite and silicon seems inactive for sodium storage, and volume change of alloy-based material faces inevitable challenges for practical applications.[4] Moreover, like in LIBs, sluggish kinetics and safety issues derived from the organic electrolyte were "perfectly inherited" in SIBs. Moreover, a relatively larger ionic radius of Na^+ (1.02 Å) induces a severe difficult intercalation/extraction process compared with that of Li^+ (0.76 Å) associated with unsatisfied cycling capability and energy storage capacity.[4] Therefore, it is expected that a breakthrough for SIBs is definitely needed in order to meet with strict requirements of applications, especially for most anticipated grid-scale stationary EES systems.[23]

1.3 Potassium-ion batteries

Owing to sharing the same reaction mechanism and cell-setup with LIBs and SIBs, potassium-ion batteries (PIBs) also attract attention as complementary EES technique in the academic community since an abundant resource and high theoretical operation voltage derived from negative reduction potential of -2.93 V *vs.* Standard Electrode Potential (close to -3.04 V of Lithium). Surprisingly, although the Shannon ionic radii of Potassium (1.38Å) is much larger than those of Li^+ (0.76 Å) and Na^+(1.02 Å), the smallest Stokes' radius and the weak Lewis acidity endow K^+ faster ion diffusion coefficient in various electrolytes compared with other metal ions. However, the larger Shannon ionic radii gives rise to sluggish transport kinetics within solid electrodes along with large volume variations upon on insertion/extraction process which caused poor reaction efficiency, constrained power output and relatively worse cycling stability. Additionally, side reaction in the electrolyte, dendrite formation and serious potential safety hazard of active K are strongly involved with extensive concern for implement of EES applications. Indeed, it is seen that the massive production and widespread applications of commercialized PIBs are far beyond the achievements that we have done at this stage.

1.4 Multivalent metal ions batteries

Before giving a description of multivalent metal ions batteries, some basic inherent parameters and cost according to different charge carries have been summarized in Table 1. It is explicitly shown that the cost of multivalent metal resource are cheaper than those in alkali metals and higher theoretical volumetric capacity of metallic anode for battery applications due to high density and multiple electrons transfers per ion. Nevertheless, the obvious drawback of multivalent metal ions is relatively low standard electrode potential corresponding to limited operation voltages. However, for a specific application purpose of grid-scale stationary EES system, the installed cost, durability, operational safety and scale-up capability become essential rather than concerns of some battery parameters for mobile applications such as gravimetric capacity.[23] In fact, multivalent metal ions batteries, excluding zinc ion batteries, are hampered by not only ambiguous charge carriers storage mechanism, but irreversible redox reaction on active metallic anode which hinders the ionic migration associated with a generation of unfavourable solid electrolyte interface in organic/aqueous electrolytes. Thus, developments are targeting on artificial passivation of the surface of the metallic anode and compatible electrolytes to bring innovations on energy-efficient batteries system.[8]

Table 1.1 Comparison of different charge carriers for rechargeable metal-ion batteries

Charge Carriers	Crust Abundance (%)	Cost ($/1b)	Standard Electrode Potential (V *vs* SHE)	Ionic Radius (Å)	Hydrated ionic radius (Å)	Theoretical Gravimetric Capacity (mAh g^{-1})	Theoretical Volumetric Capacity (mAh cm^{-3})
Li	0.002	8-11	-3.04	0.76	3.4-3.82	3862	2062
Na	2.3	1.1-1.6	-2.71	1.02	2.76-3.6	1166	1128
K	2.1	3-9	-2.92	1.38	2.01-3.31	685	610
Zn	0.0075	0.5-1.5	-0.76	0.74	3-4.7	820	5851
Mg	2.3	1-1.5	-2.36	0.72	4.12-4.2	2206	3833
Ca	4.1	-	-2.86	1	4.04-4.3	1337	2073
Al	8.2	0.5-1.5	-1.67	0.54	4.8	2980	8046

To address the issues as mentioned above, innovations on electrodes and electrolytes are eagerly needed for the burgeoned markets of intermittent sustainable power generation plants and flexible electronic devices. Responding to safe-first criteria and cost-effective purposes, aqueous zinc ion batteries (AZIBs) return to the sight of academic interests for superior EES technique recently with neutral/ mildly acidic aqueous electrolyte, instead of previous commercialized Zn-Air (first invented in 1869) and primary alkaline aqueous Zn-MnO_2 batteries (first invented in 1882). The neoteric development history of zinc ion batteries is depicted in Figure 2, which illustrates accelerated research progress devoted to investigations of each component of the batteries. Here, in this thesis, a brief configuration and principle reaction mechanism of AZIBs are introduced. Then various representative cathode materials and electrolytes, as well as tailored metallic zinc anode, are also illustrated. Through refined discussion on the advantages and challenges of AZIBs, three pieces of correlated individual research works on superb cathode materials for AIBs are presented in the following chapters.

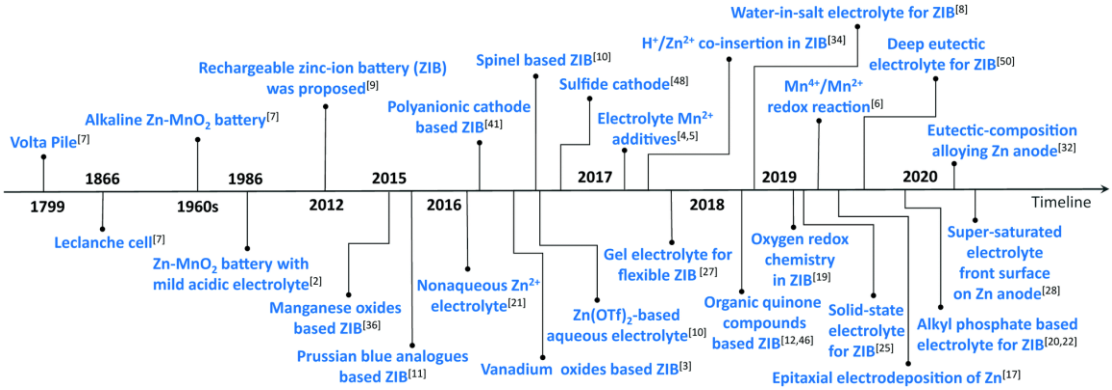

Figure 1.2. Development time line of AZIBs**.** (Reproduced with permission, Copyright © The Royal Society of Chemistry 2020).[41]

1.2 Fundamentals of aqueous zinc ions batteries

1.2.1 Basic concept of aqueous zinc ion batteries

Aqueous zinc ion batteries (AZIBs) built on aqueous neutral/mildly acidic (pH: 3.6~6.0) electrolyte have drawn great attention in the academic community, especially for large-scale stationary EES applications and flexible electronic devices. The configuration of AZIBs is illustrated in Figure 1.3, which presents similar battery components as observed in LIBs, but a metallic zinc anode was employed instead of graphite. The merits of zinc include adequate standard electrode potential (-0.76V *vs.* SHE) and

steady dissolution/deposition capacity in a water-based solution. Thus, metallic anode zinc with water-compatible characteristic can be directly adopted as anode in aqueous electrolyte without further treatment, which is undoubted superiority compared with other metal-ion batteries. Additionally, the large theoretical volumetric capacity of 5855 mAh g^{-1} and gravimetric capacity of 820 mAh g^{-1}, as well as an overwhelming ionic conductivity of aqueous electrolyte (~ 1S cm^{-1} *vs.* ~1^{-10} mS cm^{-1} for organic electrolyte), are compelling for "beyond Lithium-ion" EES applications. Last but not least, non-toxic incombustible media and viable scale-up manufacturing capability with low capital cost are mostly desirable characteristics for practical applications in grid-scale stationary EES system.[24]

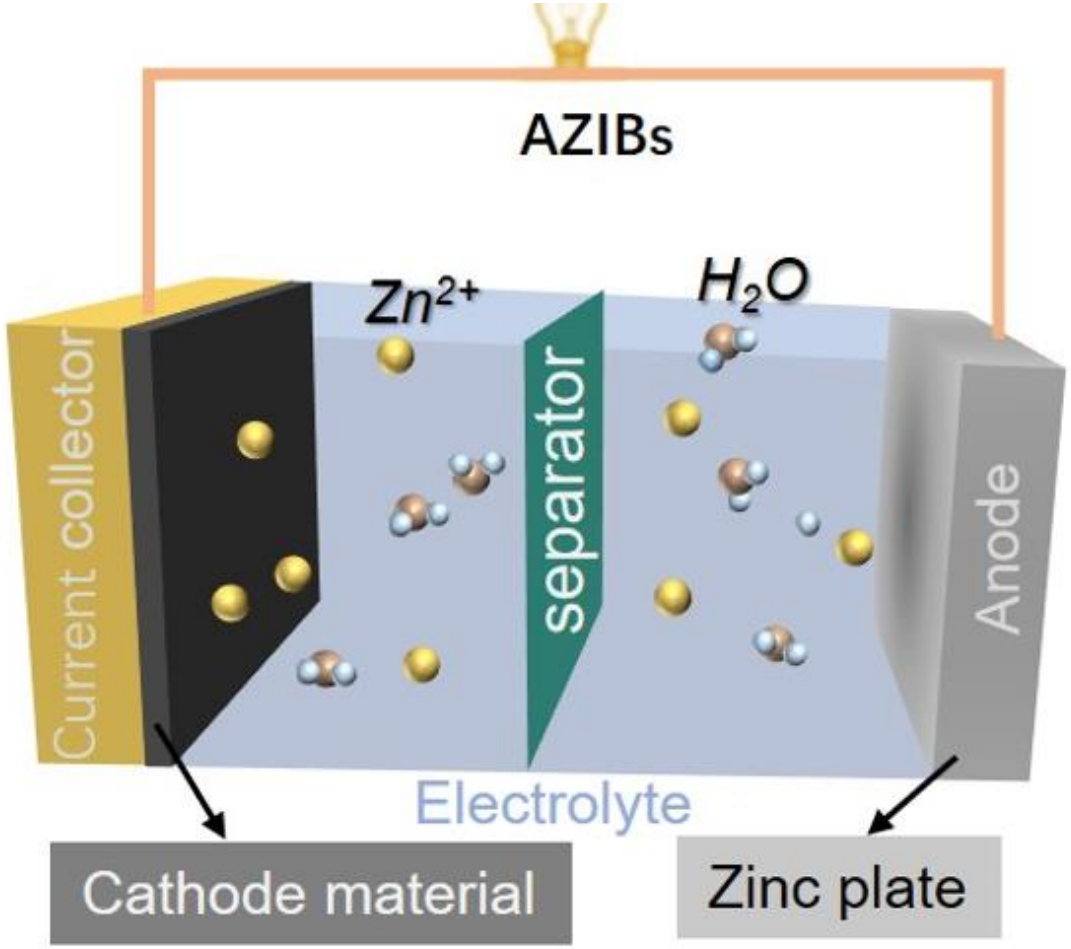

Figure 1.3. The configuration of AZIBs with demonstration of each components in the battery.

1.2.2 Energy storage mechanism

Although the investigation history of zinc ion batteries utilizing aqueous electrolyte was

initiated more than 200 years ago, the reaction mechanisms of AZIBs in the present are highly distinct from precious battery systems, in which, alkaline Zn-MnO_2 batteries equipped with concentrated KOH electrolyte are the most representative zinc-based energy storage devices that have prevailed in the primary EES market.[24] Unfortunately, the redox reaction of metallic zinc possess very poor reversibility with varied by-products ($Zn(OH)_2$, ZnO, etc.) when pH value of aqueous electrolyte above 8 (Figure 4),[25] in contrast to stripping/plating process of Zn^{2+}/Zn in AZIBs. Moreover, γ-MnO_2 cathode in alkaline electrolyte also present irreversible phase transformations which can be described in two-step reduction process, corresponding equations and scheme (Figure 5) are shown as follows:[26]

Cathode： $\gamma\text{-}MnO_2 + H_2O + e^- \leftrightarrow MnOOH + OH^-$ (1)

$MnOOH + H_2O + e^- \leftrightarrow Mn(OH)_2 + OH^-$ (2)

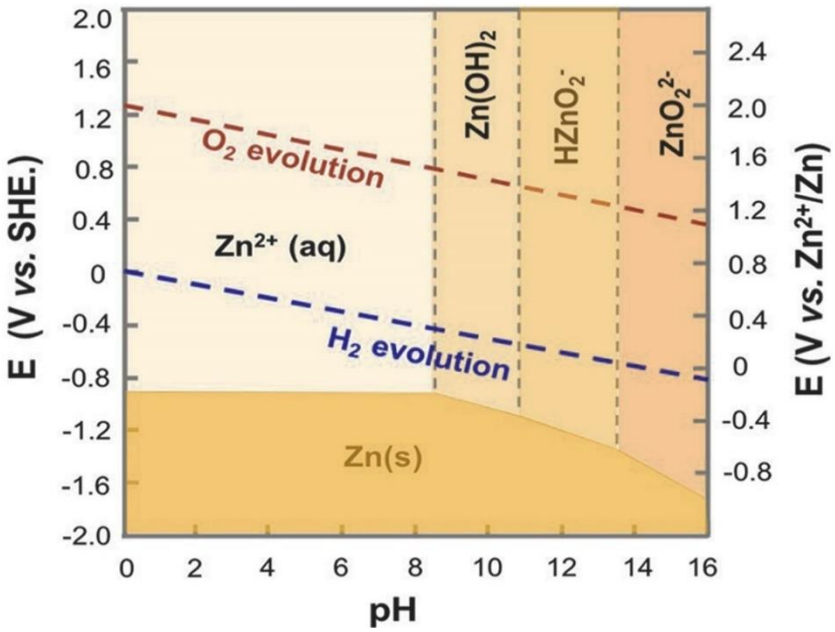

Figure 1.4. Pourbaix diagram of metallic zinc anode in aqueous electrolyte with varied formation of zinc-based products associated with different pH values.[25] (Reprinted with permission, Copyright © 2020, American Chemical Society)

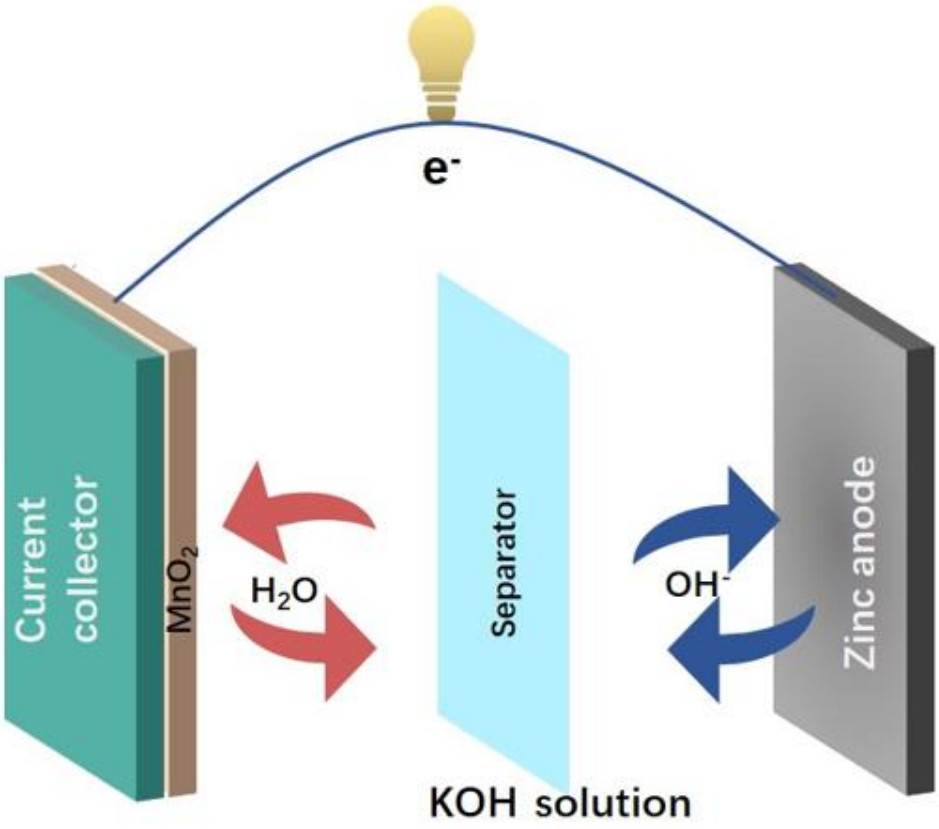

Figure 1.5. Schematic of alkaline Zn-MnO_2 batteries.

Therefore, adoptions of neutral/mildly acidic aqueous electrolytes AZIBs instead of alkaline electrolyte are fundamental factors to bring innovation on changes of Zn^{2+} storage behaviours from primary to secondary batteries mechanism. More specifically, the energy storage mechanism of AZIBs still act in accordance with the classic "rocking chair" scheme like LIBs, Zn^{2+} strips from metallic anode and transports to cathode for redox reaction upon discharge process, and same reaction run in reverse during charge process. For instance, a reaction mechanism of aqueous Zn//α-MnO_2 battery with 0.1 M $Zn(NO_3)_2$ aqueous electrolyte claimed by Xu et. al were shown as follows:[26]

Cathodic process: $Zn^{2+} + 2MnO_2 + 2e^- \leftrightarrow ZnMn_2O_4$ (3)

Anodic process: : $Zn \leftrightarrow Zn^{2+} + 2e^-$ (4)

It is seen that the reaction described above can be regarded as simple zinc (de)intercalation reaction mechanism. It is worth noting that the later studies of aqueous Zn//α-MnO_2 battery with 2M $ZnSO_4$ and 0.1 M $MnSO_4$ (additive) electrolyte gave a different reaction pathway which can be expressed as follows:[27]

Cathodic process:

$H_2O \leftrightarrow OH^- + H^+$ (5)

$$3Zn^{2+} + 6OH^{-} + ZnSO_4 + nH_2O \leftrightarrow ZnSO_4[Zn(OH)_2]_3 \cdot nH_2O \quad (6)$$

$$6MnO_2 + 6H^{+} + 6e^{-} \leftrightarrow 6MnOOH \quad (7)$$

Anodic process: :

$$3Zn \leftrightarrow 3Zn^{2+} + 6e^{-} \quad (8)$$

Overall:

$$6MnO_2 + nH_2O + ZnSO_4 + 3Zn \leftrightarrow 6MnOOH + ZnSO_4[Zn(OH)_2]_3 \cdot nH_2O \quad (9)$$

A more complicated reaction mechanism can be observed in those equations since the additional formation of zinc hydroxide sulphate precipitates on the surface of cathode materials along with conversion reaction of **α**-MnO_2. An extensive recognition of the passivation layer of zinc hydroxide sulphate is generated from proton intercalation process, which is crucial for following mechanism investigations of energy storage behaviours.

In addition to those two reaction mechanisms exhibited above, a Zn^{2+} and H^{+} co-insertion mechanism was proposed by Wang et al. recently[28], which was also extensively confirmed not only in manganese oxides[29,30,31], but in vanadium oxides[32,33] and other types of cathodes[34]. An illustration of the co-insertion mechanism scheme is depicted in Figure 6, which shows that both Zn^{2+} and proton can intercalate into cathodes framework. Similarly, however, it is mysterious to distinguish rigorous reaction steps during the co-insertion process and veritable charge carriers for capacity contribution. Thus, considerable controversies still exist in this area. For example, Li et. al. revealed a highly different reaction mechanism from previously reported researches on VO_2(B) cathode material for AZIBs application (Figure 7).[35] It was seen that a passivation layer of zinc hydroxide sulphate precipitates formed on the surface of cathode like observation in manganese oxides. Meanwhile, through first-principle calculations, the *ex-situ* measurements and analysis of electrochemical behaviour, the author gave detailed characteristics of energetics and energy storage mechanism, which surprisingly indicate more favourable formation energy of H_xVO_2 rather than Zn inserted VO_2 observed in literature. Therefore, the battery capacity is entirely contributed by proton intercalation instead of storage of Zn^{2+}.

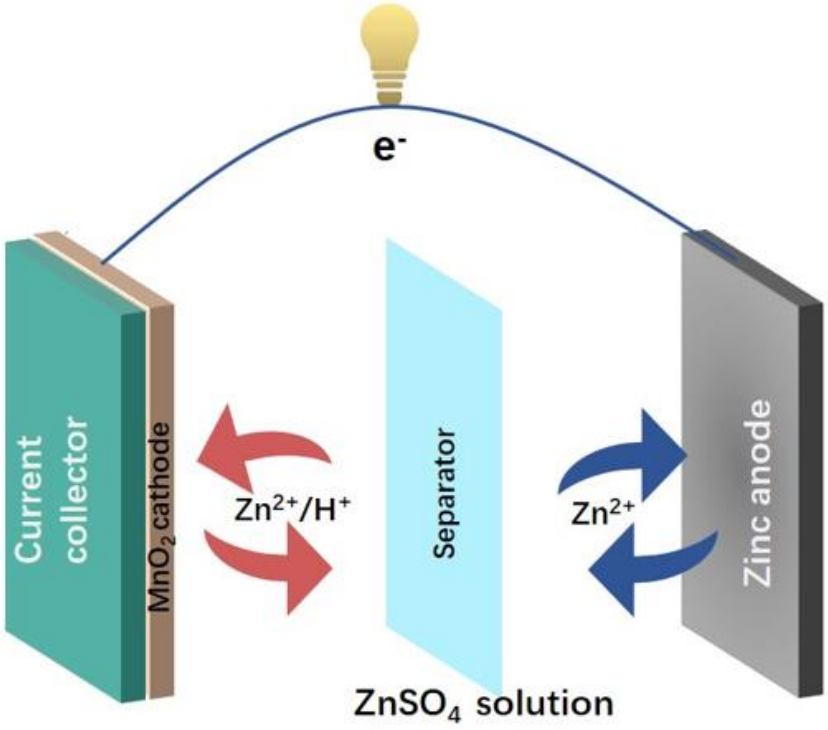

Figure 1.6. Schematic of aqueous Zn-MnO_2 batteries with neutral/mildly acidic electrolyte.

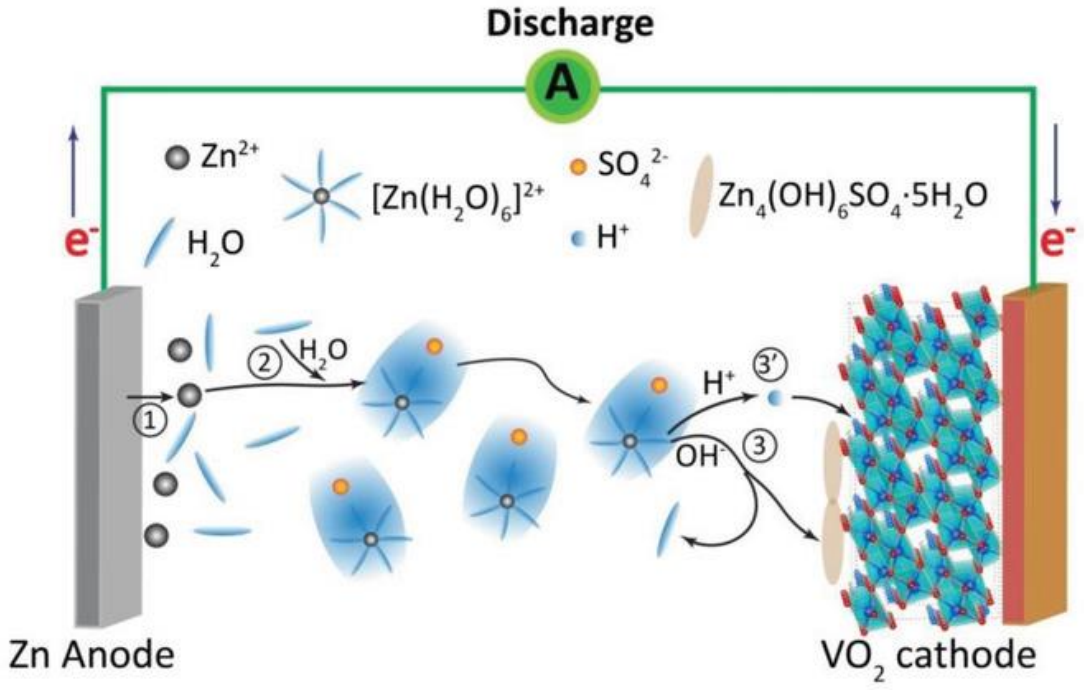

$$\frac{1}{2}Zn+\frac{1}{6}ZnSO_4+\frac{11}{6}H_2O+VO_2 \rightleftarrows \frac{1}{6}[Zn_4(OH)_6SO_4\cdot 5H_2O]\downarrow +H_{insert}VO_2$$

Figure 1.7. Schematic of Zn | ZnSO4 | VO_2(B) battery with co-insertion reaction mechanism. (Reprinted with permission from Ref.35 © 2019 WILEY-VCH Verlag

GmbH & Co. KGaA, Weinheim)

In conclusion, to data, the reaction mechanism of AZIBs according to different reaction pathways on cathodes can be determined to three main categories: Zn^{2+} (de)intercalation, conversion reaction and Zn^{2+}/H^{+} co-insertion/extraction. It can be seen that the researches of zinc storage in various cathode materials are still in infancy. Meanwhile, owing to complexity of species in aqueous electrolyte (proton, zinc ion and hydrated zinc ions), the investigation of mechanism are easily misled by phase mis-identifications and wrong interpretation of chemical states. Therefore, more efforts should be concentrated on elaboration of veritable mechanism on their fine structure evolutions during charge/discharge and chemical analysis against specific cathode materials. Additionally, exploring cathode materials are urgently needed to fully unleash the whole potential of performance of AZIBs, as the theoretical gravimetric/volume capacity of metallic zinc anode is competent to fulfil the demands of practical EES applications.

1.3 Electrolyte for aqueous zinc ion batteries

1.3.1 Aqueous electrolytes for AZIBs

Aqueous electrolytes play an important role in AZIBs and are also adopted for other metal ion batteries system due to its merits, including high ionic conductivity, low cost and ease of manufacture. As mentioned before, early attempts considering aqueous electrolyte in zinc-based batteries focused on alkaline system, which is inadequate for reversibility required by rechargeable battery applications. Therefore, AZIBs were first established on the basis of natural/mild acidic aqueous electrolyte in 2012, which gave rise to a great impact on the concept for grid-scale stationary EES applications.

Although there are many fascinating aspects of aqueous electrolytes which can be easily discovered, a certain barrier is also derived from an intrinsic property that a narrow thermodynamic stability window of bulk water with 1.23V, beyond which, the oxygen /Hydrogen evolution reaction can occur resulting in decomposition of the electrolytes.[36] However, with various amount of proper metal salts added into water, the operation window can be significantly broadened, even approaching above 3V in water-in-salt based electrolyte[37,38,39] (high concentrated salt solutions). Therefore, the majority of applied zinc salt aqueous electrolyte deliver an operational window from 0.2~2.0 V (V *vs.* Zn/Zn^{2+}) depending on varied zinc salt species and their concentration.[40]

Additionally, there are many zinc salts which have been employed in aqueous electrolyte for AZIBs. A brief comparison of their electrochemical properties was concluded in Table 2. It should be emphasised that the most extensively used aqueous electrolytes are $ZnSO_4$ and $Zn(CF_3SO_3)_2$ in AZIBs application, which should be attributed to more stable anions group and less water-induced side reactions compared with NO_3^- ,Cl^- and CH_3COO^- upon charge/discharge process.[41] Meanwhile, faster kinetics and better reversibility of aqueous electrolyte containing $Zn(CF_3SO_3)_2$ were detected compared with $ZnSO_4$ electrolyte. This is owing to bulky $CF_3SO_3^-$ moieties which can shield Zn^{2+} from surrounding water molecules and alleviated solvation effects.[42] A similar phenomena can also be observed in Zinc(II) Bis(trifluoromethanesulfonyl)imide ($Zn(TFSI)_2$) electrolyte as a larger anion group can occupy the solvation sheath instead of water. Thus, hydrolysis and side reactions can be effectively reduced.[43] Nevertheless, it should be noted that the increase of cost and viscosity with reduced ionic conductivity should be considered as a trade-off of battery performance with increased concentration of zinc triflate or $Zn(TFSI)_2$ in aqueous electrolyte.[43,44] In addition to conventional zinc salts-based aqueous electrolyte, some additives were explored to prevent specific cathode materials from self-dissolution by tailored equilibrium of ions concentration between cathode material and electrolyte. For instance, $MnSO_4$/$Mn(CF_3SO_3)_2$ and Na_2SO_4 for were adopted for stabilizing manganese oxides[42,45,46,47] and sodium vanadate cathodes[32], respectively.

Table 1.2. Electrochemical properties of different aqueous electrolytes adopted for AZIBs

Categories of electrolytes with concentration	Ionic conductivity (S cm^{-1})	pH value	Coulombic efficiency of zinc anode (%)	Solubility (g/100g H_2O)	Ref.
1M KOH	~0.5	~14	<50	121	[48]
0.1M $Zn(NO_3)_2$	-	5.2	-	120	[26]
2M $Zn(CH_3COO)_2$	-	-	~80	30	[49]
30M $ZnCl_2$	2.9 x 10^{-2}	-	95.4	408	[50]
3M $Zn(CF_3SO_3)_2$	3.47	~3.6	100	14.6	[51]
3M ZnSO4	~1.5	3.4	~75	57.7	[51,48,45]
1M Zn $(TFSI)_2$ + 20M LiTFSI	-	~7	99.5	-	[48]
1M Zn $(TFSI)_2$ + 21M LiTFSI	-	-	100	-	[52]
3M $Zn(CF_3SO_3)_2$ + 0.1M $Mn(CF_3SO_3)_2$	~6	3.8	~93	-	[45]

1.3.2 Aqueous gel electrolyte for AZIBs

Quasi-solid-state aqueous gel electrolytes possess flexible polymeric network with filled aqueous electrolyte, which are richly endowed by nature to be employed in AZIBs system not only for replacing separator, but offering liquid-like ionic conductivity like aqueous electrolytes. Moreover, many functional properties can be grafted on gel electrolytes because of abundant functional groups, which endows capabilities of self-healing, temperature response and anti-freezing functionalities. Therefore, it is seen that a huge potential of quasi-solid-state AZIBs are compelling in applications of wearable/flexible electronic devices with high safety and robust mechanical features.

To date, several gel electrolytes have been invented for the purpose such as fumed silica, xanthan gum, poly(vinyl alcohol), polyacrylamide and their hierarchical composites. A comparison of those gel electrolyte can be found in Table 1.3, in which, the features of electrolytes sufficiently exhibit their capabilities for application in AZIBs system.

Table 1.3. Electrochemical feature and functionalities of gel electrolytes for AZIBs.

Gel electrolytes	***Ionic conductivities (S cm^{-1})***	***Functionalities***	***Ref.***
Fumed silica	8.1×10^{-3}	Prohibition of Zn dendrite growth	[53]
Gelatine	6.15×10^{-3}	Flexible and robust mechanical properties; Prohibition of Zn dendrite growth	[32,54]
Xanthan gum	1.65×10^{-2}	Prohibition of Zn dendrite growth and flexible feature	[55]
Poly(vinyl alcohol)	1.26×10^{-2}	Shape memories and flexible feature	[56,57,58,59]
Polyacrylamide	1.65×10^{-2} @ room temperature	Self-healing, flexible and robust mechanical properties	[60,61]
Glycerol and ethylene glycol with polyurethane acrylates/polyacrylamide	1.68×10^{-2}@ room temperature 1.46×10^{-2}@ -20˚C	Anti-freezing, flexible and robust mechanical properties	[62]

In conclusion, according to the studies mentioned above, it was seen that enormous efforts have been dedicated into studies of aqueous electrolytes and their gel-based quasi-solid-state electrolytes in AZIBs. Owing to those merits from water based

features, AZIBs can be regarded as one of the best candidates to fulfil the demands of grid scale stationary and flexible EES applications. However, water-induced side reactions and unsatisfied columbic efficiency also require more concerns for selection of adequate aqueous electrolytes. Meanwhile, it is necessary to explore a specific electrolyte in details with standard criteria, otherwise, it is hard to evaluate their authentic electrochemical parameters for practical applications. Moreover, understanding different features of aqueous electrolytes are also imperative to consider a compatibility of developed cathode materials, which can critically impact on battery performance.

1.4 Cathode materials for aqueous zinc ion batteries

1.4.1 Manganese oxides

Manganese oxides have gained extensive interests in EES techniques because of various valance states and crystallographic structures. More explicitly, various crystallographic phase of MnO_2, such as α, β, γ, δ, ε and todorokite type, have been intensively studied at initial research stage of AZIBs due to a high theoretical specific capacity of 308 mAh g^{-1} for single electron reaction of $Mn^{3+} \leftrightarrow Mn^{4+}$, along with a relatively high discharge plateau (~1.3V *vs.* Zn/Zn^{2+}) compared with vanadium oxides. Furthermore, lower valance of manganese ions in compounds such as $ZnMn_2O_4$[51], Mn_2O_3[63] and Mn_3O_4[64,65] have also been explored as viable cathode materials for AZIBs. Therefore, it was expected that a higher energy density of manganese oxides could be achieved. Nevertheless, the resulting performance of manganese oxides cathode presented unsatisfied specific capacity and cycling stabilities because of irreversible structure transformation where Jahn-Teller instability occurs and generation of Mn^{2+} (soluble) species derived from disproportionation reaction of Mn^{3+} during discharge process.[66] To overcome the issues, Pan *et al.* first proposed an additive of Mn^{2+} in electrolyte which can effectively prohibit structure collapse from self-dissolution with alleviated active materials loss, and thus excellent performance of 285 mAh g^{-1} and 92% capacity retention after 5000 cycling tests were attained.[27] Accordingly, further studies of manganese oxides-based cathodes all employed additives of Mn^{2+} salts selected on the basis of anions categories of adopted zinc salts in aqueous electrolyte. It should be noted that the Mn^{2+} from additive and self-dissolution can also electro-oxidized/deposited to MnO_2 in the same aqueous electrolyte for AZIBs in accordance

with the following equation[46,67,68,69] which could exaggerate specific capacity of manganese-based oxides due to two electrons transfer reaction ($Mn^{2+}\leftrightarrow Mn^{4+}$) and exceed manganese species, but fewer scholars mentioned in their reported studies.

$$Mn^{2+} + 2H_2O \leftrightarrow MnO_2 + 4H^+ + 2e^- \quad (11)$$

It is interesting that only few papers claimed that there is a dramatic discrepancy of observed capacity regarding the inserted products and suggested mechanism[70] and the capacity contribution of electro-deposition from Mn^{2+} in aqueous electrolyte could dominate in aqueous Zn-MnO_2 batteries.[71] In addition to interference from Mn^{2+} dissolution/deposition, the energy storage mechanism of manganese-based oxides for AZIBs mentioned before are still in dispute, even though many *in/ex-situ* characterizations were carried out to unravel the principles governing manganese oxides electrochemistry. Therefore, it is necessary to create a standard system to evaluate aqueous Zn-MnO_2 batteries under identical conditions in further researches.

1.4.2 Vanadium oxides

Beyond manganese-based cathode for AZIBs, vanadium oxides are particularly fascinating because of versatile crystal structures, open frameworks with high stability and multiple redox reaction states of vanadium (V^{3+},V^{4+} and V^{5+}) both contributing on relatively larger specific capacity (>350 mAh g^{-1}) and long-cycling stability.[72] Additionally, unlike ambiguous reaction mechanism and discrepant performance observed in manganese oxides for AZIBs, insertion of Zn^{2+} (occasionally accompanied with water molecule) and co-insertion of H^+ and Zn^{2+} are extensively recognized as dominated energy storage mechanism in vanadium-oxide based cathodes for AZIBs.[41] The reported diverse vanadium oxides composing different configurations of polyhedral VO_x chains, layers or 3D frameworks with the two prevailed reaction schemes were illustrated in Figure 8.[41] Among them, the open frameworks of layered V_2O_5[73], V_3O_8[74] and $VOPO_4$[75,76] gained the most attention because of superior rate capability and favourable stability observed in previous researches. This is owing to tuneable crystal structures by pre-intercalation of diverse cations and water as “pillars” which are accommodated within layers of VO_x polyhedrons, which can endow significant improvements on electrochemistry and intrinsic properties for AZIBs applications from five aspects of inhibited “lattice breathing”, screen effect, compensated capacity loss, enhanced ionic diffusion and electronic conductivity.[77]

For instance, a Zn^{2+} pre-intercalated σ-V_2O_5 cathode materials was successfully developed for high performance AZIBs by Kundu et al. in 2016, which triggered great interests in these materials, so-called vanadium bronzes, by instituting pre-intercalated ions in V_2O_5 frameworks, such as $Mg_{0.25}V_2O_5{\cdot}nH_2O$[78], $Ca_{0.25}V_2O_5{\cdot}nH_2O$[79], $Na_{0.33}V_2O_5{\cdot}nH_2O$[80], $Ag_{0.4}V_2O_5{\cdot}nH_2O$[81], $K_{0.5}V_2O_5{\cdot}nH_2O$[82], $(NH_4)_{0.25}V_2O_5{\cdot}nH_2O$[83] and $M_xV_2O_5{\cdot}nH_2O$[84] (M: transition metal ions of Cu, Fe, Mn, Co, Ni). However, misinterpreted crystallographic phase of V_2O_5 (σ and δ) and lack of systematic comparison between pre-inserted cations effects in vanadium bronzes under identical conditions hindered disclosure of true electrochemical properties and reaction behaviours of as-obtained vanadium bronzes. Therefore, there is few investigation on the relationship between fine structures of vanadium bronzes with specific pre-inserted cations and zinc storage mechanism at present. Moreover, a detailed zinc diffusion pathway and accommodation sites are also crucial for design and optimization of novel vanadium bronzes in AZIBs applications.

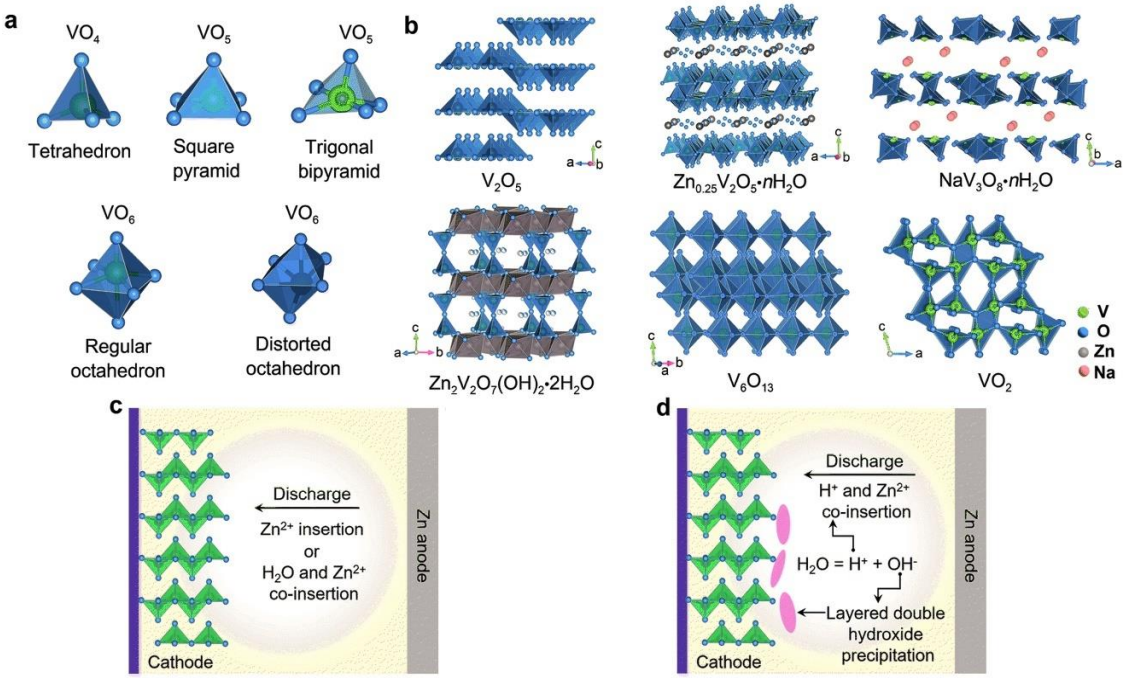

Figure 1.8. a) Various VO_x polyhedron, b) Crystallographic structures of reported various vanadium oxides and two dominated reaction mechanism of c) Zn^{2+}/water accompanied Zn^{2+} insertion and b) co-insertion of H^+ and Zn^{2+} for vanadium oxides.[41] (Reproduced with permission, Copyright © The Royal Society of Chemistry 2020)

1.4.3 Prussian blue analogues

Prussian blue analogues (PBAs) are also prevalent as promising host materials for

metal-ions batteries due to 3D rock-salt-type cubic open frameworks composing of intersecting tunnels for rapid diffusion of charge carriers.[85] Typically, a general formulation of PBAs can be written as $A_xM_1[M_2(CN)_6]_y \cdot zH_2O$, in which, A refers to metal ions accommodated in tunnels of cubic cavities, and two potential redox sites of $M_1^{2+/3+}$ and $M_2^{2+/3+}$ stand for transition metal ions bridged by ligand of cyanide ion with alternate arrangement to construct the frameworks. The H_2O can either stay in the cubic cavities, or take position of $[M_2(CN)_6]^{(1+x)-}$ ligands forming a defective motif of the lattice. Furthermore, the majority of prepared PBAs derived precursors of potassium ferricyanide(III) or potassium hexacyanoferrate(II) and other transition metal salts, thus these PBAs can be also rewritten as metal hexacyanoferrate (HCF). It was found in lithium-/ sodium-ion batteries that a stable defect occurs in PBAs which can not only provide alternative pathway for guest ions migration rather than conventional <100> tunnels, but alleviate distortion of <111> cooperative displacement during excess ions insertion.[86] An illustration of defected and normal lattice of PBAs with inserted guest ions within the cavities (A sites) is shown in Figure 9 (a) and (b), respectively. Nevertheless, unexpected defects can also induce a random distribution of the metal-ligand bridges and excessive interstitial water molecule, which can degrade stability of the lattice and block guest ion diffusion. Thus, a rational design of defected PBAs materials is crucial to unleash the full potential for battery applications.

Figure 1.9. (a) Defected PBAs with vacancy inside of cubic lattice (one of the spatial configurations). **(**b) Normal PBAs analogues with A sites occupied by guest ions.[87] (Reproduced with permission, Copyright © The Royal Society of Chemistry 2020)

To date, although the developed PBAs possessed the highest operating voltage of 1.5-1.7 V *vs.* Zn/Zn^{2+} compared with other cathode materials for AZIBs. Generally, there is

a limited specific capacity of <70 mAh g^{-1} and fast degradation of performance attained in the majority of previous studied PBAs for AZIBs[72], such as CuHCF[88,89], ZnHCF[90,91], NiHCF[92], FeHCF[93,94], and CoHCF[94]. One reason is that there is only single redox specie of $Fe^{3+/2+}(CN)_6$ in frameworks contributing to the specific capacity. Taking the example of ZnHCF, Zhang et al. reported a ZnHCF | 1M $ZnSO_4$ | Zn battery with a specific capacity of 65.4 mAh g^{-1} at current density of 1C (60 mA g^{-1}) and 24% capacity decay after 100 cycling tests. Additionally, verified redox reactions from Fe(II/III) ligand and varied amount of zinc species in the active material upon discharge/charge process implies feasible zinc storage properties and electrochemical behaviours.[91] Nevertheless, limited specific capacity associated with an energy density of 100 Wh kg^{-1} (on the basis of the total mass of active material) is much lower than those of manganese-/vanadium oxides (> 200 Wh kg^{-1}).[95] Therefore, two-redox species of Co(III/II) and Fe(III/II) were developed to fabricate CoHCF for AZIBs applications recently. The corresponding results presented remarkable enhancement of specific capacity (173.4 mAh g^{-1} @ 0.3 A g^{-1}),[96] which clearly prove the feasibility of introducing active redox species for improved performance of PBAs in AZIBs applications.

In conclusion, it is seen that tremendous progress has been achieved in AZIBs for cathode materials researches, and many promising strategies on material design have been proposed. However, comparing with developed cathode material categories for lithium-ion batteries, there are few competent material candidates which can be utilized for AZIBs so far due to sluggish diffusion kinetics derived from large hydrated ionic radii and strong electrostatic of bivalent charge charrier (Zn^{2+}) with host frameworks as well as competitive insertion species from aqueous electrolyte. The gravimetric energy/power density of representative cathode materials for AZIBs have been displayed in the Ragone plot (Figure 10). The ultimate obstacle of developing high performance AZIBs system are still related to studies of cathode materials such as ambiguous reaction mechanism and unsatisfied specific capacity compared with the merits of zinc anode. Therefore, more systematic analysis of reaction characteristics and novel materials development should be addressed for bringing breakthrough in this field.

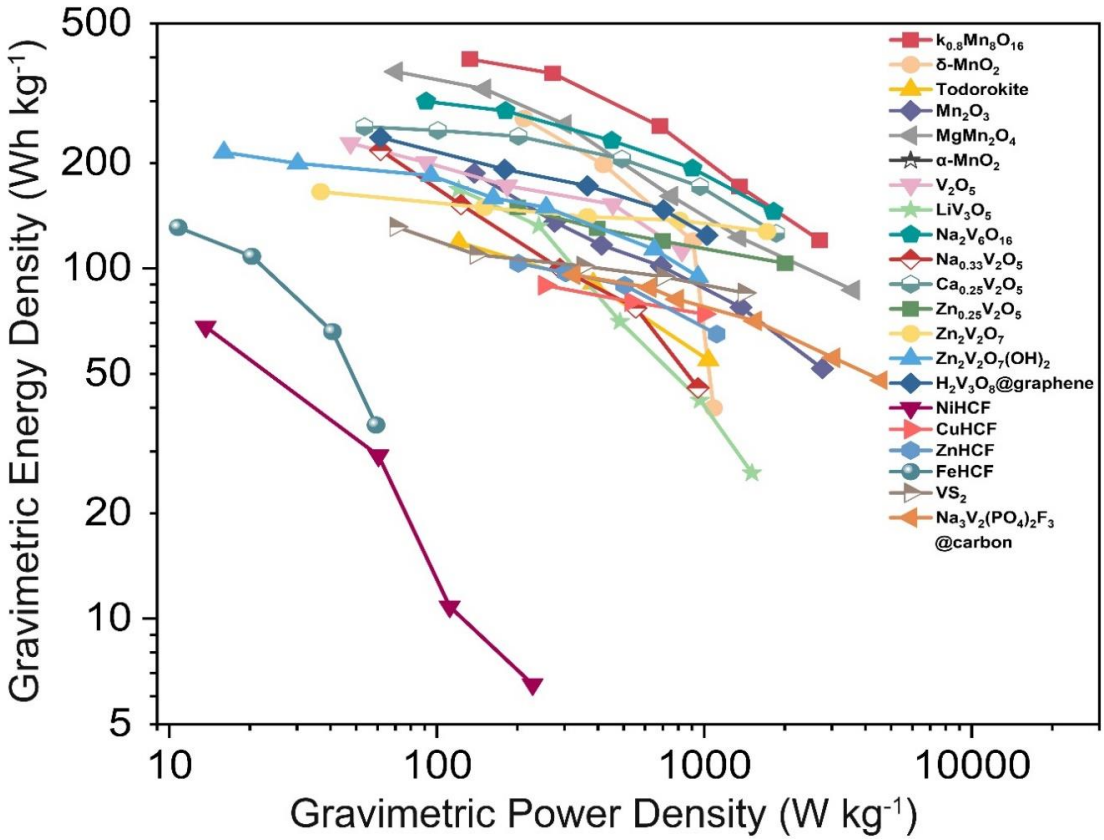

Figure 1.10. Ragone plot of representative cathode materials for AZIBs.

1.5 Prospects and challenges

In this chapter, the summarized advantages and drawbacks of AZIBs techniques are first discussed. Accordingly, hindrance derived from insufficient performance of cathode materials and intrinsic issue of aqueous electrolyte substantially turned into the challenges of their extensive applications in EES system. Therefore, some promising strategies will be proposed, which could offer opportunities for the future development of novel materials for practical applications.

1.5.1 Advantages and applications

As mentioned earlier, AZIBs techniques possess unparalleled merits from many aspects including cost, safety, performance, environmental impacts and manufacturing feasibility. Because of these benefits from neutral/mild acidic aqueous electrolytes and adequate metallic zinc anode. Through great efforts on development of cathode materials for AZIBs, the performance has approached that of Li-ion batteries (Figure

1.11), which could dominate complementary markets of Li-ion batteries in the near future, especially for grid-scale stationery and flexible electronic EES systems.

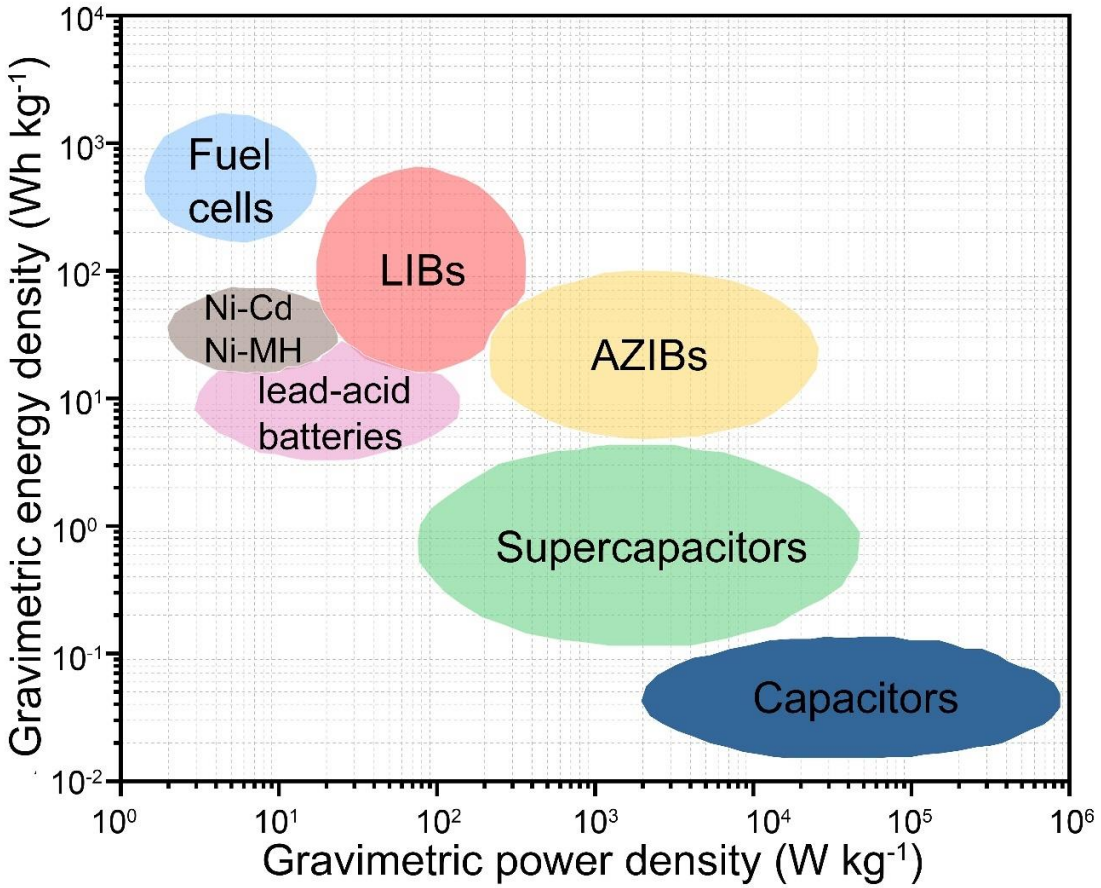

Figure 1.11. Ragone plot of comparison between various EES techniques. (N.B. the collected performance data of zinc ion batteries from literature are main based on active mass of cathode materials, not from cell-level perspective.) (Reprinted (adapted) with permission from (Ref.25). Copyright (2020) American Chemical Society.)

1.5.2 Drawbacks and challenges

As discussed above, some clear drawbacks and issues still exist in this field, such as limited operating voltage window of aqueous electrolyte, water-induced side reactions and sluggish diffusion kinetics of charge carriers seriously confine the energy density of the devices and resulting in unstable features of cathode materials during charge/discharge process. Additionally, ambiguous zinc storage mechanism and misinterpreted electrochemical, structural, and chemical states characteristics in previous studies provide disputable performance for practical applications, especially for manganese-based cathodes. Therefore, it is essential to establish a critical evaluation system with standard evaluation parameters for the studies in order to fulfil urgent

demands of novel EES techniques. Moreover, even though the march of AZIBs have made remarkable innovations in the last few years, it still stays at the initial stage of EES techniques for particle applications. To date, it should be noted that there are only few reported prototypes of a cell-level AZIBs (Pouch cell or 18650 cylinder cell), which have been invented and characterized to compare with other commercialized EES products. Therefore, the record of performance should be evaluated, and engineering technique on cost-effective fabrication of high performance AZIBs are also needed as synergetic development with materials chemistry/physics in this field. Although it is seen that numerous challenges are still out there waiting, the strategies of novel material investigations integrated with advanced material designs from physicochemical structural modifications, such as defects engineering, heterojunction composites and interfacial functionality, could ultimately conquer the field as occurred in other matured EES techniques.

1.6 Reference

1 B. X. Hu, C. Zou, C. Zhang and Y. Li, *IEEE Power and Energy* Magazine, **2017**, 15, 20–31

2 Y. Hu, *Nat Energy*, **2016**, 1, 16042

3 T. Kim, W. Song, D. Son, L. K. Ono and Y. Qi, *J. Mater. Chem. A,* **2019**, 7, 2942-2964.

4 P. K. Nayak, L. Yang, W. Brehm and P. Adelhelm, *Angew. Chem. Int. Ed.,* **2018**, 57, 102.

5 B. Scrosati, J. Hassoun and Y. K. Sun, *Energy Environ. Sci.,* **2011**, 4, 3287-3295.

6 M. D. Slater, D. Kim, E. Lee and C. S. Johnson, *Adv. Funct. Mater.,* **2013**, 23, 947-958.

7 J. C. Pramudita, D. Sehrawat, D. Goonetilleke and N. Sharma, *Adv. Energy Mater.,* **2017**, 7, 1602911.

8 Y. Liang, H. Dong, D. Aurbach and Y. Yao, *Nat. Energy*, **2020**, 5, 646–656.

9 M. J. Park, H. Y. Asl and A. Manthiram, *ACS Energy Lett.,* **2020**, 5, 2367–2375.

10 M. Winter, B. Barnett and K. Xu, *Chem. Rev.,* **2018**, 118, 11433–11456.

11 D. Di Lecce, R. Verrelli and D. Di Lecce, *Green Chem.* **2017**, 19, 3442–3467.

12 X. Cheng, R. Zhang, C. Zhao and Q. Zhang, *Adv. Mater.,* **2018**, 30, 1800561.

13 V. Etacheri, R. Marom, R. Elazari, G. Salitra and D. Aurbach, *Energy Environ. Sci.,* **2011**, 4, 3243

14 M. R. Palacín, A. de Guiber, *Science*, **2016**, 351,2353292

15 C. Liu, J. Yuan, R. Masse, X. Jia, W. Bi and Z. Neale, *Adv. Mater.,* **2020**, 1905245.

16 K. Xu, *Chem. Rev.,* **2014**, 114, 11503–11618

17 X. Zhang, A. Wang, X. Liu and J. Luo, *Acc. Chem. Res.*, 2**019**, 52, 3223-3232.

18 C. T. Love, E. C. S. Electrochem, A. Lett, C. T. Love, O. A. Baturina and K. E. Swider-lyons, *ECS Electrochem. Lett.,* **2014**, 4, A24.

19 G. Martin, L. Rentsch, M. Höck and M. Bertau, *Energy Storage Mater.*, **2020**, 6, 171–179.

20 H. Ambrose, *J Ind Ecol.,* **2020**, 24, 80–89.

21 C. Masquelier and L. Croguennec, *Chem. Rev.,* **2013**, 113, 6552–6591.

22 Y. Fang, J. Zhang, L. Xiao, X. Ai, Y. Cao and H. Yang, *Adv. Sci.,* **2017**, 4, 1600392.

23 C. Vaalma, D. Buchholz and S. Passerini, *Curr. Opin. Electrochem.,* **2018**, 9, 41-48.

24 D. H. Doughty, P. C. Butler, A. A. Akhil, N. H. Clark and J. D. Boyes, *Electrochem. Soc. Interface,* **2010**, 19, 49.

25 X. Jia, C. Liu, Z. G. Neale, J. Yang and G. Cao, *Chem. Rev.,* **2020**, 120, 7795–7866

26 C. Xu, B. Li, H. Du and F. Kang, *Angew. Chem. Int. Ed.,* 2012, **51**, 933–935.

27 H. Pan, Y. Shao, P. Yan, Y. Cheng, K. S. Han, Z. Nie, C. Wang, J. Yang, X. Li, P. Bhattacharya, K. T. Mueller and J. Liu, *Nat Energy,* **2016**, 1, 16039.

28 W. Sun, F. Wang, S. Hou, C. Yang, X. Fan, Z. Ma and T. Gao, *J. Am. Chem. Soc.*, **2017**, 139, 9775–9778.

29 Q. Zhao, X. Chen, Z. Wang, L. Yang, R. Qin, J. Yang, Y. Song, K. Yang, Y. Cui, H. Chen and F. Pan, *Small*, **2019**, 15, 1904545.

30 G. Liu, H. Huang, R. Bi, X. Xiao, T. Ma and L. Zhang, *J. Mater. Chem. A,* **2019**, 7, 20806-20812.

31 J. Huang, Z. Wang, M. Hou, X. Dong, Y. Liu, Y. Wang and Y. Xia, *Nat. Commun.*, **2018**, 9, 1–8.

32 F. Wan, L. Zhang, X. Dai, X. Wang, Z. Niu and J. Chen, *Nat. Commun.*, **2018**, 9, 1–11.

33 W. Liu, L. Dong, B. Jiang, Y. Huang and X. Wang, *Electrochim. Acta*, **2019**, 320, 134565.

34 T. Xin, Y. Wang, N. Wang, Y. Zhao, H. Li, Z. Zhang and J. Liu, *J. Mater. Chem. A,* **2019**, 7, 23076-23083

35 Z. Li, S. Ganapathy, Y. Xu, Z. Zhou and M. Sarilar, *Adv. Energy Mater.,* **2019**, 9, 1900237.

36 W. Manalastas, S. Kumar, V. Verma, L. Zhang, D. Yuan, M. Srinivasan*, ChemSusChem,* **2019**, 12, 379.

37 D. P. Leonard, Z. Wei, G. Chen, F. Du and X. Ji, *ACS Energy Lett.,* **2018**, 3, 373–374.

38 L. Suo, F. Han, X. Fan, H. Liu, K. Xu and C. Wang, *J. Mater. Chem. A,* **2016**, 4, 6639-6644.

39 L. Suo, O. Borodin, T. Gao, M. Olguin, J. Ho, X. Fan, C. Luo, C. Wang and K. Xu, *Science*, **2015**, 350, 938-943.

40 S. Liu, L. Kang, J. M. Kim, Y. T. Chun, J. Zhang and S. C. Jun, *Adv. Energy*

Mater., **2020**, 10, 2000477.

41 N. Zhang, X. Chen, M. Yu, Z. Niu, F. Chen, J. Chen*, Chem. Soc. Rev.,* **2020**, 49, 4203–4219.

42 N. Zhang, F. Cheng, Y. Liu, Q. Zhao, K. Lei, C. Chen, X. Liu and J. Chen, *J. Am. Chem. Soc.*, **2016**, 138, 12894–12901.

43 F. Wang, O. Borodin, T. Gao, X. Fan, W. Sun, F. Han, A. Faraone, J. A. Dura, K. Xu and C. Wang, *Nat. Mater.*, **2018**, 17, 543–549.

44 Z. Liu, Y. Huang, Y. Huang, Q. Yang, X. Li, Z. Huang and C. Zhi, *Chem. Soc. Rev.,* **2020**, 49, 180-232.

45 N. Zhang and F. Cheng, J. Liu, L. Wang, X. Long, X. Liu, F. Li and J. Chen, *Nat. Commun.*, 2000, **8**, 1–9.

46 W. Liu, X. Zhang, Y. Huang, B. Jiang and Z. Chang, *J. Energy Chem.*, 2021, **56**, 365–373.

47 X. Wu, Y. Xiang, Q. Peng, X. Wu, Y. Li, F. Tang, R. Song, Z. Liu, Z. He and X. Wu, *J. Mater. Chem. A,* **2017**, 5, 17990-17997.

48 F. Wang, O. Borodin, T. Gao, X. Fan, W. Sun, F. Han, A. Faraone, J. A. Dura, K. Xu and C. Wang, *Nat. Mater.*, **2018**, 17, 543–549.

49 G. Li, Z. Yang, Y. Jiang, C. Jin, W. Huang and X. Ding, *Nano Energy*, **2016**, 25, 211–217.

50 X. Wu, Y. Xu, C. Zhang, D. P. Leonard, A. Markir, J. Lu, and X. Ji, j Li and J. Chen, *J. Am. Chem. Soc.,* **2019**, 141, 6338–6344.

51 N. Zhang, F. Cheng, Y. Liu, Q. Zhao, K. Lei and C. Chen, *J. Am. Chem. Soc.,* **2016**, 138, 12894–12901.

52 F. Wan, Y. Zhang, L. Zhang, D. Liu, C. Wang, L. Song and Z. Niu, *Angew. Chem. Int. Ed.*, **2019**, 58, 7062.

53 A. Mitha, H. Mi, W. Dong, I. Sik, J. Ly, S. Yoo and S. Bang, *J. Electroanal. Chem.*, **2019**, 836, 1–6.

54 J. Zhao, H. Ren, Q. Liang, D. Yuan, S. Xi, C. Wu, W. Manalastas, J. Ma, W. Fang, Y. Zheng, C. Du, M. Srinivasan and Q. Yan, *Nano Energy*, **2019**, 62, 94–102.

55 S. Zhang, N. Yu, S. Zeng, S. Zhou, M. Chen, J. Di and Q. Li, *J. Mater. Chem. A,* **2018**, 6, 12237-12243.

56 Y. Zeng, X. Zhang, Y. Meng, M. Yu, J. Yi, Y. Wu, X. Lu and Y. Tong, *Adv. Mater.,* **2017**, 29, 1700274.

57 W. Qiu, Y. Li, A. You, Z. Zhang, G. Li, X. Lu and Y. Tong, *J. Mater. Chem. A,*

2017, 5, 14838-14846.

58 Q. Li, J. Guo, L. Xie, C. Li, X. Wang and J. Zhao, *J. Mater. Chem. A,* **2018**, 14594–14601.

59 H. Cao, F. Wan, L. Zhang, X. Dai, S. Huang, L. Liu and Z. Niu, *J. Mater. Chem. A,* **2019**, 11734–11741.

60 H. Li, Z. Liu, G. Liang, Y. Huang, Y. Huang, M. Zhu, Z. Pei, Q. Xue, Z. Tang, Y. Wang, B. Li and C. Zhi, *ACS Nano,* **2018**, 12, 3140–3148.

61 Z. Wang, F. Mo, L. Ma, Q. Yang, G. Liang, Z. Liu, H. Li, N. Li, H. Zhang, and C. Zhi, *ACS Appl. Mater. Interfaces,* **2018**, 10, 44527–44534.

62 F. Mo, G. Liang, Q. Meng, Z. Liu, H. Li, J. Fan and C. Zhi, *Energy Environ. Sci.,* **2019**, 12, 706–715.

63 B. Jiang, C. Xu, C. Wu, L. Dong, J. Li and F. Kang, *Electrochim. Acta*, **2017**, 229, 422–428.

64 J. Hao, J. Mou, J. Zhang, L. Dong and W. Liu, *Electrochim. Acta*, **2018**, 259, 170–178.

65 C. Zhu, G. Fang, J. Zhou, J. Guo, Z. Wang, C. Wang, J. Li, Y. Tang and S. Liang, *J. Mater. Chem. A,* **2018**, 6, 9677-9683.

66 B. Lee, H. R. Lee, H. Kim, K. Y. Chung, B. W. Cho and S. H. Oh, *Chem. Commun.,* **2015**, 51, 9265-9268.

67 Y. Li, S. Wang, J. R. Salvador, J. Wu, B. Liu, W. Yang, J. Yang, W. Zhang, J. Liu and J. Yang, *Chem. Mater.,* **2019**, 31, 2036–2047.

68 D. Chao, W. Zhou, C. Ye, Q. Zhang, Y. Chen, L. Gu, K. Davey and S. Qiao, *Angew. Chem. Int. Ed.,* **2019**, 58, 7823.

69 B. Wu, G. Zhang, M. Yan, T. Xiong, P. He, L. He and X. Xu, *Small,* **2018**, 14, 1703850.

70 L. E. Blanc, D. Kundu and L. F. Nazar, *Joule*, **2020**, 4, 771–799.

71 X. Guo, J. Zhou, C. Bai, X. Li and G. Fang, *Mater. Today Energy*, **2020**, 16, 100396.

72 G. Fang, J. Zhou, A. Pan and S. Liang, *ACS Energy Lett.,* **2018**, 3, 10, 2480–2501.

73 Y. Oka and T. Yao, *J. Solid State Chem.*, **1997**, 329, 323–329.

74 P. Hu, T. Zhu, X. Wang, X. Wei, M. Yan, J. Li, W. Luo, W. Yang, W. Zhang, L. Zhou, Z. Zhou and L. Mai, *Nano Lett.*, **2018**, 18, 1758–1763.

75 V. Verma, S. Kumar, W. Manalastas Jr., J. Zhao, R. Chua, S. Meng, P.

Kidkhunthod, and M. Srinivasan, *ACS Appl. Energy Mater.,* **2019**, 2, 8667–8674.

76 Z. Wu, Y. Wang, L. Zhang, L. Jiang, W. Tian, C. Cai, J. Price, Q. Gu and L. Hu, *ACS Appl. Energy Mater.,* **2020**, 3, 3919–3927.

77 X. Yao, Y. Zhao, F. A. Castro and L. Mai, *ACS Energy Lett.,* **2019**, 4, 771–778.

78 F. Ming, H. Liang, Y. Lei, S. Kandambeth, M. Eddaoudi and H. N. Alshareef, *ACS Energy Lett.*, **2018**, 3, 2602–2609.

79 C. Xia, J. Guo, P. Li, X. Zhang and H. N. Alshareef, *Angew. Chemie Int. Ed.*, **2018**, 57, 3943–3948.

80 P. He, G. Zhang, X. Liao, M. Yan, X. Xu, Q. An, J. Liu and L. Mai, *Adv. Energy Mater.*, **2018**, 8, 1–6.

81 L. Shan, Y. Yang, W. Zhang, H. Chen, G. Fang, J. Zhou and S. Liang, *Energy Storage Mater.*, **2019**, 18, 10–14.

82 S. Islam, M. H. Alfaruqi, D. Y. Putro, V. Soundharrajan, B. Sambandam, J. Jo, S. Park, S. Lee, V. Mathew, J. Kim, *J. Mater. Chem. A,* **2019**, 7, 20335-20347.

83 B. Tang, J. Zhou, G. Fang, F. Liu, C. Zhu, C. Wang, A. Pan and S. Liang, *J. Mater. Chem. A*, **2019**, 7, 940–945.

84 Y. Yang, Y. Tang, S. Liang, Z. Wu, G. Fang, X. Cao, C. Wang, T. Lin, A. Pan and J. Zhou, *Nano Energy*, **2019**, 61, 617–625.

85 D. Chen, M. Lu, D. Cai, H. Yang and W. Han, *J. Energy Chem.*, **2021**, 54, 712–727.

86 K. Hurlbutt, S. Wheeler, I. Capone and M. Pasta, *Joule*, **2018**, 2, 1950–1960.

87 A. Paolella, C. Faure, V. Timoshevskii, S. Marras, G. Bertoni, A. Guerfi, A.Vijh, M. Armand and K. Zaghib, *J. Mater. Chem. A,* **2017**, 5, 18919-18932

88 Z. Jia, B. Wang and Y. Wang, *Mater. Chem. Phys.*, **2015**, 149, 601–606.

89 V. Renman, D. O. Ojwang, M. Valvo and C. P. G, *J. Power Sources,* **2017**, 369, 146–153.

90 L. Zhang, L. Chen, X. Zhou and Z. Liu, *Sci Rep.,* **2015**, 5, 18263.

91 L. Zhang, L. Chen, X. Zhou and Z. Liu, *Adv. Energy Mater.,* **2015**, 5,1400930.

92 K. Lu, B. Song, J. Zhang and H. Ma, J. Power Sources, 2016, 321, 257–263.

93 Z. Liu, P. Bertram and F. Endres*, J Solid State Electrochem,* **2021**, 21, 2021–2027.

94 Q. Yang, F. Mo, Z. Liu, L. Ma, X. Li, D. Fang, S. Chen, S. Zhang and C. Zhi, *Adv. Mater.,* **2019**, 31, 1901521.

95 P. He, Q. Chen, M. Yan, X. Xu, L. Zhou, L. Mai and C. Nan, *EnergyChem,* **2019**,

1, 100022.

96 L. Ma, S. Chen, C. Long, X. Li, Y. Zhao, Z. Liu, Z. Huang, B. Dong, J. A. Zapien and C. Zhi, *Adv. Energy Mater.,* **2019**, 9, 1902446.

Chapter 2.

Investigations of δ-$Ni_{0.25}V_2O_5 \cdot nH_2O$ and its analogues cathodes for high performance aqueous zinc ion batteries

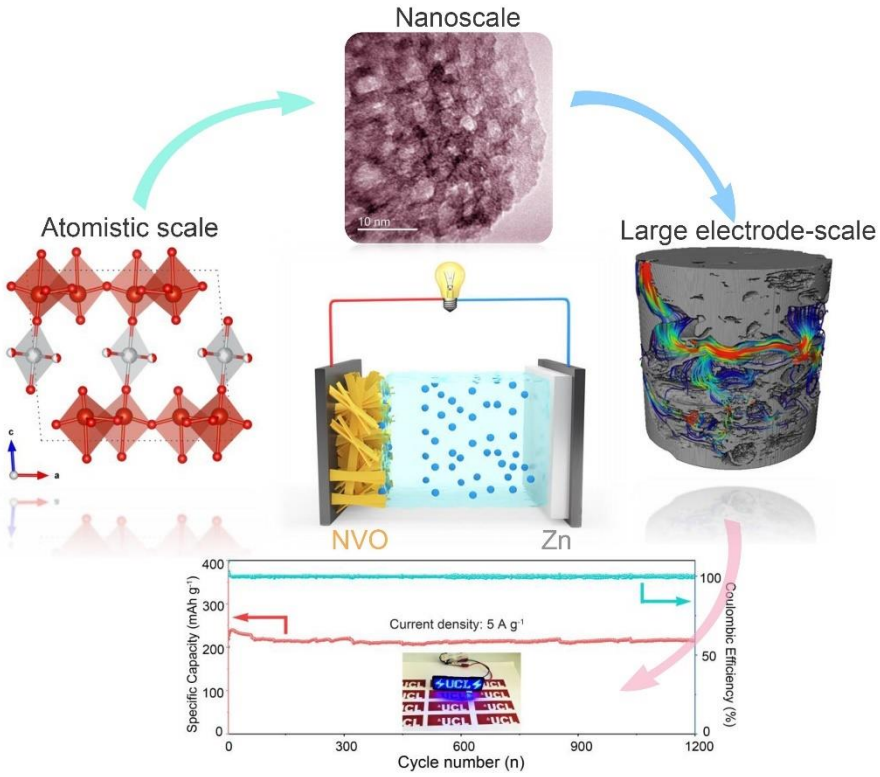

2.1 Introduction

With extensive use of new and renewable energy harvesting technologies to deal with serious environmental issues, there is an unprecedented rise in demand for cost-effective and reliable electrochemical energy storage (EES) equipment. As the most successful commercialized secondary ion batteries, lithium-ion batteries (LIBs) exhibit high energy density and cycling durability, which brought extraordinary technological revolutions in many aspects of life.[1] Nevertheless, considering the rising cost of lithium resources and safety hazards caused by the inherent chemical properties of metallic lithium and adopted combustible ester electrolytes; aqueous rechargeable batteries have gained great interests as promising alternatives, especially for grid-scale EES applications.[2] Among them, aqueous zinc-ion batteries (AZIBs) have received dramatic attention on the basis of neutral/mild acidic aqueous system, which is attributed to the remarkable merits of metallic zinc.[3,4,5,6] Because of that, enormous efforts have been dedicated to studies on cathode materials such as manganese oxides[9,10], vanadium oxides[11,12] and Prussian blue analogues.[7,8] Although higher ionic conductivity is obtained in the aqueous electrolyte[13], a much stronger electrostatic interaction exists between Zn^{2+} and large radii of hydrated charge carriers compared with other alkali-metal ions.[14,15] In this respect, there are severe choices of adequate hosts for the high-performance purposes. Whereas, diverse layered vanadium bronzes step into the spotlight since the multiple valence offering theoretical specific capacity above 300 mAh g^{-1} and tuneable interlayer spacing facilitating Zn^{2+} fast migration.[16,17] In addition, the pre-inserted guest species accommodated within interlayer spacing of VO_x polyhedron slabs, such as metal cations, H_2O or organic molecules, has been proven to optimize physicochemical properties of host materials effectively. Features such as extended cycling life, rapid ion diffusion from screen effect, inhibited lattice breath and enhanced electronic conductivity by tuned electronic structures.[18,19,20] To date, various vanadium bronzes have been studied, with pre-inserted ions of Zn[17], Mg[16], Ca[21], Na[19], Mn[22], and Cu[23] However, owing to crystallographic phase complexities of V_2O_5 host (e.g. α, δ, γ and σ), the zinc storage mechanism evaluations on specific frameworks may vary. Otherwise, a misinterpreted local coordination of intercalated charge carriers with different vanadium polyhedral in phase varied V_2O_5 host skeletons will definitely bring a deviation of cognition for primary principles in AZIBs, which have been observed in comparison of previously reported δ- and σ-type vanadium bronzes.[24,25,26,27,28]

Meanwhile, to further enhance interfacial diffusion efficiency of charge carriers between solid and liquid phases in battery system, introducing porous structures have been widely demonstrated as effective approaches for high performance electrode.[29,30] Nevertheless, the majority of synthetic routes for this purpose are template derived and require enormous time-consuming work and complicated process.[31,32]

In this regard, this thesis presents a study of hydrated δ-Ni(Co)$_{0.25}$V$_2$O$_5$ (i.e. NVO and CVO) adopted as cathode materials for AZIBs which show remarkable specific capacity of 402 mAh g^{-1} and 326.8 mAh g^{-1}, respectively, at 0.2 A g^{-1}. Moreover, the excellent cycle stability of NVO was obtained with only 2% specific decay after 1200 cycles. These two distinct δ-vanadium bronzes are for the first time utilized in battery applications. Meanwhile, comparison regarding the various crystalline phases of vanadium bronzes are discussed, and efforts have been made to elucidate the underlying reaction mechanisms, which are achieved by multiple *ex-situ* characterizations including X-ray diffraction (XRD), X-ray photoelectrons spectrometer (XPS), Raman, energy dispersive spectroscopy (EDS), High-Resolution Transmission Electron Microscope (HRTEM) and DFT calculations. In particular, we proposed the design strategy and deep insight of our high-performance cathodes from multi-scale investigations to illuminate the promoting electrochemical reaction kinetics and superior zinc storage behaviours.

2.2 Experimental Section

2.2.1 Material synthesis

All chemicals were purchased from Sigma U.K. and employed without further purification. In a typical synthesis of hydrated δ-Ni(Co)$_{0.25}$V$_2$O$_5$·0.74H$_2$O, 1.5 mmol of commercial V$_2$O$_5$ powder was dissolved in a beaker with 35 mL deionized water (D.I. water), then the solution was vigorously stirred for 30 minutes accompanied with addition of 0.5 mmol of nickel(II)/ cobalt(II) acetate tetrahydrate and stirred separately for 15 minutes. After that, 2.2 mL acetic acid was dropwise injected into the mixed solution until the pH of 2.75 was attained. The as-obtained solution kept stirring for 30 minutes and further transferred to a 50 mL autoclave. The reaction temperature and dwelling time were set to 210°C for 48 hours. After cooling down to room temperature, the bronze colour precipitates were washed several times with ethanol and D.I. water,

and then dried by freeze-drying machine for 2 days.

2.2.2 Material characterizations

XRD: The detected angle range performed by a STOE SEIFERT diffractometer using Mo (0.7093 Å) X-ray radiation source is $2°<2\theta<45°$. Through scanning electron microscope (SEM, Carl Zeiss EVO MA10), transmission electron microscope (TEM, JEOL, JEM-2100 and ARM200F) and XPS (Thermo Scientific K-alpha photoelectron spectrometer), the morphology and chemical states were characterized, respectively. the data process of XPS was carried out initially by calibrating adventitious carbon with a binding energy at 284.8 eV, then the area of the peaks were fixed according to a ratio of 1:2 for the $2p_{1/2}$: $2p_{3/2}$. Meanwhile, FWHM of corresponding peaks ($2p_{1/2}$ and $2p_{3/2}$) were set as same length for each valance states. Moreover, the distance between two peaks of $2p_{1/2}$ and $2p_{3/2}$ for each valance states and elements were adjusted according to literature. Additionally, Raman Spectroscopy (Renishaw Raman microscope spectrometer with a laser wavelength of 514.5 nm) and attenuated total reflectance Fourier transform infrared spectrometer (FTIR, ATRFTIR, BRUKER, platinum ATR) were performed and the mass change upon increased temperature was attained by a Thermogravimetric analyzer (TGA) (PerkinElmer TGA 4000 System). The mass of the active substance for fabrication of electrode was weighed by the analytical balance (Ohaus; δ=0.01mg). Near-edge X-ray absorption fine structure (NEXAFS) was carried out by our collaborator, Mr. Liqun Kang in Dr. Ryan Wang' group, and performed under the beamline of B07 equipped with dipole synchrotron radiation of soft X-ray (50 ~ 2800 eV) at Diamond Light Source.

2.2.3 Electrochemical evaluations

The as-obtained NVO and CVO cathode materials were mixed with binder (polyvinylidene fluoride (PVDF) dissolved in 1-Methyl-2-pyrrolidinone(NMP)) and conductive agent (Super P Carbon) with a weight ratio of 7 : 1: 2, respectively. Then, printing homogeneous mixture on a current collectors (hydrophilic carbon paper) with a loading mass around 2.5 mg cm^{-1}. Subsequently, the printed electrodes were dried in a vacuum oven at 70°C for 12 hours. Finally, the completely dried electrodes were cut into disc with diameter of 14 mm and then assembled in a CR2032 coin-like cell with zinc plate as anode and 3 M ZnSO4/ $Zn(CF_3SO_3)_2$ aqueous electrolytes. A scheme of

coin cell modules are illustrated in Figure 2.1. The galvanostatic charge-discharge (GCD) measurements were performed by the NEWARE battery test system for specific capacity and cycle stability testing, and a use of the VMP3 Biologic electrochemical workstation was carried out to acquire other electrochemical properties, such as cyclic voltammetry (CV) and electrochemical impedance spectroscopy (EIS).

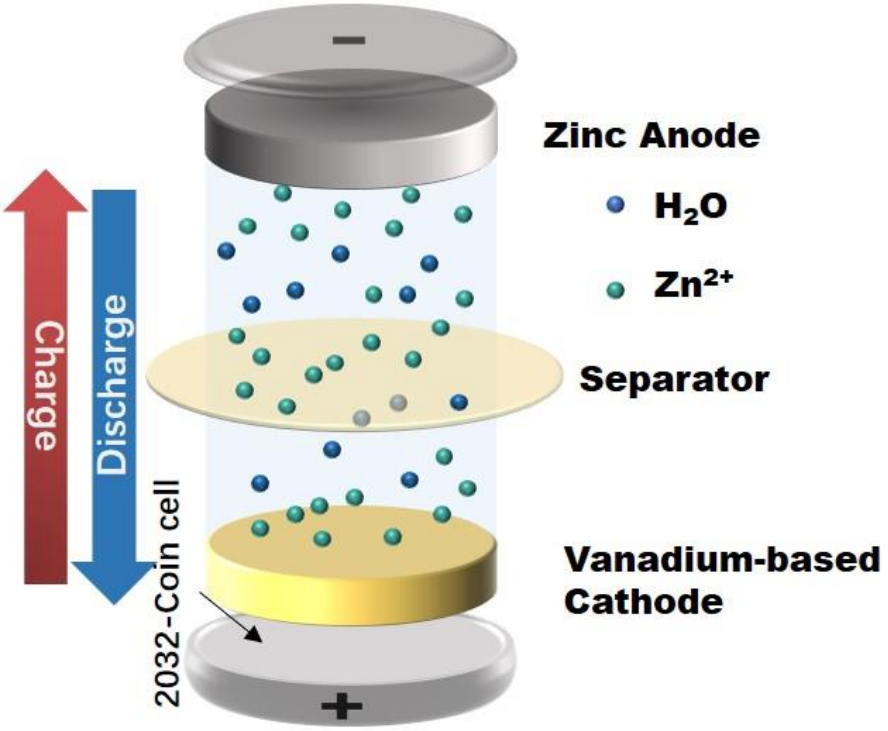

Figure 2.2.1. A scheme of each components in assembled 2032 type coin cells for AZIBs.

2.2.4 Computational methods

The periodic Density Functional Theory (DFT, CRYSTAL17) calculations[33] were achieved in collaboration with Dr. Kit McColl in Prof. Furio Cora's group from Department of Chemistry in UCL. The corresponding results hare incorporated in this thesis. In addition, hybrid-exchange functional B3LYP[34] was adopted to acquire electronic correlation and exchange and dispersion effects were performed by Grimme's semiclassical D3 scheme.[35,36,37] Moreover, the insertion energy of each Zn^{2+} was calculated by equation:

$$\Delta E_{inse} = E(Zn_xNi_{0.25}V_2O_5{\cdot}H_2O) - E(Ni_{0.25}V_2O_5{\cdot}H_2O) - xE(Zn_{(s)}) \quad (1)$$

Meanwhile, the energy of metallic zinc was determined by energy of sublimation, 1st and 2nd ionisation energies (Equation 2)

$$E(Zn_{(s)}) = E(Zn^{2+}) + E_{sub}(Zn_{(s)}) + E_{i(1)}(Zn) + E_{i(2)}(Zn) \quad (2)$$

The model of as-obtained δ-$Ni_{0.25}V_2O_5 \cdot 0.74H_2O$ adopted in DFT calculations was based on a reference structure of δ-$Mg_{0.25}V_2O_5 \cdot H_2O$,[38] in which, Mg^{2+} can be equivalently substituted by Ni^{2+} in our case. During the calculations, a unit cell with the expanded primitive cell (2×1×1) of the δ-$Ni_{0.25}V_2O_5 \cdot H_2O$ possesses lattice parameters of 11.7865 Å, 7.2324 Å and 10.2698 Å for a,b and c, respectively. In particular, the calculation for inserted site A of Zn^{2+} with stoichiometry of $Zn_{0.0625}Ni_{0.25}V_2O_5 \cdot H_2O$ were performed by using (4×1×1) unit cell in order to avoid the influence of a periodic image of Zn^{2+} in the following cell.

2.2.5 X-ray computed tomography analysis

X-ray microscopy and nano-computed tomography (nano-CT)(Zeiss Xradia Versa 520 and Ultra 810) were employed to examine the 3D microstructure of as-prepared electrode at multi-length scales with voxel resolution of 0.4 and 0.063 μm, respectively.[39] Meanwhile, The reconstruction was achieved by built-in Feldkamp-Davis-Kress (FDK) and filtered-back projection algorithm.[40,41] 3D visualization and pore-size distribution were obtained by Avizo v9.5 software (ThermoFisher Scientific). Moreover, the X-ray nano-CT data equipped the XLab in Avizo was utilized for calculating tortuosity factor and effective diffusion coefficient. The boundary condition with a concentration difference of 1000 mol m^{-3} was established within a simulation domain of inlet and outlet. Furthermore, the comparison of the diverse flow rate between the reference (porosity ε = 1) and as-obtain sample can deliver information of tortuosity and effective diffusion coefficient.[41]

2.3 Results and discussion

The synthesis process of hydrated NVO and CVO micro-ribbons was achieved by a single-step hydrothermal method. The as-obtained powders possess bronze colour exhibited in Figure 2.3.1.

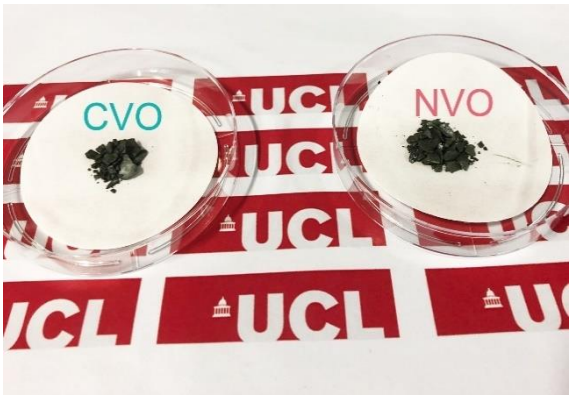

Figure 2.3.1. Digital photo of as-prepared NVO and CVO exhibiting bronze-like colour.

Additionally, as shown in Figure 2.3.2a,b a porous self-template structure of NVO was examined by scanning tunnelling electron microscopy (STEM). The typical size of the micro-ribbon is more than 10 μm in length and over 100 nm in width, and the uniform porous structures could be attributed to a metal-ligands bridging fashion induced self-assemble growth mechanism.[42] Moreover, SEM and elemental mapping characterizations in Figure 2.3.2c,d were carried out to uncover the morphology of the materials with a clearly verified uniform distribution of Ni and V elements. Through EDS analysis, an element ratio of V to Ni was 8.8:1. Similarly, the SEM image and elemental mapping of as-prepared CVO also exhibit the same order geometry morphologies with uniform elemental distribution in Figure 2.3.3a,b.

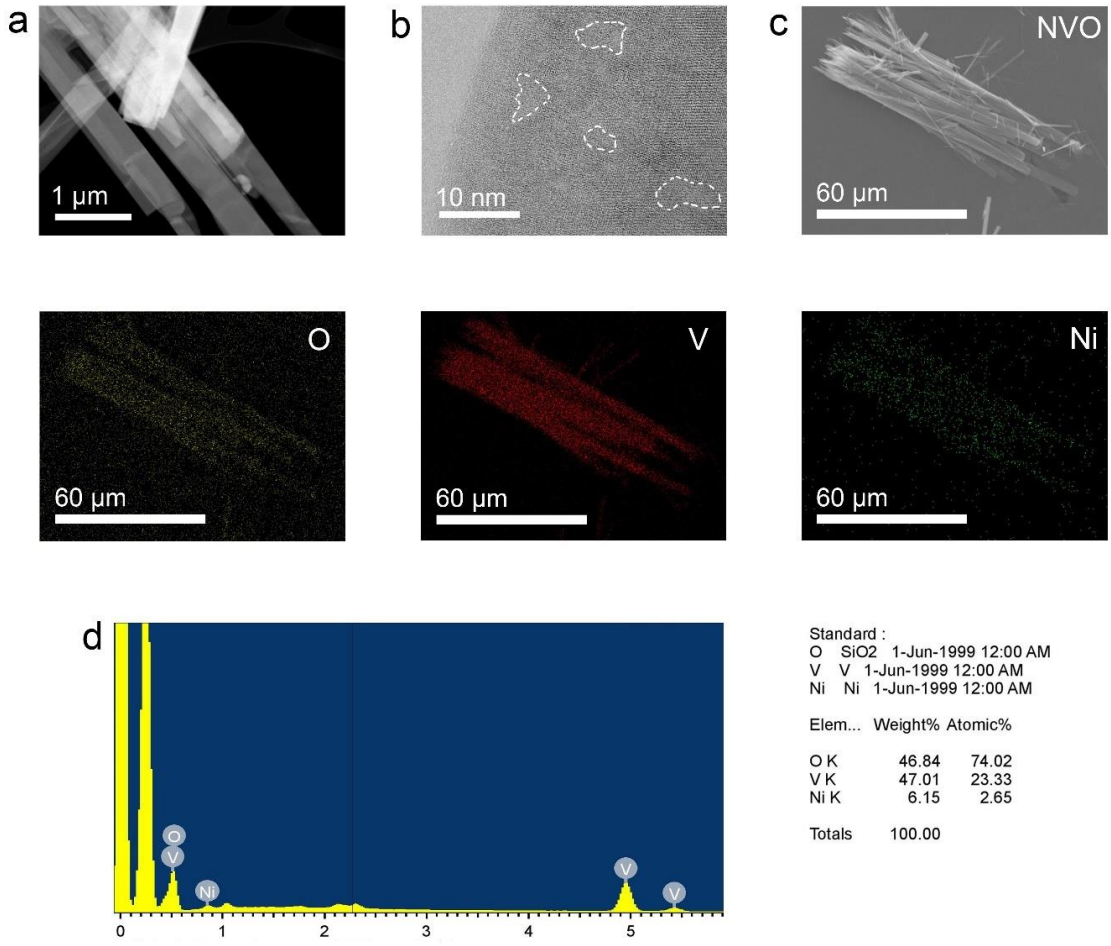

Figure 2.3.2. (a, b) STEM image, (c) SEM and elemental mapping, (d) EDX of the as-obtained NVO.

The following XRD patterns in Figure 2.3.3c clarified that the crystallographic structure of both materials can be indexed to standard PDF pattern (JCPDS No. 88-0580) of monoclinic δ-$Ni_{0.25}V_2O_5{\cdot}0.98H_2O$.[24,43] With refinement of crystal structure in Figure 2.3.4, lattice parameters and space group (C2/m monoclinic) are acquired for as-prepared NVO (table 2.3.1). More explicitly, the main intensive peak of NVO referred to the (001) plane with 2θ of 3.94° corresponding to the d-spacing of 10.3 Å, and other two conspicuous peaks at 11.67° and 11.85° stand for (110) and (003) facets, respectively. Comparably, there is a slight shift of the (001) plane to decreased 2θ position in CVO XRD pattern, which can be explained as an enlarged d-spacing from 10.3 to 10.5Å along with c-axis by instituting hydrated hexa-aqua Ni^{2+} (4.04 Å) to Co^{2+}(4.23 Å).

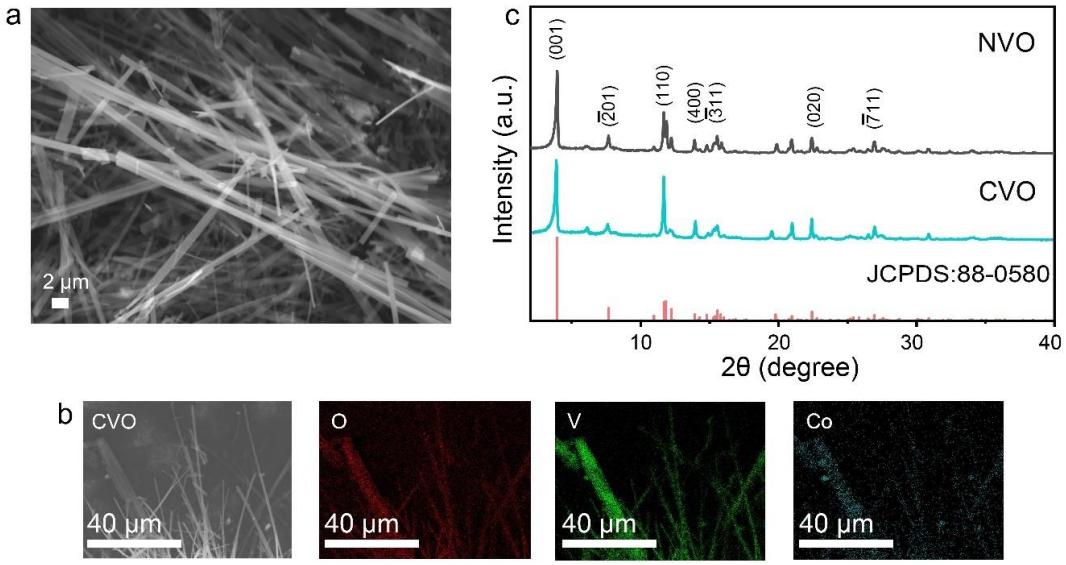

Figure 2.3.3. (a, b) SEM image and elemental mapping of CVO, (c) XRD patterm of the as-obtained NVO and CVO, respectively.

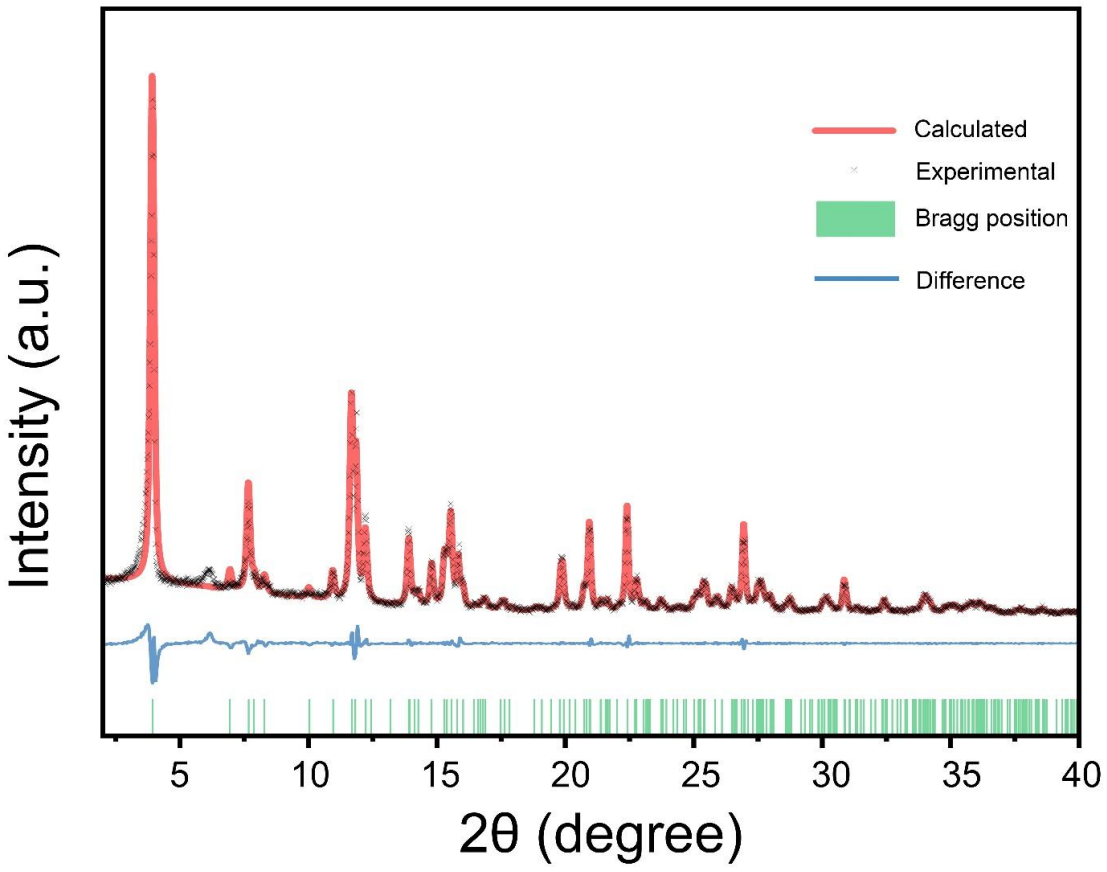

Figure 2.3.4. XRD refinement of as-prepared NVO.

Table 2.3.1. Lattice parameters of standard and as-obtained NVO sample.

	phase	a	b	c	β	V
standard	monoclinic $Ni_{0.22}V_2O_5$	11.7560 ± 0.0010	3.6490 ±0.0010	10.3640 ± 0.0020	95.030 ± 0.010	442.88
sample	$Ni_{0.25}V_2O_5$	11.7629 ±0.0012	3.6528 ±0.0003	10.4118 ± 0.0014	95.156 ± 0.019	445.55 (+0.60%)

It should be clarified that the NVO (Figure 2.3.5a) has a critically varied atomic-level structure from the previously reported vanadium bronzes such as δ-$Ca_{0.24}V_2O_5 \cdot nH_2O$[21] (Figure 2.3.5b), σ-$M_xV_2O_5 \cdot nH_2O$ (M = Zn^{2+} or Mg^{2+})[16,17] (Figure 2.3.5c). Among them, the σ-$M_xV_2O_5 \cdot nH_2O$ structure consists of a "double-layer" configuration constructed by various interconnected VO_x (x = 4, 5, 6) polyhedrons. While, in the δ-$M_xV_2O_5 \cdot nH_2O$ structure (M = Ni^{2+}, Co^{2+} or Ca^{2+}), each bilayers in the framework possess the same coordination as layers in α-V_2O_5, which only compose of VO_5 and VO_6. In addition, the relatively large Ca^{2+} in the δ-V_2O_5 framework coordinate with three apical oxygen ions in the layers, that is, one is in a layer but the other two are bonded with adjacent layer. In contrast, Ni^{2+} (Co^{2+}) only coordinates with two oxygen ions within layers through the axial direction. Therefore, more numbers of apical oxygen ions in NVO(CVO) compared with δ-$Ca_{0.24}V_2O_5 \cdot nH_2O$ can be observed resulting in more accessible Zn^{2+} accommodation sites in this case. It is seen that even though both σ- and δ- phase vanadium bronzes possess a bilayer V_2O_5 hosts, the distinct nature of intercalation properties within these two phases can be expected, since the local environment of fine structures varied in each cases will strongly influence on Zn^{2+} migration and accommodations.

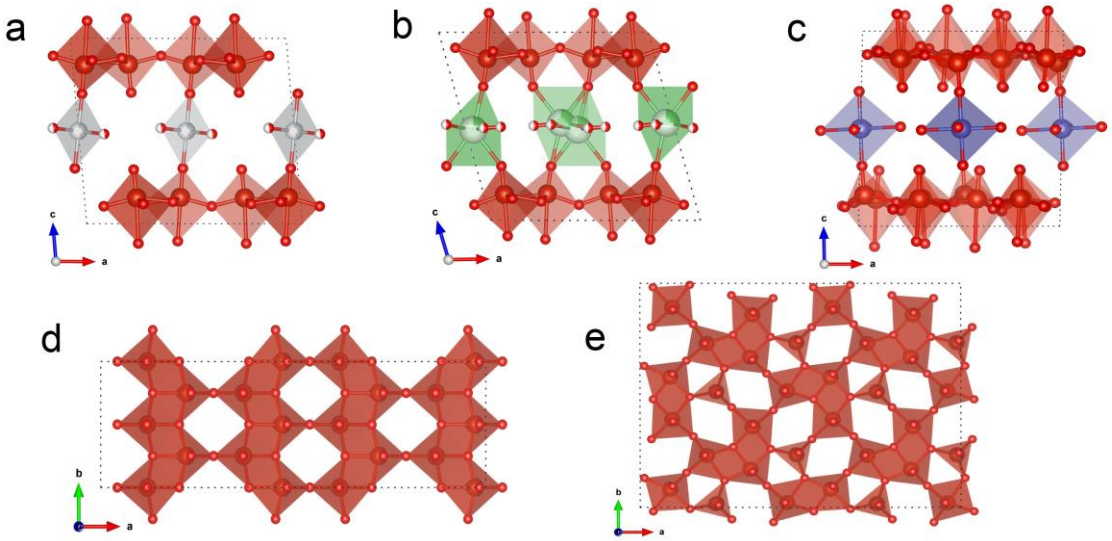

Figure 2.3.5. Crystallographic structures of (a) δ-$M_{0.25}V_2O_5 \cdot nH_2O$ (M = Ni, Co) (b) δ-$Ca_{0.25}V_2O_5 \cdot nH_2O$, and (c) σ-$M_{0.25}V_2O_5 \cdot nH_2O$ (M = Zn, Mg), projected along b direction. (d) Crystal structures of a individual V_2O_5 slab in δ-$M_{0.25}V_2O_5 \cdot nH_2O$ (M = Ni, Co, Ca) and (b) σ-$M_{0.25}V_2O_5 \cdot nH_2O$(M = Zn, Mg), projected along c-axis, respectively. Large red spheres and small red spheres refer to V atom and O atom,

respectively. Coordination polyhedra are reflected by shaded regions, and partially filled spheres refer to fractionally occupied sites.

The Raman spectrum of NVO presented several peaks in the sphere of 100-1200 cm^{-1} which refer to various vibration modes (Figure 2.3.6c).[44,45,46] More explicitly, the Raman shift of 104 and 175 cm^{-1} can be interpreted as a translation mode derived from relative motions between two layers.[47] The intensified peak at 175 cm^{-1} represents the long-range order of in-plane slabs along ab direction in the host.[48] Moreover, the band at 965 cm^{-1} can be interpreted to the stretching mode of terminal apical V=O, which exhibits a red shift compared with that of α-V_2O_5 (994 cm^{-1}).[49] This phenomenon can be explained as an extension of the V=O owing to a coordination of Ni^{2+} with apical oxygen in vanadyl bond resulting in a liner enlarged d-spacing along the *c*-axis. A similar observation of the decreased Raman shifts can be also found in Li inserted V_2O_5 with 984 cm^{-1} in previous study.[50] Furthermore, a Raman shift occurred at 505 cm^{-1} is caused by the bending mode of V-O, and may overlap with Ni-O vibration mode, which generally possesses a similar Raman shifts in this region.[51,52] It is seen a band at 684 cm^{-1} stands for the antisymmetric stretching mode of V-O-V.[50] In addition to Raman spectrum, FITR spectrum of NVO in Figure 2.3.6a exhibits a series of absorption bands corresponding to the various vibration modes in terms of V-O, V-O-V, V=O, Ni-O, OH and H-O-H, from low to high wavenumbers, respectively.[53,54,55,56] Moreover, the intermolecular water not only detected by FTIR results, but use of TGA to quantify the weight percentage of water content in as-prepared NVO sample. According to the TGA result in Figure 2.3.6b, there is 6.2% weight loss in the temperature sphere of 150-475°C, indicating that the stoichiometric formula of the NVO should be written as δ-$Ni_{0.25}V_2O_5 \cdot 0.74H_2O$.

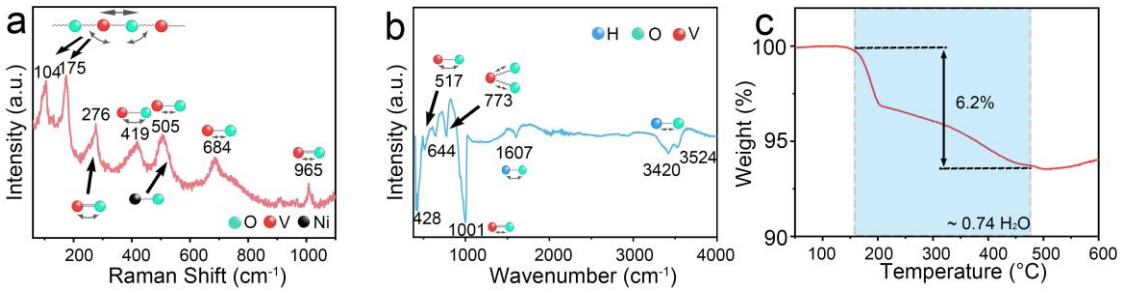

Figure 2.3.6. (a) Raman; (b) FTIR spectrum and (c) TGA analysis of the NVO pristine powder.

After comprehensively identifying elemental and structural information of NVO, the material was assembled into a coin cell type battery equipped with 3M $ZnSO_4$ as electrolyte to evaluate the electrochemical performance. Figure 2.3.7a shows the galvanostatic charge/discharge (GCD) profiles of NVO at different current densities from 0.2 to 5 A g^{-1}, where several plateaus can be identified arising from paired redox reactions upon Zn^{2+} insertion/extraction. Meanwhile, a high specific capacity of 402 mAh g^{-1} was observed at a current density of 0.2 A g^{-1}. Impressively, there is specific capacity of 164 mAh g^{-1} attained even after rising 25-fold current density to 5A g^{-1}. In addition, the rate performance of NVO is further exhibited in Figure 2.3.7b, in which the current density is gradually increased from 0.2 A g^{-1} to 5 A g^{-1}, and then revert to the initial current density with 8 cycles in each steps. It is also seen that NVO cathodes can provide dramatically stable cycling performance under various current densities, which obtained a capacity retention of 95% with specific capcity of 381 mAh g^{-1} when the current density was restored to 0.2 A^{-1}. Accordingly, the recovery of excellent capacities at other current densities was also achieved with high specific capacity of 320, 274, 221, 186, and 147 mAh g^{-1} at 0.5, 1, 2, 3, and 5 A g^{-1}, respectively. Meanwhile, the corresponding coulombic efficiency (CE) is above 99% indicating a highly reversibility during the reactions. Figure 2.3.7c presents the first three cycles of CV curves for NVO electrode at a scan rate of 0.2 mV s^{-1}. It is noticed that reversible (de)intercalation of Zn^{2+} occurred after the first asymmetric discharge/charge process, which maintains the same shape and position of multiple redox pairs in rest of cycles, which further verified the stability of NVO cathode in the GCD profiles with transient initial activation. Additionally, The long-term stability of NVO electrode under various current densities was investigated through extended cycles measurements (Figure 2.3.7d, e). Specifically, there is only a 10% decreased specific capacity of 347 mAh g^{-1} occurred after 50 cycles at a current density of 0.2 A g^{-1}, which is superior than other reported vanadium bronzes even tested under relatively higher current density of 1 A g^{-1}, e.g. there is 23.7% drop of the capacity after 100 cycles for $NH_4V_4O_{10}$[57], a 31.6% of capacity decay after 50 cycles for $Li_xV_2O_5 \cdot nH_2O$[58], and 26.5% of capacity attenuation after 50 cycles for $Cu_xV_2O_5 \cdot nH_2O$[23]. Moreover, a higher capacity retention of 98% after 1200 cycles was attained at a high rate of 5 A g^{-1} against to a capacity of 218 mAh g^{-1} @ 2nd cycle, and a LED display can be easily lighted up by as-fabricated AZIB illustrated in inset of Figure 2.3.7c. All cycling results were detected with over

99% Coulombic efficiency implying a robust reversibility of electrochemical performance.

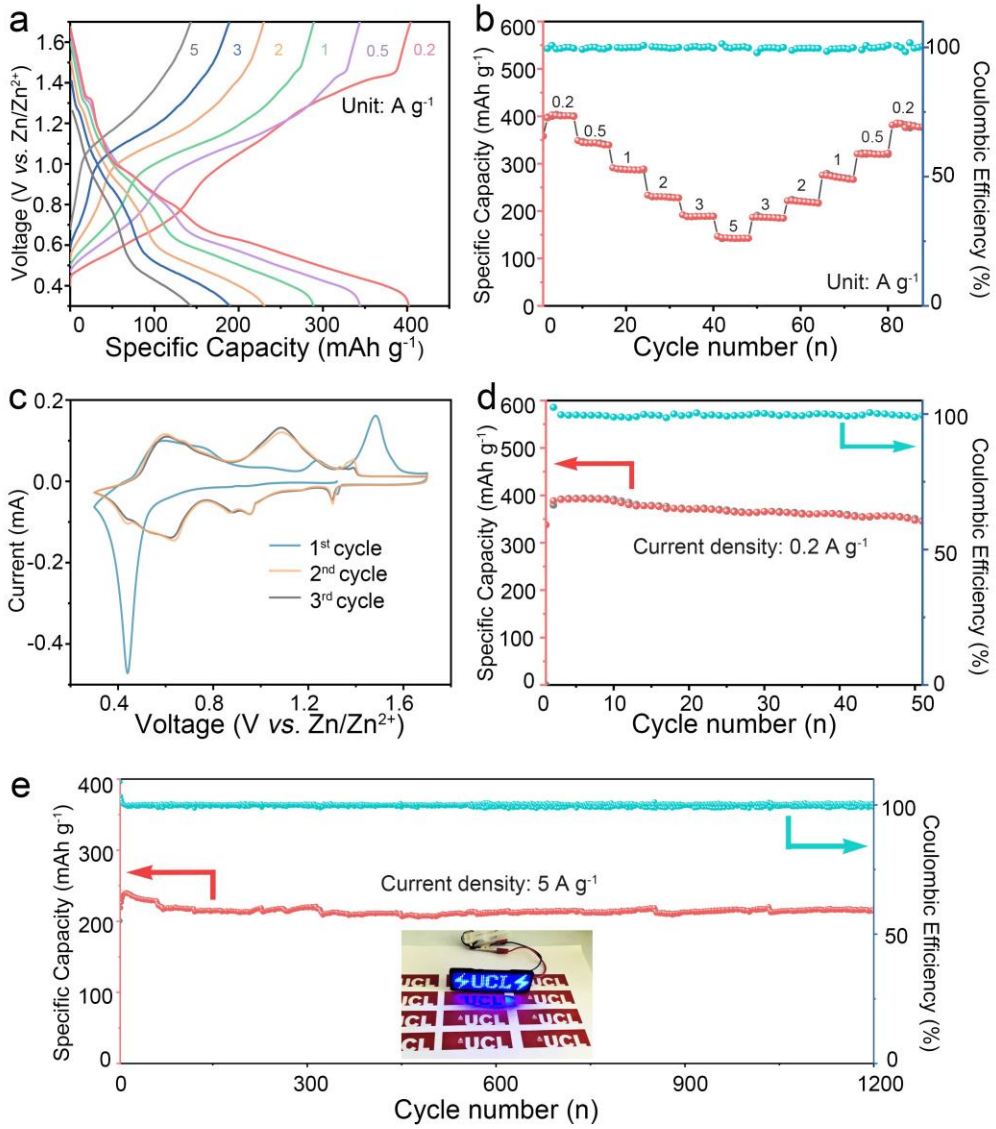

Figure 2.3.7. (a) Galvanostatic charge-discharge profiles and (b) rate performance for NVO | $ZnSO_4$ | Zn battery at different current densities, respectively; (c) The first three cycles of Cyclic voltammetry curves at the scan rate of 0.2 mV s^{-1} for NVO cathode; Long-cycling stability evaluation of NVO at (d) 0.2 and (e) 5 A g^{-1}, respectively. Inset in e depicting the as-fabricated batteries lightening the LED display.

Additionally, the performance was also verified by a substitution of 3M $ZnSO_4$ electrolyte with same concentrated Zn $(CF_3SO_3)_2$. It is observed that a similar durability of battery rate and long-term cycling performance was achieved with steady power output even after 1500 cycles measurements (Figure 2.3.8).

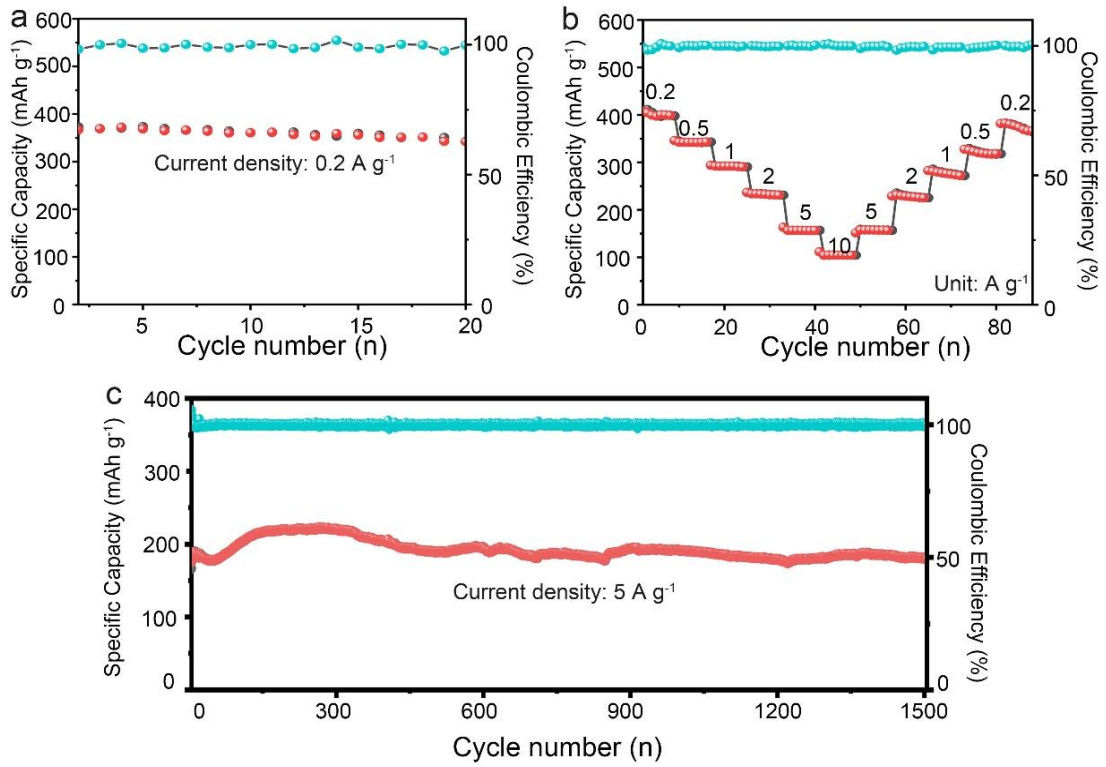

Figure 2.3.8. NVO//Zn battery performance evaluated by using 3M $Zn(CF_3SO_3)_2$ as electrolyte, GCD cycling performance of NVO at (a) 0.2 A g^{-1} and (c) 5 A g^{-1}, respectively; (b) Rate performance of NVO electrode at different current densities from 0.2 to 10 A g^{-1}.

Meanwhile, it is seen that a relatively high maximum energy/power density of 286.6 Wh kg^{-1} and 3920.8 W kg^{-1} were achieved in NVO//3M $Zn(CF_3SO_3)_2$// Zn cell, which can be observed in a Ragone plot in Figure 2.3.9, compared with other developed cathodes.

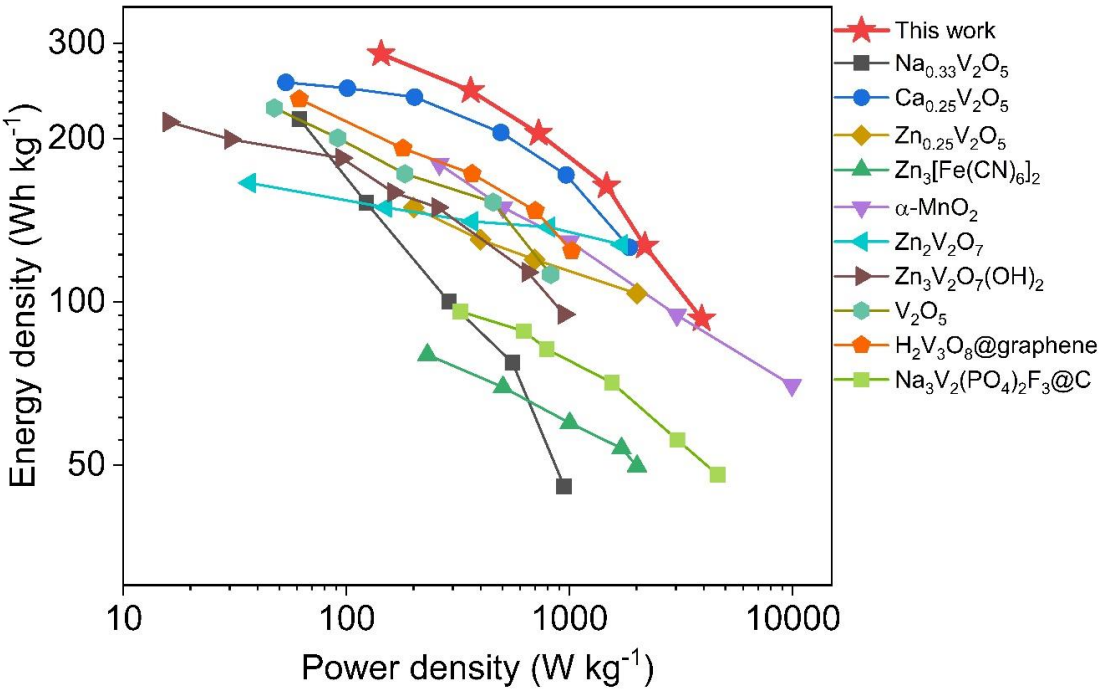

Figure 2.3.9. Ragone plot of energy/power density of as-prepared NVO-Zn batteries and different reported cathodes (based on active mass of cathode materials).

For comparison, it is known that the as-obtained CVO possesses similar atomic level structure compared with NVO. Therefore, the CVO cathode was also tested for AZIBs application (Figure2.3.10). The resulting specific capacity of 326.8 mAh g^{-1} with only 0.7% capacity decay was attained at a current density of 0.2 A g^{-1} after 30 cycles. Furthermore, it also showed a capacity retention of 95% with capacity of 144.4 mAh g^{-1} after 500 cycles at 5 A g^{-1} and good rate performance when the varied current density applied. Despite the fact that the obtained battery performance of CVO is lower than NVO electrode, the results are still amongst the highest reported cathodes for AZIBs applications.

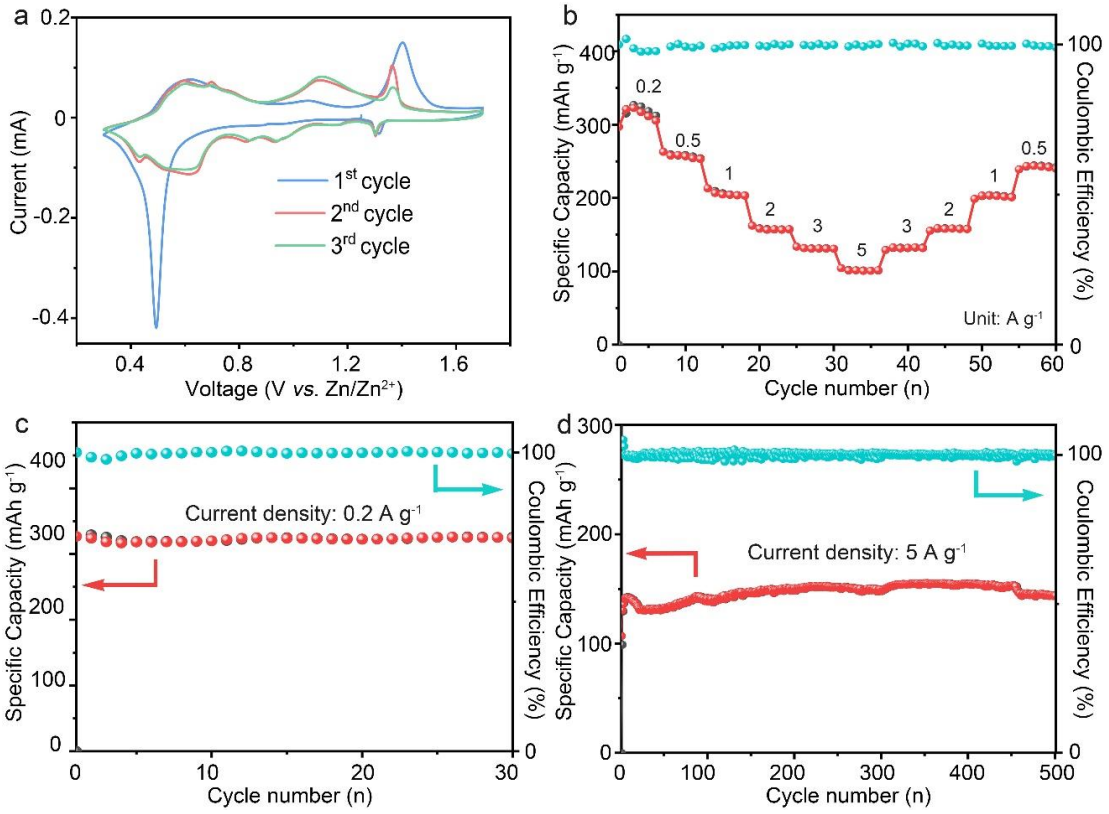

Figure 2.3.10. (a) CV curves of CVO electrode at 0.2 mV s^{-1}; (b) Rate performance of CVO electrode at different current densities from 0.2 to 5 A g^{-1}, and long-term cycling stability of the CVO electrode at the current density of (c) 0.2 A g^{-1} and (d) 5 A g^{-1}, respectively.

To clarify the varied specific capacity of CVO and NVO, *ex-situ* EIS was adopted for investigations of ions transport properties and resistance at initial and final states of cycling tested batteries measured under identical conditions (Figure 2.3.11). It is seen that a summarized electrochemical impedance parameters of both electrodes at different states are presented in Table 2.3.2, according to the fitted equivalent circuit results, which present cycle-dependent resistance and ions transport properties. More specifically, both electrodes of NVO and CVO before charge/discharge treatments possess much better electrochemical behaviour than those cycled cathodes. Moreover, the cycled NVO electrode exhibits superior performance than cycled CVO, which is reflected by a lower combined internal resistance (R_s = 2.85 Ω) and interfacial charge resistance (R_{ct} = 22.38 Ω) for NVO compared with those in CVO with 4.82 Ω and 59.77 Ω for R_s and R_{ct} respectively. The enhanced inherent conductivity and facilitated interfacial charge migration properties are responsible for observed high performance of NVO during cycling tests, and the variation with CVO electrode could be attributed

to unstable feature of Co ion in framework which will be discussed later in structural and elemental evaluation *via* multiple *ex-situ* characterizations. Thus, the comparison of these two electrodes highlights the importance of adequately selecting pre-intercalated cations in vanadium bronzes prior to the measurements.

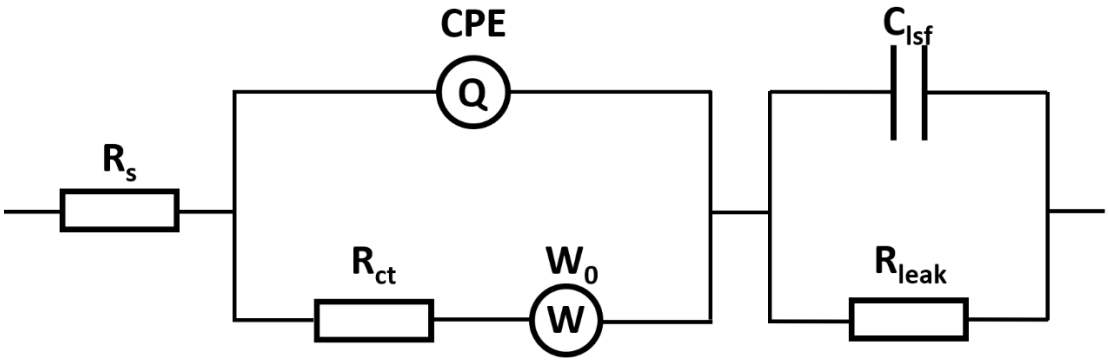

Figure 2.3.11a. The equivalent circuit for EIS

R_s: Combined internal resistance, including the interfacial contact resistance of the material with current collector, the ohmic resistance of electrolyte and the intrinsic resistance of current collector.

R_{ct}: Interfacial charge transfer resistance, representing the resistance of electrochemical reactions at the electrode surface.

W_0: Warburg element, describing the transfer and diffusion of the electrons and electrolyte ions in the pores of the electrode materials.

CPE: Constant phase element.

C_{lsf}: Element account for the low-frequency surface capacitance.

R_{leak}: Leakage resistance at low frequency.

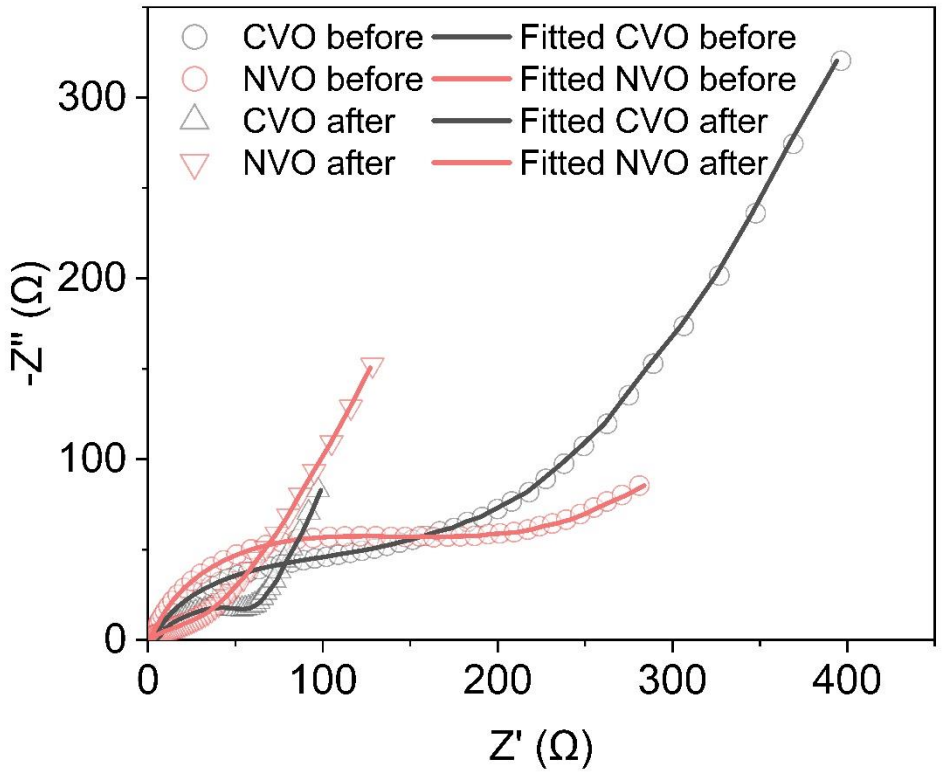

Figure 2.3.11 b. Nyquist plot of the NVO and CVO electrodes at initial and after 100 charge/discharge cycled states.

Table 2.3.2. Comparison of Equivalent circuit parameters for NVO and CVO

Electrode	R_s (Ω)	R_{ct} (Ω)	W_0 ($\Omega*s^{0.5}$)	CPE ($mF*s^N$)	C_{lsf} (mF/cm^2)	R_{leak} (Ω)
CVO before	3.67	91.47	226.4	0.036 (N=0.74)	1.15	44.46
NVO before	0.58	183.6	76.43	0.25 (N=0.67)	0.52	17.01
CVO after	4.82	59.77	28.98	0.62 (N=0.63)	9.32	85.20
NVO after	2.85	22.38	23.69	0.89 (N=0.58)	2.06	69.91

Additionally, in order to investigation of benefits from pre-intercalated ions, a slight

modification of the synthetic protocol was conducted by getting rid of nickel and cobalt acetate precursors in preparation process. Accordingly, the resulting product possesses a crystallgraphic structure precisely macthed with $V_3O_7{\cdot}H_2O$ (JCPDS 28-1433), which also exhibits layered structure composing of V_3O_8 slabs with coorination of VO_5 and VO_6 polymorphs,[59] which have similar features as mentioned in crystal structures of δ-$Ni(Co)_{0.25}V_2O_5{\cdot}nH_2O$. Moreover, electrochemical measurements were performed to compare with NVO and CVO electrodes. Figure 2.3.12c presents the first 3 cycles of the CV curves for $V_3O_7{\cdot}H_2O$, in which there are two conspicuous pairs of redox peaks upon cathodic/anodic reactions, and the subsequent GCD measurements illustrates high initial capcities of 354 mAh g^{-1} and 225 mAh g^{-1} under current density of 0.2 and 5 A g^{-1}, respectively. However, inferior cycling stability and rate capbility are observed in Figure 2.3.12 (d-f). i.e. 58.4% and 50% capcity attenuation at 0.2 A g^{-1} and 5 A g^{-1} for 50 and 5000 cycling tests, respectively, The unsatisfactory performance of $V_3O_7{\cdot}H_2O$ cathode could be attributed to a rapid deterioration of the structure because of stronge electrostatic force. As the result, the introduction of pre-inserted cations could be a feasible solution.[18,19,20]

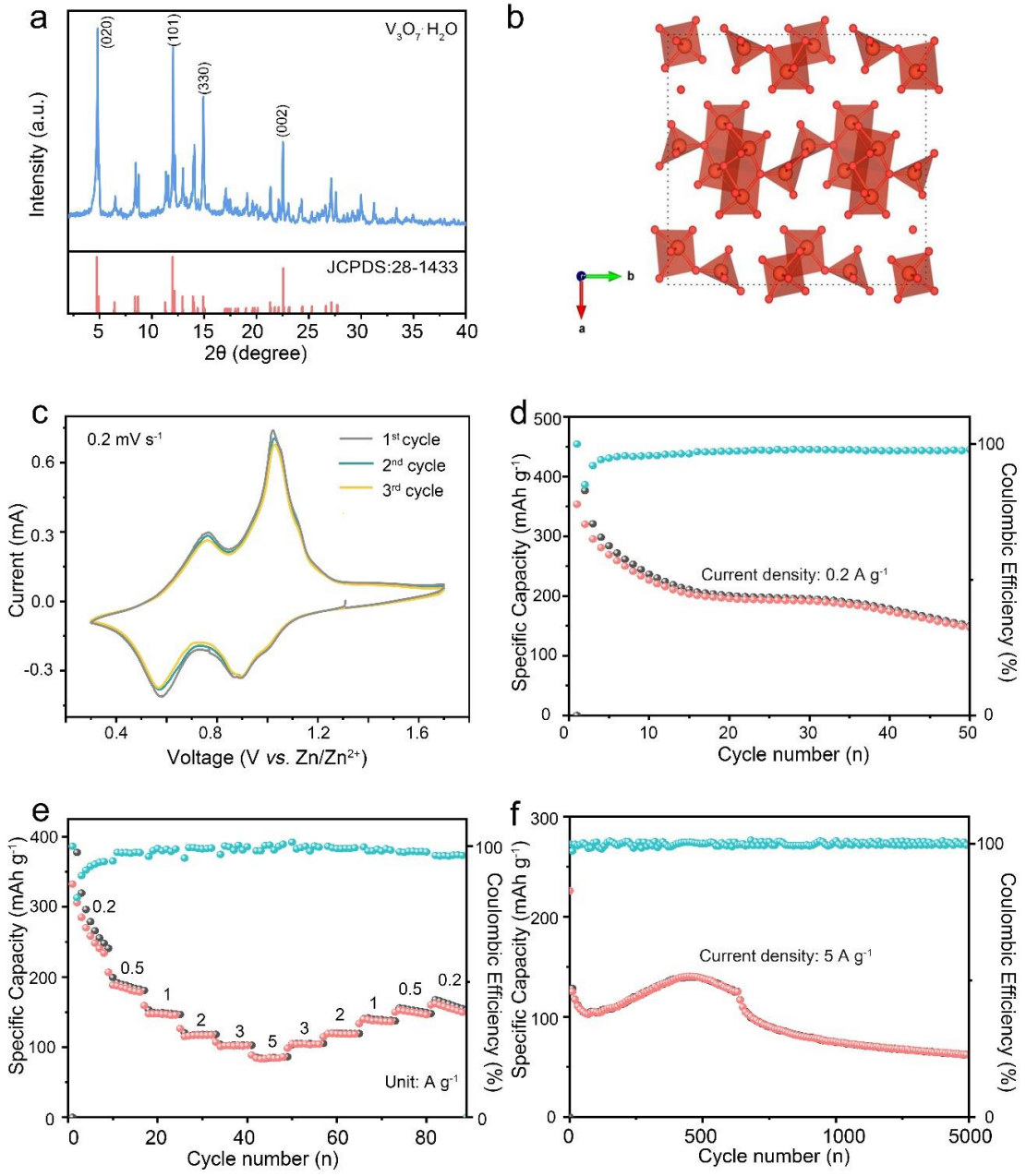

Figure 2.3.12. (a) XRD plot of $V_3O_7 \cdot H_2O$ cathode; (b) Crystallographic structure of $V_3O_7 \cdot H_2O$ projected along the c axis (O atoms of the water molecules are shown as induvial small red ball without exhibition of H atom); (c) First three cycles of CV plots at the scan rate of 0.2 mV s^{-1}; (d) GCD tests on $V_3O_7 \cdot H_2O$ electrode at 0.2 A g^{-1} for 50 cycles; (e) Rate performance at varied current densities from 0.2 to 5 A g^{-1}; (f) Long-term cycling durability of the electrode at the current density of 5 A g^{-1}.

In addition, according to the disscussion above, it is seen that remarkable performance was achieved in NVO for AZIBs applications, and a summerized battery performance comparsion of different characteristics on reported vanadium oxides was illustrated in

Table 2.3.3.

Table 2.3.3. Battery performance comparison of NVO with some reported vanadium-based cathode materials.

Cathode materials	Voltage [V]	Electrolyte	Specific capacity[mAh g^{-1}]	Retention[%] /Cycle	Ref.
$Na_{1.1}V_3O_{7.9}$@rGO	0.4-1.4	1 M $Zn(CF_3SO_3)_2$	191 (50 mA g^{-1})	85/500 (1 A g^{-1})	[60]
$Na_{0.33}V_2O_5$	0.2-1.6	3 M $Zn(CF_3SO_3)_2$	253.7 (200 mA g^{-1})	93/1000(1 A g^{-1})	[19]
σ-$Zn_{0.25}V_2O_5$ ·n H_2O	0.5-1.4	1 M $ZnSO_4$	282 (300 mA g^{-1})	80/1000(2.4A g^{-1})	[17]
δ-$Ca_{0.25}V_2O_5$ ·nH_2O	0.6-1.6	1 M $ZnSO_4$	340 (0.2 C)	78/5000(80 C)	[21]
σ-$Mg_{0.34}V_2O_5$·n H_2O	0.1-1.8	3 M $Zn(CF_3SO_3)_2$	330 (100 mA g^{-1})	95/1000 (1Ag^{-1})	[16]
$Na_2V_6O_{16}$·3H_2O	0.2-1.6	3M $Zn(CF_3SO_3)_2$	352 (50 mA g^{-1})	75/500 (1Ag^{-1})	[61]
$K_2V_6O_{16}$·2.7H_2O	0.4-1.4	1 M $ZnSO_4$	217 (200 mA g^{-1})	82/500 (6Ag^{-1})	[62]
$Zn_3V_2O_7(OH)_2$·2H_2 O	0.2-1.8	1 M $ZnSO_4$	213 (50 mA g^{-1})	68/300 (0.2Ag^{-1})	[63]
LiV_3O_8	0.6-1.2	1 M $ZnSO_4$	267 (15 mA g^{-1})	90/65 (0.13Ag^{-1})	[64]
$Na_3V_2(PO_4)_2F_3$	0.8-1.9	2 M $Zn(CF_3SO_3)_2$	65 (80 mA g^{-1})	97/4000 (1Ag^{-1})	[65]
V_2O_5·nH_2O	0.2-1.6	3 M $Zn(CF_3SO_3)_2$	381 (50 mA g^{-1})	71/900 (6 Ag^{-1})	[66]
δ-$Ni_{0.25}V_2O_5$ ·nH_2O	0.3-1.7	3M $ZnSO_4$	389 at 2nd cycle (200 mA g^{-1})	89/50 (0.2 Ag^{-1})	This work
			218 at 2nd cycle for (5 A g^{-1})	98/1200 (5Ag^{-1})	
		3 M $Zn(CF_3SO_3)_2$	370 at 2nd cycle (200 mA g^{-1})	93/20 (0.2Ag^{-1})	
			188 at 8th cycle (5 A g^{-1})	96/1500 (5Ag^{-1})	

In addition to performance evalutions, a gradually movements of radox peaks toward to same direction was observed as the scan rates increased from 0.1 to 0.5 mV s^{-1}, from which a quantitative assessment of the Zn^{2+} storage kinetics in the as-prepared cathode material can be achieved (Figure 2.3.13a). According to the equation, a power-law relationship is obeyed[16]:

$$I = aV^b$$

where, *i* refers to peak current and *v* stands for sweep rate in CV measurements. Hence, the b values can be acquired by a fitted slope with log(*i*) *vs.* log(*v*) profile.

In our case, the *b* values attained from the six conspicuous redox peaks are 0.39, 0.79, 0.75, 0.60, 0.52, and 0.64, respectively, manifesting that a diffusion-controlled behavior of charge storage dominate in NVO cathode (Figure 2.3.13b). A further evaluation of capacitive- and diffusion-controlled kinetics of the cathode material are presented in CV curve at a scan rate of 0.4 mV s^{-1}, in which a capacitance contribution accounts for 33.5% among all current responses (Figure 2.3.13c). Moreover, when the CV scan rates increases from 0.1 mV s^{-1} to 1 mV s^{-1}, it is observed that the proportion of capacitance contribution coherently raised from 21.5% to 45.3%. in Figure 2.3.11d. This phenomenon indicates that the kinetics are mostly determined by charge carrier diffusion at low sweep rates, while the capacitive behavior gradually rules the zinc storage reactions at higher scan rates. In addition to CV analysis, Galvanostatic Intermittent Titration Technique (GITT) was uzilized to acquire the diffusion coefficient of Zn^{2+} in NVO and CVO electrode during the (de)intercalation process (Figure 2.3.13 e-h). It is seen that *D* values of NVO is higher than CVO, which further confirms the better rate capability in NVO electrode as disscussed above. Moreover, both of the materials possess *D* values in the sphere of 10^{-8} to 10^{-10} cm^2 s^{-1}, indicating enhanced ion diffusion kinetics compared with reported σ-$M_{0.25}V_2O_5 \cdot nH_2O$ (M=$Zn^{2+}$and K^+) [17, 67].

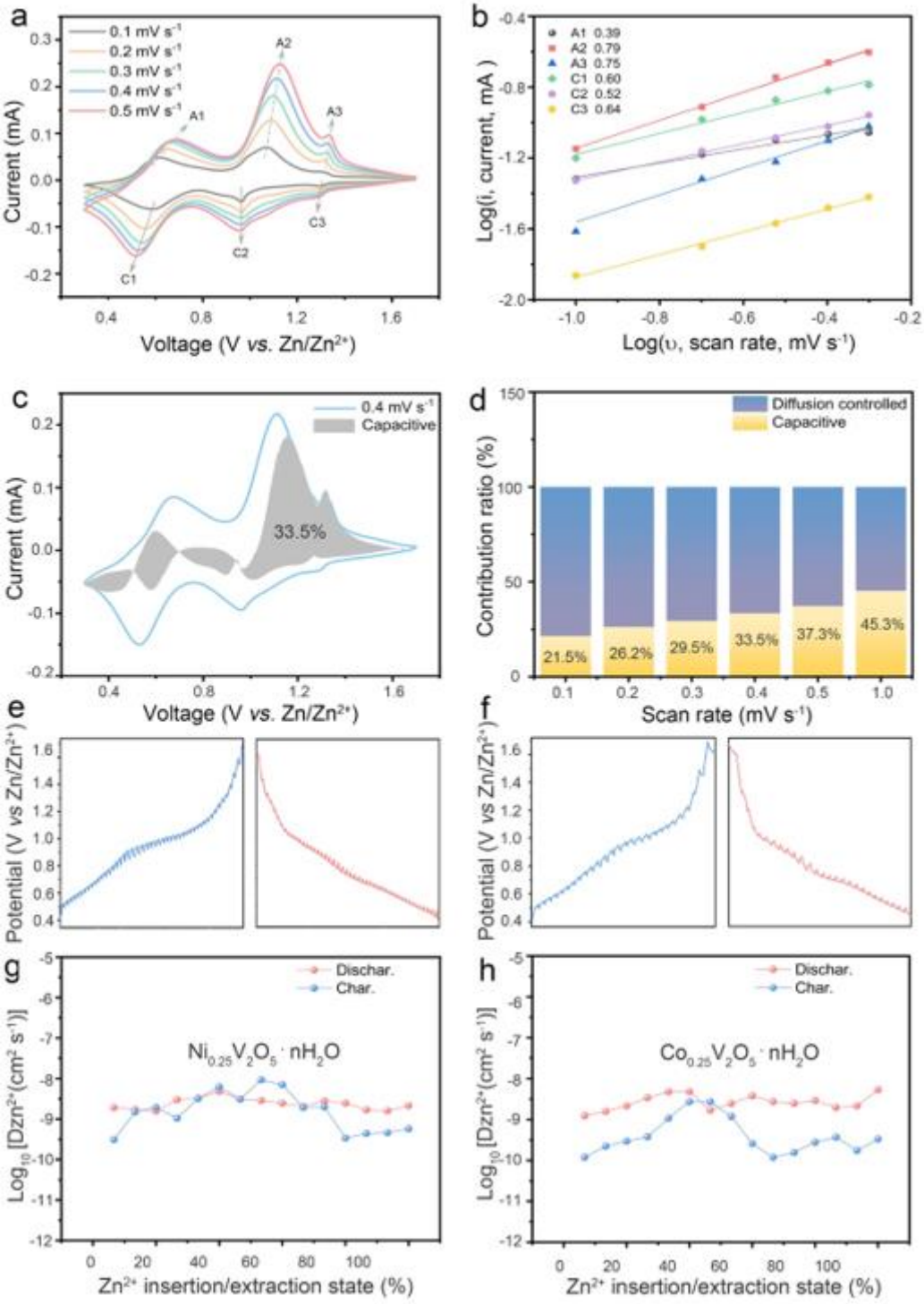

Figure 2.3.13. (a) The CV curves of the NVO electrode with varied scan rates from 0.1 to 0.5 mV s^{-1}; (b) *b* value originated from log *i vs.* log *v* plots on basis of the CV reuslts at picked oxidation/reduction states; (c) Capacitive contribution (grey region) at 0.4 mV s^{-1} in CV curve of the NVO electrode, and (d) the capacity contributions ratio between capacitive and diffusion controlled processes at different scan rates; GITT profiles and resulting zinc ion diffusion coefficients for (e, g) NVO and (f, h) CVO electrode, respectively.

Combined with *ex-situ* XPS, XRD and TEM characterizations, the possible Zn^{2+} reaction mechanism in NVO electrode was studied. In order to verify the varied chemical states of the original, charged and discharged NVO electrodes, *ex-situ* XPS analysis were carried out, and the corresponding results of core-level spectra of V 2p are shown in Figure 2.3.14a with obvious variations of binding energys indicating change of valence states upon Zn^{2+} (de)intercalation process. More explicitly, the polyvalent states of V^{4+} and V^{5+} appearing in the prisine NVO material are in accord with other reported vanadium bronzes with observation of partial reduction. It is seen that the binding energies of V^{4+} ($2p_{3/2}$: 516.2 eV) and V^{5+} ($2p_{3/2}$: 517.5 eV) maintains almost the same positions in the pristine and fully discharged states of NVO.Whereas, an intensified V^{4+} species with an emerged peak at 515.5 eV referring to V^{3+} indicate a significant reduction of V oxidation states in fully discharged state of NVO electrode. Through analysis of peak area proportion, a notable reduction of the average V valence states from $V^{4.69+}$ to $V^{4.03+}$ was observed, in pristine and discharged NVO samples, respectively. In contrast, the V^{3+} component disappears in fully charged NVO electrode and two dominant peaks at binding energy of 517.6 eV and 516.3 eV occurs instead, which can be assigned to V^{4+} and V^{5+} species, respectively, giving rise to an average valence state of $V^{4.78+}$. The above results indicate that the V species undergoes a highly reversible redox reaction during the (de)intercalation of Zn^{2+}. In addition, the chemical states of Ni species in NVO were also determined by *ex-situ* XPS (Figure 2.3.14b). The intense peak at a binding energy of 865.3 eV stands for Ni^{2+} $2p_{3/2}$ in pristine sample but hardly retrieve the precise signal positions of Ni 2p in fully charged/discharged due to a weak intensity of peaks. This may be owing to the partial removal of Ni during the reactions, and the interference from surface contaminated by conductive agent and binder mixed electrode, the following demonstration will be achieved by a characterization of varied amount of Ni species in the electrode *via ex-situ* EDS measurement. It should be emphasised that this phenomenon has also been reported in other AZIBs electrodes, and could be considered as a displacement/intercalation reaction mechanism.[7,68,69,70,71] Moreover, Figure 2.3.14c shows the Zn 2p core-level XPS spectrum of the fully discharged/charged NVO electrodes. The dominant peak of Zn^{2+} $2p_{3/2}$ is found at 1023.4 eV corresponding to the inserted Zn^{2+} in the NVO cathode during discharge process, whereas the attenuated intensity peak at 1022.1 eV observed in the fully charged NVO sample demonstrates partial residual Zn^{2+} species remains

upon charged process, which is consistent with previous researches.[16,17] It should be noted that all *ex-situ* XPS measurements were carried out on the samples which had been exposed to ambient environment for several hours, that is, V^{3+} (especially in the surface of tested electrode) could be slightly oxdized to higher vanlent states. Therefore, the result of average valence states of vanadium species could be overestimated in this case. Therefore, the following NEXAFS could offer more accurate information on the evulation of chemical states during the reactions.

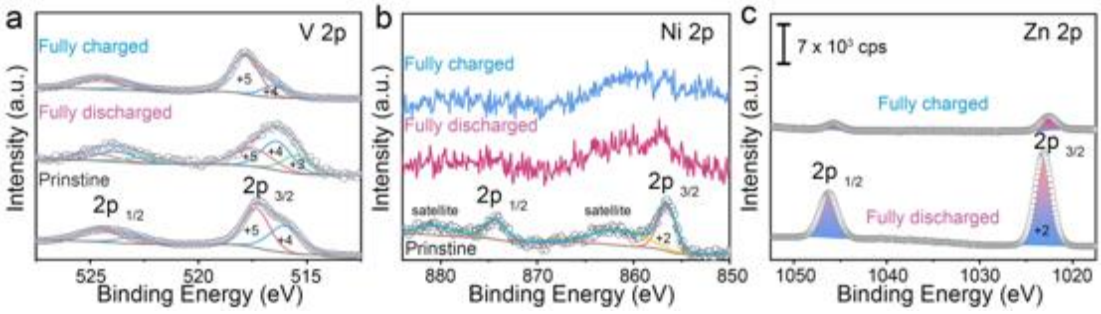

Figure 2.3.14. *Ex-situ* XPS core-level spectra of the (a) V 2p, (b) Ni 2p and (c) Zn 2p in pristine, fully charged and fully discharged states of the NVO cathodes, respectively.

After elucidating the changes of the chemical states, the structural evolution of the NVO cathode material upon charge/discharge process were characterized by *ex-situ* XRD, TEM and Raman. As shown in Figure 2.3.15, *ex-situ* XRD analysis clarified the dynamic structure evolution of NVO electrode under different charge/discharge states of the 1st and 20th cycles with an applied current density of 0.2 A g^{-1}. The electrode was firstly immersed in the 3M $ZnSO_4$ electrolyte for 48 hours with following XRD measurement to compare with the prinstine NVO sample. It is worth noting that the crystal plane possesses negligible changes after immersion, which demonstrates a stable crystal structure of NVO cathode in the as-obtained electrolyte. Upon a deep discharge to 0.3 V in the first cycle, the 2θ of (001) changes from 3.94° to 3.76°, reflecting a interlayer spacing mildly expands from 10.3Å to 10.8Å after inserting Zn^{2+}/H_2O, which is highly different with an observation of intensive contraction of the interlamination in previously reported σ-$Zn_{0.25}V_2O_5 \cdot nH_2O$ at the first fully discharged state.[17] However, this phenomenon in the present investigation are consistent with the recent study of layered V_3O_8 as host frameworks for AZIBs.[72] Moreover, after introduction of Zn^{2+} into the host lattice, the new phase becomes highly reversible in the rest of the cycles, i.e. retrieving the same reflection position at each fully discharged

states. Similarly, when the electrodes were fully charged to 1.7 V in the 1st and 20th cycles, a steady change of interlayer spacing from 10.8 to 13.5 Å was attained. The large extension to 13.5 Å could be considered as incorporation of extra H_2O molecules from the electrolyte after Zn^{2+} was extracted.[73] Additionally, the reflection sites of the (001) facet were also reversible at each charge/discharge states. For instance, the *d*-space (13.5Å) at fully charged state initially drops to 10.5 Å with a discharge process to 1.2 V, followed by an expansion to 11.2 Å after further discharge to 0.75 V. Comparably, during the charge process, two states of 0.8 V and 1.25 V possess the same (001) reflection positions, interpreted as *d*-space of 11.2 Å and 10.5 Å, respectively. Since a complexity of inserted species (Zn^{2+}, H_2O and zinc complex) within the NVO cathode, it is difficult to clarify the fine structure evolutions but only simultaneously variations of interlayer spacing can be observed. Furthermore, the reversible movements of (600) (*a*-axis), (020) (*b*-axis) and (711) facets in certain regions show opposite direction compared with the (001) plane, demonstrating a three-dimensional structural evolution of NVO cathode material upon charge/discharge process. This revealed behaviour is in contrast to the majority of other reported vanadium bronze based cathodes for AZIBs which presented coexisting multiphases, reflecting by split peaks of (001) plane and other highly distinct phase generated. It can be concluded that the *ex-situ* XRD measurement of NVO cathode material sufficiently verified its robust reversibility as adequate host for AZIB applications .

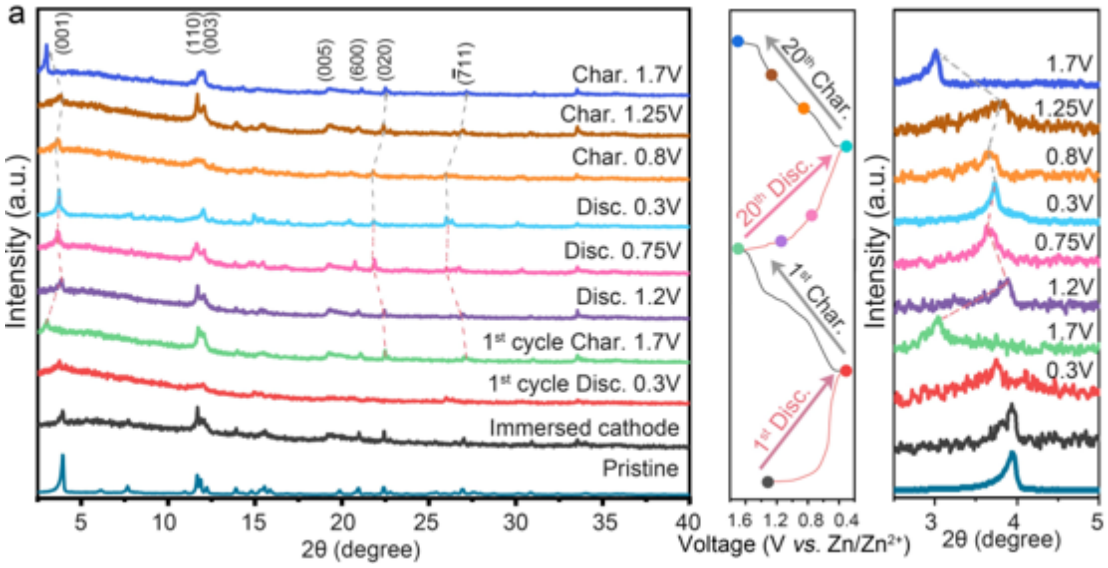

Figure 2.3.15 *Ex-situ* XRD characterization of the NVO cathodes upon varied charge/discharge states, and its corresponding GCD profiles at 0.2 A g^{-1}.

A further confimation of observed structral evolution in NVO electrode was carried out by *ex-situ* TEM, which clearly presents the significant variation of (004) d-space at each fully charge/discharge states in concert with previous investigations (Figure 2.3.16). More explicitly, the relatively small *d*-space of 0.27 nm indexed to the (004) plane at the fully discharged state is consistent with an observation of contracted interlayer spacing along the *c*-axis, while the expanded (004) plane with *d*-space of 0.34 nm was found in the fully charged state of NVO cathode.

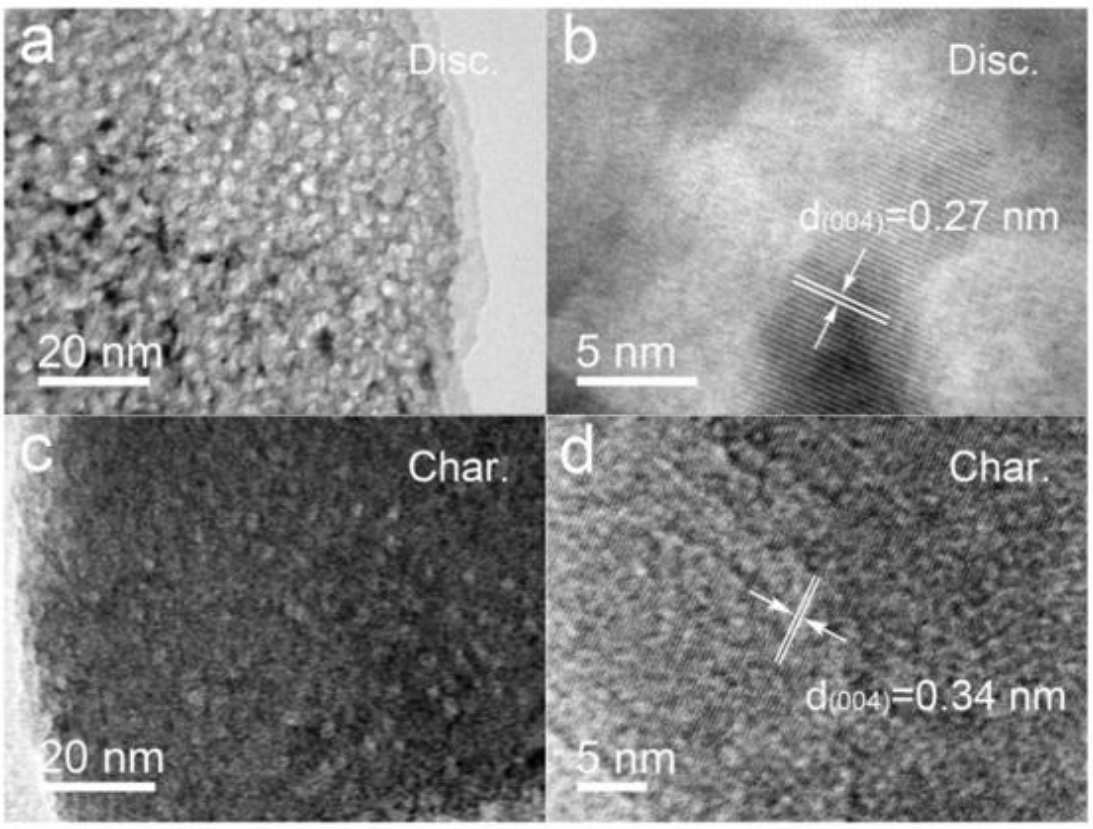

Figure 2.3.16. *Ex-situ* TEM graphics of the NVO cathode at fully discharged (a, b) and charged (c, d) states in 20th cycle

Additionally, *ex-situ* SEM and EDS were employed to investigate the morphology and element information of zinc anode after cycling tests. It can be seen that a small amount of dendrite formed on the surface of the cycled zinc anode with only extra sulfur species detected by EDS characterization, which is reasonable for adopted zinc sulfate electrolyte systems (Figure 2.3.17).

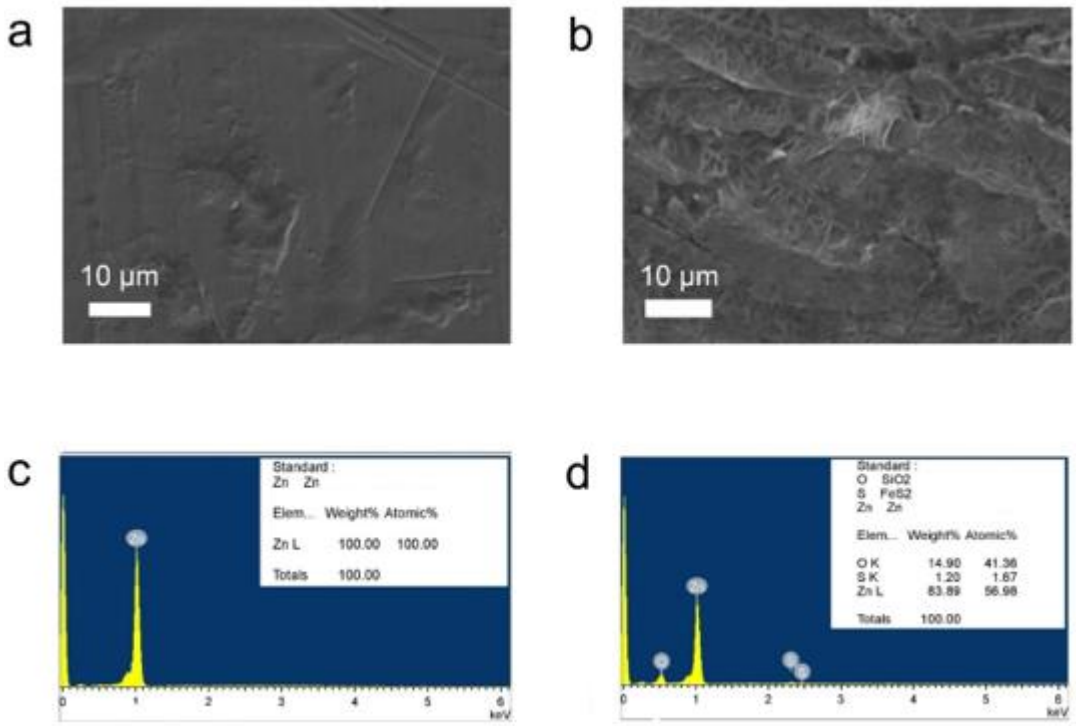

Figure 2.3.17. SEM images on surface of (a) pristine and (b) cycled zinc anode. Related elemental analysis of zinc anodes are presented in (c) and (d) for pristine and cycled states, respectively.

Moreover, *ex-situ* EDS characterizations were also performed on NVO and CVO electrodes at fully charge/discharge states in 1st and 20th cycles, respectively, which is exhibited in Figure 2.3.18. Through analysis of the results, the calculated chemical formulas at each states can be regraded as $Ni_{0.23}V_2O_5 \cdot nH_2O$ (pristine), $Ni_{0.23}ZnV_2O_5 \cdot nH_2O$ (1st discharged), $Ni_{0.11}Zn_{0.9}V_2O_5 \cdot nH_2O$ (1st charged), $Ni_{0.19}Zn_{1.16}V_2O_5 \cdot nH_2O$ (20th discharged) and $Ni_{0.11}Zn_{0.27}V_2O_5 \cdot nH_2O$ (20th charged), respectively. Surprisingly, it is seen that the Ni can reversibly migrate within the host concurrent with Zn^{2+} insertion/extraction. In contrast, the pristine $Co_{0.23}V_2O_5 \cdot nH_2O$ cathode undergoes dramatic Co content loss after cycling, reflecting with chemical formulas of $Co_{0.23}Zn_{1.3}V_2O_5 \cdot nH_2O$ (1st discharged), $Co_{0.08}Zn_{0.29}V_2O_5 \cdot nH_2O$ (1st charged), $Co_{0.06}Zn_{1.09}V_2O_5 \cdot nH_2O$ (20th discharged) and $Co_{0.05}Zn_{0.34}V_2O_5 \cdot nH_2O$ (20th discharged), repectively. Accordingly, the absence of Co ions in V_2O_5 framework within the cycling tests can result in inevitable irreversible structural evolutions. Hence, an inferior cycling capbility was observed in CVO cathode.

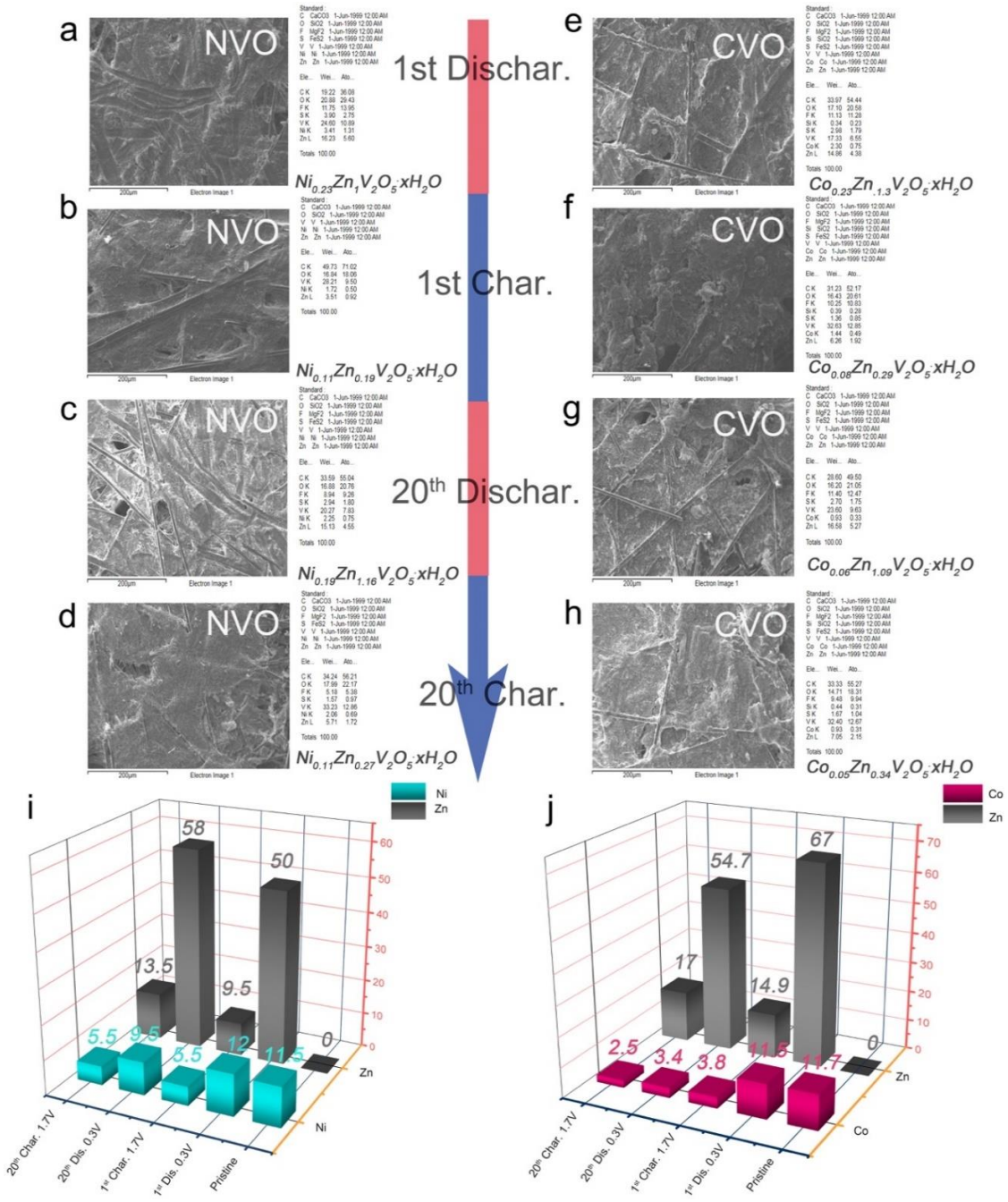

Figure 2.3.18. *Ex-situ* EDS measurements of cycled NVO and CVO cathodes at varied charge/discharge states.

A further comparsion of structural reversibility between NVO and CVO eletrodes was achieved by characterizations of *ex-situ* Raman spectra on different charge/discharge states at 1st and 20th cycles, respectively (Figure 2.3.19). The Raman shifts of all characterized NVO electrode maintained at almost the same position upon different states except a small split peak appeared at 153 cm^{-1} in the fully charged NVO electrode after 20 cycles treatment. This can be interpreted as a slight loss of nickel “pillars” in

the host lattice[74], giving rise to a weakened interaction and long-range order between the host layers. Whereas, the equivalent peak in CVO electrode occurs at a lower Raman shift of 142 cm^{-1}, associated with a notable red shift of the peak from 1006 cm^{-1} to 993 cm^{-1} after fully charged. For the evidence given above, it is seen that *ex-situ* EDS and *ex-situ* Raman results are in concordance with with previous characterizations, demonstrating that the NVO cathode possess superior robust crystal structure with high reversibility as Zn^{2+} storage host compared with CVO and other reported vanadium-bronze based cathodes.

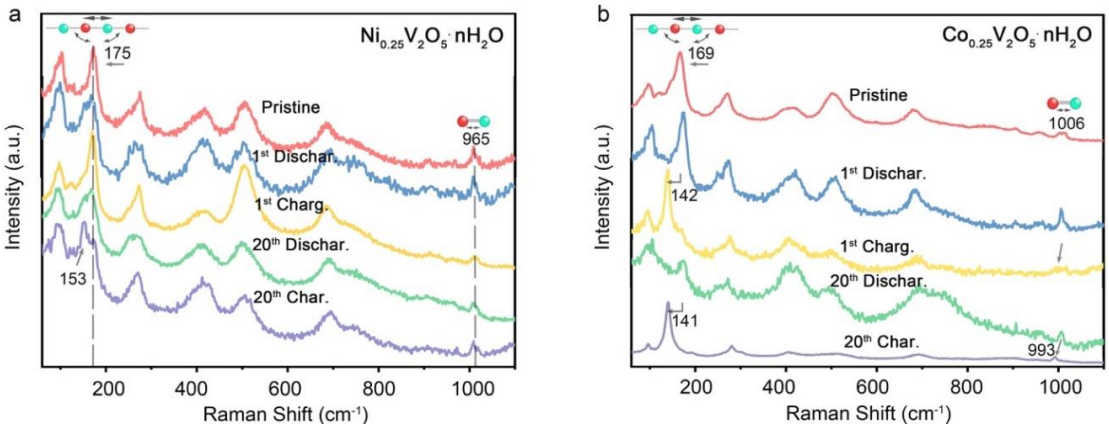

Figure 2.3.19. *ex-situ* Raman spectra characterizations of (a) NVO and (b) CVO at varied charge/discharge states.

In addition to above characterizations of structural and chemical evolutions, NEXAFS was performed to investigate the electron and coordination configurations of both NVO and CVO cathode materials (Figure 2.3.20). It is seen that the Ni L-edge NEXAFS spectrum offers details of electron transition from Ni 2*p* to 3*d*. More explicitly, two main absorption characters of the spit-orbital splitting, i.e. L_3-edge ($2p_{3/2}$ to *3d*) located in range of 850-855 eV; and L_2-edge ($2p_{1/2}$ to 3*d*) within a sphere of 862-872 eV [75,76]. The multiplets in the range of L_3-edge indicates a high-spin Ni^{2+} electronic structure and almost octahedral coordination configurations for all characterized NVO samples[77]. Moreover, two absorption peaks marked with A (851.4eV) and B (853.4eV) in L_3-edge area stands for the d^8L ground state and $d^9\underline{L}$ ground state, respectively. [78,79,80,81] The energy variations of these two peaks associate with Δ_{energy} of *p-d* charge-transfer and *d-p* hybridization intensity. [78,79,80,81] Thus, the peak B shifts to the higher energy in discharged NVO material, implying an increase in Δ_{energy} and a decrease in *d-p* hybridization, because the two O axial anions in NiO_6 octahedron are coordinated with

the V_2O_5 bilayers, and the rest of the four anions are shared with inserted Zn^{2+} which can be affected by additional *d-p* hybridization between Zn *3d* and O *2p* and reduced *d-p* hybridisation between Ni *3d* and O *2p*. In addition, the V L-edge and O K-edge are presented in Figure 2.3.20b, which can be allocated to V $2p_{3/2}$ to V *3d* (535-530 eV) of L_3-edge, V $2_{1/2}$ to V *3d* (520-528eV) of L_2-edge and O 1s to *d-p* hybridization (above 527eV).[82,83,84,85,86] Furthermore, it is further confirmed that there is a mixed oxidation states of V^{4+} and V^{5+} in pristine and fully charged samples through observation of V L_3-edge. Weaker absorption features of V L_3-edge and O K-edge in fully discharged NVO electrode indicate reduced oxidation states of V species with more V^{3+} / V^{4+}, which confirms the previous observation from XPS. Notably, there is a tiny peak around 511.2 eV implying a second order absorption characteristic of Zn L_3-edge, verifying the existence of Zn species in discharged cathode. Comparatively, it is seen that Co $2p_{3/2}$ L_3-edge (775-785 eV) and $2p_{1/2}$ L_2-edge (790-795 eV) in Figure 2.3.20c directly provide the electronic transition from Co *2p* to *3d* unoccupied vacancy valence state, indicating a high-spin Co^{2+} in octahedral polymorph coordinated with O atoms.[77,87,88,89] and further proved by a shoulder peak at 775.8 eV in pristine CVO cathode.[87] Nevertheless, no Co species can be characterized in cycled CVO samples, which is manifested in an irreversible process of Co species leaching out of V_2O_5 frameworks during charge/discharge reactions. Similar to previous observation of NVO cathode, the results of the CVO NEXAFS spectra specific to V L-edge and O K-edge are presented in Figure. 2.3.20d, which clearly clarify the oxidation states changes of V during charge/discharge process. Therefore, the unstable features of CVO cathode compared with NVO cathode are sufficiently verified by multiple experimental characterizations.

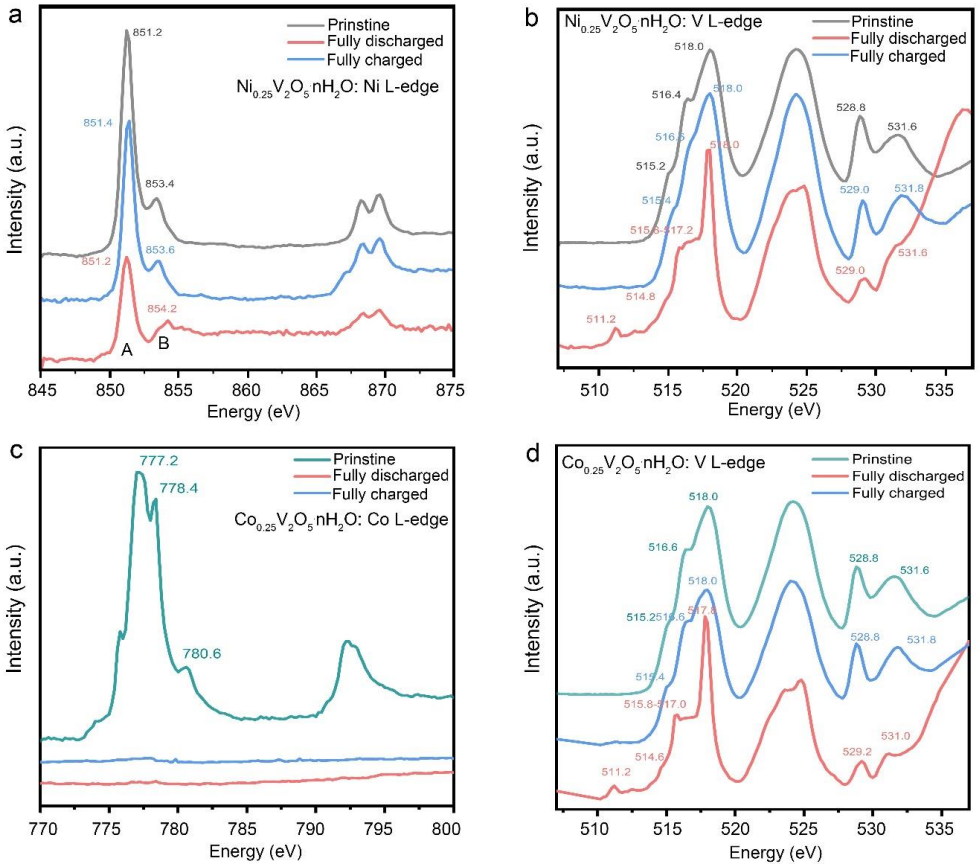

Figure 2.3.20. NEXAFS spectra of (a) Ni and (b) V L-edge for pristine, 20th cycles discharged/charged NVO electrode, respectively. NEXAFS spectra of (c) Co and (d) V L-edge for pristine, 20th cycles discharged/charged CVO electrode, respectively.

Although the electrochemical reaction behaviours of NVO electrode have been comprehensively discussed above, the atomic-level structural evolutions and charge carriers migration from energy profile perspective are crucial to unravel zinc storage mechanism. For computational perspective, the standard composition of $Ni_{0.25}V_2O_5 \cdot H_2O$ was reproduced by DFT calculations with only 1% deviation in lattice parameters compared with experimental values, which exhibited in Table 2.3.4.

Table 2.3.4. DFT-calculated structural details of $Zn_xNi_{0.25}V_2O_5{\cdot}H_2O$ phases.

Stoichiometry	Zn^{2+} Site	ΔE (eV)	Voltage per Zn^{2+} (V)	*a* (Å)	*b* (Å)	*c* (Å)	β (°)	Vol (Å^3)
$Ni_{0.25}V_2O_5{\cdot}0.74H_2O$ (Expt.)				11.7560	3.6490	10.3640	95.03	442.88
$Ni_{0.25}V_2O_5{\cdot}H_2O$ (DFT)				11.7865 (+0.3%)	3.6162 (-0.9%)	10.2698 (-0.9%)	94.21	436.521 (-1.4%)
$Zn_{0.0625}Ni_{0.25}V_2O_5{\cdot}H_2O$	A		2.122	11.7983 (+0.1%)	3.6200 (+0.1%)	10.1520 (-1.1%)	94.27	427.81 (-1.0%)
$Zn_{0.125}Ni_{0.25}V_2O_5{\cdot}H_2O$	A	+0.000	1.879	11.8257 (+0.3%)	3.6228 (+0.2%)	10.0079 (-2.6%)	93.74	427.81 (-2.0%)
$Zn_{0.125}Ni_{0.25}V_2O_5{\cdot}H_2O$	B	+0.356	1.701	11.8432 (+0.4%)	3.6235 (+0.2%)	9.9694 (-2.9%)	92.84	426.88 (-2.2%)
$Zn_{0.125}Ni_{0.25}V_2O_5{\cdot}H_2O$	C	+0.692	1.533	11.8275 (+0.3%)	3.6292 (+0.4%)	10.0884 (-1.8%)	94.33	431.79 (-2.2%)
$Zn_{0.125}Ni_{0.25}V_2O_5{\cdot}H_2O$	D	+0.039	1.538	11.8129 (+0.2%)	3.6266 (+0.3%)	10.0909 (-1.7%)	94.81	429.74 (-1.6%)
$Zn_{0.25}Ni_{0.25}V_2O_5{\cdot}H_2O$	A + A		1.426	11.8111 (+0.2%)	3.6431 (+0.7%)	9.9247 (-3.4%)	93.78	424.65 (-2.7%)
$Zn_{0.375}Ni_{0.25}V_2O_5{\cdot}H_2O$	A + A + B		1.042	11.8070 (+0.2%)	3.6416 (+0.7%)	9.9376 (-3.2%)	94.21	423.87 (-2.9%)
$Zn_{0.5}Ni_{0.25}V_2O_5{\cdot}H_2O$	'split interstitial'		1.087	12.0570 (+2.3%)	3.6918 (+2.1%)	9.5210 (-7.3%)	93.33	423.07 (-3.1%)

Moreover, there are two available channels existing in NVO material viewed along the *b* axis (Figure 2.3.21a). Among them, Ni^{2+} occupies half of the sites in the channel, while there is no species occupy the sites in channel II, offering a path for Zn^{2+} migration along the b direction. Considering a case of small amount of Zn^{2+} intercalation, four possible Zn^{2+} intercalated sites can be found during the first discharge of NVO electrode, represented by A-D (Figure 2.3.21b), in which, the Site A is in channel I and the rest of sites are all in channel II. According to the calculations, optimized geometries of Zn^{2+} in each sites and their corresponding energy are presented in Figure 2.3.21c.

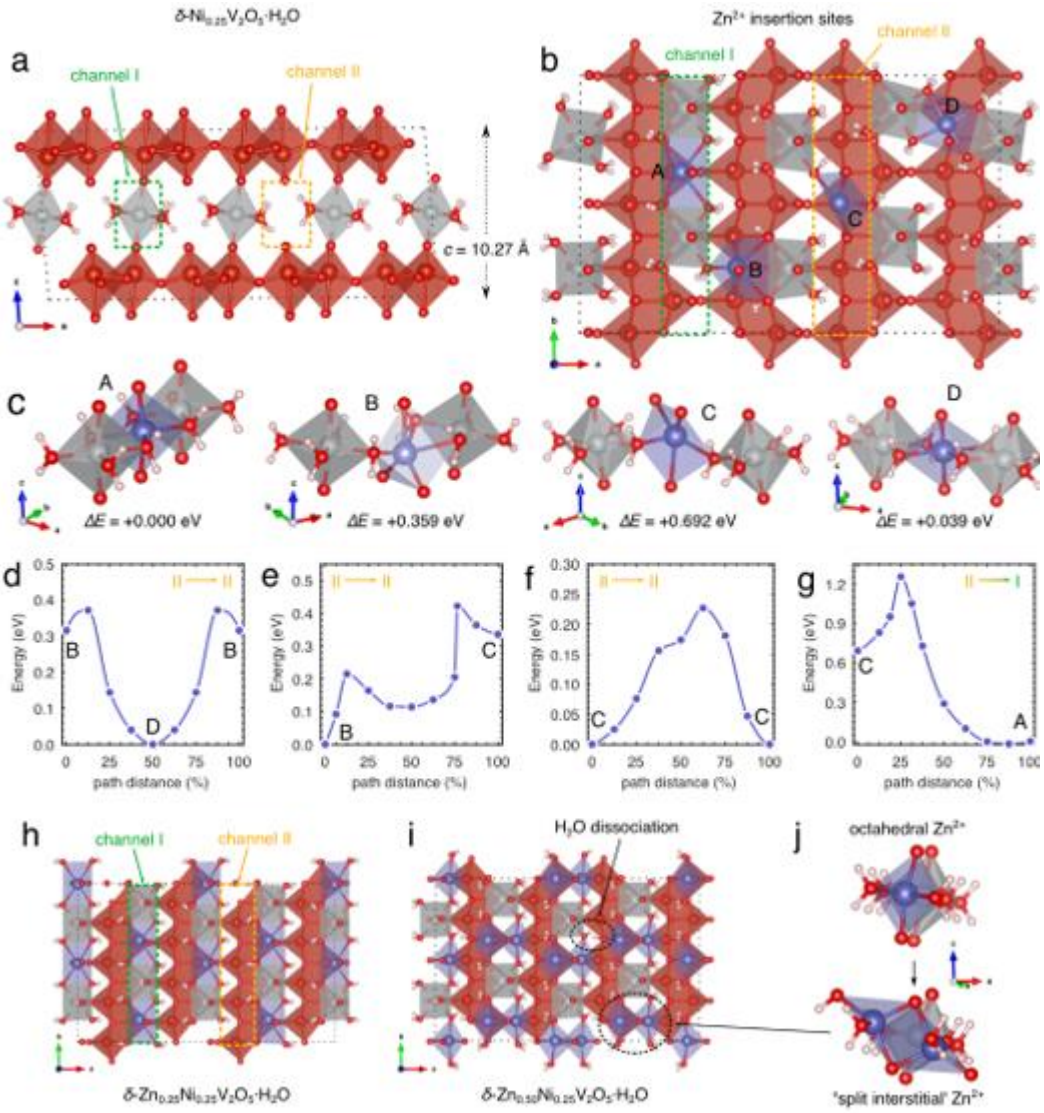

Figure 2.3.21. (a) B3LYP-D3 calculated structure of NVO sample, highlighting channels I and II. Large/ small red spheres refer to V and O ions, respectively, grey spheres and blue spheres stand for Ni and Zn ions, respectively; (b) Inserted sites A, B, C and D for zinc ions on basis of a stoichiometry of $Zn_{0.125}Ni_{0.25}V_2O_5{\cdot}H_2O$. (c) Local coordination and corresponding energy of sites A – D; Energy profiles for Zn^{2+} migration along channel I through (d), (e) and (f) pathways, and along from channel II to channel I through (g) pathway. (h) Stable arrangement of Zn^{2+} at A sites with a stoichiometry of $Zn_{0.25}Ni_{0.25}V_2O_5{\cdot}H_2O$, implying an open accesses channel II for further insertion. (i) Reordered Zn^{2+} with dissociation of partial H_2O in $Zn_{0.50}Ni_{0.25}V_2O_5{\cdot}H_2O$. (j) Demonstration of the geometrical transition between octahedral and 'split interstitial' Zn^{2+} in $Zn_{0.50}Ni_{0.25}V_2O_5{\cdot}H_2O$.

It is seen that A and D are the most stable sites with iso-energy (ΔE = 0.039 eV). At

these locations, the Zn^{2+} possesses nearly octahedral polymorph and shares edges with both two NiO_6 octahedrons and two axial O^{2-} in the host layers. In site A, the distorted O-Zn-O axial bond derives from contraction of interlayer spacing of the host layers, which is opposite to the linear O-Ni-O bond in channel I (Figure 2.3.22). At location of D, the rotated adjacent NiO_6 octahedrons stabilize the Zn^{2+} between them (Figure 2.3.23).

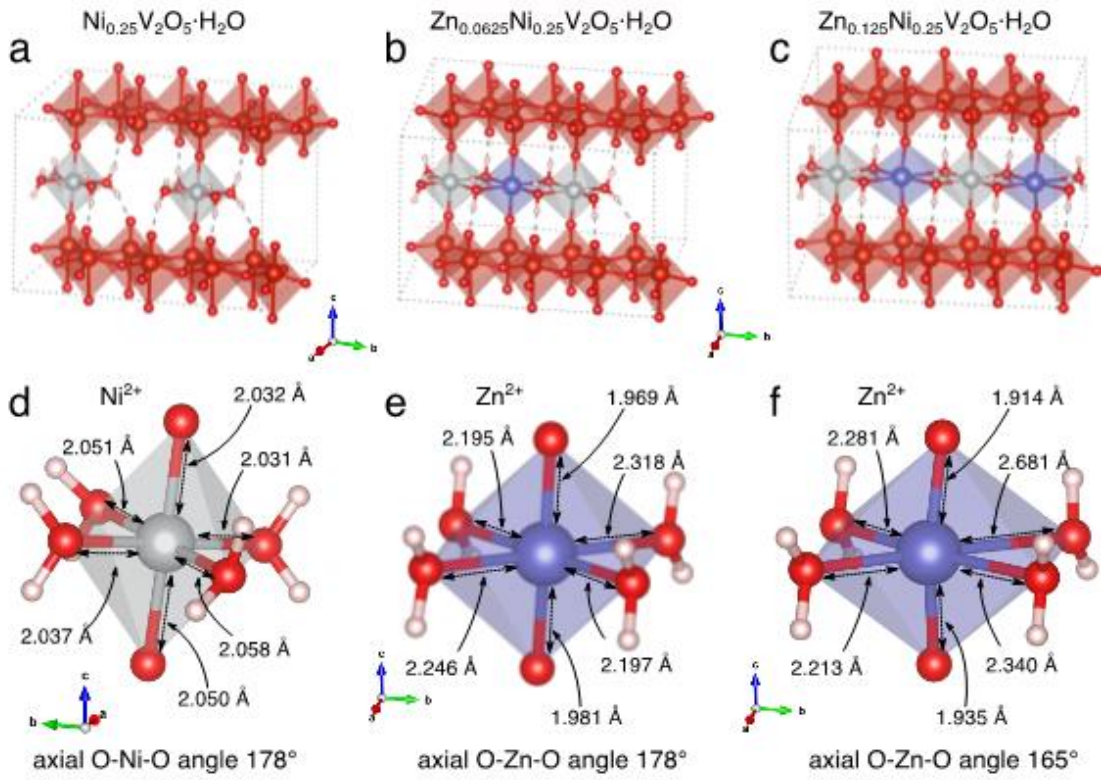

Figure 2.3.22. Geometry of octahedral Ni^{2+} and Zn^{2+} at A sites with varied concentrations. (a), (b) and (d) exhibit the positions of Ni^{2+} and Zn^{2+} in a (4 × 1 × 1) unit cell; And the relative local geometry of the ions with bond parameters are presented in (d), (e) and (f); As increasing amount of Zn^{2+} inserted into cell, the lattice parameter of c decrease as the enhancement of interaction between Zn^{2+} and host layers, and the there is a distortion of O-Zn-O bond from a linear geometry. Therefore, the intercalation voltage per Zn is reduced (Table 2.3.3), associated with a reduction of Zn^{2+} stability.

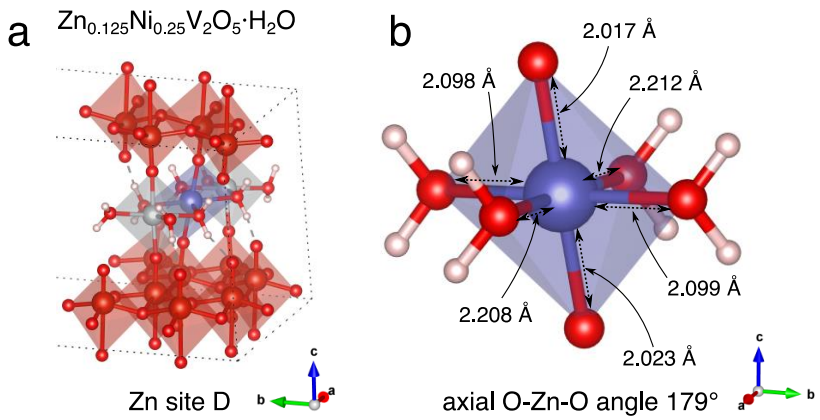

Figure 2.3.23. Geometry of Zn^{2+} octahedron at D sites with a stoichiometry of $Zn_{0.125}Ni_{0.25}V_2O_5 \cdot H_2O$.

At positions of B and C in channel II, Zn^{2+} octahedrons share edges with three apical O^{2-} in the bilayers, and possess either three (B site) or two (C site) bonds coordinated with H_2O in the *ab* plane. The energy variations between B and C sites is owing to more favourable coordination with Zn^{2+} at the B position. Moreover, for the Zn^{2+} intercalation in each of these positions with forming a stoichiometry of $Zn_{0.125}Ni_{0.25}V_2O_5 \cdot H_2O$, the interlayer spacing (c-axis) shrinks compared to the pristine NVO material (Table 2.3.3) because of strengthened interaction between Zn^{2+} and the bilayers. This phenomenon is in accordance with the calculation results of Wu et al.[90] Investigations of the Zn^{2+} diffusion along channel II at low concentrations of zinc ions indicate that Zn^{2+} ions must move along the path between the positions in the order of B→D→B→C→C→B (Figure 2.3.24), and then over again in the next unit cell.

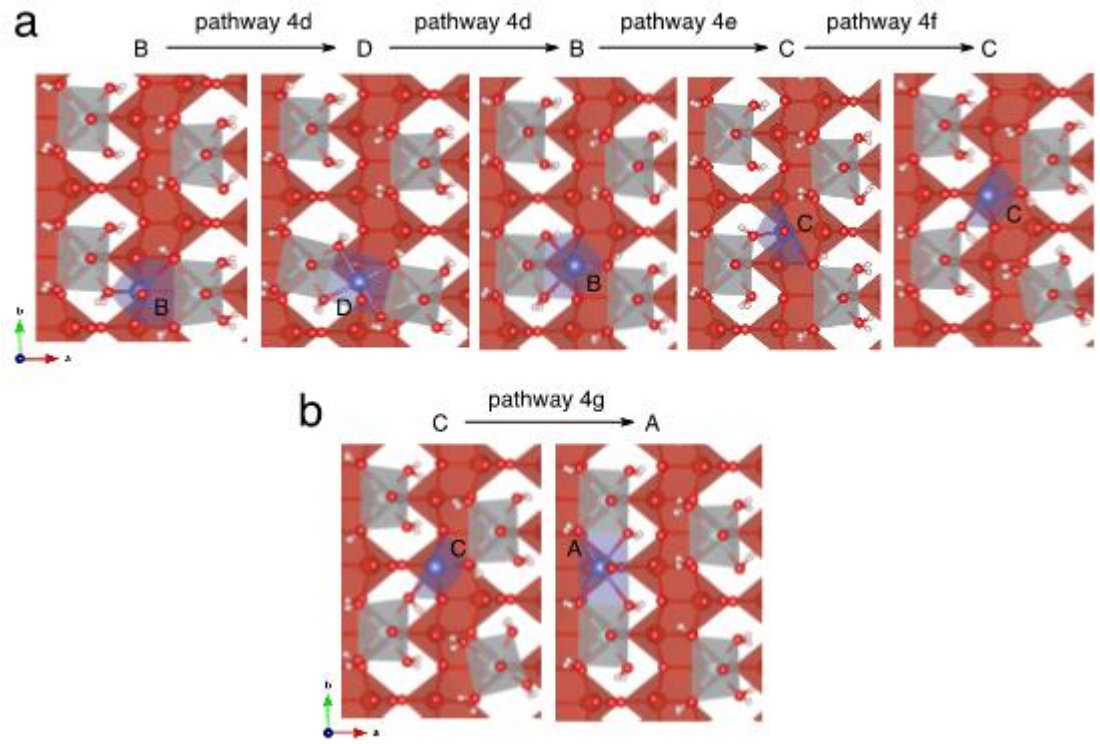

Figure 2.3.24. Demonstration of Zn^{2+} diffusion in the structure, viewed along the *c* axis. (a) presents Zn^{2+} migrating between sites along channel II. (b) presents Zn^{2+} migrating from site C (channel II), to site A (channel I).

Figures 2.3.21d-f present energy profiles of the migration pathway. It is seen that even the maximum activation barrier is below 0.5 eV, for individual jump, which implies rapid diffusion properties of Zn^{2+} along channel II at room temperature. Additionally, when viewing the structure along the *a*-axis, the diffusion path along channel II follows a "Z-shaped" motif because Zn^{2+} prefer to have a coordination closer to one of the host layers than the other in respective sites (Figure 2.3.25). In order to occupy channel I, there is only one path for Zn^{2+} migration, which is from C to A site. Thus, the energy profile for the migration is shown in Figure 2.3.18g which presents an activation barrier of +0.563 eV. Nevertheless, the energy barrier for opposite migration from A to C reaches +1.2 eV, since the A site for inserted Zn^{2+} coordination is more stable than the C site. This activation energy is hard to overcome at room temperature. Hence, Zn^{2+} will prefer to accumulate at A site rather than reverse back (Figure 2.3.26). According to the above description, it is understood that Zn^{2+} can move along the entire length of channel II, and conquer the obstacle to migrate from C (channel II) to A site (channel I). With successively inserted Zn^{2+} filling with channel II, the ultimately resulting stoichiometry can be regard as $Zn_{0.25}Ni_{0.25}V_2O_5 \cdot H_2O$ (Figure 2.3.21h). Meanwhile,

Zn^{2+} will still be capable of moving along the open channel II, implying a feasibility for further intercalation. Furthermore, the high reverse barrier for extraction of Zn^{2+} from A site is hardly overcame at room temperature. The experimentally observed deintercalation of Zn^{2+} (and Ni^{2+}) upon charge process must be associated with structural rearrangement when more charge carrier insert into the cathode material with a stoichiometry of $Zn_{0.25}Ni_{0.25}V_2O_5 \cdot H_2O$. Therefore, with structural rearrangement, Zn^{2+} (and Ni^{2+}) will be able to escape from the cathode material after fully charged treatment.

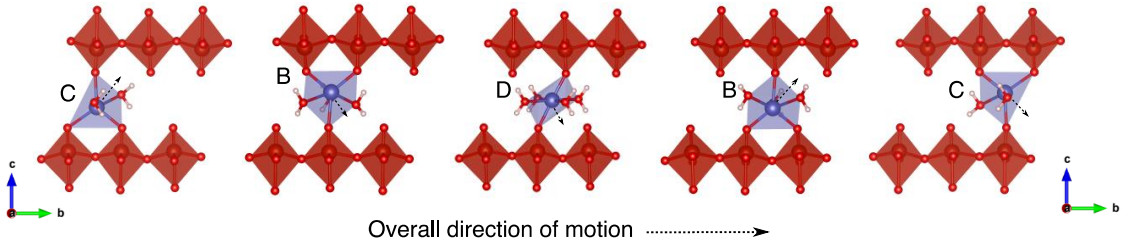

Figure 2.3.25. Geometry of Zn^{2+} in coherent sites when moving along channel II, viewed along the *a*-axis. The apical O^{2-} of the host sheets are offset from each other along the *b*-direction, so Zn ions in B or C sites coordinate to two O-ions in one layer, and one in the adjacent layer. The Zn ion resides closer along the *c* direction to the V_2O_5 layer to which it forms two Zn-O bonds. Moving between sites, results in a 'zig-zag' migration pathway.

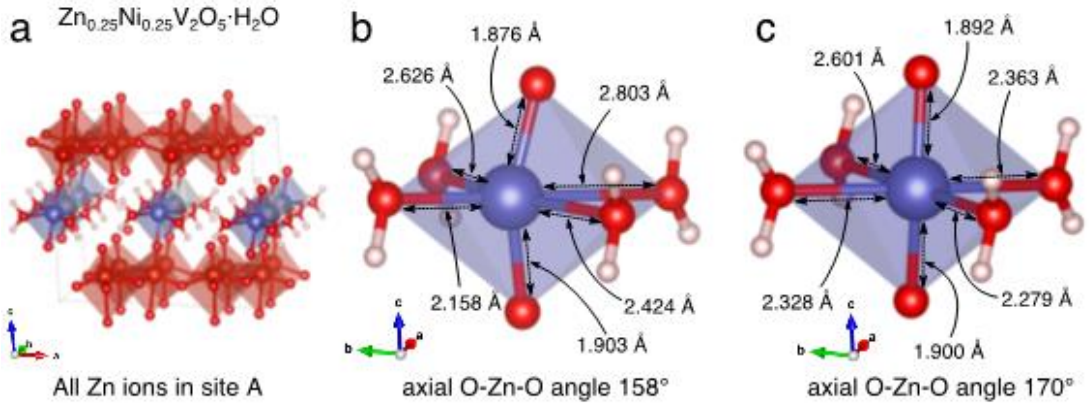

Figure 2.3.26. Geometry of two Zn^{2+} at A sites with a stoichiometry of $Zn_{0.25}Ni_{0.25}V_2O_5 \cdot H_2O$.

In addition to the investigation of low zinc concentrated NVO material, an extension of

the scope of studies to $Zn_xNi_{0.25}V_2O_5 \cdot H_2O$ (x>0.25) was adopted as all A sites have been filled in this case. More Zn^{2+} were inserted into channel II generating a new phase with a stoichiometry of $Zn_{0.375}Ni_{0.25}V_2O_5 \cdot H_2O$. During the successive intercalation process, the further contraction of the interlayer *c* parameter and reduced axial O-Zn-O bond angle can be observed in Zn octahedrons at the A sites. Finally, the V_2O_5 bilayers became too tight to maintain octahedral coordination of Zn^{2+} within channel I at A sites. The following structural rearrangement will occur, that is, the Zn^{2+} at A sites will transform along the *a* axis orientation, bonding with two O^{2-} in one host layer, and one O^{2-} in the adjacent layer (Figure 2.3.27).

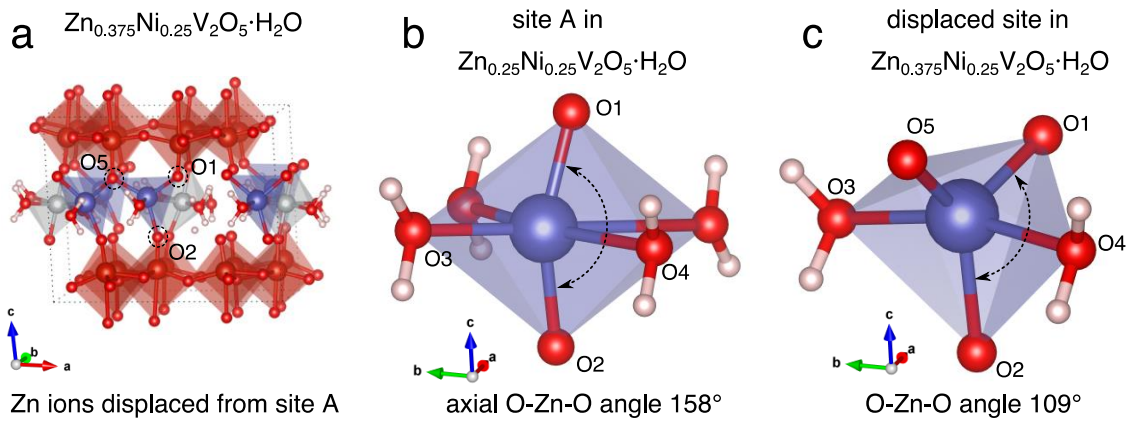

Figure 2.3.27. Geometrical transition of Zn^{2+} migrating from a stoichiometry of $Zn_{0.25}Ni_{0.25}V_2O_5 \cdot H_2O$ to $Zn_{0.375}Ni_{0.25}V_2O_5 \cdot H_2O$. (b) Continuous contraction of the interlayer space *c* causes an growing distortion of the axial O1-Zn-O2 bonds in Zn^{2+} octahedron. Eventually, (c) resulting in displacement of Zn^{2+} along the *a* axis with loss of two coordination with O^{2-} along horizontal interlayer direction, but additional coordination with $O5^{2-}$ in one of the host layers.

With further increasing Zn species in NVO electrode with a stoichiometry of $Zn_{0.5}Ni_{0.25}V_2O_5 \cdot H_2O$, two Zn ions will occupy a position between the A sites instead of only one Zn^{2+}, thus forming a "split interstitial" geometry as a stable configuration (Figure 2.3.21h). The new coordination environment of Zn^{2+} geometry can increase the energy of Zn^{2+} and reduce the activation barrier for migration in comparison with the most stable insertion sites.[91] Hence, the "split gap" Zn^{2+} ions may move in the structure and can be extracted during charge through an interstitial mechanism.

Moreover, when the stoichiometry of NVO cathode material reaches to

$Zn_{0.5}Ni_{0.25}V_2O_5 \cdot H_2O$, the DFT calculations suggest that there is some dissociation of interlayer H_2O which will occur in the host interlayer space (Figure 2.3.21f). This result was also provided from both previous DFT calculations[90] and FTIR spectroscopy investigations of solvated protons in $V_2O_5 \cdot nH_2O$ gel.[92] However, it is too complex to evaluate fully discharged structure of NVO cathode material *via* DFT methods because of dissociated water from frameworks. Through reviewing the experimental XRD results in Figure 2.3.15, the expanded interlayer space (10.8Å) of the fully discharged electrode was observed compared to that of the pristine material (10.3Å). From DFT perspective, it is only observed that the gradual shrinkage of the interlayer *c* parameter with further adding Zn^{2+} into the host lattice (Table 2.3.3), but it should be clarified that the intercalation of Zn^{2+} was only considered to form a cathode material with a stoichiometric of $Zn_{0.5}Ni_{0.25}V_2O_5 \cdot H_2O$, which is only about half concentration of zinc species in fully discharged NVO sample observed from the EDS analysis. Beyond this point, it could be speculated that the interlayer spacing will begin to expand again. This hypothesis could be verified by a DFT calculations form Wu et al, where the results exhibit a shrinkage of the unit cell volume for $Zn_xV_2O_5 \cdot H_2O$ ($0<x<0.5$), and followed by an expansion when $x>0.5$ in $Zn_xV_2O_5 \cdot H_2O$. The results are in agreement with the investigations from DFT and experimental structural evolution results.

In addition to the DFT simulations, the macroscopic 3D-morphology of the as-fabricated NVO electrode was characterized by X-ray micro-computed Tomography (Figure 2.3.28a). It should be emphasized that the examined electrode was a slice of hydrophilic carbon paper printed with a mixture of NVO active material, binder and conductive agent (see details in experimental section). It is seen that a tough thin layer of the mixture sites above the carbon matrix. Furthermore, a close-up area within the reconstructed virtual slice in Figure 2.3.28b shows a fine microstructure of solid phase of electrode and the tiny hole, which exceeds the capability of imaging resolution from X-ray micro-CT. Hence, in order to capture all the details of the as-prepared electrode, a higher resolution (nano-CT) was performed, and the result is shown in Figure 2.3.28c. It is observed that different phases of NVO (light gray), hole (black), and carbon (dark gray) are easy to be distinguished. After using thresholding segmentation to extract the pore phases based on the grey scale level, the pore phase with color-coded pore size distributions can be visualized through skeletonization of the virtual slice (Figure 6d), from which it can be seen that a complex 3D structure and wide distribution of pore sizes in electrode. Moreover, Figure 2.3.28e shows the streamline of simulated diffusion flux according to the reconstructed pore structure. From above results, the measured porosity ε is 0.18, and the calculated tortuosity factor is 2.57, which provide an effective diffusion coefficient of 0.07, indicating a superior reactant transport capability of as-fabricated NVO electrode compared with those in the LIBs.[93]

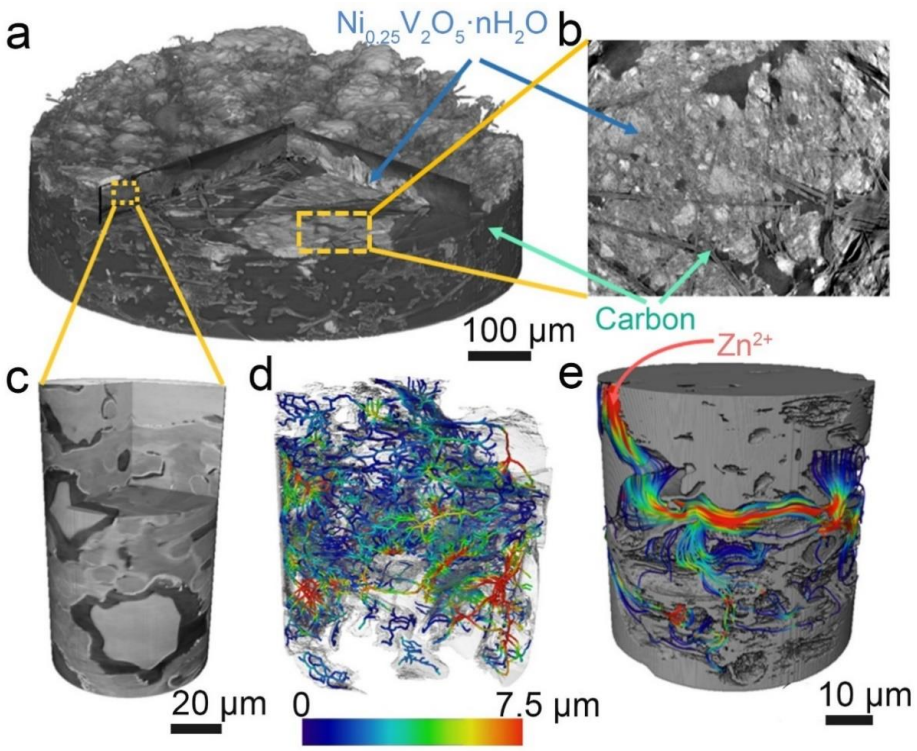

Figure 2.3.28. Multi-length scale characterization of the as-prepared NVO electrode. (A) 3D reconstructed NVO electrode by X-ray micro-CT; (b) Virtual slice of close-up area in the electrode; (c) 3D reconstructed NVO electrode by X-ray nano-CT; (d) Pore phase skeletonized for exhibition of local pore size distribution with colour; (e) demonstration of the flux distribution upon diffusion simulation *via* the streamline on basis of the reconstructed pore morphology.

2.4 Conclusion

Highly porous hydrated δ-$Ni_{0.25}V_2O_5$ micro-ribbon was successfully synthesized by a simple single-step hydrothermal method. Through comprehensive characterizations on electrochemical features, it was found that the as-obtained NVO cathode material possesses a highly reversible capacity of 402 mAh g^{-1} at current density of 0.2 A g^{-1}, and superior cycling stability of 98% capacity retention after 1200 cycles at 5 A g^{-1}. The following adopted multi-scale experimental characterization techniques and DFT simulations sufficiently elucidate the Zn^{2+} (de)intercalation mechanism within the electrode. Most importantly, it is the first attempt to reveal the atomic-level arrangement on the basis of Zn^{2+} migration and accommodation characteristics in the vanadium bronze cathode, highlighting the crucial correlation of the pre-inserted ions and the host layer frameworks on varied electrochemical performance and structural evolutions, which proposed routes to rationally design high performance vanadium bronze type

cathode for AZIBs applications with well defined microstructures and electrochemical behaviours. Moreover, combining structural benefits from the self-template mesoporous nanobelts NVO material, and equipped hydrophilic porous carbon paper as current collector, this effectively boosted the charge carrier diffusion kinetics *via* optimized interfacial reactions. Meanwhile, the outstanding structural configuration with high reactant transport within the as-fabricated electrode successfully verified by X-ray nano CT technology is the first time to be adopted in investigations of AZIBs.

2.5 Reference

1 V. Etacheri, R. Marom, R. Elazari, G. Salitra and D. Aurbach, *Energy Environ. Sci.*, **2011**, *4*, 3243–3262.

2 H. Kim, J. Hong, K.-Y. Park, H. Kim, S.-W. Kim and K. Kang, *Chem. Rev.*, **2014**, *114*, 11788–11827.

3 J. Lai, H. Zhu, X. Zhu, H. Koritala and Y. Wang, *ACS Appl. Energy Mater.*, **2019**, *2*, 1988–1996.

4 C. Xu, B. Li, H. Du and F. Kang, *Angew. Chem. Int. Ed.*, **2012**, *51*, 933–935.

5 J. Zhou, L. Shan, Z. Wu, X. Guo, G. Fang and S. Liang, *Chem. Commun.*, **2018**, *54*, 4457–4460.

6 F. Wang, O. Borodin, T. Gao, X. Fan, W. Sun, F. Han, A. Faraone, J. A. Dura, K. Xu and C. Wang, *Nat. Mater.*, **2018**, *17*, 543–549.

7 G. Li, Z. Yang, Y. Jiang, C. Jin, W. Huang, X. Ding and Y. Huang, *Nano Energy*, **2016**, *25*, 211–217.

8 Z. Jia, B. Wang and Y. Wang, *Mater. Chem. Phys.*, **2015**, *149*, 601–606.

9 N. Zhang, F. Cheng, Y. Liu, Q. Zhao, K. Lei, C. Chen, X. Liu and J. Chen, *J. Am. Chem. Soc.*, **2016**, *138*, 12894–12901.

10 B. Lee, H. R. Lee, H. Kim, K. Y. Chung, B. W. Cho and S. H. Oh, *Chem. Commun.*, **2015**, *51*, 9265–9268.

11 L. Li, Q. Zhao, Z. Luo, Y. Lu, H. Ma, J. Hu, Y. Li, J. Chen, L. Liu and W. Huang, *Sci. Adv.*, **2018**, *4*, eaao1761.

12 G. Dawut, Y. Lu, L. Miao and J. Chen, *Inorg. Chem. Front.*, **2018**, *5*, 1391–1396.

13 M. Winter and R. J. Brodd, *Chem. Rev.*, **2004**, *104*, 4245–4270.

14 G. S. Gautam, P. Canepa, R. Malik, M. Liu, K. Persson and G. Ceder, *Chem. Commun.*, **2015**, *51*, 13619–13622.

15 F. Wan, L. Zhang, X. Dai, X. Wang, Z. Niu and J. Chen, *Nat. Commun.*, **2018**, *9*, 1656.

16 F. Ming, H. Liang, Y. Lei, S. Kandambeth, M. Eddaoudi and H. N. Alshareef, *ACS Energy Lett.*, **2018**, *3*, 2602–2609.

17 D. Kundu, B. D. Adams, V. Duffort, S. H. Vajargah and L. F. Nazar, *Nat. Energy*, **2016**, *1*, 16119.

18 X. Yao, Y. Zhao, F. A. Castro and L. Mai, *ACS Energy Lett.*, **2019**, *4*, 771–778.

19 P. He, G. Zhang, X. Liao, M. Yan, X. Xu, Q. An, J. Liu and L. Mai, *Adv. Energy*

Mater., **2018**, *8*, 1702463.

20 M. Yan, P. He, Y. Chen, S. Wang, Q. Wei, K. Zhao, X. Xu, Q. An, Y. Shuang, Y. Shao, K. T. Mueller, L. Mai, J. Liu and J. Yang, *Adv. Mater.*, **2018**, *30*, 1703725.

21 C. Xia, J. Guo, P. Li, X. Zhang and H. N. Alshareef, *Angew. Chem. Int. Ed.*, **2018**, *57*, 3943–3948.

22 C. Liu, Z. Neale, J. Zheng, X. Jia, J. Huang, M. Yan, M. Tian, M. Wang, J. Yang and G. Cao, *Energy Environ. Sci.*, **2019**, 19–21.

23 Y. Yang, Y. Tang, S. Liang, Z. Wu, G. Fang, X. Cao, C. Wang, T. Lin, A. Pan and J. Zhou, *Nano Energy*, **2019**, *61*, 617–625.

24 Y. Oka and T. Yao, *J. Solid State Chem.*, **1997**, *329*, 323–329.

25 Y. Oka, O. Tamada, T. Yao and N. Yamamoto, *J. Solid State Chem.*, **1996**, *126*, 65–73.

26 P. Y. Zavalij and M. S. Whittingham, *Acta Crystallogr. Sect. B Struct. Sci.*, **1999**, *55*, 627–663.

27 P. M. Marley and S. Banerjee, *Inorg. Chem.*, **2012**, *51*, 5264–5269.

28 H. Katzke and W. Depmeier, *Phase Transitions*, **1996**, *59*, 91–104.

29 C. Sun, S. Rajasekhara, J. B. Goodenough and F. Zhou, *J. Am. Chem. Soc.*, **2011**, *133*, 2132–2135.

30 T. Jiang, F. Bu, X. Feng, I. Shakir, G. Hao and Y. Xu, *ACS Nano*, **2017**, *11*, 5140–5147.

31 K. X. Wang, X. H. Li and J. S. Chen, *Adv. Mater.*, **2015**, *27*, 527–545.

32 C. Yan, G. Chen, X. Zhou, J. Sun and C. Lv, *Adv. Funct. Mater.*, **2016**, *26*, 1428–1436.

33 R. Dovesi, A. Erba, R. Orlando, C. M. Zicovich-Wilson, B. Civalleri, L. Maschio, M. Rérat, S. Casassa, J. Baima, S. Salustro and B. Kirtman, *Wiley Interdiscip. Rev. Comput. Mol. Sci.*, **2018**, *8*, 1–36.

34 F. Corà, M. Alfredsson, G. Mallia, D. S. Middlemiss, W. C. Mackrodt, R. Dovesi and R. Orlando, in *Principles and Applications of Density Functional Theory in Inorganic Chemistry II*, Springer Berlin Heidelberg, Berlin, Heidelberg, **2004**, 171–232.

35 S. Grimme, S. Ehrlich and L. Goerigk, *J. Comput. Chem.*, **2011**, *32*, 1456–1465.

36 S. Grimme, J. Antony, S. Ehrlich, and H. Krieg, *J. Chem. Phys.*, **2010**, *132*, 154104.

37 S. Grimme, A. Hansen, J. G. Brandenburg and C. Bannwarth, *Chem. Rev.*, **2016**,

116, 5105–5154.

38 G. Sai Gautam, P. Canepa, W. D. Richards, R. Malik and G. Ceder, *Nano Lett.*, **2016**, *16*, 2426–2431.

39 X. Lu, O. O. Taiwo, A. Bertei, T. Li, K. Li, D. J. L. Brett and P. R. Shearing, *J. Power Sources*, **2017**, *367*, 177–186.

40 X. Lu, T. Li, A. Bertei, J. I. S. Cho, T. M. M. Heenan, M. F. Rabuni, K. Li, D. J. L. Brett and P. R. Shearing, *Energy Environ. Sci.*, **2018**, *11*, 2390–2403.

41 S. R. Daemi, C. Tan, T. Volkenandt, S. J. Cooper, A. Palacios-Padros, J. Cookson, D. J. L. Brett and P. R. Shearing, *ACS Appl. Energy Mater.*, **2018**, *1*, 3702–3710.

42 C. K. Tsung, J. Fan, N. Zheng, Q. Shi, A. J. Forman, J. Wang and G. D. Stucky, *Angew. Chem. Int. Ed.*, **2008**, *47*, 8682–8686.

43 J. L. Andrews, S. Singh, C. Kilcoyne, P. J. Shamberger, G. Sambandamurthy and S. Banerjee, *MRS Commun.*, **2017**, *7*, 634–641.

44 L. Abello, E. Husson, Y. Repelin and G. Lucazeau, *Spectrochim. Acta Part A Mol. Spectrosc.*, **1983**, *39*, 641–651.

45 B. Yan, L. Liao, Y. You, X. Xu, Z. Zheng, Z. Shen, J. Ma, L. Tong and T. Yu, *Adv. Mater.*, **2009**, *21*, 2436–2440.

46 R. Baddour-Hadjean, M. B. Smirnov, K. S. Smirnov, V. Y. Kazimirov, J. M. Gallardo-Amores, U. Amador, M. E. Arroyo-De Dompablo and J. P. Pereira-Ramos, *Inorg. Chem.*, **2012**, *51*, 3194–3201.

47 C. Julien, J. P. Guesdon, A. Gorenstein, A. Khelfa and I. Ivanov, *Appl. Surf. Sci.*, **1995**, *90*, 389–391.

48 R. Manikandan, C. Justin Raj, M. Rajesh, B. C. Kim, S. Y. Park, B. B. Cho and K. H. Yu, *Electrochim. Acta*, **2017**, *230*, 492–500.

49 D. Vernardou, E. Spanakis, G. Kenanakis, E. Koudoumas and N. Katsarakis, *Mater. Chem. Phys.*, **2010**, *124*, 319–322.

50 R. Baddour-Hadjean, E. Raekelboom and J. P. Pereira-Ramos, *Chem. Mater.*, **2006**, *18*, 3548–3556.

51 S. I. Cordoba-Torresi, A. Hugot-Le Goff and S. Joiret, *J. Electrochem. Soc.*, **1991**, *138*, 1554–1559.

52 B. B. Li, X. Q. Xiu, R. Zhang, Z. K. Tao, L. Chen, Z. L. Xie, Y. D. Zheng and Z. Xie, *Mater. Sci. Semicond. Process.*, **2006**, *9*, 141–145.

53 Y. Xu, H. Dong, M. Zhou, C. Zhang, Y. Wu, W. Li, Y. Dong and Y. Lei, *Small Methods*, **2018**, 1800349.

54 C. Tripon, D. Toloman, M. Aluas, C. Filip and I. Ardelean, *J. Optoelectron. Adv. Mater.*, **2006**, *8*, 1129–1131.

55 Y. Liu, B. Shen, X. Liu, Y. Wu, X. He and Q. Li, *Int. J. Electrochem. Sci.*, **2017**, *12*, 5483–5491.

56 M. Xue, J. Ge, H. Zhang and J. Shen, *Appl. Catal. A Gen.*, **2007**, *330*, 117–126.

57 B. Tang, J. Zhou, G. Fang, F. Liu, C. Zhu, C. Wang, A. Pan and S. Liang, *J. Mater. Chem. A*, **2019**, *7*, 940–945.

58 Y. Yang, Y. Tang, G. Fang, L. Shan, J. Guo, W. Zhang, C. Wang, L. Wang, J. Zhou and S. Liang, *Energy Environ. Sci.*, **2018**, *11*, 3157–3162.

59 Oka, Y., Yao, T., & Yamamoto, N. (1990). *Journal of Solid State Chemistry*, **1990**, *89*, 372-377.

60 Y. Cai, F. Liu, Z. Luo, G. Fang, J. Zhou, A. Pan and S. Liang, *Energy Storage Mater.*, **2018**, *13*, 168–174.

61 V. Soundharrajan, B. Sambandam, S. Kim, M. H. Alfaruqi, D. Y. Putro, J. Jo, S. Kim, V. Mathew, Y. K. Sun and J. Kim, *Nano Lett.*, **2018**, *18*, 2402–2410.

62 B. Sambandam, V. Soundharrajan, S. Kim, M. H. Alfaruqi, J. Jo, S. Kim, V. Mathew, Y. Sun and J. Kim, *J. Mater. Chem. A*, **2018**, *6*, 15530–15539.

63 C. Xia, J. Guo, Y. Lei, H. Liang, C. Zhao and H. N. Alshareef, *Adv. Mater.*, **2018**, *30*, 1705580.

64 M. H. Alfaruqi, V. Mathew, J. Song, S. Kim, S. Islam, D. T. Pham, J. Jo, S. Kim, J. P. Baboo, Z. Xiu, K. S. Lee, Y. K. Sun and J. Kim, *Chem. Mater.*, **2017**, *29*, 1684–1694.

65 W. Li, K. Wang, S. Cheng and K. Jiang, *Energy Storage Mater.*, **2018**, *15*, 14–21.

66 M. Yan, P. He, Y. Chen, S. Wang, Q. Wei, K. Zhao, X. Xu, Q. An, Y. Shuang, Y. Shao, K. T. Mueller, L. Mai, J. Liu and J. Yang, *Adv. Mater.*, **2018**, *30*, 1703725.

67 B. Tang, G. Fang, J. Zhou, L. Wang, Y. Lei, C. Wang, T. Lin, Y. Tang and S. Liang, *Nano Energy*, **2018**, *51*, 579–587.

68 L. Shan, Y. Yang, W. Zhang, H. Chen, G. Fang, J. Zhou and S. Liang, *Energy Storage Mater.*, **2019**, *18*, 10–14.

69 M. Morcrette, P. Rozier, L. Dupont, E. Mugnier, L. Sannier, J. Galy and J. M. Tarascon, *Nat. Mater.*, **2003**, *2*, 755–761.

70 K. Kirshenbaum, D. C. Bock, C. Lee, Z. Zhong, K. J. Takeuchi, A C. Marschilok, E. S. Takeuchi, Science, **2015**, *347*, 149-154.

71 V. Bodenez, L. Dupont, M. Morcrette, C. Surcin, D. W. Murphy and J. M. Tarascon, *Chem. Mater.*, **2006**, *18*, 4278–4287.

72 P. Hu, T. Zhu, X. Wang, X. Wei, M. Yan, J. Li, W. Luo, W. Yang, W. Zhang, L. Zhou, Z. Zhou and L. Mai, *Nano Lett.*, **2018**, *18*, 1758–1763.

73 M. Yan, P. He, Y. Chen, S. Wang, Q. Wei, K. Zhao, X. Xu, Q. An, Y. Shuang, Y. Shao, K. T. Mueller, L. Mai, J. Liu and J. Yang, *Adv. Mater.*, **2018**, *30*, 1703725.

74 Baddour-Hadjean, R., Navone, C., & Pereira-Ramos, J. P., *Electrochimica Acta*, **2009**, *54*, 6674-6679.

75 D. Asakura, E. Hosono, Y. Nanba, H. S. Zhou, J. Okabayashi, C. M. Ban, P. A. Glans, J. H. Guo, T. Mizokawa, G. Chen, A. J. Achkar, D. G. Hawthron, T. Z. Regier and H. Wadati, *Aip Adv*, **2016**, *6*.

76 W. W. Gu, H. X. Wang and K. Wang, *Dalton T*, **2014**, *43*, 6406-6413.

77 F. M. F. Degroot, *J Electron Spectrosc*, **1994**, *67*, 529-622.

78 J. Vanelp, B. G. Searle, G. A. Sawatzky and M. Sacchi, *Solid State Commun*., **1991**, *80*, 67-71.

79 G. Ghiringhelli, A. Piazzalunga, C. Dallera, T. Schmitt, V. N. Strocov, J. Schlappa, L. Patthey, X. Wang, H. Berger and M. Grioni, *Phys. Rev. Lett.*, **2009**, *102*.

80 G. Vanderlaan, J. Zaanen, G. A. Sawatzky, R. Karnatak and J. M. Esteva, *Phys. Rev. B*, **1986**, *33*, 4253-4263.

81 J. Jeong, K. J. Park, E. J. Cho, H. J. Noh, S. B. Kim and H. D. Kim, *J Korean Phys Soc*, **2018**, *72*, 111-115.

82 S. Lee, T. L. Meyer, C. Sohn, D. Lee, J. Nichols, D. Lee, S. S. A. Seo, J. W. Freeland, T. W. Noh and H. N. Lee, *Apl Materials*, **2015**, 3(12), 126109.

83 C. L. Chen, C. L. Dong, Y. K. Ho, C. C. Chang, D. H. Wei, T. C. Chan, J. L. Chen, W. L. Jang, C. C. Hsu, K. Kumar and M. K. Wu, *EPL (Europhysics Letters)*, **2013**, 101(1): 17006.

84 D. Maganas, M. Roemelt, M. Havecker, A. Trunschke, A. Knop-Gericke, R. Schlogl and F. Neese, *Phys. Chem. Chem. Phys.*, **2013**, *15*, 7260-7276.

85 D. Maganas, M. Roemelt, T. Weyhermuller, R. Blume, M. Havecker, A. Knop-Gericke, S. DeBeer, R. Schlogl and F. Neese, *Phys. Chem. Chem. Phys*., **2014**, *16*, 264-276.

86 R. J. O. Mossanek, A. Mocellin, M. Abbate, B. G. Searle, P. T. Fonseca and E. Morikawa, *Physical Review B*, **2008**, 77(7), 075118.

87 D. K. Bora, X. Cheng, M. Kapilashrami, P. A. Glans, Y. Luo and J. H. Guo, *J. Synchrotron Rad*., **2015**, *22*, 1450-1458.

88 L. Lukashuk, N. Yigit, H. Li, J. Bernardi, K. Fottinger and G. Rupprechter, *Catal Today*, **2019**, *336*, 139-147.

89 S. Y. Istomin, O. A. Tyablikov, S. M. Kazakov, E. V. Antipov, A. I. Kurbakov, A. A. Tsirlin, N. Hollmann, Y. Y. Chin, H. J. Lin, C. T. Chen, A. Tanaka, L. H. Tjeng and Z. Hu, *Dalton T*, **2015**, *44*, 10708-10713.

90 T. Wu, K. Zhu, C. Qin and K. Huang, *J. Mater. Chem. A*, **2019**, 7(10), 5612-5620.

91 K. McColl and F. Corà, *J. Mater. Chem. A*, **2019**, *7*, 3704–3713.

92 J. Livage, P. Barboux, J. C. Badot and N. Baffier, *MRS Proc.*, **1988**, *121*, 167.

93 S. R. Daemi, C. Tan, T. Volkenandt, S. J. Cooper, A. Palacios-Padros, J. Cookson, D. J. L. Brett and P. R. Shearing, *ACS Appl. Energy Mater.*, **2018**, 1, 3702–3710.

Chapter 3

Defected vanadium bronzes as superb cathodes in aqueous zinc-ion batteries

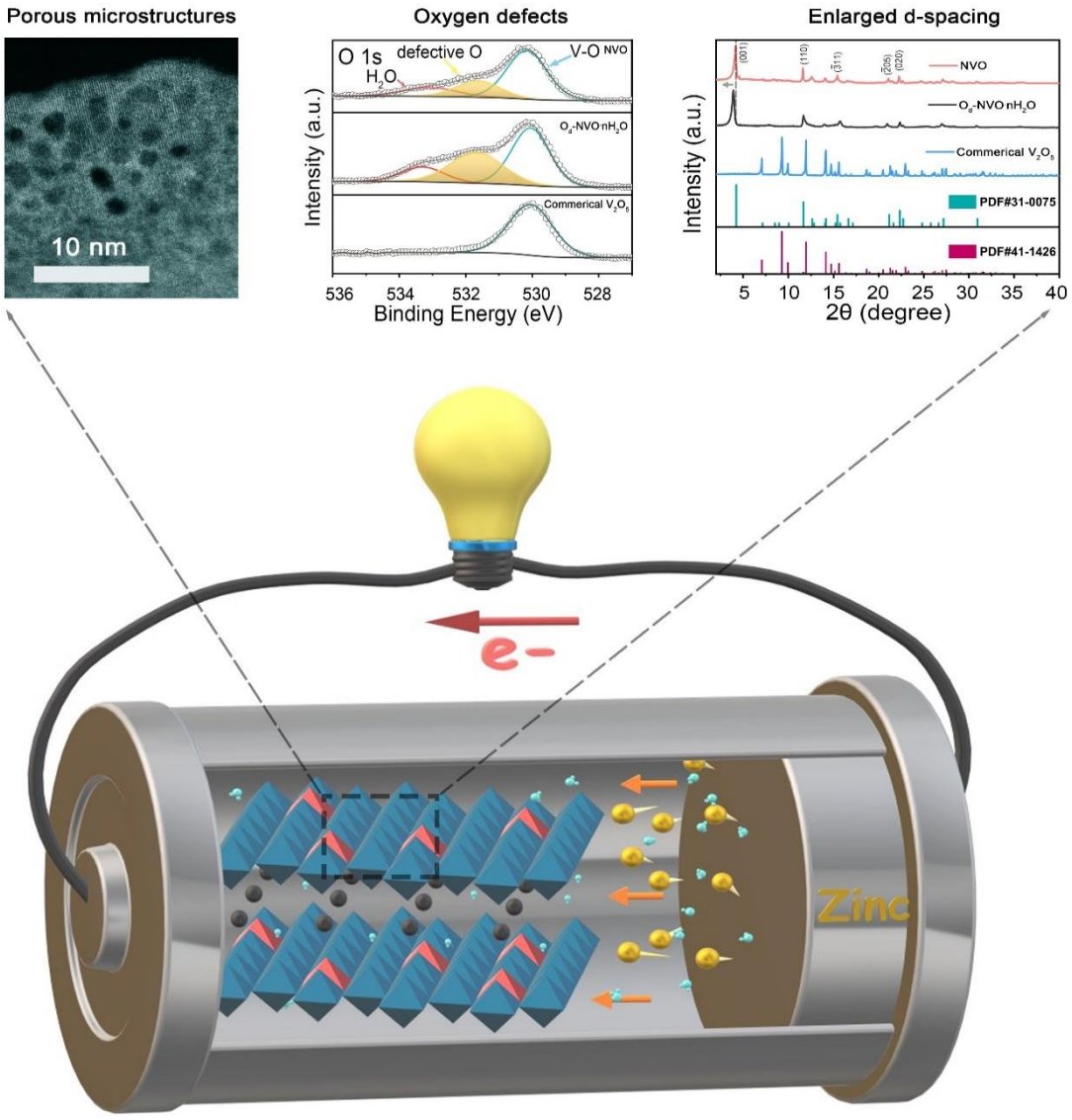

3.1 Introduction

The widespread concerns of limited natural resources, safety and environmental impacts of conventional energy storage technologies have triggered plenty of researches on sustainable battery systems to meet the emerging global market demands.[1] Alkali metal-ions batteries have made impressive progress on improving safety by introducing all-solid-state[2,3] or water-in-salt electrolyte[4,5] approaches, but the resulting specific capacity is still insufficient (<200 mAh g^{-1}). Meanwhile, the relatively poor ionic conductivity of those invented electrolytes with high cost are critically impeding their practical applications.[6,7,8,9] AZIBs are the most promising candidates for bringing sustainable revolution on novel energy storage technologies. This is owing to many merits of metallic zinc anode and low-cost natural/mild acidic zinc salts aqueous electrolytes such as high theoretical capacity of 820 mAh g^{-1}, adequate redox potential of -0.76V *vs.* SHE and superior ionic conductivity. These features endow AZIBs with competitive performance, especially for large-scale EES and portable electronic devices[10,11]. Nevertheless, due to the relatively large ionic radii of the hydrated Zn^{2+} and strong electrostatic interaction of divalent zinc species, there are still many prominent challenges existing in particular to designing competent cathode materials[12,13]. Until now, various cathode materials have been investigated for AZIBs applications.[14] Among them, vanadium oxides present a relatively high theoretical capacity (> 300 mAh g^{-1}) owing to the active redox states of V (III to V) upon the zinc insertion/extraction reactions.[15] In addition, the majority of vanadium oxides possess 2D crystal structures which can deliver capacious accessible channels for rapid charge carriers diffusion.[16,17,18] Furthermore, layered structures can be deliberately tailored by pre-inserted foreign cations to form novel host with enlarged interlayer space and distinct physicochemical properties[19,20,21], such as metal dichalcogenide[22], δ-MnO_2[23], and vanadium bronzes[24]. Various attempts based on vanadium bronzes cathodes have been reported, which still suffer from irreversible phase transformation or electrostatic induced structural collapse, corresponding to unfavourable cycling stability and rate performance.[25] Moreover, although the well-proven enhancement of battery performance achieved by cathode-electrolyte interface optimization was extensively investigated in LIBs, similar studies in AZIBs are still rather rare.[26,27] Additionally, the introduction of lattice H_2O molecules into vanadium-based cathodes for AZIBs has been verified with a dramatic reduction of Zn^{2+} effective charge through generating a

shielding layer of hydroxyl groups and/or water molecules which can improve the interaction with an aqueous medium. Therefore, the activation energy required for interfacial transfer becomes lower with electrostatic interaction.[28,29,30,31,32] Meanwhile, there are limited reports on vanadium based cathode with a suggestion of tailored electronic/micro-structure to promote charge transfer properties by introducing oxygen defects.[33,34] Hence, it is essential to develop a general route to overcome the inherent deficiencies of the vanadium-bronze cathodes and further unlock the energy storage mechanism, so as to further improve the battery performance for satisfying practical applications.

In this work, abundant defects (i.e. oxygen defects, ammonium ions and lattice H_2O molecules) have been introduced into a V_2O_5 host, which was further etched by fluoride during the preparation. The resulting novel oxygen-deficient hydrated ammonium vanadium bronze (O_d-NHVO·nH_2O) possesses highly different electrochemical properties and microstructures compared with conventional ammonium vanadium bronze, $NH_4V_4O_{10}$ (NHVO). Hence it was adopted as a cathode for investigation for AZIBs. It is seen that the deliberately tailored O_d-NHVO·nH_2O have a large specific surface area and expanded interlayer space which effectively boosts Zn^{2+} diffusion kinetics not only within inside of the solid phase, but also at the interface between cathode and aqueous electrolyte. Additionally, enriched structural defects also tuned electronic structures which were verified to attenuate ionic diffusion energy barriers in this study significantly. Therefore, the corresponding as-fabricated O_d-NHVO·nH_2O//Zn batteries exhibited a specific capacity of 435 mAh g^{-1} at 0.2A g^{-1}, and a cycling capability of 106.5% capacity retention after 1500 cycles at 10A g^{-1}. Notably, the O_d-NHVO·nH_2O presents a significant improvement of rate performance from 19% in original NHVO cathode to 43% of the capacity retention when the current density was increased 28 times from 0.5A g^{-1} to 14 A g^{-1}. Moreover, both experimental and computational methods have been performed to elaborately clarify the two-pronged approaches combined with oxygen deficiency and interplanar engineering for enhancement of zinc storage mechanism, which offers a universal strategy for designing high-performance vanadium oxides cathodes and provides deep insights into exploring synergy of oxygen deficiency and pre-inserted "pillar" functions.

3.2 Experimental section

3.2.1 Material synthesis

Both NHVO and O_d-NHVO·nH_2O were synthesized by a single-step hydrothermal reaction, but the amount of reduction reagent and extra additive in precursor were varied in each cases. In a typical preparation process of NHVO, 5 mmol NH_4VO_3 was dissolved in 30 mL deionized water, following a vigorous stirring for 10 minutes at ambient environment. Then 2 mmol of oxalic acid was dissolved into the previous solution with extra stirring for 30 minutes. 6 mmol of oxalic acid and 1 mmol of NH_4F were successively added into same concentrated NH_4VO_3 solution for preparing O_d-NHVO·nH_2O. Finally, both of two as-obtained solutions were transferred to a 50 mL Teflon autoclave, respectively, along with heat treatment of 180°C for 6 hours in the air-circulated oven. The resulting bronze-colour precipitates were washed several times with D.I. water and ethanol, collected by centrifugation and dried in a freeze-drying machine for 2 days.

3.2.2 Characterizations

FT-IR spectrum was carried out by Attenuated Total Reflection Fourier Transform Infrared spectrometer (ATRFTIR, BRUKER, Platinum-ATR), and All X-ray diffraction (XRD) plots were examined by a Mo Kα radiation source (λ = 0.7093Å) STOE SEIFERT diffractometer. The detected angle 2θ was selected from 2° to 45°. In addition, the morphology of the as-prepared samples were characterized by scanning electron microscope (SEM, Carl Zeiss EVO MA10), and microstructures information was attained by transmission electron microscope (TEM JEOL, JEM-2100). Moreover, the chemical states with elemental details are measured by X-ray photoelectron spectrometer (XPS, Thermo Scientific K-α photoelectron spectrometer with Al source). The resulting XPS data were analysed by Casa XPS software, and the adventitious carbon was calibrated with a binding energy of 284.8 eV. After that, the peak areas were fixed according to a ratio of 1:2 for the $2p_{1/2}$: $2p_{3/2}$ in each valence states, and FWHM of the corresponding peaks ($2p_{1/2}$ and $2p_{3/2}$) maintained the same length during deconvolution process. Meanwhile, the distance between two peaks of $2p_{1/2}$ and $2p_{3/2}$ for each valance states and elements were adjusted according to literature.

Thermogravimetric analyzer (TGA) (PerkinElmer TGA 4000 System) was carried out to evaluate weight loss during annealing process in N_2 atmosphere.

3.2.3 Electrochemical evaluations

The CR-2032 coin cell was implemented as a two-electrode testing device for battery performance evaluations. In addition, Swagelok cells were employed for all CV, EIS and *ex-situ* structural/chemical evaluations. The cathode electrodes was manufactured through mixing as-prepared active materials with polyvinylidene fluoride dissolved 1-Methyl-2-pyrrolidinone solution (binder, Sigma-Aldrich) and Super-P (conductive agent, Sigma-Aldrich) in a ratio of 7:1:2. Then, the as-obtained slurry was printed on a hydrophilic carbon matrix, and following transferred to a vacuum oven for drying at 70°C for overnight. The dried electrodes were cut into a disc with 14mm diameter and then weighed by an electronic analytical balance (Ohaus; δ = 0.01mg). The weighted loading mass of the active material is about 1.5-2.5 mg cm^{-2} with thickness of 250-350μm printed on carbon paper. For other component in aqueous zinc ion batteries, zinc metal foil (99.9%) was directly utilized as anode without further treatments. The aqueous electrolyte was prepared by directly dissolve $Zn(CF_3SO_3)_2$ (Sigma-Aldrich) into D.I. water forming a 3M zinc salt solution. Moreover, glass fiber (GF/A, Whatman) was cut into disc with 18mm diameter as the separator. Finally, the CV, EIS and battery performance measurements were evaluated by the VMP3 biological potentiostat and Neware instruments, respectively.

3.2.4 DFT Calculation

The calculation of density functional theory (DFT) was achieved in collaboration with Dr. Ningjing Luo and Professor Guoliang Chai. The simulations were carried out by utilizing VASP (Vienna ab initio simulation package).[35,36] The exchange-correlation function was achieved by the generalized gradient approximation (GGA) of Perdew–Burke–Ernzerhof (PBE)[37]. N, O, H, and V adopted a valence electron configuration of $2s^2 2p^3$, $2s^2 2p^4$, $1s^1$ and $3p^6 3d^5 4s^1$, respectively, provided by the projector-augmented-wave (PAW) potentials.[38] Moreover, the cut-off energy of plane-wave basis was regulated at 520 eV. To avoid the influence of periodic boundary conditions, oxygen vacancies from defect calculations were modelled by a $NH_4V_4O_{10}$ supercell of 1×3×1. Additionally, in order to integrate the strong Coulomb repulsion of partially filled valence d shell of vanadium atoms, U_{eff} = 3.0 eV (J=0 eV) based on simplified GGA+U method were adopted according to the literature.[39] The optB86-vdW functional, an

optimized exchange van der Waals functionals, were equipped to combine the van der Waals interactions in the systems.[40] All the atoms coordinates were fully relaxed until the magnitude of forces were less than 0.02 eV / Å per atom.

In order to evaluate the mobility of Zn^{2+} in the perfect and oxygen-defective NHVO, the climbing-image nudged elastic band method (CI-NEB) was also applied to determine the diffusion barrier. Furthermore, to characterize all transition state structures, the vibrational frequencies were calculated.[41]

3.3 Results and discussions

The preparation of NHVO and O_d-NHVO·nH_2O cathode materials was realized by a facile hydrothermal reaction. The additional amount of oxalic acid and NH_4F additive was utilized to synthesize O_d-NHVO·nH_2O generating significant morphological changes from flower-like architecture to urchin-like nanobelt, compared with the original NHVO sample (Figure 3.3.1a,b). Similarly, in contrast to the observed microstructure of NHVO sample from TEM image in Figure 3.3.1c, the TEM characterization of O_d-NHVO·nH_2O presents a highly porous motif with distinguishable lattice fringe indexed to the (205) crystal plane, which is shown in Figure 3.3.1d. The porosity may be attributed to the synergistic effect of reducing agent and NH_4F in precursors, which provide enriched defects and etched microstructure.[42,43]

In order to further examine the porosity of the as-obtained samples, BET characterization was performed, which critically unravelled a relatively high specific surface area of 57.1 $m^2\ g^{-1}$ for O_d-NHVO·nH_2O sample in comparison to that of NHVO with 20.6 $m^2\ g^{-1}$. Additionally, there is a dominant pore diameter of 2 nm characterized by pore size distribution (Figure 3.3.3a,b), which is in good agreement with the results observed from the HRTEM image in Figure 3.3.1d.

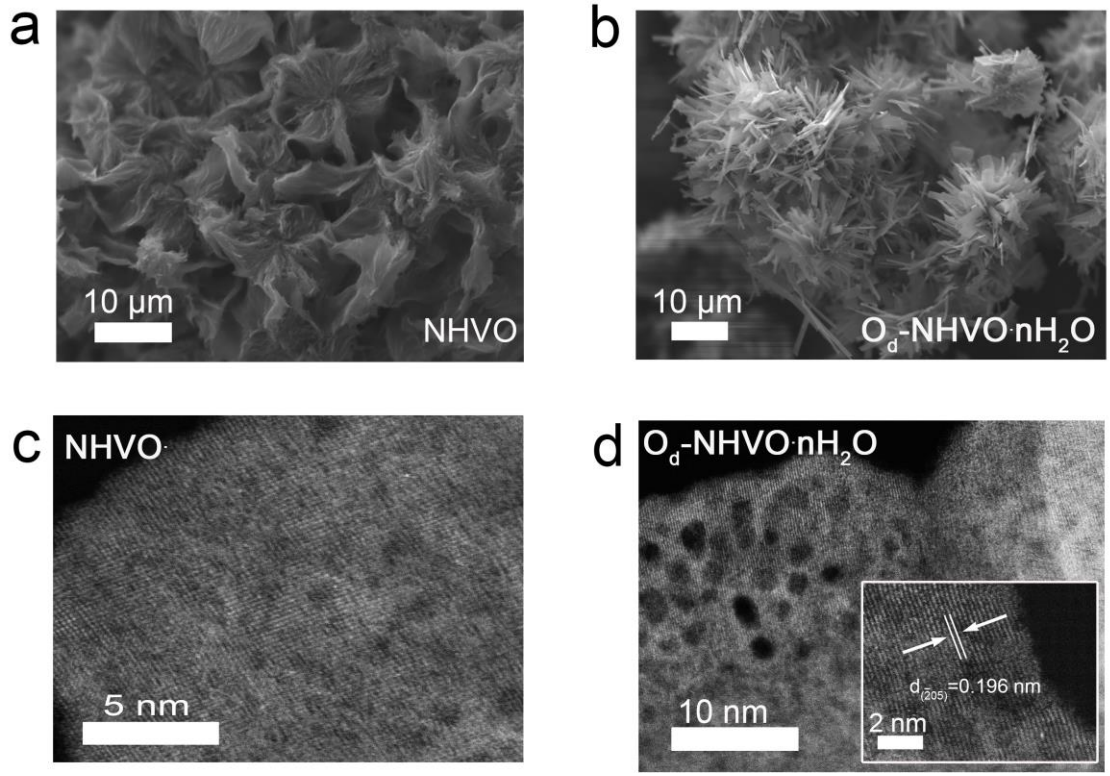

Figure 3.3.1. SEM results of a) NHVO and b) O_d-NHVO·nH_2O; HRTEM of as-prepared c) NHVO and d) O_d-NHVO·nH_2O, respectively.

Furthermore, the XRD characterization in Figure 3.3.2a indicates that the as-obtained NHVO sample matches well with standard pattern indexed to monoclinic crystallographic phase of $NH_4V_4O_{10}$ (JCPDS: 31-0075) in the *C2/m* space group, which is comprised of V_2O_5 bilayers stacking along <001> (*c* axis) direction and pre-inserted ammonium ion within the interplane as 'pillar'.[44] Comparably, O_d-NHVO·nH_2O has a similar diffraction pattern with notable specific characteristics which can be indexed to the same crystalline phase as observed in NHVO sample, but a slight shift of the (001) peak to the lower degree (3.9°) was observed, corresponding to an enlarged interlayer spacing of 10.4 Å in the O_d-NHVO·nH_2O sample compared with 9.6 Å of the as-obtained NHVO. In addition, commercial V_2O_5 (JCPDS: 41-1426) was also employed as a comparable sample to investigate the effects of pre-inserted NH_4^+ in V_2O_5 host on electrochemical behaviours for AZIBs applications. Figure 3.3.2b shows the comparison features of the FITR spectra for NHVO, O_d-NHVO·nH_2O, and commercial V_2O_5 samples, respectively. It is seen that the absorption bands for different materials possess numerous similar vibration modes which refer to V-O bending, V-O-V and V=O stretching modes at wavenumbers of 472 cm^{-1}, 756 cm^{-1} and 987 cm^{-1} for O_d-

$NHVO{\cdot}nH_2O$, respectively.[45,46] Accordingly, similar features of 454 cm^{-1}, 744 cm^{-1} and 945cm^{-1} were detected for NHVO, respectively. Moreover, the relatively higher characterized absorption bands at 999 cm^{-1} in commercial V_2O_5 compared with the two as-prepared samples can be interpreted as absence of pre-inserted cations coordinated with apical oxygen resulting in a more intense V=O band. This result is consistent with the observation of the axial expansion of the (001) d-space from the XRD characterizations, and is also in accordance with previous FTIR studies of Li^+ pre-inserted V_2O_5.[47] In particular, the absorption bands at 1412 and 3177 cm^{-1} correspond to the symmetric bending mode and asymmetric stretching modes of NH_4^+, respectively,[44] confirming the presence of NH_4^+ in both NHVO and O_d-$NHVO{\cdot}nH_2O$ samples. In addition, it is also observed that there were two notable bands at 1644 and 3556 cm^{-1} associated with the bending and stretching vibration modes of H-O, respectively,[46] which imply that H_2O molecules exist in O_d-$NHVO{\cdot}nH_2O$.

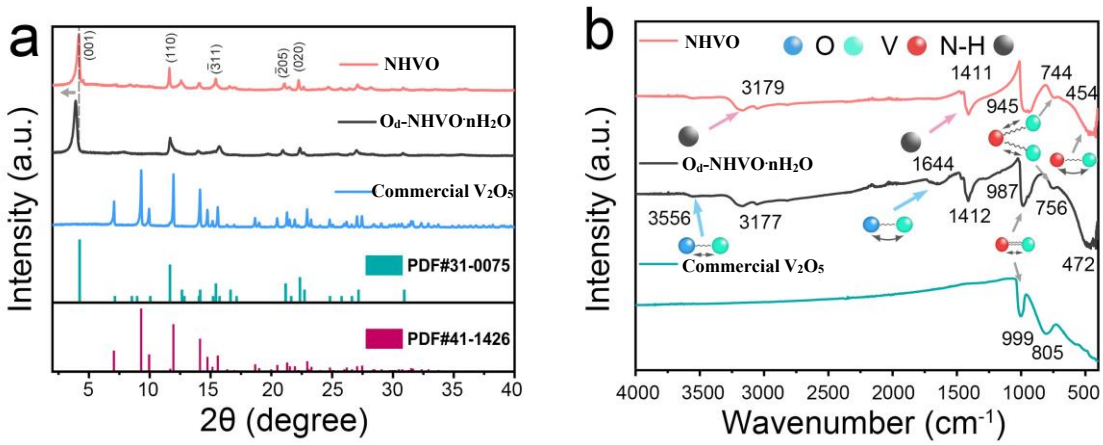

Figure 3.3.2. (a) XRD plots and (b) FTIR spectra of NHVO, O_d-$NHVO{\cdot}nH_2O$ and commercial V_2O_5, respectively.

Moreover, TGA was performed to examine the weight loss during temperature increase. It should be emphasized that not only H_2O molecules, but also partial NH_4^+ hydrolyzed species can escape from the framework during the heat treatment. Hence, it is hard to acquire the precise amount of H_2O content from the TGA characterization. However, the TGA curves in Figure 3.3.3c illustrate that the weight loss of the O_d-$NHVO{\cdot}nH_2O$ sample is greater than that of NHVO. Electron paramagnetic resonance (EPR; Figure 3.3.3d) further confirms the evidence of enriched oxygen deficiency in O_d-$NHVO{\cdot}nH_2O$ sample, reflected as the distinct signal in the spectrum at $g \approx 1.98$ assigned to the V^{4+} species resulting in unsaturated oxygen (oxygen vacancies) in the lattice. The

EPR result is in agreement with reported reduced vanadium(V) compound with oxygen vacancies in the literature.[48]

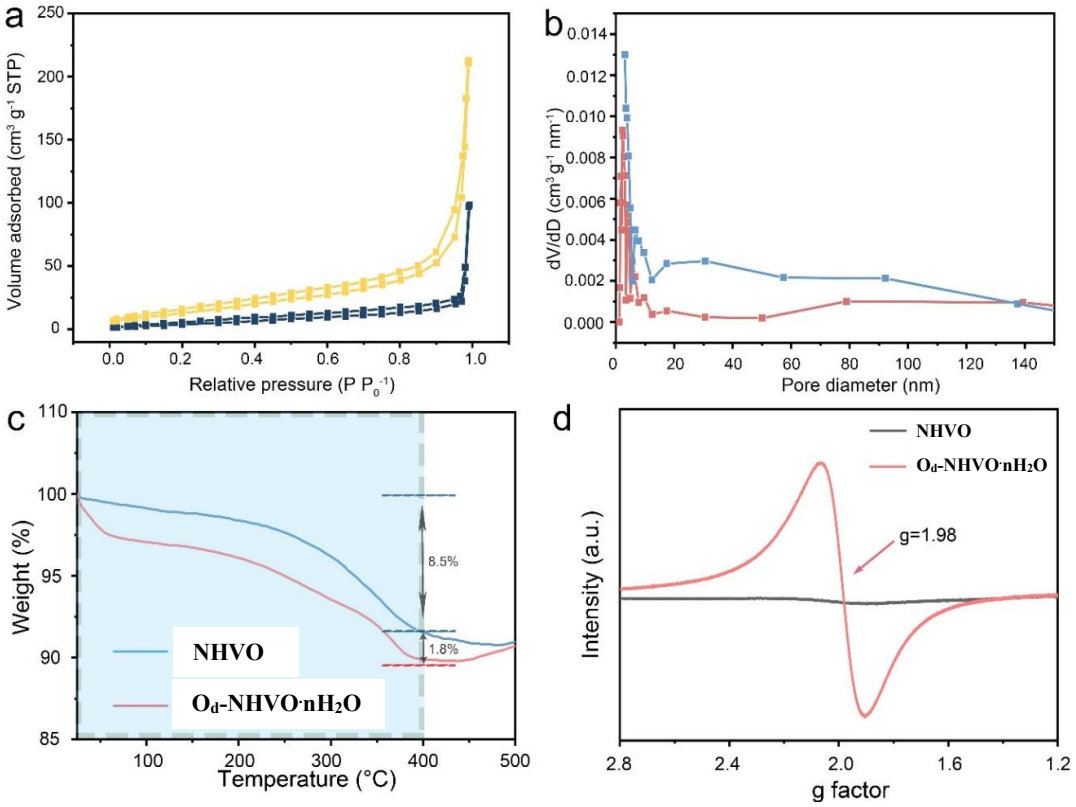

Figure 3.3.3 a) N_2 adsorption-desorption isotherm (yellow: O_d-NHVO·nH_2O, dark blue: NHVO) b) and corresponding pore size distribution measurements (light blue: O_d-NHVO·nH_2O, red: NHVO). c) TGA analysis and d) EPR spectra of as-prepared NHVO and O_d-NHVO·nH_2O samples, respectively.

Additionally, the XPS result also suggests the presence of NH_4^+ for both NHVO and O_d-NHVO·nH_2O from the N1s core level spectrum characterizations, which are shown in Figure 3.3.4a. In order to quantitatively analyse the elemental N concentration in the as-obtained samples, the relative sensitivity factors were adopted to calculate the variation of NH_4^+ species, revealed by a ratio of N:V, that is, a ratio of 1:3.94 and 1:3.9 for NHVO and O_d-NHVO·nH_2O, respectively. It shows the negligible change of nitrogen concentration after specific treatments in the preparation. Moreover, the V 2p core energy level spectrum exhibits a hybrid valance states compared with commercial V_2O_5 (Figure 3.3.4b), which illustrates a partial reduction of V^{5+} oxidation states on introducing pre-inserted cations into the V_2O_5 frameworks. More explicitly, the peak at a binding energy of 517.3±0.2 eV in all characterized samples is designated to V^{5+} $2p_{3/2}$, whereas the peak with a lower binding energy of 516.1 eV can be indexed to V^{4+} $2p_{3/2}$,

which only occur in NHVO And O_d-NHVO·nH_2O samples. This suggests similar oxidation states of V species observed in previous reported studies on vanadium bronzes.[48,50,51] In addition, the average valance states of vanadium was calculated on the basis of the ratio of each V species peak areas showing that a relatively higher oxidation state of $V^{4.74+}$ (NHVO) compared with $V^{4.65+}$ (O_d-NHVO·nH_2O). This result confirmed our assumption of oxidation states, since more reducing agent (oxalic acid) was used in the precursor, resulting in more oxygen defects with evident reduction of the V oxidation states in O_d-NHVO·nH_2O, which will be further discussed in the DFT calculations (*vide infra*). Figure 3.3.4c presents the O 1s core level energy spectra of all samples. It is worth noting that both O_d-NHVO·nH_2O and NHVO possess obvious defective oxygen species peaks at a binding energy of 531.6 eV, which is consistent with previous reported oxygen defects in vanadium oxides.[52,53,54,55] In addition, the proportion of defective oxygen concentration in O_d-NHVO·nH_2O and NHVO samples, respectively, is calculated as a ratio between two oxygen species, i.e. $O_{defective}$: $O_{Vanadyl}$ and were 27:73 and 43:57 for NHVO and O_d-NHVO·nH_2O, respectively, which indicates more enriched oxygen deficiency can be achieved by simple manipulation of the reducing agent concentration in this case. Moreover, it should be emphasized that there is no trace of F species detected from XPS characterizations of the survey and core-level spectrum of the F 1s in NH_4F treated O_d-NHVO·nH_2O sample (Figure 3.3.5).

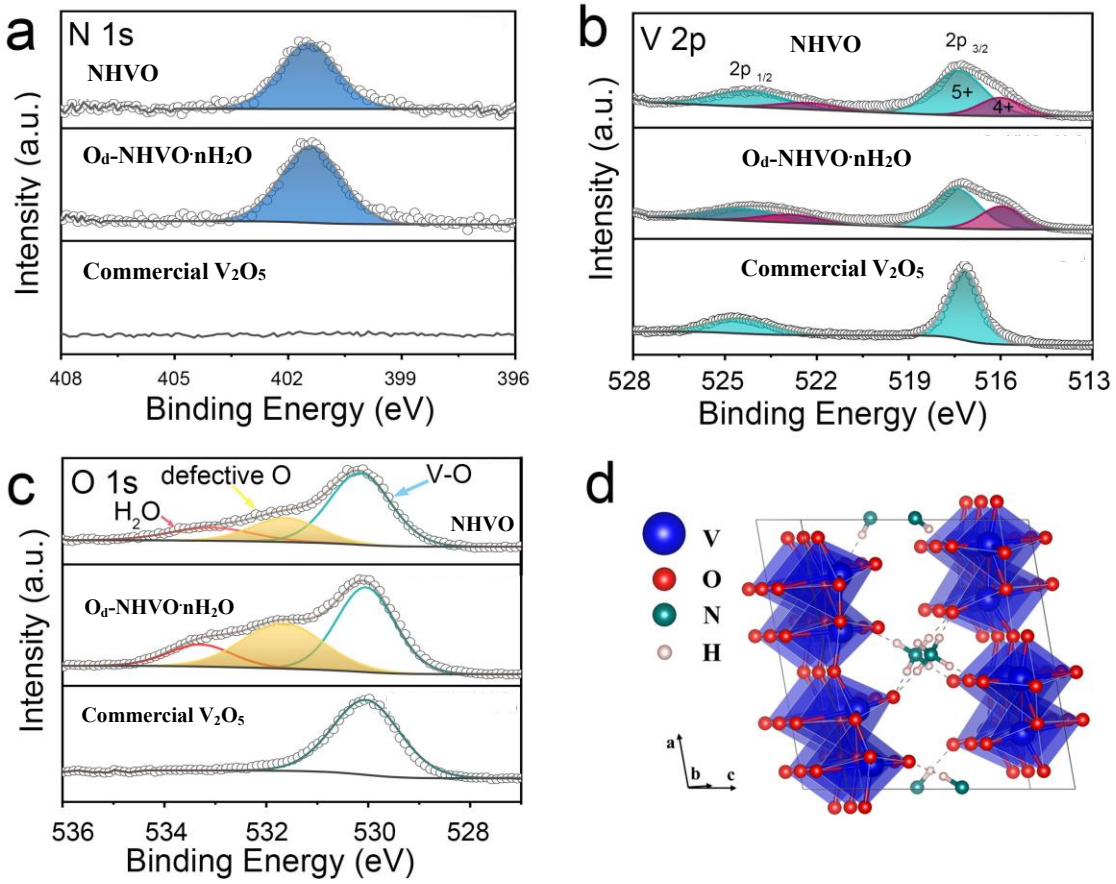

Figure 3.3.4. SEM results of a) NHVO and b) O_d-NHVO·nH_2O; c) HRTEM of as-prepared O_d-NHVO·nH_2O; d) XRD plots and e) FTIR spectra of NHVO, O_d-NHVO·nH_2O and commercial V_2O_5, respectively; XPS spectra of the f) N 1s, g) V 2p and h) O 1s in NHVO, O_d-NHVO·nH_2O and commercial V_2O_5, respectively; i) The calculated most stable geometry of $NH_4V_4O_{10}$ supercell according to GGA+U functional.

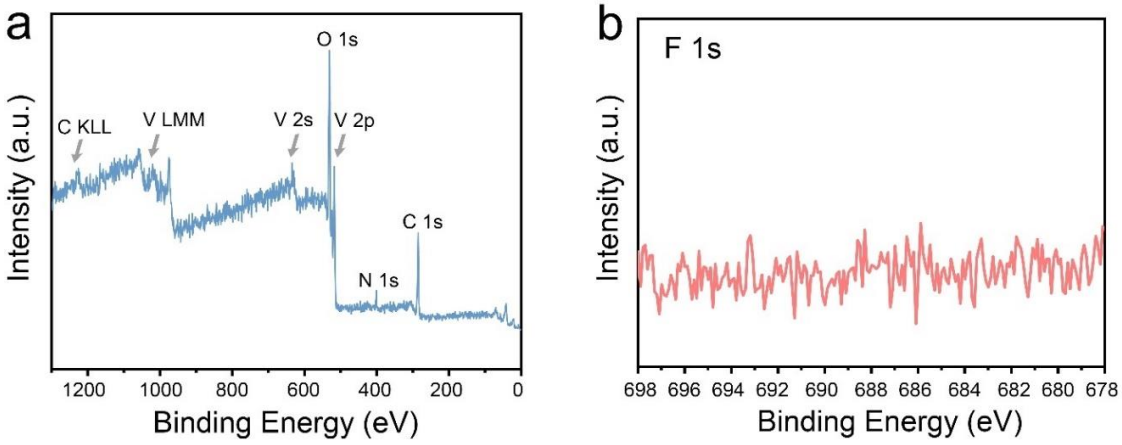

Figure 3.3.5. a) XPS survey spectrum of O_d-NHVO·nH_2O and its b) core level spectrum of F 1s.

However, it is crucial to incorporate additional NH_4F in the precursor, which is responsible for not only generating a highly porous microstructure by etching effects, but also for adjusting the pH value in the aqueous solution during the hydrothermal reaction (Figure 3.3.6). As a result, it is seen that an impurity phase was observed in the XRD pattern, shown in Figure 3.3.6, where a control-group sample of O_d-$NHVO{\cdot}nH_2O$ was prepared by the same recipe but excluding NH_4F as an additive. Additionally, the partial occupancy of N sites can lead to numerous potential NHVO microstructural geometries. Therefore, 1 × 3 ×1 super pixel of NHVO was constructed for DFT calculation, based on our calculations of total energies on various configurations of simulated NHVO. Accordingly, Figure 3.3.1i illustrates the structure with the lowest total energy, in which the N-H...O hydrogen bonds derived from three NH^{4+} were coordinated with adjacent O atoms in V_2O_5 bilayers (more discussion in the DFT section).

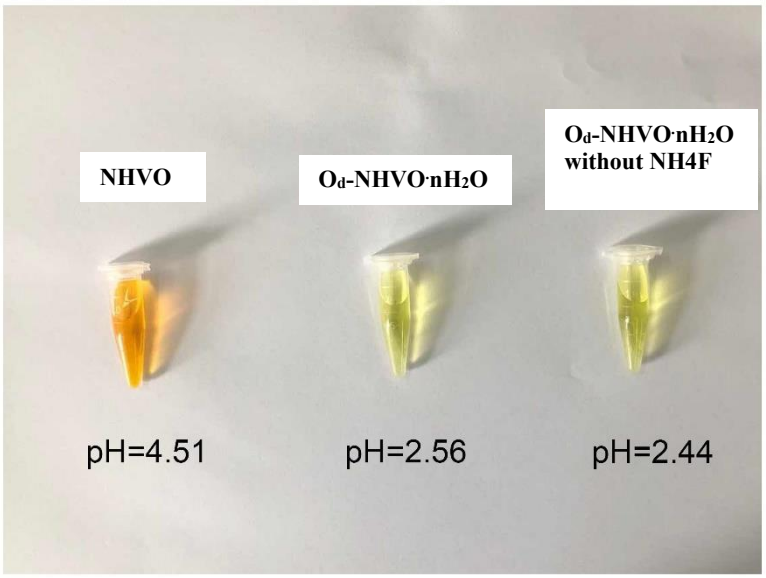

Figure 3.3.6. pH values of varied precursor solution: NHVO, O_d-$NHVO{\cdot}nH_2O$ and O_d-$NHVO{\cdot}nH_2O$ without adding NH_4F, respectively.

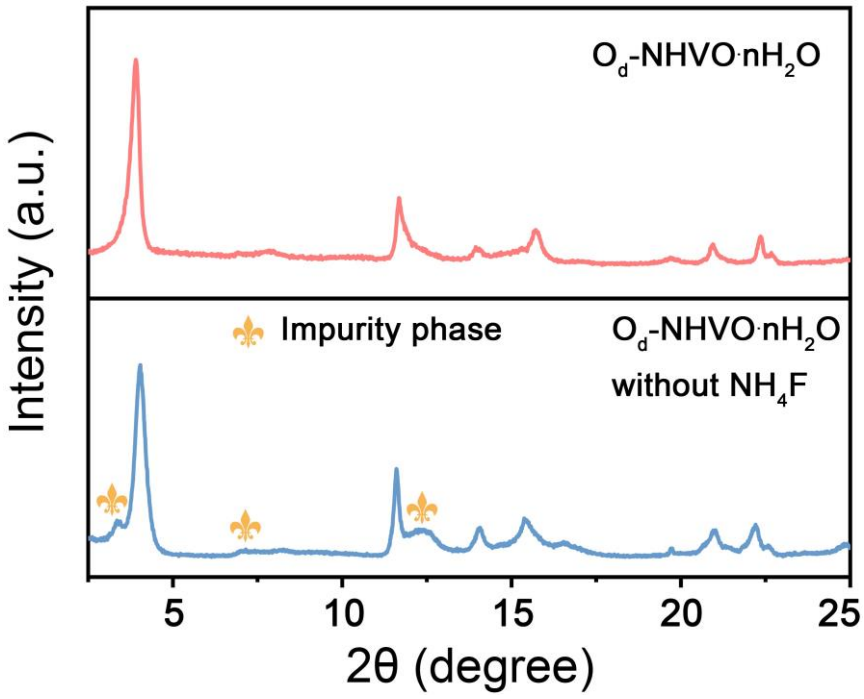

Figure 3.3.7. XRD patterns of as-obtained O_d-NHVO·nH_2O and O_d-NHVO·nH_2O without adding NH_4F.

In addition to the characterizations of the pristine samples, the NHVO, O_d-NHVO·nH_2O and commercial V_2O_5 samples were fabricated into coin-cell and Swagelok-cell configurations for electrochemical property evaluations. Figure 3.3.8a shows GCD profiles of NHVO and O_d-NHVO·nH_2O at various current densities from 0.5 to 14 A g^{-1}. The distinct plateaus in the charge/discharge curves can be distinguished with specific potentials, which are in consistent with the multiple redox pairs positions observed in CV curves during anodic/cathodic reactions (Figure 3.3.8b). In addition, it is seen that there are relatively steady changes of the GCD profiles and CV patterns during the first three cycles in O_d-NHVO·nH_2O compared with those of NHVO, which suggest a higher reversibility of Zn^{2+} (de)intercalation in the O_d-NHVO·nH_2O cathode material. Moreover, a further study on long-cycling stability of O_d-NHVO·nH_2O electrode at a low current density of 0.2 mA g^{-1} was conducted, also exhibited a better performance compared with NHVO electrode, that is, the maximum specific capacities are 405 mAh g^{-1} and 435 mAh g^{-1} for NHVO and O_d-NHVO·nH_2O electrodes, respectively, corresponding with the long-cycling stabilities of 86% and 92% capacity retention after 50 cycles for NHVO and O_d-NHVO·nH_2O electrodes, respectively. Meanwhile, both of the cathode materials presented >99% Coulombic efficiency (CE) during GCD measurements. This could be interpreted as a sluggish insertion kinetics of Zn^{2+} in the

commercial V_2O_5 electrode owing to a lack of "lubricants" (lattice H_2O/NH_4^+)[23,56] and inadequate interlayer space. Moreover, the rate performance was characterized by stepwise increasing of the applied current density from 0.5 to 14 A g^{-1} and eventually back to 0.5 A g^{-1} with 10 cycles at each step (Figure 3.3.8d). Notably, O_d-NHVO·nH_2O electrode presents remarkable rate capability and reversibility, which reflect as specific capacities of 406 mAh g^{-1} at 0.5 g^{-1} in the initial steps and 175 mAh g^{-1} at 14 A g^{-1}, retaining 43% specific capacity after 28-fold rise in current densities. Meanwhile, when the applied current density returns to 0.5 A g^{-1}, the specific capacity still remains at 401 mAh g^{-1} in the last 10 cycles, which indicates a robust reversibility compared with the majority of reported vanadium based cathodes for AZIBs.[57,58,59,60,61] On the contrary, NHVO electrode exhibits inferior rate capability reflecting with a specific capacity of 382 mAh g^{-1} at 0.5 A g^{-1} and 71 mAh g^{-1} at 14 A g^{-1}. From the results, only 19% specific capacity was retained, suggesting relatively large energy barriers, which can inhibit the rapid diffusion of Zn^{2+}. Additionally, in the case of a current density of 10A g^{-1}, superior reversibility and high capacity retention have been verified in both O_d-NHVO·nH_2O and NHVO electrode after 1500 cycling measurements (Figure 3.3.8e). More explicitly, it is seen that both NHVO and O_d-NHVO·nH_2O electrodes present negligible capacity degradation with specific capacities of 244 mAh g^{-1} and 138 mAh g^{-1} for the last cycle for O_d-NHVO·nH_2O and NHVO electrodes, respectively.

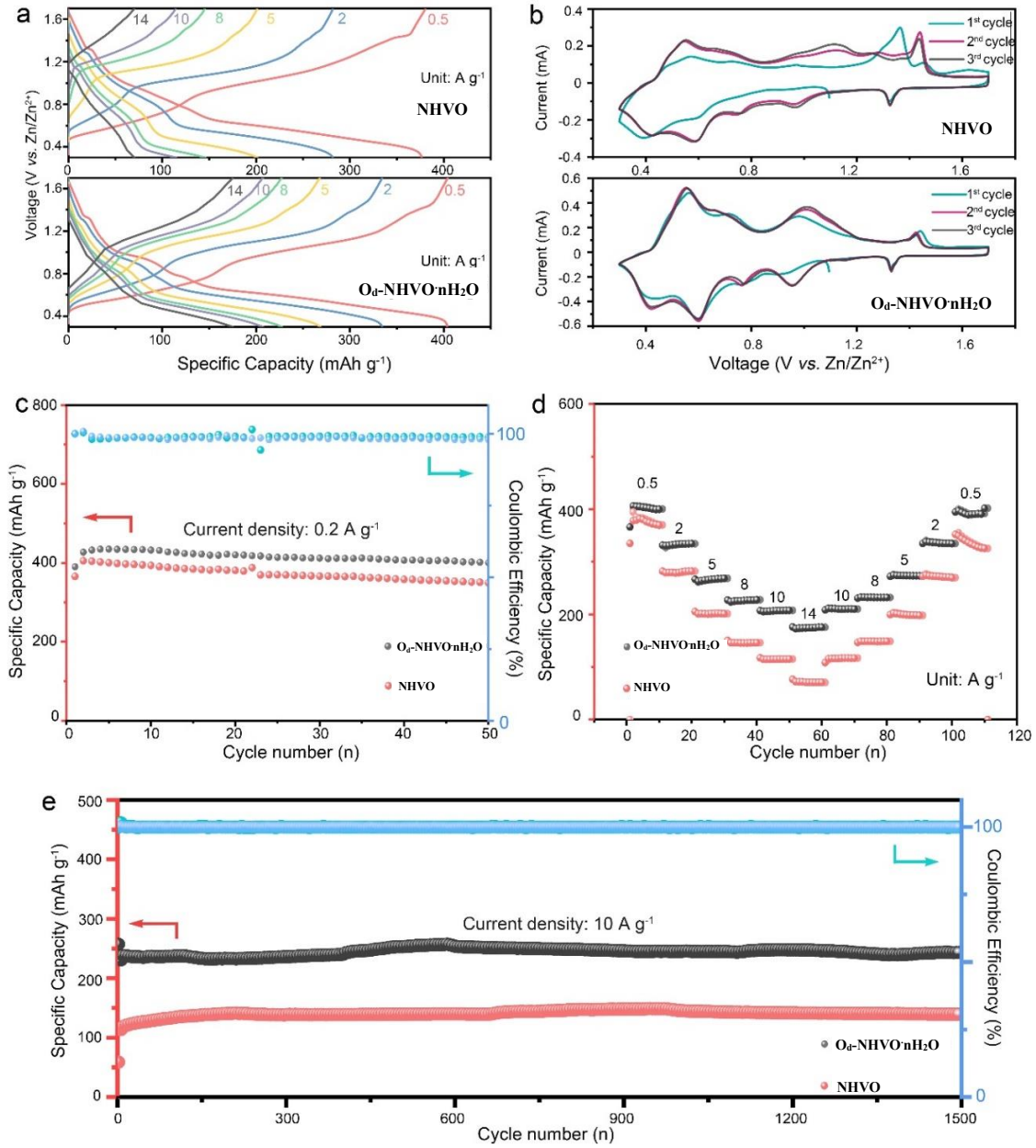

Figure 3.3.8. a) GCD profiles for NHVO and O_d-NHVO·nH_2O electrode measured at different current densities; b) CV curves of NHVO and O_d-NHVO·nH_2O electrode at a scan rate of 0.2 mV s^{-1} for the first three cycles; c) Cycling stability measurements of NHVO and O_d-NHVO·nH_2O cathodes at 0.2 A g^{-1}; d) Rate performance of NHVO and O_d-NHVO·nH_2O batteries; e Cycling stability measurements of NHVO and O_d-NHVO·nH_2O electrode at 10 A g^{-1}.

In contrast, the battery equipped with cathode material of commercial V_2O_5 experienced a long-term activation process with a gradually raised specific capacity from 109 mAh g^{-1} at initial cycle to 256 mAh g^{-1} at 25th cycles (Figure 3.3.9a). Similarly, in Figure 3.3.8b, it can be seen that the unfavourable rate performance was attained in

commercial V_2O_5 electrode, where the battery suffers from both poor specific capacity and longstanding activation. Furthermore, long-cycling stability evaluation of commercial V_2O_5 electrode illustrates a much longer activation period along with unsatisfied specific capacity performance during 1500 cycling measurement (Figure 3.3.9c). Consequently, the demonstrated results above sufficiently indicate that the O_d-$NHVO{\cdot}nH_2O$ cathode material possesses superior specific capacity and improved long-cycling reversibility under varied GCD treatments, which could be attributed to the promoted Zn^{2+} diffusion kinetics derived from the highly porous structure and introduced lattice defects. Moreover, deliberately introduced lattice H_2O molecules and NH_4^+ not only provides a charge shielding screen to alleviate the electrostatic interaction between the host sheets and the divalent charge carriers, but also contribute to expansion of the double-layer structures and inhibits "lattice breathing".[23,62]

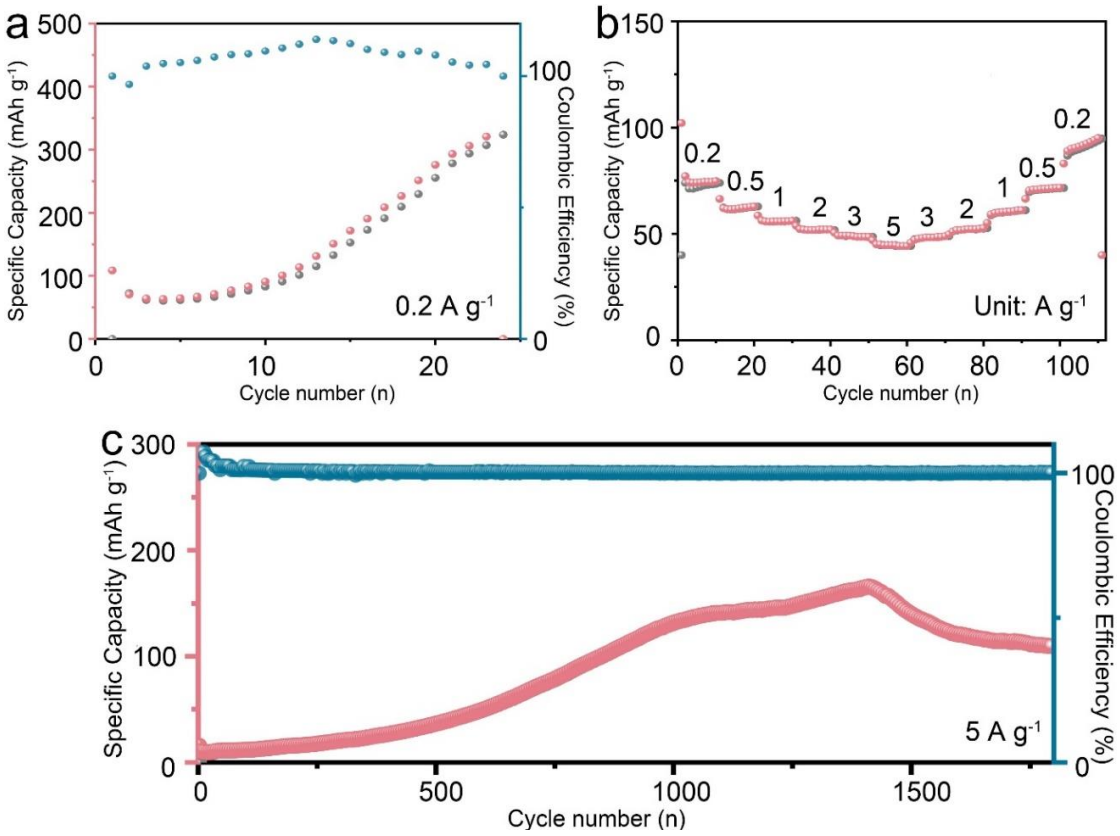

Figure 3.3.9. GCD measurements for commercial V_2O_5 cathodes: a) long-cycling stability test at 0.2 A g^{-1}; b) rate performance of the cells measured under current density of 0.2, 0.5, 1, 2, 3, 5 A g^{-1}, respectively; c) long-cycling stability test of the cells at 5 A g^{-1}.

The Ragone plot (Fig. 3.3.10) illustrates that the O_d-NHVO·nH_2O electrode possesses a energy density of 288 Wh kg^{-1} and a power density of 358 W kg^{-1} based on calculation from the mass of cathode material, which outperform many previous reported cathodes, such as σ-$Zn_{0.25}V_2O_5$·nH_2O (250 Wh kg^{-1})[50], $K_2V_8O_{21}$ (222.3 Wh kg^{-1})[63], δ-$Ca_{0.25}V_2O_5$·nH_2O (267 Wh kg^{-1})[64], $Na_3V_2(PO4)_2F_3$ @ C(97.5 Wh kg^{-1})[65], $Zn_3V_2O_7(OH)_2$·$2H_2O$ (214 Wh kg^{-1})[66] and $Zn_2V_2O_7$ (166 Wh kg^{-1})[67].

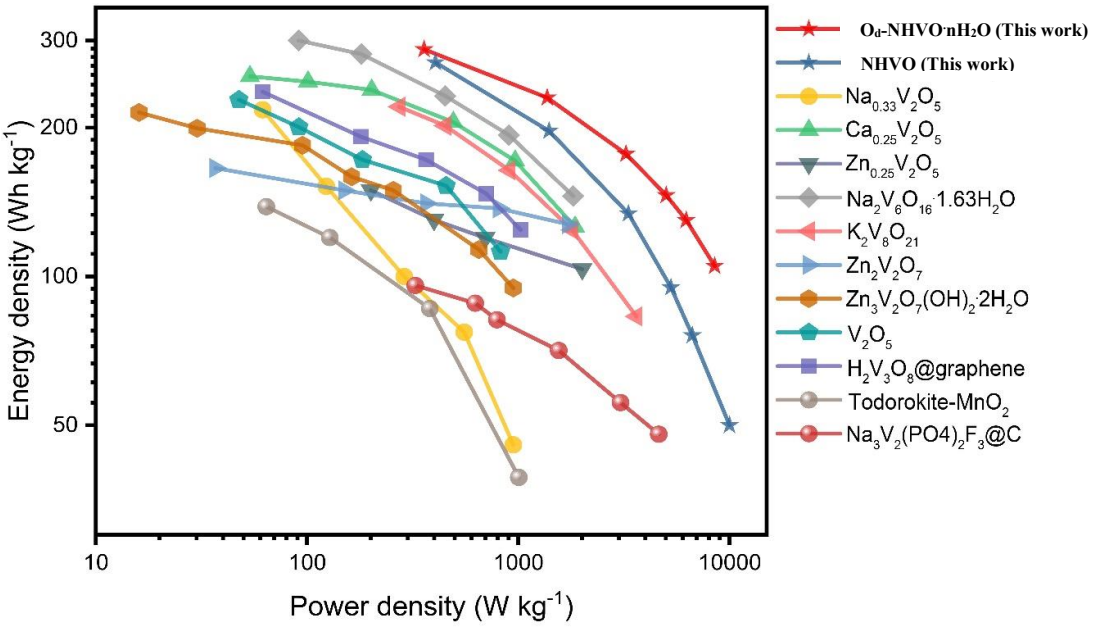

Figure 3.3.10. Ragone plot of as-prepared O_d-NHVO·nH_2O and NHVO electrodes compared with other reported cathodes for AZIBs.[7,8,9,10,11,12,13,14,15,16,17]

In order to study the inherent cycle-dependent ion transport characteristics of the as-prepared electrodes, EIS was performed to determine the combined ohmic resistance (R_s) and charge transfer resistance (R_{ct}) in the initial and cycled states. By analysing the EIS diagram in Figure 3.3.11, a relatively lower R_s of NHVO (0.64 Ω) and O_d-NHVO·nH_2O (0.68 Ω), respectively, was observed compared with measured commercial V_2O_5 electrode (R_s =1.93 Ω) (Table 3.3.1), which can be interpreted by enhanced electronic conductivity benefited from tailored electronic structures by pre-inserted ions. Additionally, the R_{ct} of O_d-NHVO·nH_2O (33.4 Ω) at the pristine state indicates a significant improved charge transport kinetics at the interface between electrode and electrolyte, compared with that of as-fabricated NHVO (R_{ct} =128.8 Ω) and V_2O_5 batteries (R_{ct} = 186.2 Ω) evaluated under identical conditions. The results

confirm a dramatic electrochemical improvement through interfacial engineering, such as high porosity, hydroxyl-functionalized surface and structural defects, on O_d-NHVO·nH_2O. Furthermore, even after cycling treatments, the R_{ct} of O_d-NHVO·nH_2O (22.5 Ω) electrode also shows better feature than those of both NHVO (52.6 Ω) and commercial V_2O_5 (128.8Ω) electrodes, which further verifies its highly electrochemical reversibility with superior ionic diffusion kinetics benefitting from pre-intercalation and defects strategy.

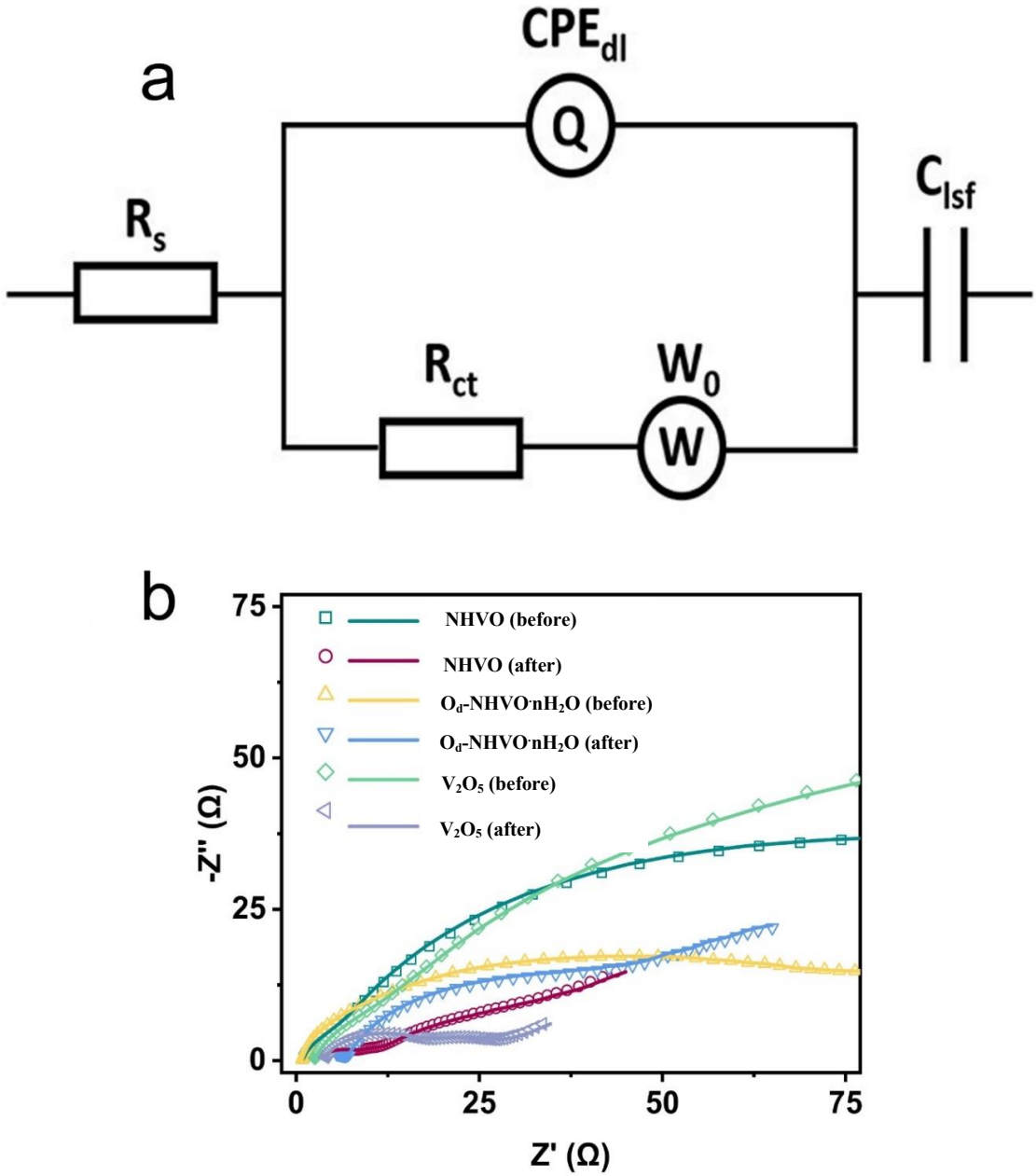

Figure 3.3.11. a) The equivalent circuit of fitted EIS. b) EIS of NHVO, O_d-NHVO·nH_2O and commercial V_2O_5 at pristine and after GCD cycling treatment, respectively.

Table 3.3.1. EIS parameters

NB: (R_s: Combined internal resistance, R_{ct}: Interfacial charge transfer resistance)

Electrode	R_s (Ω)	R_{ct} (Ω)
NHVO before	0.64	128.8
NHVO after	2.78	52.6
O_d-NHVO·nH_2O before	0.68	33.4
O_d-NHVO·nH_2O after	2.20	22.5
Commercial V_2O_5 before	1.93	186.2
Commercial V_2O_5 after	1.56	33.6

In addition, the capacity contribution was evaluated from calculation of capacitive- and diffusion-controlled reaction behaviours on NHVO and O_d-NHVO·nH_2O electrode, which is shown in Figure 3.3.12. The quantified CV curves and resulting diagram (Figure 3.3.12a, b) obviously demonstrate that a 74% capacitive contribution among the whole current response was attained in O_d-NHVO·nH_2O electrode at a sweep rate of 0.5 mV s^{-1}, which is higher than 43% capacitive contribution observed in NHVO electrode at the same scan rate (Figure 3.3.12c, d).

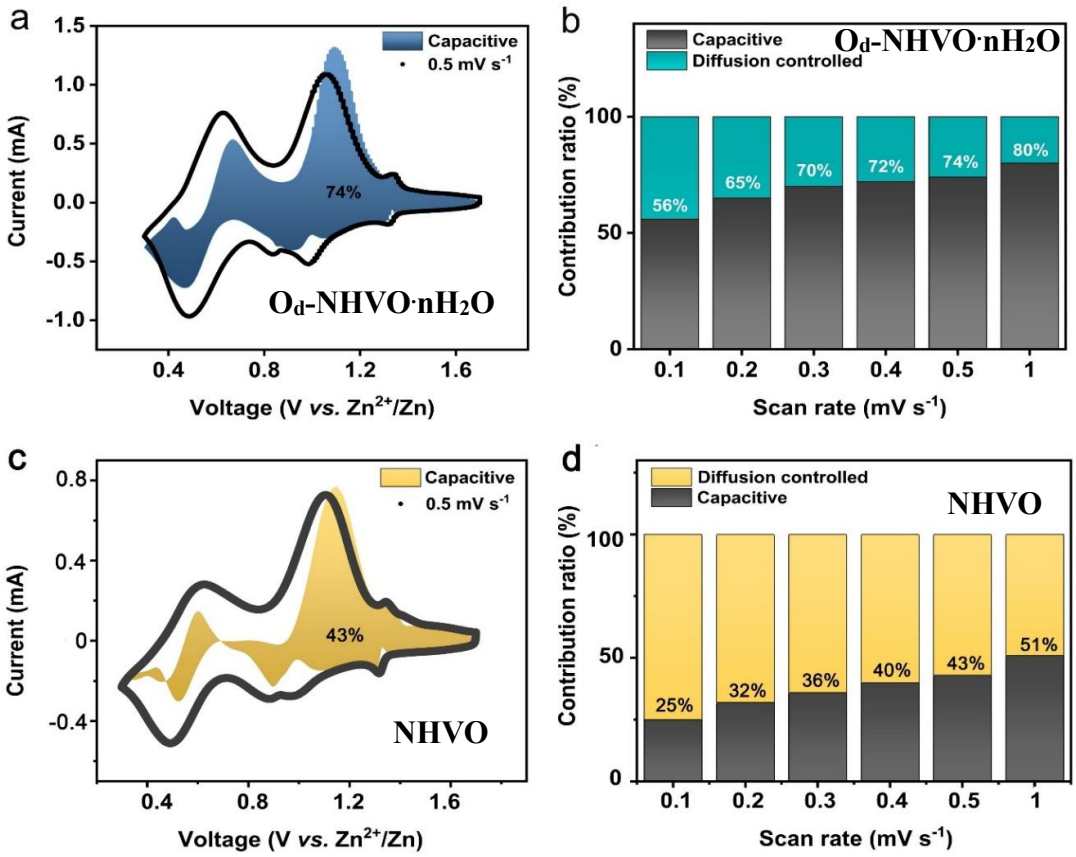

Figure 3.3.12. a) CV curve of the O_d-NHVO·nH_2O electrode at scan rate of 0.5 mV s^{-1} illustrating a capacitive contribution (blue region) among total current response; b) the proportion of capacitive- and diffusion-controlled contributions of the as-prepared O_d-NHVO·nH_2O electrode; c) CV curve of NHVO electrode at scan rate of 0.5 mV s-1 presenting a capacitive contribution (yellow region) among total current response; d) the proportion of capacitive- and diffusion-controlled contributions of the as-prepared NHVO electrode.

Likewise, there is a trend of increasing fraction of capacitive contribution along with the scan rates rise from 0.1 to 1 mV s^{-1} in the two electrodes. From the results, the predominant capacitive-controlled Zn^{2+} storage behaviour of O_d-NHVO·nH_2O cathode material is responsible for the observed superior rate performance, compared with other as-obtained materials. The evolutions of reaction behaviour from CV profiles were performed by the equation shown as follows: [68]

$$I=aV^b$$

The above equation is adopted to illustrate reaction behaviours of varied redox pairs from CV profiles, which reflect as the coefficient *b* values, i.e. $b = 1$ refers to capacitive response, and $b = 0.5$ stands for absolute diffusion-controlled Faradaic (de)intercalation

behaviour.[69] Hence, the three redox pairs was selected for calculation, and the results are shown in Figure 3.3.13, More explicitly, the *b* values of O_d-NHVO·nH_2O electrode are 0.71, 1.01, 1.04, 0.88, 0.76 and 0.75, corresponding to marked redox peaks, suggesting ubiquitous surface related capacitive reaction rather than the relatively low *b* value of NHVO electrode (0.33, 0.98, 0.92, 0.62, 0.77, and 0.71), indicating a diffusion-controlled behaviour in the NHVO electrode. Furthermore, according to the CV curves at each scan rates, the overpotential gap of O_d-NHVO·nH_2O electrode between the peaks of A1(A2) and C1(C2) redox pairs are smaller than those in NHVO electrode, which correspond to a relatively strong polarization along with an inhibited (de)intercalation of Zn^{2+} in NHVO compared with O_d-NHVO·nH_2O material. Accordingly, it is worth evaluating their diffusion kinetics from an experimental perspective, thereby strengthening the evidence of enhanced kinetics through micro-/electronic-structural optimizations of O_d-NHVO·nH_2O.

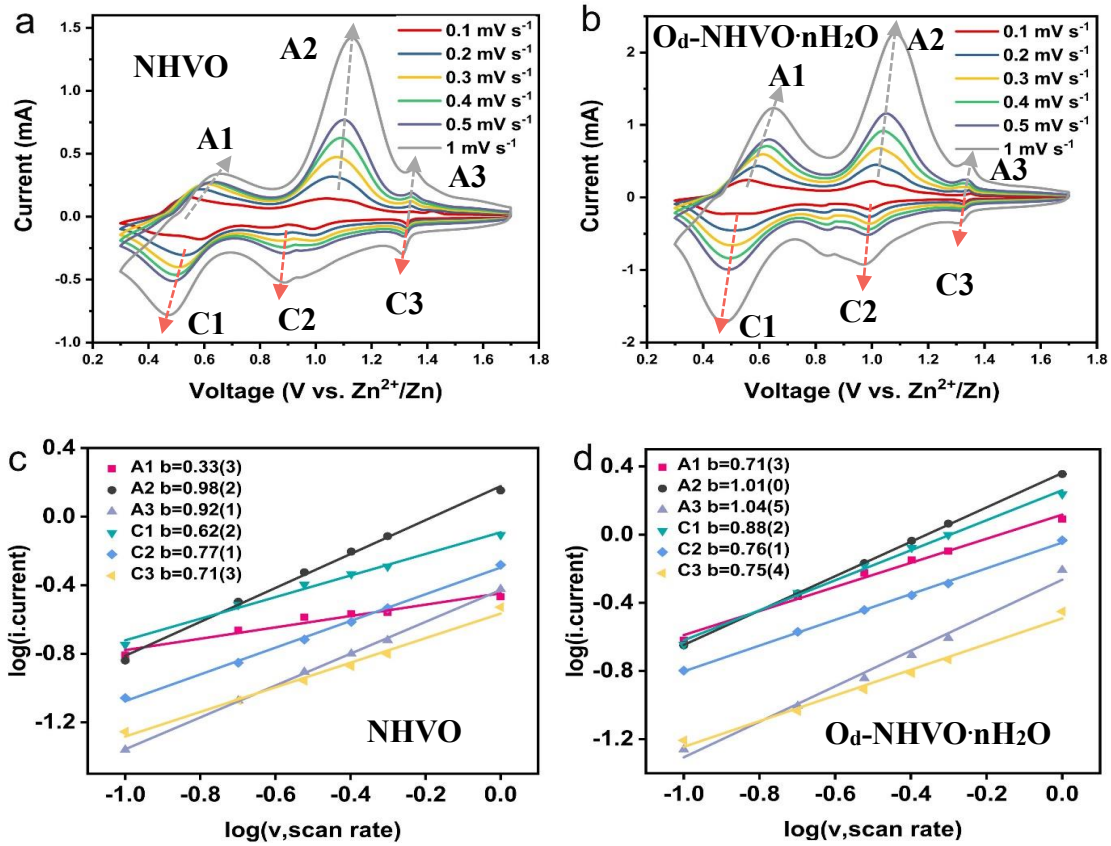

Figure 3.3.13. a,c) The CV curves of the NHVO battery under increasing scan rates from 0.1 mV s^{-1} to 1 mV s^{-1} and calculated *b* for selected peaks; b,d) the The CV curves of the O_d-NHVO·nH_2O battery under increasing scan rates from 0.1 mV s^{-1} to 1 mV s^{-1} and calculated *b* for selected peaks.

Figure 3.3.14 illustrates the calculated D_{zn}^{2+} during the charge/discharge processes for both NHVO and O_d-NHVO·nH_2O electrodes, which shows that the O_d-NHVO·nH_2O possesses higher D_{zn}^{2+} (10^{-8}-10^{-9} cm^2s^{-1}) than that of NHVO electrode (10^{-9}-10^{-10} cm^2s^{-1}). Therefore, the large proportion of pseudocapacitive reaction behaviour in O_d-NHVO·nH_2O *via* determination of diffusion kinetics from CV and GITT analyses critically verified the feasibility of introducing defects and pre-inserted cations strategy to effectively enhance the rate capability and reversibility of cathode materials for AZIBs.

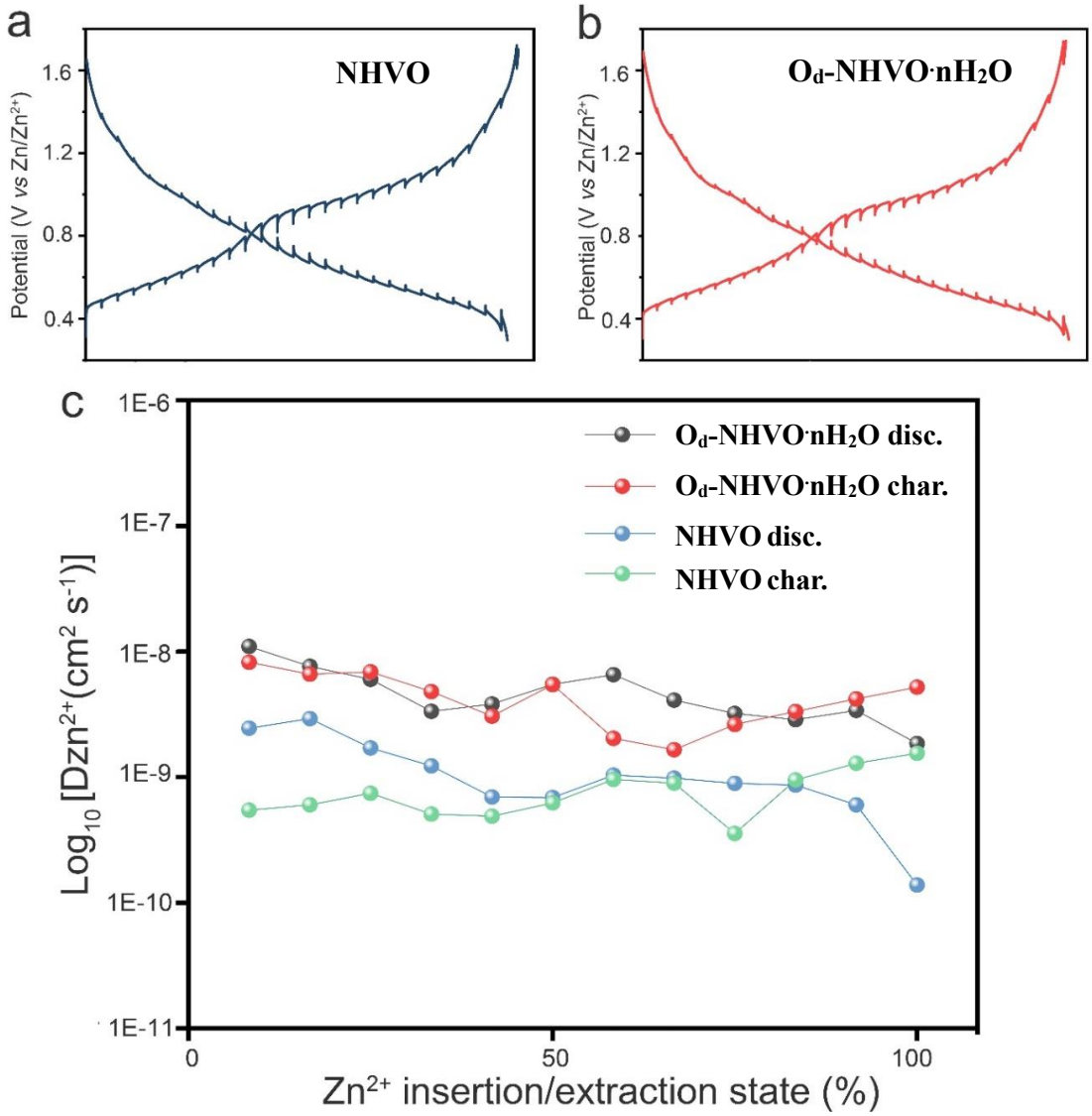

Figure 3.3.14. a,b) GITT profiles of as-fabricated NHVO and O_d-NHVO·nH_2O batteries applied current density of 50 mA g^{-1} and (c) the calculated Zn^{2+} diffusion coefficients for NHVO and O_d-NHVO·nH_2O at charge/discharge processes.

In addition to electrochemical behaviour investigations of as-prepared cathode materials, *ex-situ* XRD and *ex-situ* XPS were employed to reveal the high reversibility in terms of crystallographic structure and chemical states evolutions of the O_d-$NHVO{\cdot}nH_2O$ material during Zn^{2+} insertion/extraction process. Figure 3.3.15 presents an evident reduction of vanadium oxidation states with a weak signal of V^{5+} ($2p_{3/2}$: 517.4 eV) but two distinct valance states of V^{3+} ($2p_{3/2}$: 515.5 eV) and V^{4+} ($2p_{3/2}$: 516.2 eV) species at fully discharged state of O_d-$NHVO{\cdot}nH_2O$. Whereas, it is seen that the V^{3+} species disappear along with increased intensity of V^{5+} peak from observation of fully charged O_d-$NHVO{\cdot}nH_2O$ electrode, which almost fully recover to pristine state of the electrode, but possesses a slight higher oxidation states due to partial loss of pre-inserted N. The similar phenomena are consistent with previously reported vanadium bronzes as cathode materials for AZIBs.[49,50] Moreover, Figure 3.3.15b illustrates the core level spectrum of Zn 2p which clearly indicate that there is no trace of zinc signal detected in the pristine O_d-$NHVO{\cdot}nH_2O$ electrode. Whereas, an intensive peak in the Zn 2p spectrum ($2p_{3/2}$: 1022.8 eV) was observed in the fully discharged O_d-$NHVO{\cdot}nH_2O$ electrode, suggesting the insertion of Zn^{2+} in the cathode. After the charging treatment, the majority of zinc species were extracted from the O_d-$NHVO{\cdot}nH_2O$ electrode reflecting as a pair of subtle peaks in accordance with the binding energy of Zn 2p. Similar results of chemical states evolutions on zinc can be also found in other previous studies for AZIBs.[70] Figure 3.3.15c verifies that the NH_4^+ species (N 1s: 401.5 eV) is always present in the O_d-$NHVO{\cdot}nH_2O$ electrode regardless of the charge/discharge states, which indicates a robust feature of NH_4^+ "pillar" anchored within the bilayers V_2O_5 framework. As a consequence, the reversible chemical states and stable pre-inserted cation of the O_d-$NHVO{\cdot}nH_2O$ electrode verified by *ex-situ* XPS indicates that cycling stable characteristics during the electrochemical reactions. After elucidating the different chemical states upon the Zn^{2+} (de)intercalation process, the crystalline phase evolution of O_d-$NHVO{\cdot}nH_2O$ electrode at varied charge/discharge states were examined by *ex-situ* XRD. Figure 3.3.15d shows the *ex-situ* XRD characterizations of O_d-$NHVO{\cdot}nH_2O$ electrode at varied charge/discharge states of 1st and 10th cycles with applied current density of 0.5A g^{-1}, respectively, according to the distinguished plateaus in the GCD profiles. It is worth noting that there is a reversible phase transformation between O_d-$NHVO{\cdot}nH_2O$ and $Zn_3V_2O_7(OH)_2{\cdot}2H_2O$ (JCPDS No.87-0417, space group: $P\bar{3}m1$) at fully charge states and fully discharge states as well as charged state of 0.8V in 10th cycle, respectively.

The similar phenomena was also recognized in previous investigations on $V_6O_{13}{\cdot}nH_2O$[30], $Cu_{0.1}V_2O_5{\cdot}0.08H_2O$[42] and $K_2V_8O_{21}$[60]. In addition, a close-up region of the (001) reflection site of O_d-NHVO·nH_2O cathode (2^o <2θ<5^o) exhibits clear steady shift towards higher 2θ values from 13.1 to 10.7 Å at 1st charged state and 10th discharge state, respectively, suggesting a contraction of interlayer space upon discharge process. The interlayer space can recur a large *d*-space in association with low 2θ value, indicating a reduced electrostatic interaction within the interplane due to the extraction of Zn^{2+}.[50] Therefore, the highly reversible phase transition of O_d-NHVO·nH_2O electrode further confirms a robust cycling capability and provides insight into the Zn^{2+} storage mechanism upon dynamic microstructural evaluation.

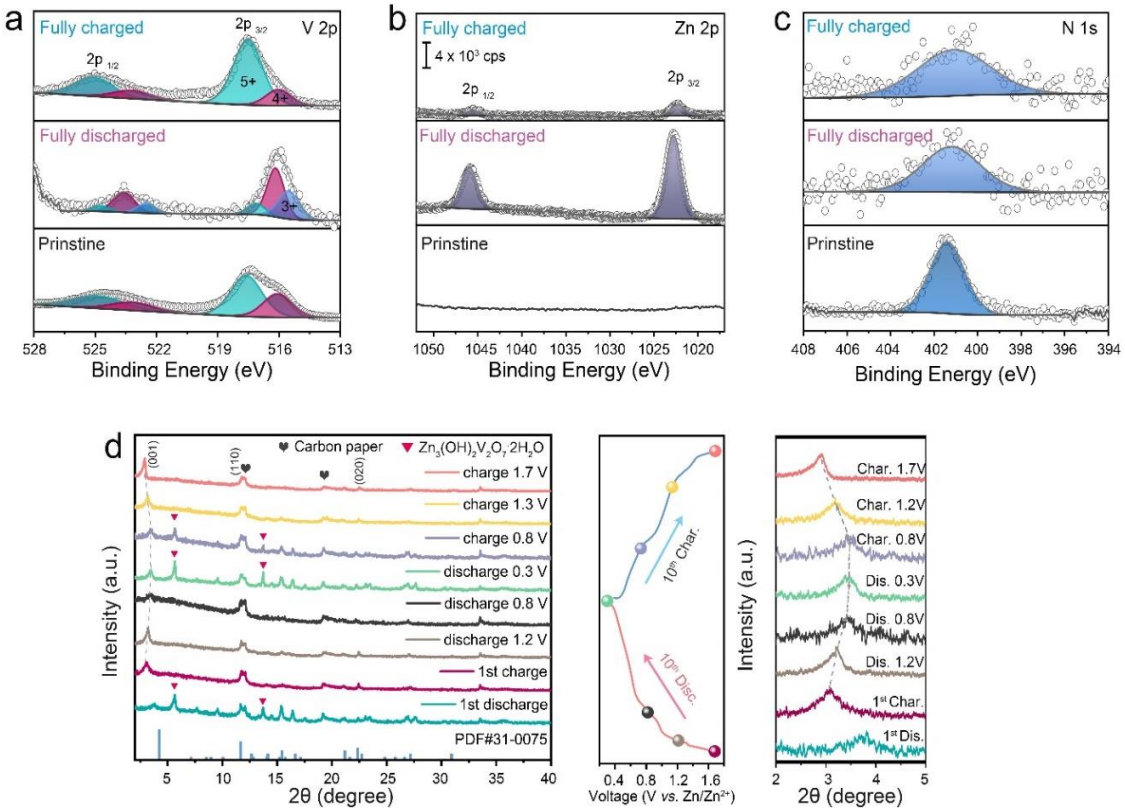

Figure 3.3.15 *Ex-situ* XPS spectra of a) V 2p , b) Zn 2p and c) N 1s at initial, charge/discharge states of the O_d-NHVO·nH_2O electrode, respectively; d) XRD patterns of the O_d-NHVO·nH_2O electrode measured under different charge/discharge states in both 1st and 10th cycles.

In order to clarify the structural variation between O_d-NHVO·nH_2O and NHVO materials, DFT simulation was utilized to illustrate the formation and related characteristics of oxygen vacancies in O_d-NHVO·nH_2O, as well as the electrostatic

interaction between inserted Zn^{2+} and apical oxygen. As mentioned above, the NHVO crystallographic structure was reconstructed in our studies as a 1×3×1 supercell ($(NH_4)_3V_{24}O_{60}$) to simulate the oxygen point vacancies.

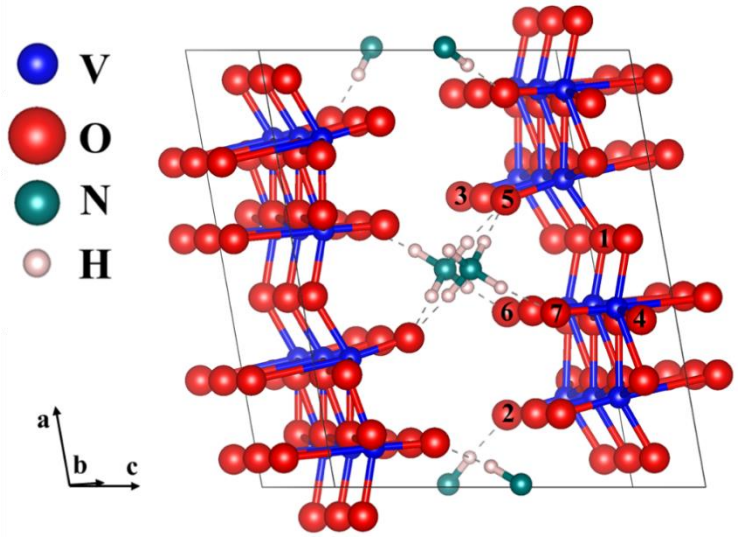

Figure 3.3.16. The simulated most stable geometries of 1×3×1 $NH_4V_4O_{10}$ supercell labelled with varied oxygens. O1 has two coordination and apical O3 only coordinate with one V. O4 has three coordination. and O2, O5, O6, and O7 possess extra hydrogen bonds with NH_4^+.

Since the hydrogen bonds between NH_4^+ and oxygen are relatively weak compared with chemical bonds, varied oxygens with different coordination numbers and those with hydrogen bonds with NH_4^+ were selected for defect calculations, which are labelled in Figure 3.3.16. The equation, showed as follows, was adopted to calculate the formation energy of varied oxygen point vacancies, and corresponding results are exhibited in Table 1:

$$E_f = E_{(NHVO\ (VO))} + 1/2E_{(O2)} - E_{(NHVO)} \quad (1)$$

where E_f is the formation energy of deficient oxygens in the NHVO supercell. Additionally, $E_{(NHVO\ (VO))}$ and $E_{(NHVO)}$ are the energies of NHVO lattice with or without oxygen vacancies, respectively. $E_{(O2)}$ is the energy of oxygen.

Table 3.3.2. The formation energies of varied oxygen point vacancies achieved by GGA+U functional.

Label	(see Figure3.3.16)	Formation energy (eV)
O1		1.89
O2		2.37
O3		2.49
O4		2.03
O5		2.53
O6		1.81
O7		1.83

The formation energies in the sphere of 1.81~2.53 eV suggest endothermic formation process of oxygen point vacancies. The lowest formation energy of O6 vacancy is 1.81 eV, which is very close to other oxygen vacancy sites. In particular, there are two coordination of vanadium and hydrogen bond with O6, respectively, which possess a similar coordination environment of O7. However, the slight difference is that the O7 is closer to adjacent NH_4^+ in contrast to the coordination of two vanadium ions of O1. Therefore, considering the high similarity of local coordination environment in each simulated structures, the projected density of states (PDOS) and the total density of states (TDOS) were calculated for perfect NHVO and oxygen deficient NHVO, to elucidate the rationale of the low defect formation energy.

When oxygen vacancies are formed along with the release of electrons, the resulting NHVO (i.e. O_d-NHVO·nH_2O) exhibits *n*-type characteristics with oxygen deficiency. As presented in Figure 3.3.17b, the defect states (gap states) of O_d-NHVO·nH_2O with vacancies in the O6 position is closer to the Fermi level than those of pristine NHVO (Figure 3.3.17a).

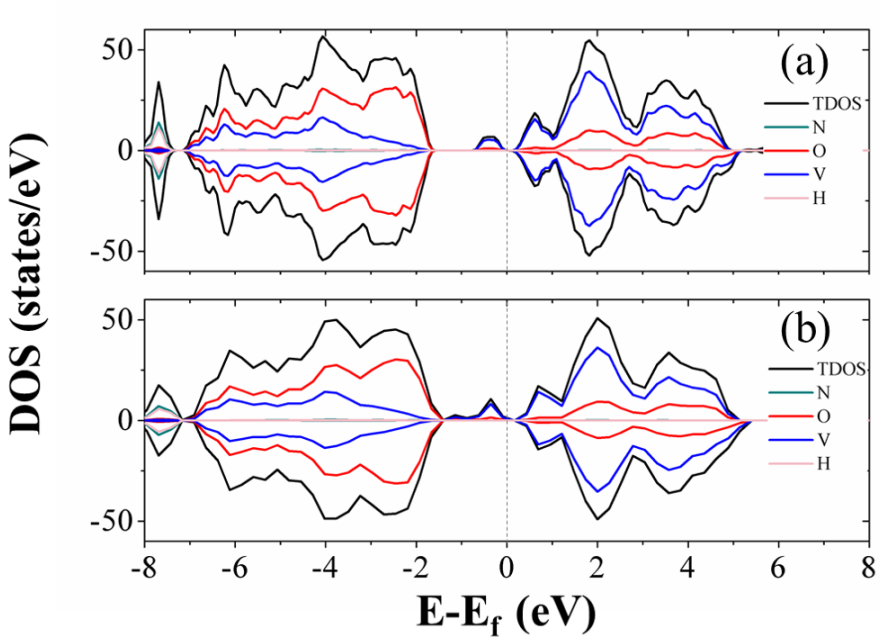

Figure 3.3.17. The PDOS and TDOS of (a) perfect NHVO and (b) O6 deficient NHVO. The dotted lines refer to the Fermi levels.

Moreover, owing to being closer to the conduction band minimum (CBM) of defect states in O_d-NHVO·nH_2O, rather than the pristine NHVO, the electrons are more easily excited from the donor level into the conduction band, thereby increasing the electronic conductivity of O_d-NHVO·nH_2O with oxygen defects. In Figure 3.3.18, it is also observed that the remaining TDOSs of sites, i.e. O1, O4, and O7, also possess two peaks (defect states) below the Fermi level (-1~0 eV). Additionally, those with more peaks below the Fermi level have an average defect formation energy of 1.89 eV, while the remaining oxygen point vacancies only showed one peak around 0.5 eV have an average defect formation energy of 2.46 eV, thus, the value difference is 0.57 eV. When extracting O1, O4, O6 and O7, the TDOS suggests that more vanadium ions are reduced.

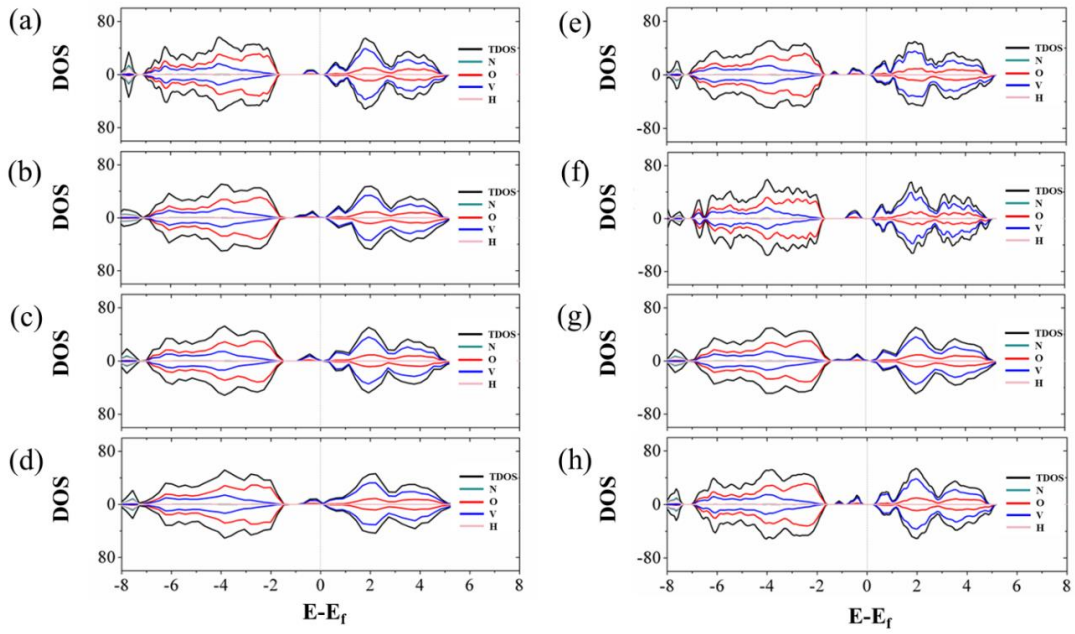

Figure 3.3.18. The PDOS and the TDOS of (a) pristine NHVO and O_d-NHVO·nH_2O with potential oxygen deficiency of (b) O1, (c) O2, (d) O3, (e) O4, (f) O5, (g) O6, (h) O7, respectively. The dotted lines refer to the Fermi levels.

Moreover, calculation of the corresponding spin density of the pristine NHVO and O_d-NHVO·nH_2O with oxygen deficiency at O1~O7 sites were performed to confirm our statements, which is shown in Figure 3.3.19. Compared with spin density of pristine NHVO, it can be seen that the oxygen deficiencies at the O1, O4, O6 and O7 positions could generate more localized electrons than oxygen deficiencies of O2, O3 and O5 positions. More explicitly, these yielding localized electrons from O1, O4, O6 and O7 positions are on the additional two vanadium sites adjacent to the vacancies. Whereas, only one vanadium has localized electrons at the O2, O3, and O5 positions. In short, oxygen deficiencies induced localized electrons can stabilize the system with reduced total energy. Hence, the O6 point vacancy is calculated as the most stable oxygen vacancy owing to more generated local electrons around it. As the results, it is most likely to occur in the reduced NHVO. In addition, the formation of oxygen deficiencies in NHVO can effectively alleviate the potential electrostatic force of Zn^{2+} which can forcefully promotes the reversible (de)intercalation of Zn^{2+} with thermoneutral Gibbs free energy.[33] Therefore, enhanced electronic conductivity and reduced electrostatic effectively improved the reversibility of Zn^{2+} reaction process, consequently with superior capacity and rate performance owing to introduced oxygen vacancies

convincingly verified by our DFT results.

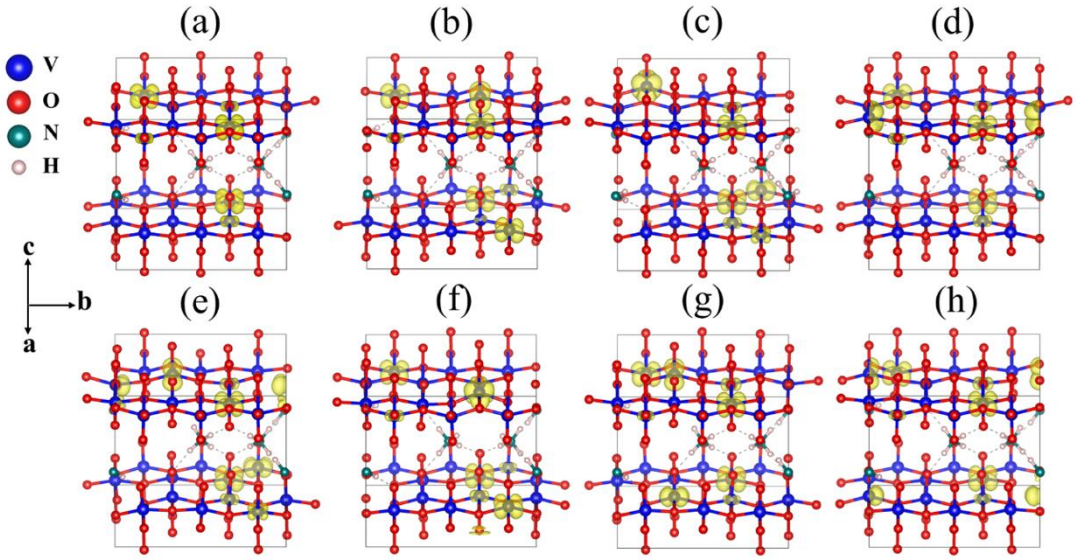

Figure 3.3.19. Spin densities for (a) pristine NHVO and reduced O_d-NHVO·nH_2O with an oxygen vacancy at (b) O1, (c) O2, (d) O3, (e) O4, (f) O5, (g) O6 and (h) O7 sites, respectively. The isosurface is set at 0.01 electrons $Å^{-3}$.

In addition, in order to study the influence of oxygen vacancies in NHVO on ionic transport properties, the CI-NEB method was used to study the minimum energy migration pathway and energy barriers for pristine and oxygen deficient NHVO.[71] The previous investigation of NHVO elucidated that the diffusion along with the c axis direction presented dramatic energy barrier of 2.89 eV.[72] Therefore, we selected the diffusion pathway along <010> direction with most stable and metastable intercalated sites for Zn^{2+} with corresponding structures exhibited in Figure 3.3.20 and Figure 3.3.21.

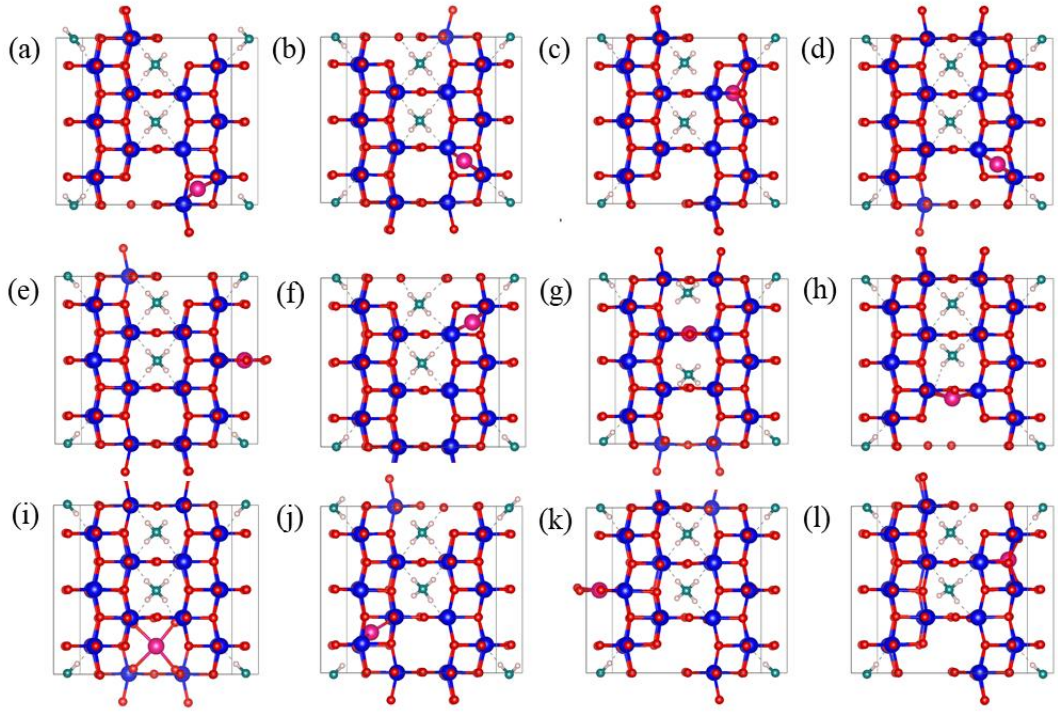

Figure 3.3.20. The intercalation sites in (a)-(i) are the inequitable sites for Zn^{2+} in pristine NHVO, where the most stable and metastable intercalation sites are (e) and (f), respectively. The intercalation site (j) adjacent to the oxygen vacancy. The most stable and metastable intercalation sites in oxygen deficient NHVO are (k) and (l), respectively. (blue (V), red(O), green(N), fuchsia(Zn) and light pink(H)).

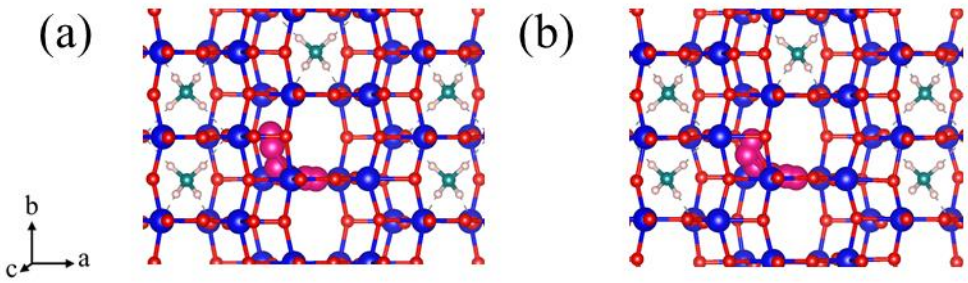

Figure 3.3.21. The diffusion pathways viewed along <001> direction in (a) pristine NHVO and (b) oxygen deficient NHVO. (blue (V), red(O), green(N), fuchsia(Zn) and light pink(H)).

The insertion energies of Zn^{2+} in pristine and oxygen deficient NHVO were calculated, respectively, which were utilized to determine the most and metastable intercalated sites,

according to the equation shown as below:

$$E_{in} = E_{NVO-Zn} - E_{NVO} - E_{Zn} \quad (2)$$

Where the E_{in} is the intercalation energy of Zn^{2+}, E_{NVO-Zn} refers to the total energy of pristine and oxygen deficient NHVO with the intercalation of Zn^{2+}. E_{NVO} stands for the total energy of pristine and oxygen deficient NHVO. E_{Zn} donate as the energy of bulk Zn.

Table 3.3.3. The intercalation energy (E_{in}) of Zn^{2+} of the most stable, metastable, and near defect sites in pristine and oxygen deficient NHVO.

Label	E_{in} (eV)	Label	E_{in}(eV)
Pristine-NHVO		Defective-NHVO	
4	1.17	Defect-site	1.10
5	0.71	5	0.70
6	0.98	6	0.85

It should be noted that the defective site in O_d-NHVO·nH_2O refer to the intercalation site close to the oxygen point vacancy. Similarly, the intercalation site of 4 in pristine NHVO is comparable to the defect site. When evaluating the Zn^{2+} intercalation energies of these intercalation sites in pristine and oxygen deficient NHVO, it is found that the oxygen vacancies can facilitate the Zn^{2+} (de)intercalations since a lower insertion energy during the reactions and the achievable highest reduction value of 0.13 eV. Thus, this is consistent with the view of previous studies, which is beneficial to the diffusion process with more smooth potential energy surface.[33] Additionally, the corresponding minimum energy migration pathways are demonstrated in Figure 3.3.22. The diffusion energy barrier in pristine NHVO is 0.82 eV, whereas the diffusion energy barrier in oxygen deficient NHVO is 0.58 eV. Hence, it is seen as obvious reduction of Zn^{2+} diffusion energy barrier derived from introduced oxygen vacancy in treated NHVO.

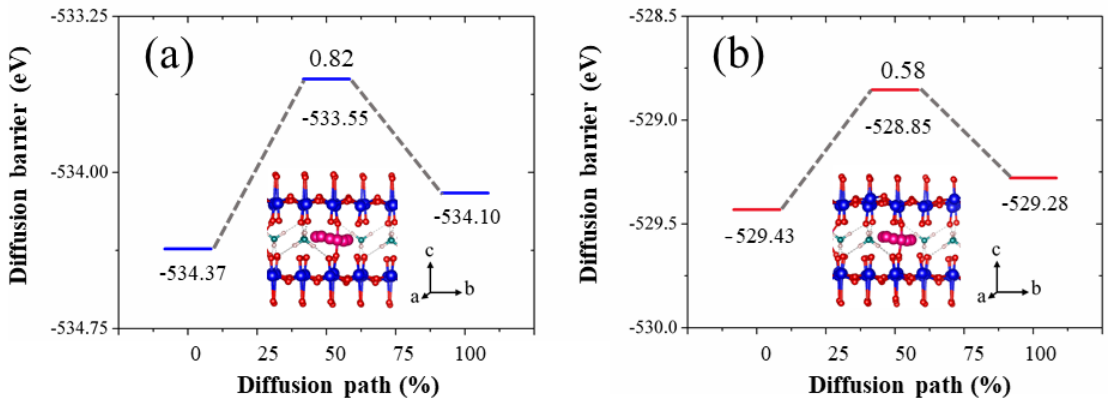

Figure 3.3.22. The diffusion energy barrier and minimum energy migration pathway of Zn^{2+} in (a) pristine-NHVO and (b) oxygen deficient NHVO. (blue (V), red(O), green(N), fuchsia(Zn) and light pink(H)).

3.4 Summary

By inducing defects engineering from cations, lattice H_2O and oxygen vacancies to vanadium bronzes, it a proof-of-concept demonstration for designing superior cathode materials in AZIBs applications has been provided. The elaborately tailored O_d-NHVO·nH_2O cathode exhibites high performance at both low rate and high rate of 0.2 A g^{-1} and 10 A g^{-1} for 435 mAh g^{-1} and 244 mAh g^{-1}, respectively, even after 1500 cycles. Moreover, remarkable rate capability of 43% capacity remained after 28 fold raised current densities from 0.5 A g^{-1} to 14 A g^{-1}, which was observed in O_d-NHVO·nH_2O electrode. In addition, the corresponding electrochemical and structural behaviours were comprehensively investigated by multiple *ex-situ* characterizations and DFT simulation, revealing an encouraged Zn^{2+} diffusion kinetics, excellent reversibility as well as predominately capacitive-controlled rapid energy storage behaviours compared with untreated NHVO electrode. Additionally, the DFT results illustrate the different possibilities of oxygen deficient sites, migration pathways with corresponding energy and their resulted beneficial effects on electrochemical properties not only for facilitating the diffusion characteristics of Zn^{2+}, but also for improving the electronic conductivity in O_d-NHVO·nH_2O electrode. Therefore, inducing oxygen defects and structural modifications provides feasible routes to adjust the electronic- and micro-structures of vanadium-based cathodes to realize advanced AZIBs applications.

3.5 Reference

1 N. Günter and A. Marinopoulos, *Journal of Energy Storage*, 2016, **8**, 226–234.

2 F. Zheng, M. Kotobuki, S. Song, M. O. Lai and L. Lu, *J. Power Sources*, 2018, **389**, 198–213.

3 Y. Gong, K. Fu, S. Xu, J. Dai, T. R. Hamann, L. Zhang, G. T. Hitz, Z. Fu, Z. Ma, D. W. Mcowen, X. Han, L. Hu and E. D. Wachsman, *Mater. Today*, 2018, **21**, 594–601.

4 B. Safe, L. Suo, O. Borodin, Y. Wang, X. Rong, W. Sun, X. Fan, S. Xu, M. A. Schroeder, A. V Cresce, F. Wang, C. Yang, Y. Hu, K. Xu and C. Wang, *Adv. Energy Mater.*, 2017, **7**, 1701189.

5 M. R. Lukatskaya, J. I. Feldblyum and D. G. Mackanic,*Energy Environ. Sci.*, 2018, **11**, 2876–2883.

6 J. Gon, B. Son, S. Mukherjee, N. Schuppert, A. Bates, O. Kwon, M. Jong, H. Yeol and S. Park, *J. Power Sources*, 2015, **282**, 299–322.

7 C. Sun, J. Liu, Y. Gong, D. P. Wilkinson and J. Zhang, *Nano Energy*, 2017, **33**, 363–386.

8 L. Suo, O. Borodin, W. Sun, X. Fan, C. Yang, F. Wang, T. Gao, Z. Ma, M. Schroeder, A. Von Cresce, S. M. Russell, M. Armand, A. Angell, K. Xu and C. Wang, *Angew. Chem., Int. Ed.*, 2016, **85287**, 7136–7141.

9 H. Chen, Z. Zhang, Z. Wei, G. Chen, X. Yang, C. Wang and F. Du, *Sustainable Energy Fuels*, 2020, **4**, 128–131.

10 F. Wang, O. Borodin, T. Gao, X. Fan, W. Sun, F. Han, A. Faraone, J. A. Dura, K. Xu and C. Wang, *Nat. Mater.*, 2018, **17**, 543–549.

11 M. Song, H. Tan, D. Chao and H. J. Fan, *Adv. Funct. Mater.*, 2018, **28**, 1–27.

12 J. Ming, J. Guo, C. Xia, W. Wang and H. N. Alshareef, *Mater. Sci. Eng. R Reports*, 2019, **135**, 58–84.

13 C. Li, X. Zhang, W. He, G. Xu and R. Sun, *J. Power Sources*, 2020, **449**, 227596.

14 W. Xu and Y. Wang, *Nano-Micro Lett.*, 2019, **11**, 90.

15 B. Tang, L. Shan, S. Liang and J. Zhou, *Energy Environ. Sci.*, 2019, **12**, 3288–3304.

16 D. Xiong, X. Li, Z. Bai and S. Lu, *Small*, 2018, **14**, 1703419.

17 L. Peng, Y. Zhu, D. Chen, R. S. Ruoff and G. Yu, *Adv. Energy Mater.* 2016, **6**,

1600025

18 J. Zhao, H. Ren, Q. Liang, D. Yuan, S. Xi, C. Wu, W. Manalastas, J. Ma, W. Fang, Y. Zheng, C. Du, M. Srinivasan and Q. Yan, *Nano Energy*, 2019, **62**, 94–102.

19 D. Selvakumaran, A. Pan, S. Liang and G. Cao, *J. Mater. Chem. A*, 2019, **7**, 18209–18236.

20 X. Yao, Y. Zhao, F. A. Castro and L. Mai, *ACS Energy Lett.*, 2019, **4**, 771–778.

21 J. Li, K. McColl, X. Lu, S. Sathasivam, H. Dong, L. Kang, Z. Li, S. Zhao, A. G. Kafizas, R. Wang, D. J. L. Brett, P. R. Shearing, F. Corà, G. He, C. J. Carmalt and I. P. Parkin, *Adv. Energy Mater.*, 2020, **10**, 2000058.

22 K. D. Rasamani, F. Alimohammadi and Y. Sun, *Materials Today*, 2017, **20**, 83-91.

23 X. Sun, V. Du, B. L. Mehdi, N. D. Browning and L. F. Nazar, *Chem. Mater.*, 2016, **28**, 534-542.

24 J. L. Andrews, S. Singh, C. Kilcoyne, P. J. Shamberger, G. Sambandamurthy and S. Banerjee, *MRS Commun.*, 2017, **7**, 634–641.

25 J. Zhou, L. Shan, Z. Wu, X. Guo, G. Fang and S. Liang, *Chem. Commun.*, 2018, **54**, 4457–4460.

26 H. Maleki, K. Sari and X. Li, *Adv. Energy Mater.*, 2019, **9**, 1901597

27 D. Li, S. Lu, A. Koo, K. Adair and X. Sun, *Nano Energy*, 2018, **44**, 111-120.

28 F. Wang, W. Sun, Z. Shadike, E. Hu, X. Ji, T. Gao, X. Yang, K. Xu and C. Wang, *Angew. Chem., Int. Ed.*, 2018, **57**, 11978-11981.

29 D. Kundu, S. H. Vajargah, L. Wan, B. Adams, D. Prendergast and L. F. Nazar, *Energy Environ. Sci.*, 2018, **11**, 881-892.

30 J. Lai, H. Zhu, X. Zhu, H. Koritala and Y. Wang, *ACS Appl. Energy Mater.*, 2019, **2**, 1988–1996.

31 M. Yan, P. He, Y. Chen, S. Wang, Q. Wei, K. Zhao, X. Xu, Q. An, Y. Shuang, Y. Shao, K. T. Mueller, L. Mai, J. Liu and J. Yang, *Adv. Mater.*, 2018, **30**, 1703725.

32 F. Wan and Z. Niu, *Angew. Chem., Int. Ed.*, 2019, **58**, 16358-16367.

33 Z. Batteries, M. Liao, J. Wang, L. Ye, H. Sun, Y. Wen, C. Wang, X. Sun, B. Wang and H. Peng, *Angew. Chem.*, 2020, **132**, 2293-2298.

34 Z. Li, Y. Ren, L. Mo, C. Liu, K. Hsu, Y. Ding, X. Zhang, X. Li, L. Hu, D. Ji and G. Cao, *ACS Nano*, 2020, **14**, 5581−5589.

35 Kresse, G.; Hafner, *J. Phys. Rev. B* 1993, **47**, 558.

36 Kresse, G.; Furthmuller, *J. Comput. Mater. Sci.* 1996, **6**, 15.

37 Perdew, J. P.; Burke, K.; Ernzerhof, M. *Phys. Rev. Lett.* 1996, **77**, 3865−3868.

38 BlÖchl, P. E. *Phys. Rev. B* 1994, **50**, 17953.

39 Sarkar, T.; Kumar, P.; Bharadwaj, M. D.; Waghmare, U. *Phys. Chem. Chem. Phys*. 2016, **18**, 14, 9344-9348.

40 KlimeŠ, J.; Bowler, D. R.; Michaelides, A. *Phys. Rev. B* 2011, **83**, 195131.

41 G. Henkelman, B. P. Uberuaga and H. Jonsson, *J. Chem. Phys*. 2000, **113**, 9901.

42 L. Cheng, M. Xu, Q. Zhang, G. Li, J. Chen and Y. Lou, *J. Alloys Compd.*, 2019, **781**, 245–254.

43 Y. Zhang, J. Zheng, Y. Zhao, T. Hu, Z. Gao and C. Meng, *Appl. Surf. Sci.*, 2016, **377**, 385–393.

44 E. A. Esparcia, M. S. Chae, J. D. Ocon and S. Hong, Chem. Mater., 2018, **30**, 3690–3696.

45 Y. Liu, B. Shen, X. Liu, Y. Wu, X. He and Q. Li, *Int. J. Electrochem. Sci.*, 2017, **12**, 5483–5491.

46 Y. Xu, H. Dong, M. Zhou, C. Zhang, Y. Wu, W. Li, Y. Dong and Y. Lei, *Small Methods*, 2018, **1800349**, 1800349.

47 A. M. El-sayed, S. Mohamed and A. Mousa, *J. Chin. Chem. Soc.*, 2006, **5**, 559–565.

48 W. Zhang, C. Au and H. Wan, *Appl. Catal., A,* 1999, **181**, 63-69.

49 Y. Yang, Y. Tang, S. Liang, Z. Wu, G. Fang, X. Cao, C. Wang, T. Lin, A. Pan and J. Zhou, *Nano Energy*, 2019, **61**, 617–625.

50 D. Kundu, B. D. Adams, V. Duffort, S. H. Vajargah and L. F. Nazar, *Nat. Energy*, 2016, **1**, 1–8.

51 V. Bondarenka, H. Tvardauskas, M. Senulis, A. Pašiškevičius and S. Grebinskij, *Acta Phys. Pol., A*, 2011, **119**, 135–136.

52 W. Li, D. Kong, T. Yan, M. Shi, D. Kong and Y. Feng, *J. Solid State Chem.*, 2020, **286**, 121296.

53 C. Lv, C. Yan, G. Chen, Y. Ding, J. Sun and Y. Zhou, *Angew. Chem., Int. Ed.*, 2018, **57**, 6073–6076.

54 M. Huang, J. Bian, W. Xiong and R. Zhang, *J. Mater. Chem. A*, 2018, **6**, 3602-3609

55 B. Guo, L. Chen, S. Shi, A. Ishaq, D. Wan, Z. Chen, L. Zhang, H. Luo and Y.

Gao, *RSC Adv.*, 2017, **7**, 10798–10805.

56 M. Yan, P. He, Y. Chen, S. Wang, Q. Wei, K. Zhao, X. Xu, Q. An, Y. Shuang, Y. Shao, K. T. Mueller, L. Mai, J. Liu and J. Yang, *Adv. Mater.*, 2018, **30**, 1–6.

57 Y. Yang, Y. Tang, G. Fang, L. Shan, J. Guo, W. Zhang, C. Wang, L. Wang, J. Zhou and S. Liang, *Energy Environ. Sci.*, 2018, **11**, 3157–3162.

58 B. Tang, J. Zhou, G. Fang, F. Liu, C. Zhu, C. Wang, A. Pan and S. Liang, *J. Mater. Chem. A*, 2019, **7**, 940–945.

59 P. He, G. Zhang, X. Liao, M. Yan, X. Xu, Q. An, J. Liu and L. Mai, *Adv. Energy Mater.*, 2018, **8**, 1–6.

60 L. Shan, Y. Yang, W. Zhang, H. Chen, G. Fang, J. Zhou and S. Liang, *Energy Storage Mater.*, 2019, **18**, 10–14.

61 S. Islam, M. H. Alfaruqi, B. Sambandam, D. Y. Putro, S. Kim, J. Jo, S. Kim, V. Mathew and J. Kim, *Chem. Commun.*, 2019, **55**, 3793–3796.

62 T. Wu, K. Zhu, C. Qin and K. Huang, *J. Mater. Chem. A*, 2019, **7**, 5612–5620.

63 B. Tang, G. Fang, J. Zhou, L. Wang, Y. Lei, C. Wang, T. Lin, Y. Tang and S. Liang, *Nano Energy*, 2018, **51**, 579–587.

64 W. Li, K. Wang, S. Cheng and K. Jiang, *Energy Storage Mater.*, 2018, **15**, 14–21.

65 C. Xia, J. Guo, P. Li, X. Zhang and H. N. Alshareef, *Angew. Chemie. Int. Ed.*, 2018, **57**, 3943–3948.

66 C. Xia, J. Guo, Y. Lei, H. Liang, C. Zhao and H. N. Alshareef, *Adv. Mater.*, 2018, **30**, 1–7.

67 B. Sambandam, V. Soundharrajan, S. Kim, M. H. Alfaruqi, J. Jo, S. Kim, V. Mathew, Y. K. Sun and J. Kim, *J. Mater. Chem. A*, 2018, **6**, 3850–3856.

68 G. He, M. Qiao, W. Li, Y. Lu, T. Zhao, R. Zou, B. Li, J. A. Darr, J. Hu, M.-M. Titirici and I. P. Parkin, *Adv. Sci.*, 2017, **4**, 1600214.

69 F. Ming, H. Liang, Y. Lei, S. Kandambeth, M. Eddaoudi and H. N. Alshareef, *ACS Energy Lett.*, 2018, **3**, 2602–2609.

70 B. Sambandam, V. Soundharrajan, S. Kim, M. H. Alfaruqi, J. Jo, S. Kim, V. Mathew, Y. Sun and J. Kim, *J. Mater. Chem. A*, 2018, **6**, 15530–15539.

71 G. Henkelman, B. P. Uberuaga and H. Jonsson, *J. Chem. Phys*. 2000, **113**, 9901.

72 Q. Li, X. Rui, D. Chen, Y. Feng, N. Xiao, L. Gan, Q. Zhang, Y. Yu and S. Huang, *Nano-Micro Lett*. 2020, **12**, 1-12.

Chapter 4.

Diatomic cation induced spontaneous vacancies in vanadyl Prussian blue analog for advanced aqueous zinc ion batteries

4.1 Introduction

Although LIBs currently still dominate the EES market because of high energy density and reliable energy storage/output, the limited resource, combustible organic electrolyte and environmental impacts have caused grave concerns on specific applications such as portable devices and grid-scale stationary applications.[1,2,3,4,5] Thereby, rechargeable aqueous zinc-ion batteries have been developed rapidly aiming at environmental benignity, intrinsic safety and high-cost efficiency for a practicable competitive capability as novel EES techniques for fulfilling the complementary demands of specific applications.[6,7,8,9] Moreover, owing to numerous merits of metallic zinc anode in AZIBs, high battery performance can be immediately achieved if competent cathodic host materials were eventually developed.[10] Hence, more focus is seriously needed on the investigation of cathode materials in order to unlock the entire potential of AZIBs. However, because of relatively stronger electrostatic interaction of divalent charge carrier and large ionic radii of hydrated species, the previously developed cathodes such as vanadium-based oxides, manganese-based oxides and Prussian blue analogues (PBAs) are still suffering from sluggish diffusion kinetics, fast degradation of capacity and intrinsic deficiencies in respective materials (i.e. unstable features derived from self-dissolution and irreversible phase transition and relatively low operating voltage especially for V- and Mn-based cathodes) during the charge/discharge processes, which critically impede the practical application of AZIBs as a matter of fact.[11,12,13,14,15]

Among these cathode materials, PBAs, also known as metal hexacyanoferrate (MHCF), are exceptional existence compared with the others owing to rigid 3D frameworks constructed by varied transition metals and cyanogroup, which can offer accessible channels, tuneable electrochemical properties and multiple redox-active sites for guest species with a rapid reaction kinetics and the highest discharge plateau in AZIBs applications.[16,17,18] Thus, it was expected that MHCF based cathodes could deliver high energy/power densities and robust reversibility in objective system, but it turns out to have an unsatisfactory performance with relatively low average specific capacity (< 80 mAh g^{-1}) and inferior life span ($> 20\%$ capacity attenuation within 1000 cycles) in reality.[19,20,21] For instance, ZnHCF $|$ $ZnSO_4$ $|$ Zn battery was first reported by Liu and co-workers in 2015, with an observed maximum capacity of 65.4 at 1C (60 mA g^{-1}) along with 24% capacity decay after 100 cycles and rate capacity of maintaining 49% capacity at 20C (1.2 A g^{-1}).[22] Comparably, FeHCF[23], CuHCF[24] and NiHCF[25] cathodes

also present unfavourable maximum capacity of 76, 56 and 76.2 mAh g^{-1}, respectively, associated with rate capability lower 55% capacity retention within the 10-fold increase of current densities, which could be attributed to several transition-metal dissolution in diluted aqueous electrolyte resulting in structural collapse and clarified capacity contribution from only single redox site of Fe ions (referring in particular to high-spin Fe ions in FeHCF).[26,27] Therefore, MHCF was less studied in previous researches compared with other categorises of cathodes, and indeed demands a substantial breakthrough in this field.[11,28,29]

Herein, a novel vanadyl hexacyanoferrate (VOHCF) was developed for AZIBs by utilizing redox active dual-atomic group of vanadyl cation (V=O) instead of conventional 'inert' transition-metal ions in metal hexacyanoferrate frameworks, giving rise to a unique configuration of random distribution of numerous intrinsic vacancies for the octahedral cyanoferrate ligands. Thereby, the corresponding enlarged open channels derived from vacancies and potential maximum three-electrons based redox reaction (V(III)↔V(V), Fe(II)↔Fe(III)) were verified with the record-breaking specific capacity of 213mAh g^{-1} at 0.2 A g^{-1} and 132 mAh g^{-1} at 5 A g^{-1} along with a rate capability of 62% capacity remained after 25-fold elevated current densities from 0.2Ag^{-1} to 5 A g^{-1} compared to all reported Prussian blue analogues for AZIBs applications. More impressively, owing to intrinsic unstable features, it was first proposed that ionic-conductive hydrogel surface shielding strategy in aqueous ion batteries system for not only preserves cathode materials structural stabilities, but improves the interfacial characteristics *via* functionalized hydrophilic surface with accessible ionic migration channels. As a consequence, the tailored VOHCF achieved unprecedentedly comprehensive-upgraded performance rendered as the further enhanced specific capacity of 226 mAh g^{-1} and 176 mAh g^{-1} at 0.2 and 5A g^{-1}, respectively, associated with 88% capacity retention for the superior rate capability. Meanwhile, the long-cycling stability characterizations also present remarkably robust features of the hydrogel-treated VOHCF with 95% capacity retention after 1000 cycling tests compared with only 78% in pristine VOHCF. Therefore, it is suggested feasible approach on cathode materials in AZIBs so as to break the shackles of intrinsic issues. In addition to electrochemical measurements, comprehensive investigations on physicochemical properties and structural/chemical evolutions during Zn^{2+} (de)intercalations were carried out by multiple characterizations techniques such as *ex-situ* XRD, *ex-situ* XPS and *ex-situ* Raman to clarify the reversibility and reaction

mechanisms. Moreover, a quasi-solid-state VOHCF | PAM ($Zn(CF_3SO_3)_2$) | Zn was fabricated with mechanical robustness of steadily energy output and extraordinary cycling capability with negligible capacity degradation over 2000 cycles, that is, convincingly suggesting that our as-prepared cathode materials possess strong promise for not only rapid-charge grid-scale stationary applications but wearable portable electronics.

4.2 Experimental Section

4.2.1 Material synthesis

All chemical reagents were purchased from Sigma U.K. and adopted without further purification. In typical preparations of VOHCF(III) and its control sample of VOHCF(II), 10 mmol vanadium(IV) oxide sulfate hydrate was dissolved in 50 mL D.I. water in beaker A with vigorous stirring for few hours, at the mean time, beaker B was filled with same amount of D.I. water, subsequently adding 10 mmol $K_3[Fe(CN)_6]$ (Potassium ferricyanide(III)) or $K_4Fe(CN)_6 \cdot 3H_2O$ (Potassium hexacyanoferrate(II) trihydrate) into beaker B with a stirring for 30 minutes. In final step, The as-obtained transparent solutions from the two beakers (A & B) were dropwise injected into a conical flask beforehand filled up with 50 mL D.I. water along with initially vigorous stirring for 2 hours and low rotation speed in rest of 5 days as aging process. The resulting products were collected by high-speed centrifugation and washed several times with D.I. water. Then, freeze-drying machine was operated for two days to eliminate moisture of the samples.

The alginate shielded VOHCF(III) was fabricated by single step in aqueous solution. In detail, 200 mg as-obtained VOHCF(III) was pour into a 100 mL alginate solution containing 0.3 mmol sodium alginate with continuously stirring for 30 minutes. Then, using high-speed centrifugation, the resulting product was washed several times with D.I. water and finally collected for the following freeze-drying process.

Fabrication of quasi-solid-state battery:

6g acrylamide monomer was added into 25 mL D.I. water at ambient environment under vigorous stirring for 1 hour. Subsequently, a mixture of 3.75 mg methylene-bis-acrylamide as cross linker and 75 mg ammonium persulphate as initiator were dispersed into as-obtained solution. Then, the homogeneous mixed solution was poured into a flat

mould where the pre-assembled cathode and anode had been loaded. Along with a slow evaporation of H_2O and polymerization at 50 ˚C, the quasi-solid-state polyacrylamide (PAM) hydrogel within the electrodes were generated. The as-fabricated battery was immersed into 4M $Zn(CF_3SO_3)_2$ aqueous electrolyte and dried in vacuum oven before further electrochemical measurements.

4.2.2 Material characterizations

All XRD characterizations were carried out by a STOE SEIFERT diffractometer equipped with Mo (0.7093Å) X-ray radiation source. The detected angle range was selected as $2°<2\theta<45°$. Moreover, scanning electron microscope (SEM, Carl Zeiss EVO MA10), transmission electron microscope (TEM, JEOL, JEM-2100 and ARM200F) and XPS (Thermo Scientific K-alpha photoelectron spectrometer) were adopted to clarify the morphology and chemical states of as-prepared samples, respectively. The data process of XPS was achieved by initially calibrating adventitious carbon with a binding energy at 284.8 eV through casa software. The peak areas were fixed according to a ratio of 1:2 for the $2p_{1/2}$: $2p_{3/2}$ in each valence states, and FWHM of the corresponding peaks ($2p_{1/2}$ and $2p_{3/2}$) maintained the same length during deconvolution process. Meanwhile, the distance between two peaks of $2p_{1/2}$ and $2p_{3/2}$ for each valance states and elements were adjusted according to literature. In addition, Raman Spectroscopy (Renishaw Raman microscope spectrometer with a laser wavelength of 514.5 nm) and attenuated total reflectance Fourier transform infrared spectrometer (FTIR, ATRFTIR, BRUKER, platinum ATR) were utilized, and the mass variation upon raised temperature was evaluated by a Thermogravimetric analyzer (TGA) (PerkinElmer TGA 4000 System). The mass of the active substance in fabricated electrode was weighed by the analytical balance (Ohaus; δ=0.01mg). The N_2 adsorption-desorption isotherms were characterized at 77 K (Quantachrome Autosorb-iQC), and corresponding specific surface area was analyzed from isotherms according to the BET method. The pore size distribution data was attained from desorption result based on a quenched solid density functional theory (QSDFT) especially for micro- and meso- pores <50 nm. The water contact angles was tested by an optical contact angle meter *via* the sessile-drop approach at ambient environment (FTA 1000). The water droplets were kept in a constant volume of 5 μL and dwelling time of droplets stayed on each samples were set up to 60s. The following contact angle values were analyzed

by Young–Laplace equation through using instrument software.

4.2.3 Electrochemical evaluations

The as-prepared cathode materials were mixed with conductive agent (Super P Carbon) and binder solution (polyvinylidene fluoride (PVDF) dissolved in 1-Methyl-2-pyrrolidinone(NMP) with concentration of 50mg μL^{-1}) with a weight ratio of 7 : 2 : 1. Then, the homogeneous mixed slurry was printed on a current collectors (hydrophilic carbon paper) with a loading mass around 1.5 mg cm^{-1}. Subsequently, the printed electrodes were transferred to a vacuum oven and dried at 70°C for 12 hours. Then, the completely dried electrodes were cut into disc with a diameter of 14 mm and following assembled with 18mm diameter (Whatman® glass microfiber Grade GF/A) separator and 16mm diameter metallic zinc foil in a CR2032 coin-like cell. Moreover, 4M $Zn(CF_3SO_3)_2$ aqueous electrolytes was prepared for all electrochemical measurements. A configuration of flexible cell module are illustrated in Figure 4.2.1. The galvanostatic charge-discharge (GCD) characterizations were achieved by the NEWARE battery testing system capacity and cycling stability evaluations, and the VMP3 Biologic electrochemical workstation was performed out to detect other electrochemical properties, such as cyclic voltammetry (CV) and electrochemical impedance spectroscopy (EIS).

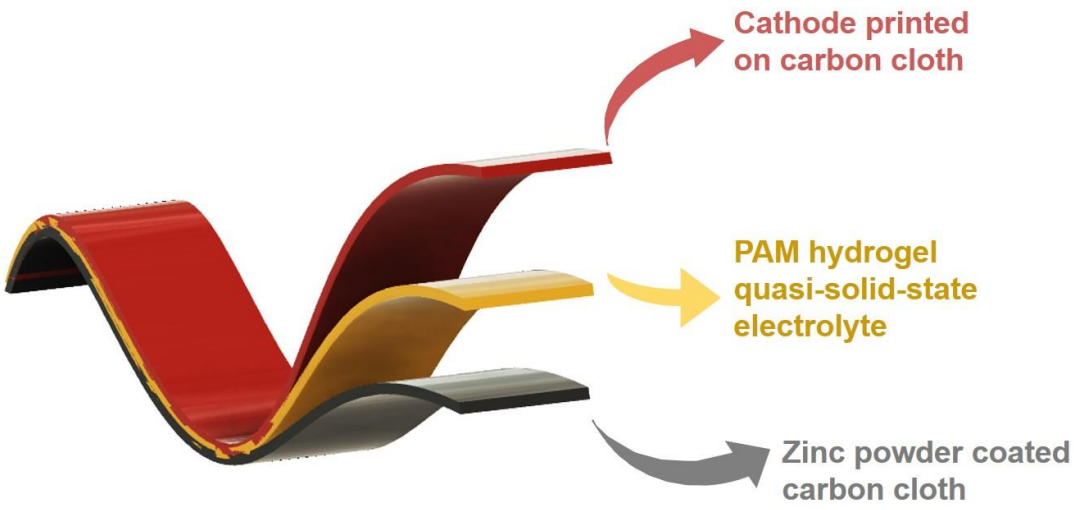

Figure 4.2.1. A configuration scheme of flexible quasi-solid-state zinc ion batteries.

4.3 Results and discussion

The synthesis of VOHCF(III) and VOHCF(II) were carried out by facile single-step co-participation method in aqueous solution. Owing to different precursors of potassium ferricyanide(III) and potassium hexacyanoferrate(II) trihydrate, the resulting products of VOHCF(III) and VOHCF(II) exhibit varied crystallinity which are illustrated in Figure 4.3.1a. It is seen that both of these two sample can be indexed to the standard XRD pattern of $(VO)_3[Fe(CN)_6]_2 \cdot 9H_2O$ (JCPDS: 42-1440), which possess a cubic unit cell belonging to the $Fm\bar{3}m$ space group.[30] Surprisingly, the structure of VOHCF is distinctive among all known Prussian blue analogues since the space occupation of oxygen in vanadyl group gives rise to numerous spontaneously developed vacancies of $Fe(CN)_6$ ligand within the framework which result in the large cavity filled with six stabilized H_2O molecules and pre-inserted K^+ from the precursor.[30] Therefore, the porous coordination atypically offer enlarged channels of connected cavities which can be expected a high diffusion kinetics for inserted guest species. Moreover, the most three intensive reflection sites at 2θ of 8.04˚, 11.35˚ and 16.09˚ represent crystal facets of (200), (220) and (400), respectively, corresponding to a calculated lattice parameters of $a=b=c=10.136(3)$ Å ($\alpha=\beta=\gamma=90^\circ$) and $a=b=c=10.1(1)$ Å ($\alpha=\beta=\gamma=90^\circ$) for VOHCF(III) and VOHCF(II), respectively. However, a relatively broader FWHM of VOHCF(II) implies the poor crystallinity and small crystal size which can be calculated *via* Scherrer equation, that is, only 6.2(6) nm for VOHCF(II) compared with 13.9(7) nm for VOHCF(III). Therefore, the change of precursor can effectively impact on crystal size in our case resulting in a defective feature in VOHCF(II), which could be responsible for the distinct electrochemical behaviours. Similarly, it is also observed conspicuous different colours of as-prepared VOHCF(III) (olivine) and VOHCF(II) (claybank), shown as the insets in Figure 4.3.1a, are attributed to varied inherent physical properties. For instance, varied oxidation states of transition metals related to different amount of inserted alkali ions in Prussian blue contribute to diverse colours of materials, i.e. $Fe^{III}Fe^{III}(CN)_6$, $KFe^{III}Fe^{II}(CN)_6$ and $K_2Fe^{II}Fe^{II}(CN)_6$ for Berlin green, Prussian blue and white, respectively.[31,32] Moreover, the SEM characterizations on VOHCF(III) and VOHCF(II) are presented in Figure 4.3.1(b) and (c), respectively, in which clusters of agglomerated fine particles are extensively observed in both samples. However, it is extremely hard to acquire high quality images from TEM characterization due to instability under the electron beam radiation during the

measurement, despite many attempts had been made (Figure 4.3.1d). The FTIR spectrum in Figure 4.3.1e presents several distinct absorption bands in VOHCF(III) sample associated with the vibrations of Fe-C bending mode (514 and 600 cm^{-1}),[33] V=O stretching mode (975 cm^{-1}),[34,35,36] Fe^{II}-C≡N stretching mode (2081 cm^{-1})[32] and two H_2O molecule related bands of stretching H-O-H and bending O-H modes at 1605 and 3632 cm^{-1},[37] respectively. Comparably, similar features of the FTIR spectrum for VOHCF(II) were observed, which possess slightly red-shift corresponding to softened vibration bonds, i.e. 503, 965 and 2060 cm^{-1}, respectively. In particular, there is a tiny peak emerged at wavelength number of 2162 cm^{-1} in VOHCF(III) which suggest the existence of Fe^{III}-C≡N stretching mode in the structure compared with absolute Fe^{II}-C≡N stretching mode in VOHCF(II) sample.[32] In addition to FTIR, Raman spectrum clearly illustrates various bands in accordance with Fe-O(lattice water)/ C stretching and deformation vibrations, vanadyl related vibrations and Fe-C≡N-M (M: transition metal) stretching vibration modes at sphere of 200-500, 600-1000 and 2070-2200 cm^{-1} for both materials, respectively.[38,39] However, the relative intensity of each peak were different between these samples especially at C≡N spectrum region, which is associated with the high sensibility of varied oxidation states of cyano-group coordinated iron ions and transition-metal ions.[23] More explicitly, the intensity of peaks at Raman shift of 2146 cm^{-1} (strong) and 2096 cm^{-1} (weak) in VOHCF(III) suggest that a strengthened coordination corresponds to the relatively higher valance states derived from Fe^{III} species and vanadyl group in VOHCF(III) than that of Fe^{II} dominated VOHCF(II). Therefore, FTIR and Raman characterizations critically reveal the chemical formation of molecules and their distinct structural features in as-prepared VOHCF samples.

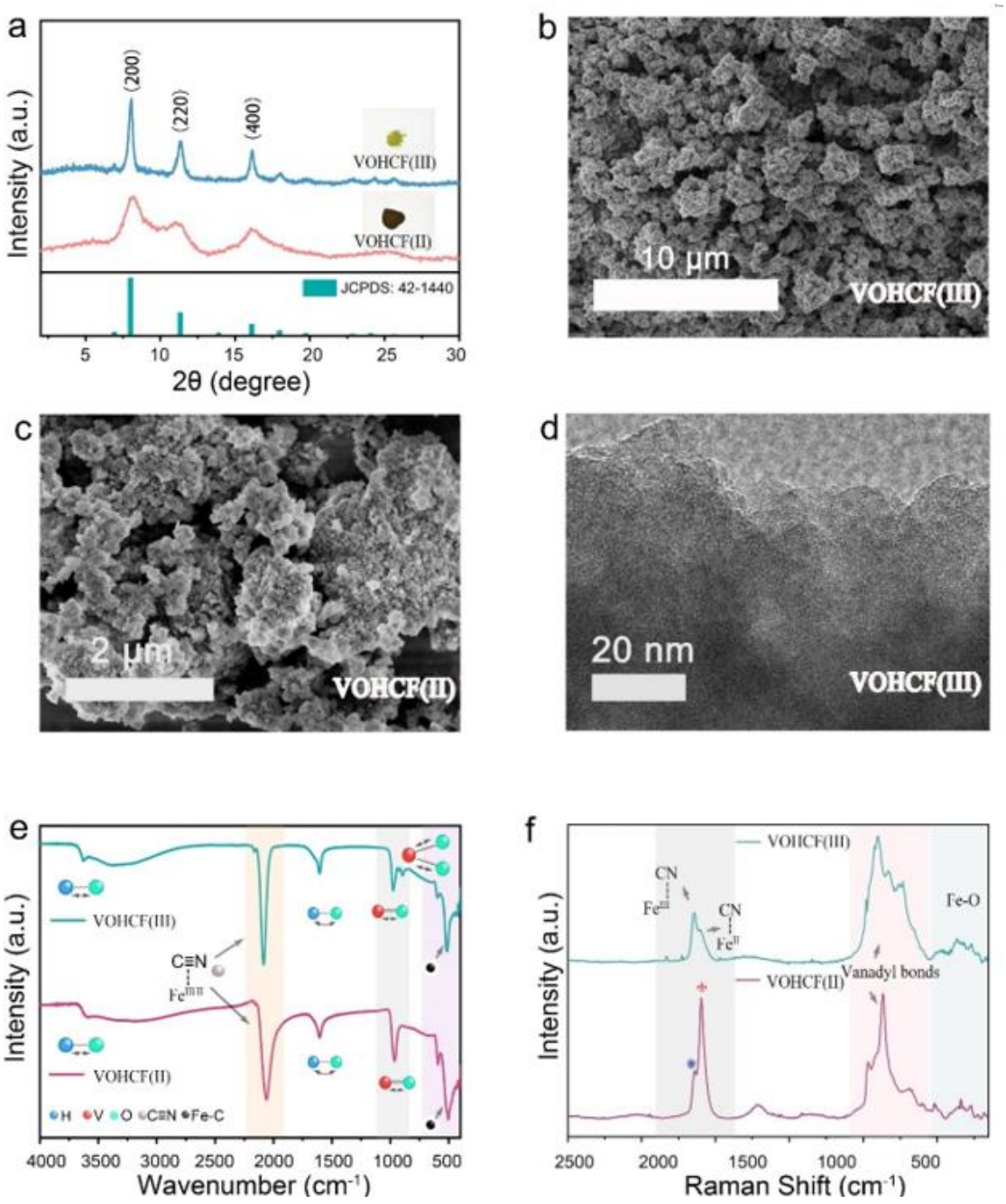

Figure 4.3.1. (a) XRD pattern of as-prepared VOHCF(III) and VOHCF(II), respectively; (b), (c) SEM characterizations of VOHCF(III) and VOHCF(II), respectively; (d) TEM image of VOHCF(III); (e), (f) FTIR and Raman spectra of VOHCF(III) and VOHCF(II), respectively.

The further evaluations of as-prepared VOHCFs were carried out by XPS to distinguish the variations of elemental details and chemical states (Figure 4.3.2). It is seen that both of VOHCF(III)/(II) are composed of mixed valence states of 4+ and 5+, but the fitted areas of each components in one sample differ to those of the other. More explicitly,

more V^{5+} specie can be observed in VOHCF(III) sample indicating a higher oxidization states of vanadium compared with VOHCF(II). Similarly, the core-level spectra of Fe 2p illustrate a split peak in VOHCF(III) indexed to Fe^{III} and small amount of Fe^{II} species, while there is only Fe^{II} component which can identified in VOHCF(II) sample. Moreover, K species were also detected in both samples derived from the precursor, which confirm the description of the material configuration mentioned above. Therefore, it is surprisingly seen that the chemical valent states of those samples are varied due to a simple change of Fe salts in the preparation process in addition to observed structural differences discussed above.

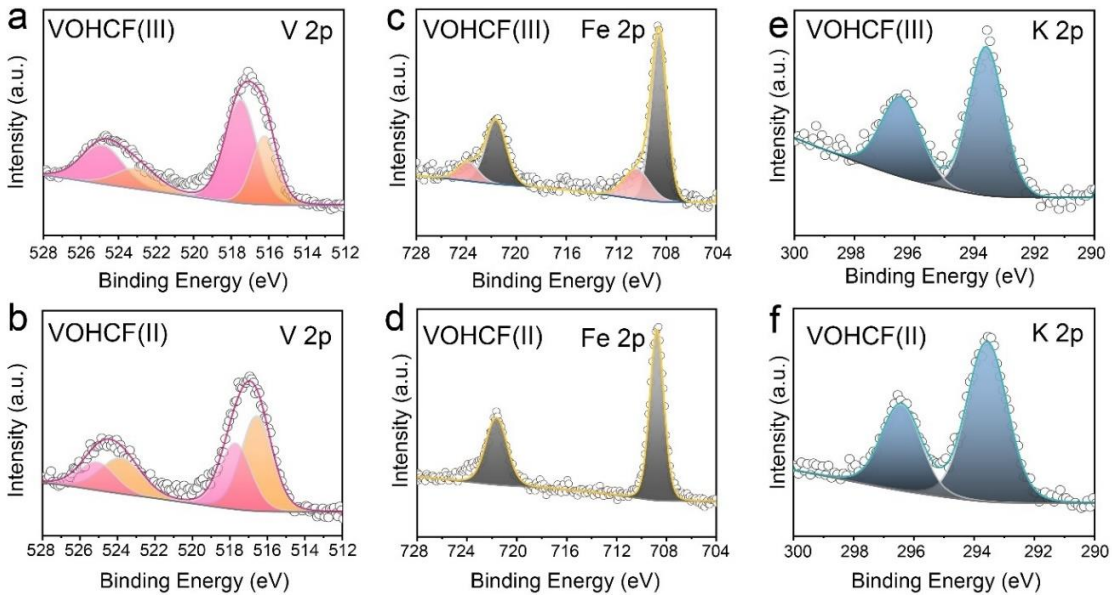

Figure 4.3.2. XPS characterizations of (a) V 2p, (c) Fe 2p and (e) K1s core level in pristine VOHCF(III) respectively; (b) V 2p, (d) Fe 2p and (f) K1s core level in pristine VOHCF(II), respectively.

In order to further elucidate elemental details, the integrated component ratio analysis were conducted by SEM-EDS, XRF and XPS (based on the relative sensitivity factors) to gather the proportion of each elements in both samples. Figure 4.33 clearly illustrates a homogeneous distribution of elemental V, K, Fe, O in both VOHCF(III) and VOHCF(II) samples observed by mapping characterizations. Moreover, elemental analysis deliver a distinct component ratio of as-prepared VOHCF(III) compared with that of VOHCF(II), that is, a relatively higher proportion of V species and less K content obtained in VOHCF(III) rather than observations in VOHCF(II), which were further confirmed by XRF and XPS analysis exhibited in Table 4.3.1. The results suggest that

there is not only a varied proportion of K accommodated in cavity (insertion sites) of the two samples, but also a discrepant ratio of framework components which could be attribute to structural defects in VOHCF(II). An additional elemental analysis of VOHCF(III) pristine powder were achieved by TEM EDS measurement (Figure A1, A2), which further confirm a same ratio (1:1.5) of V:Fe in the sample compared with SEM EDS results.

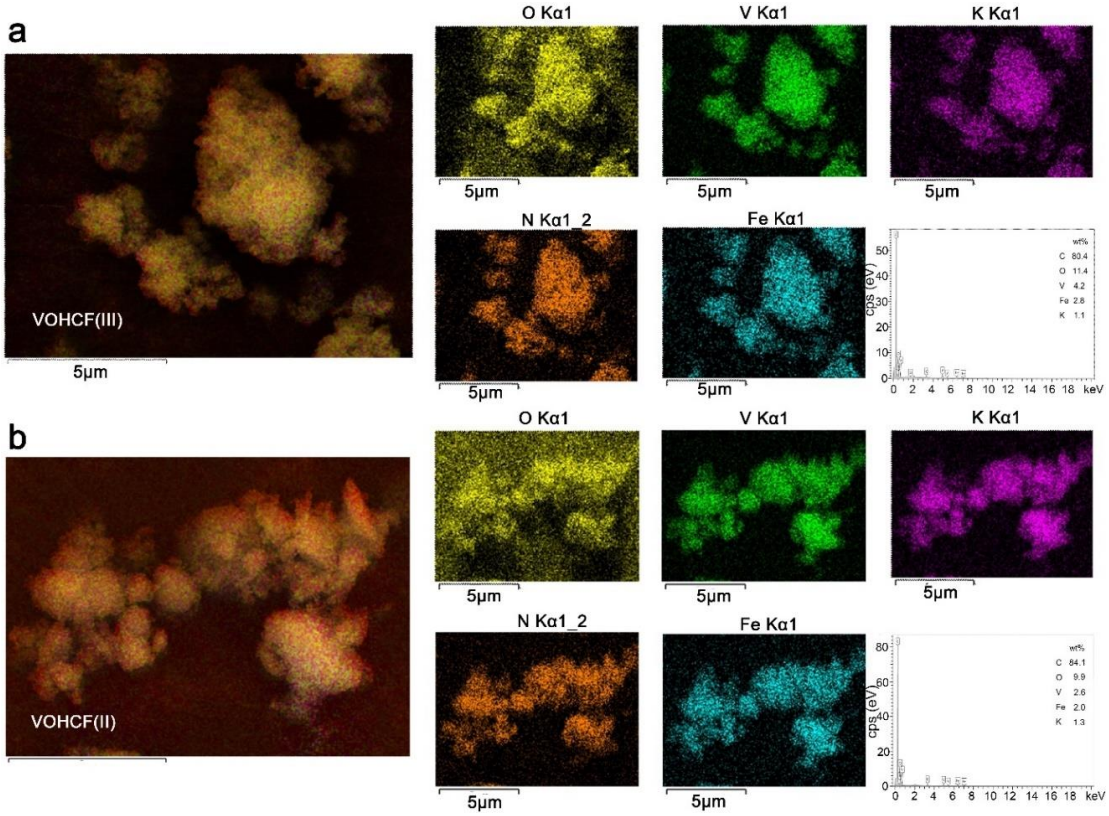

Figure 4.3.3. SEM-EDS elemental analysis of pristine VOHCF(III) and VOHCF(II) samples with corresponding mapping measurements.

Table. 4.3.1 The elemental analysis of EDS(SEM) and XRF on pristine VOHCF(III) and VOHCF(II) samples

Samples	EDS (K:V:Fe)	XRF(K:V:Fe)	XPS(K:V:Fe)
VOHCF(III)	0.6:1.5:1	0.5:1.5:1	0.7:1.7:1
VOHCF(II)	1:1.2:1	0.8:1.3:1	1.5:1.5:1

After comprehensive clarification of structural and chemical difference on the as-obtained samples from multiple characterizations, it is expected that a distinct electrochemical behaviour could occur for utilizing the materials for AZIBs

applications. Therefore, the coin cell type of VOHCF(III)/(II) | ($Zn(CF_3SO_3)_2$) | Zn battery was fabricated to evaluate the electrochemical performance in this case. Figure 4.3.4. exhibits the GCD profiles of VOHCF(III) and VOHCF(II) measured under varied current densities from 0.2 to 5 A g^{-1}, respectively, where numerous distinct plateaus can be identified in both samples upon (de)intercalation of Zn^{2+}, but each possesses different redox reaction potentials along with varied corresponding capacity contribution. More specifically, it is seen that a maximum specific capacity of 190 mAh g-1 and 112 mAh g^{-1} at 0.2 A g^{-1} for VOHCF(III) and VOHCF(II) cathodes, respectively. Meanwhile, a larger specific capacity contribution (>140 mAh g^{-1}) prevailing below 1.6 V was observed in VOHCF(III) rather than limited capacity of ~60 mAh g^{-1} in VOHCF(II) at same working potential window. that Furthermore, CV curves of VOHCF(III) and VOHCF(II) cathodes are illustrated in Figure 4.3.4b, which exhibits similar redox pairs and steady evolutions with rapid activation process in first five cycles. However, it is also seen a large current response below 1.6V in VOHCF(III) cathodes compared with that of VOHCF(II). Interestingly, it is noteworthy that the observed redox pairs possess similar potential position compared with reported vanadyl related redox reactions in vanadium oxides for AZIBs,[40,41,42,43] clarifying a relatively large capacity contribution because of relatively large proportion of vanadyl group in VOHCF(III) material. Additionally, the long-term stability of VOHCF(III) and VOHCF(II) cathodes were measured under GCD tests with current density of 0.2 A g^{-1} for 50 cycles. Specifically, there is a maximum specific capacity of 213 mAh g^{-1} achieved in VOHCF(III) cathode after few initial cycling activation, whereas only 113 mAh g^{-1} is observed in VOHCF(II) cathode suggesting a notable discrepancy of AZIBs performance. Moreover, it is observed that the capacity retention (against maximum specific capacity) of VOHCF(III) cathode approach 78% after 50 cycles at 0.2 A g^{-1}, which is lower than 90% of VOHCF(II) cathode under the identical condition. Additionally, rate performance evaluation provide remarkable capacity retention of 62% and 40% after 25-fold increased current density from 0.2 to 5 A g^{-1} in VOHCF(III) and VOHCF(II), respectively, which is attributed to large open accessible channels within the crystal structure. A further evaluation of long cycling stability measurement was conducted under current density of 5 A g^{-1} for the both cathode materials. Figure 4.3.4e shows that both of the cathodes possess robust cycling capability during 1000 cycles with only 22% and 27% capacity decay (against with maximum capacity) for VOHCF(III) and VOHCF(II), respectively.

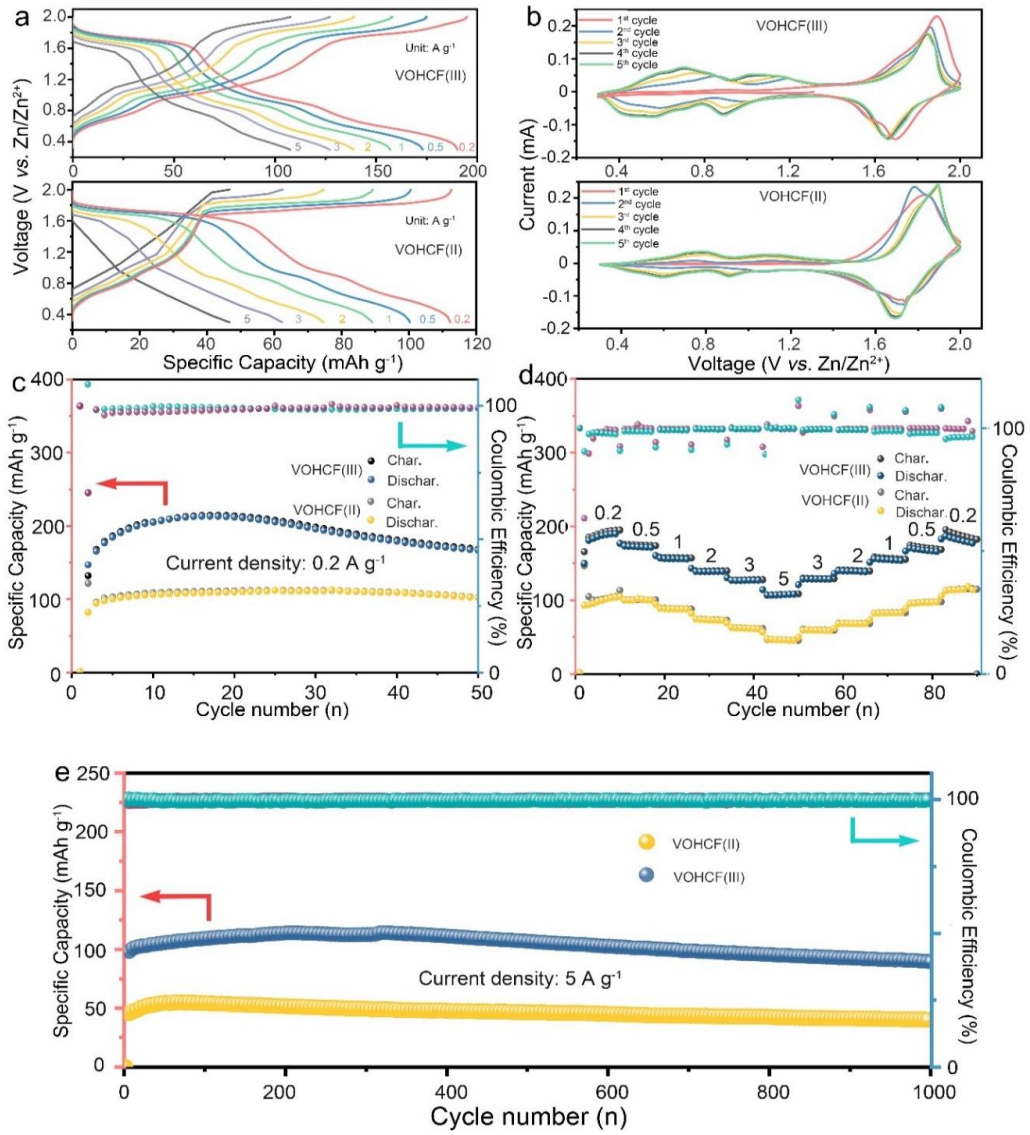

Figure 4.3.4. (a) GCD profiles of as-prepared VOHCF(III) and VOHCF(II) cathodes in first five cycles, respectively; (b) CV curves of VOHCF(III) and VOHCF(II) electrodes, respectively; (c) GCD long-cycling measurements on VOHCF(III) and VOHCF(II) cathodes under current density of 0.2A g^{-1}, respectively ; (d) rate performance evaluation of VOHCF(III) and VOHCF(II) cathodes under varied current density treatments. e) Long-term cycling measurement of VOHCF(III) under current density of 5A g^{-1}.

It is noteworthy that the specific capacity of VOHCF(II) cathode is much smaller than observation in VOHCF(III) cathode regardless of varied applied current density charge/discharge process, which could be hypothesized by not only distinct pristine crystallographic structures and vanadyl concentration, but different redox reactions reflecting with varied dynamic changes of chemical and structural states upon zinc

insertion/extraction between these samples. Hence, *ex-situ* characterizations of as-fabricated VOHCF cathodes were performed to elucidate the different electrochemical behaviours at varied charge/discharge states. Figure 4.3.5 clearly illustrates responsive chemical states at fully charge/discharge states in as-obtained 20th cycled cathodes, where both Fe 2p and V 2p species exhibit highly reversible redox features corresponding to expected three electrons transfer reactions, i.e. $Fe^{II}\leftrightarrow Fe^{III}$ and $V^{III}\leftrightarrow V^{V}$.In addition, XPS characterizations of Zn 2p core-level spectra indicate the presence of zinc species after discharge treatment of the both VOHCF(III) and VOHCF(II) samples, and small amount of that remain in materials at fully charge state, which is agreed with previous observation of vanadium based cathode materials for AZIBs.[44,45,46] It should be noted that no trace signal of K component was characterized in cycled VOHCF samples, which suggest that the pre-inserted K ions were completely replaced by high concentrated guest zinc ion species, and unable to retrieve their pristine sites after cycling treatment. The similar phenomena on irreversible pre-inserted ions in host materials were verified in previous chapter and numerous reported works.[44,47,48,49]

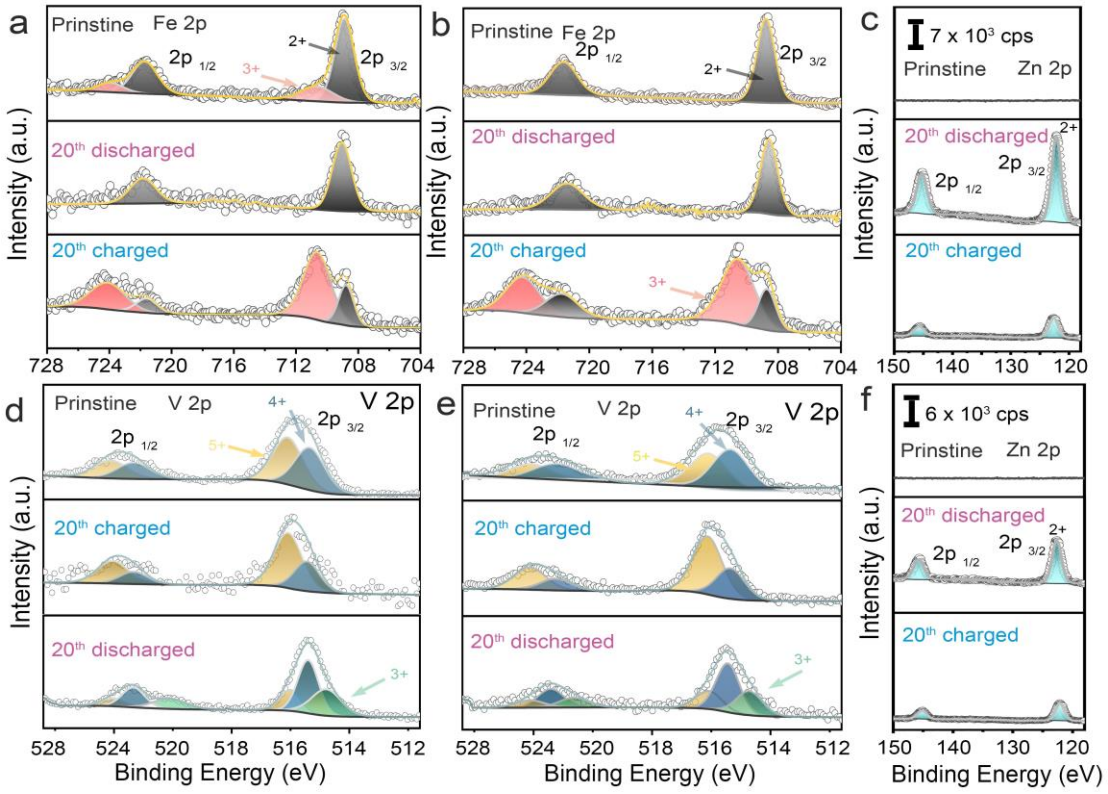

Figure 4.3.5. *ex-situ* XPS characterizations of core-level Fe 2p, V 2p and Zn 2p at pristine, charge/discharge states of (a)(b)(c) VOHCF(III) and (d)(e)(f) VOHCF(II)

cathodes.

In addition, Figure 4.3.6. exhibits the structural evolution of VOHCF(III) cathode materials at different charge/discharge states and close-up image of the peak indexed to (200) crystal facet *via ex-situ* XRD characterizations. Specifically, there is no obvious change of XRD pattern during initial charge/discharge process. However, the further cycling treatment of as-fabricated VOHCF(III) cathode impact on crystallographic structure with a clearly shift of the peak around 8° towards to higher 2θ degree, suggesting contracted *d*-spacing of <200> crystal plane along with Zn^{2+} insertion process. Inversely, the peak shift to lower 2θ degree upon zinc extraction process. It could be interpreted as the substitution of relatively weak electrostatic interaction of pristine K^{+} with the host framework compared with subsequently inserted large hydrated Zn^{2+} (4.3 Å) in VOHCF(III) materials during the intercalation reaction. Whereas the zinc deintercalation from the lattice, the H_2O molecule can accommodate in the cavity resulting large expansion of the cathode framework, which have been widely verified in previous reported studies on vanadium based cathode materials.[50] Similarly, it is also observed that the same varying tendency of peaks shift occur in other identified crystal planes which indicates a three dimensional expansion of lattice since zinc (de)intercalation reaction took place in this case. Although the crystal phase underwent dramatic changes during the reaction, the distinguished crystal structure after cycling measurement still maintains the rigid cubic unite cell motif, and there is no obvious second phase identified in *ex-situ* crystal phase characterizations. Therefore, the reversible chemical states and structural evaluations critically provide the robust cycling features of VOHCF(III)/(II) cathodes for AZIBs applications.

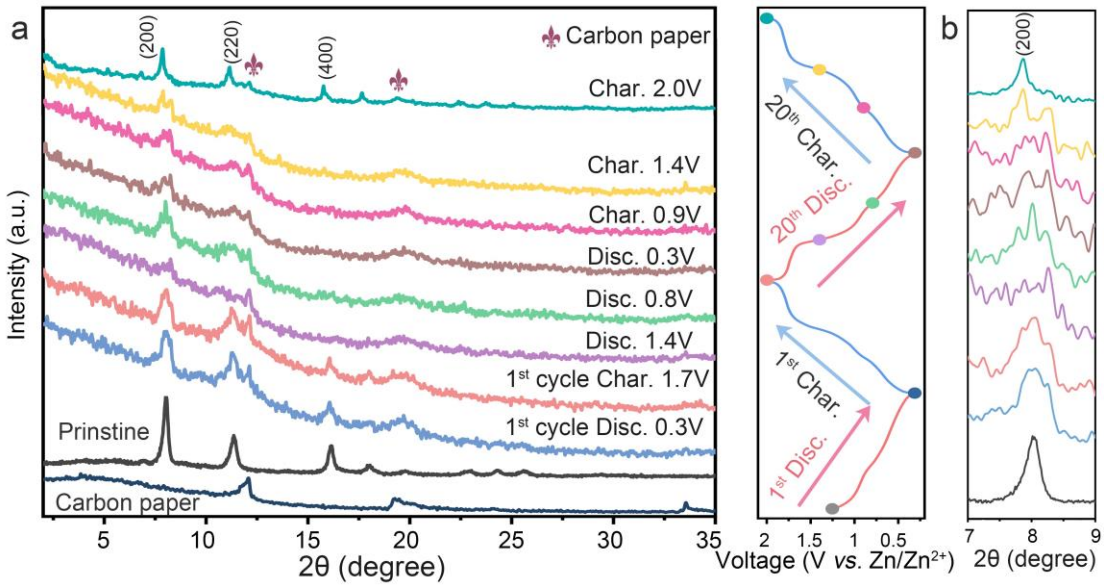

Figure 4.3.6. *Ex-situ* XRD characterizations of VOHCF(III) cathodes at varied charge/discharge states.

Further analysis of electrochemical properties of VOHCF(III) cathode material were conducted by capacitive-diffusion contribution calculations according to as-obtained CV curves at varied sweep rates from 0.1 to 1mV s^{-1}. Figure 4.3.7 illustrates a calculated CV plot under a scan rate of 0.5 mV s^{-1}, which indicate a 91% capacitive controlled redox reaction in VOHCF(III) cathode. Moreover, the following analysis of all scan rates CV plots suggest a mutual growth behaviour between sweep rates and capacitive for all current response, which clarify the faradaic-pseudocapacitance depended energy storage mechanism in this cathode material. Additionally, a further calculation on identified redox pairs in as-obtained CV plots were also performed to evaluate different reaction behaviours at specific discharge/charge states. More explicitly, Figure 4.3.7c depicts various labelled redox pairs in anodic/cathodic reactions under different sweep rates, which were calculated by the equation shown as follows:[44]

$$I=aV^{b}$$

The detailed description of the equation have been presented in the previous chapter 3 in this thesis, and the corresponding results are illustrated in Figure 4.3.7d. It is seen that the fitted b values of A1, 2, 3, C1, 2, 3 are 0.93, 1, 0.95, 0.99, 0.92 and 1, respectively, suggesting a capacitive dominated reaction behaviour in each potential states which is in coincidence with CV plots analysis. Hence, the evaluations of electrochemical reaction behaviour of VOHCF(III) cathode verify a capacitive-like zinc ions storage mechanism which highly differ form other reported vanadium based

cathode for AZIBs.[51,52,53] Meanwhile, the capacitive dominated reaction behaviour have been extensively proved as a favourable property for significantly enhanced rate capability and rapid reaction kinetics,[54] thus the VOHCF(III) cathode material presents promising capability for fast-charge required grid-scale stationary energy storage technique.

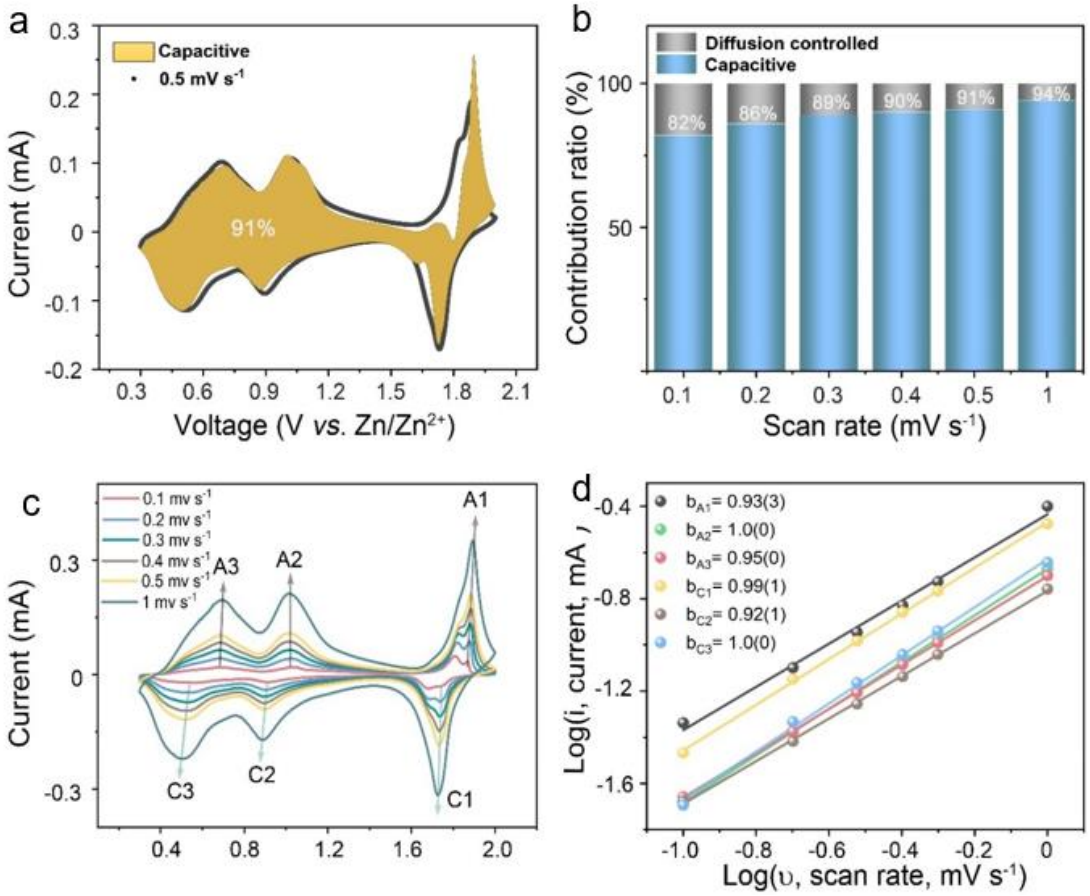

Figure 4.3.7. (a) Capacitive contribution (grey region) at 0.5 mV s^{-1} in CV curve of VOHCF(III), and (b) the capacity contributions ratio between capacitive and diffusion controlled processes at different scan rates; (c) The CV curves of VOHCF(III) cathode with varied scan rates from 0.1 to 0.5 mV s^{-1} corresponding to the (d) *b* value originated from log *i vs.* log *v* plots on basis of the CV results at picked oxidation/reduction states.

After comprehensive demonstration of VOHCF(III)/(II) cathodes capability for AZIBs applications, there are inevitable issues such as self-dissolution and poor interfacial mass transfer feature existing among the majority of cathode materials for aqueous metal ions batteries due to strong polar solvent (H_2O molecule) and inadequate surface properties of inorganic/organic cathode materials, which are essentially hindering the

battery performance in practical applications.[21,55] Therefore, developing protection layers on cathode materials is a vital approach to conquer the issues and has been well-demonstrated in alkali-metal-ions batteries systems.[56,57] However, artificially coated carbon layers or conductive polymers could give rise to electrochemical inert surface or complexity of interfacial interaction resulting decreased specific capacity, inhomogeneity of coupling decoration and degraded ionic diffusion kinetics.[58] Furthermore, the majority of reported surface coating materials adopted in organic electrolyte system are incapable for aqueous media since inherent instable feature and hydrophilic property induced faint interaction with hydrated charge carriers.[59] Therefore, it is essential to discover a novel type of surface protection layers to fulfil the specific needs in AZIBs applications. Sodium alginate was considered in this case as a promising candidate for the purpose due to multiple functional groups, environmental-friendly and low cost properties.[60] Most importantly, it can form robust hydrogel film by cross linking with multivalence metal ions such as Ca^{2+}, Zn^{2+}, Co^{2+}, Al^{3+} and Mn^{2+},[61,62] which have been extensively demonstrated in previous reported studies on metal sodium alginate hydrogels and also tested in our case on vanadyl ions which is show in Figure 4.3.8a. Surprisingly, the generated metal alginate hydrogels possess not only superior mechanical properties, but well-structured accessible channels for ions migration.[63,64] Therefore, it is usually considered as quasi-solid-state electrolyte for battery applications.[65] However, in order to unleash the entire potential of battery performance, aqueous electrolyte is more preferable in general energy storage system since a higher ionic conductivity (~10^3 higher than hydrogel based electrolyte) and mild interfacial effects.[8] Hence, an *in-situ* self-confinement growth of alginate hydrogel on active materials surface by exhausting shallow surface dissolved vanadyl ions until an equilibrium was reached, which offer a facile preparation approach, minimized impacts on active materials and reliable interfacial connection without numerous external factors effects derived from heat or redox chemical reagent treatments. The details of the preparation procedure have been provided in the experimental section, and the following alginate shielded VOHCF(III) electrodes are shown in Figure 4.3.8(b) where the glass fiber separator disassembled from coin cell with pristine VOHCF(III) electrode was dyed with obvious colour pattern suggesting self-dissolution of active materials during few cycling measurement. In contrast, alginate shielded VOHCF(III) electrode present negligible change of colours on the separator under identical condition. In addition, more conspicuous observation of

electrode stability was also found in Figure 4.3.8(c), in which both electrodes (pristine and alginate shielded VOHCF(III)) were soaked in the electrolyte for 48 hours. From the results, it is seen that the electrolyte containing alginate shielded VOHCF(III) electrode possesses more crystal transparent colour than that of pristine VOHCF(III), which is agree with previous observation in coin cells.

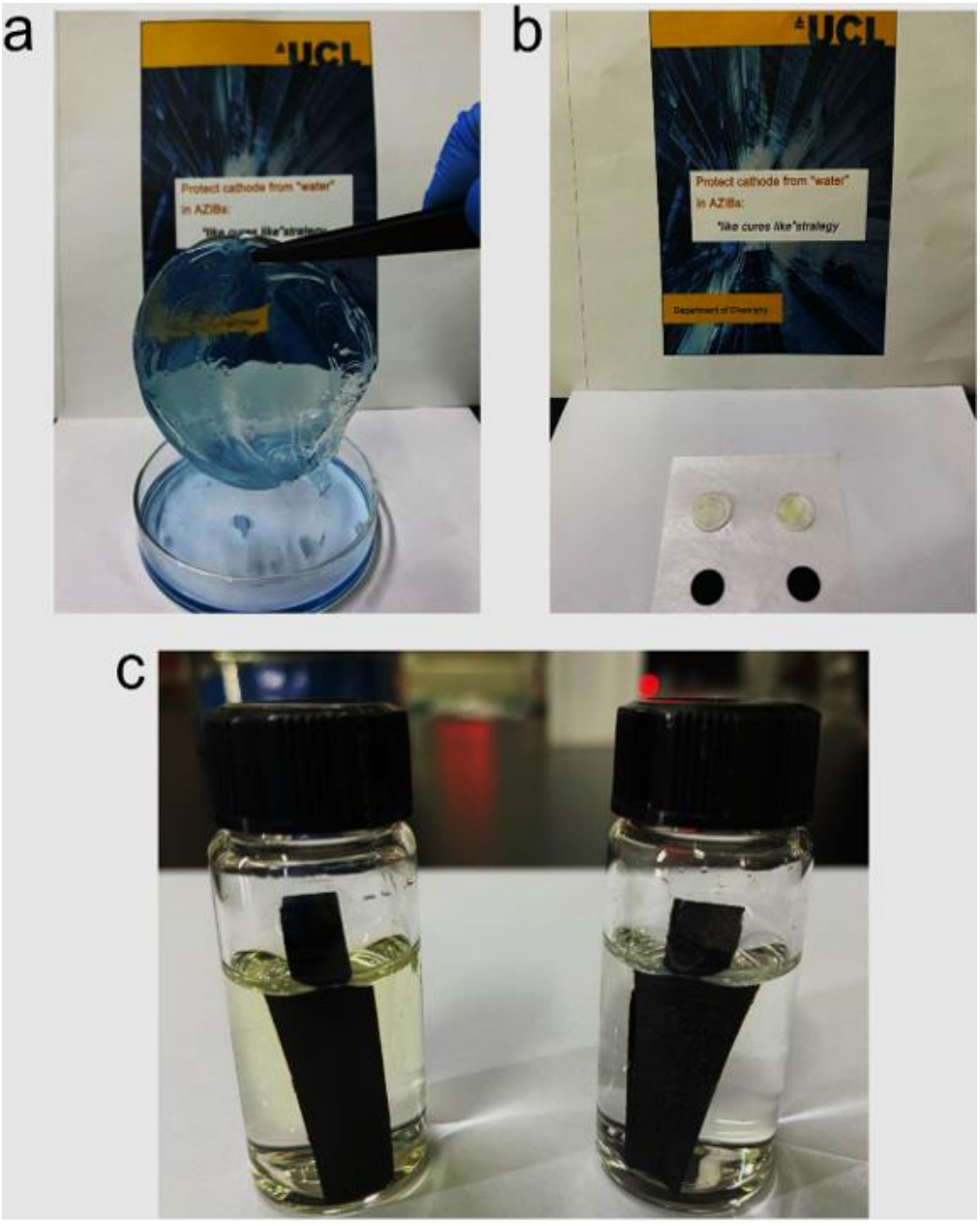

Figure 4.3.8. Photograph images of (a) vanadyl alginate hydrogel film; comparison between (b) hydrogel shielded and pristine VOHCF(III) electrodes and separator in coin cell, and (c) both electrode soaked in electrolyte respectively.

Figure 4.3.9a depicts a scheme of as-prepared VOHCF(III) improved by alginate layer for optimized battery performance in AZIBs application. The consequent battery performance evaluations were carried out to determine the enhanced properties after surface modification. Figure 4.3.9b illustrate a long cycling stability result of alginate shielded VOHCF(III) cathode in AZIBs with outstanding capacity retention of 96% and 86% (against to the maximum capacity of 228 mAh g^{-1}) for 50^{th} and 100^{th} cycles, respectively. Moreover, the rate capability of alginate shielded VOHCF(III) was performed with stepwise raised current density from 0.2 to 10 A g^{-1}, which present a capacity retention of 81.5% after 50-fold increase of current density and high specific capacity of 184 mAh g^{-1} even at 10 A g^{-1}. Meanwhile, the additional long-term cycling tests were conducted on alginate shielded VOHCF(III) electrode with or without 5 cycles activation under current density of 0.2 A g^{-1}. Consequently, it was observed that both cycling measurements present robust stability of 81% and 80% capacity retention (against maximum capacity of 131 and 176 mAh g^{-1}) after 2200 and 1200 cycles, respectively. The activation process can significantly enhance the specific capacity which could be interpreted as thorough extraction of potassium ions from framework resulting in sufficient accommodation sites for Zn^{2+} intercalations.

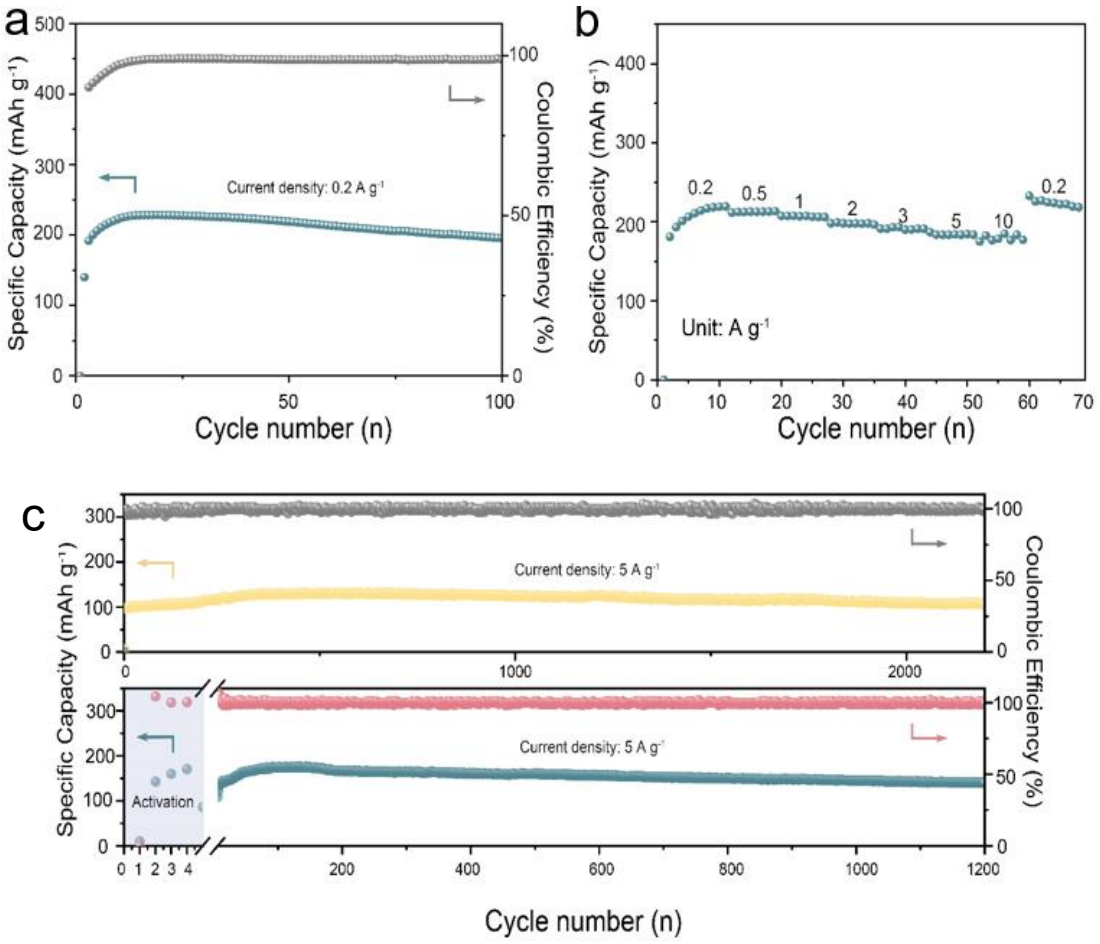

Figure 4.3.9. (a) long-cycling stability at current density of 0.2 A g^{-1}, (b) rate performance at difference current densities raised from 0.2 to 10 A g^{-1} and (c) long-cycling stability of alginate shielded VOHCF(III) electrode at current density of 5 A g^{-1} with/without initial electrochemical activity.

In order to comprehensively evaluate improvements of battery performance with untreated VOHCF(III) electrode, a radar diagram of comparison between pristine and alginate shielded VOHCF(III) on specific capacity and cycling capability were exhibited in Figure 4.3.10a. It is seen that a remarkable enhancement of specific capacity was achieved in treated VOHCF(III) electrode with 226 and 176 mAh g^{-1} against with 213 and 132 mAh g^{-1} in pristine VOHCF(III) electrode at 0.2 and 5 Ag^{-1}, respectively. Moreover, the rate capability also present significant improvement with 88% capacity retention after current density increased from 0.2 to 5A g^{-1} compared with only 62% at the same applied current density. Meanwhile, the dramatically enhanced cycling stability can also be characterized under identical conditions, that is, 96% and 95% capacity retention in alginate shielded VOHCF(III) cathode compared with 78%

and 78% in untreated VOHCF(III) cathode at 0.2 and 5 A g^{-1} for 50 and 1000 cycles, respectively. Therefore, the strategy of surface modification on vanadyl Prussian blue analogue with hydrogel protection layer is feasible to overcome the intrinsic issues of cathode materials in aqueous electrolyte system. Additionally, it is noteworthy that the achieved battery performance of alginate shielded VOHCF(III) surpass all reported Prussian blue analogues and the majority of developed cathode materials for AZIBs application. More explicitly, the specific capacity of as-obtained shielded VOHCF(III) electrode exhibit the highest values at a series of applied current densities among all reported Prussian blue analogues cathodes for AZIBs.[26] Furthermore, the maximum energy/power density of 230 Wh kg^{-1} and 9871W kg^{-1}, respectively achieved in this work present overwhelming energy storage capability compared with reported cathode materials for AZIBs, and even superior than LIBs, supercapacitor and lead-acid batteries on basis of only considering active mass of both anode and cathode components (inset of Figure 4.3.10c).[66]

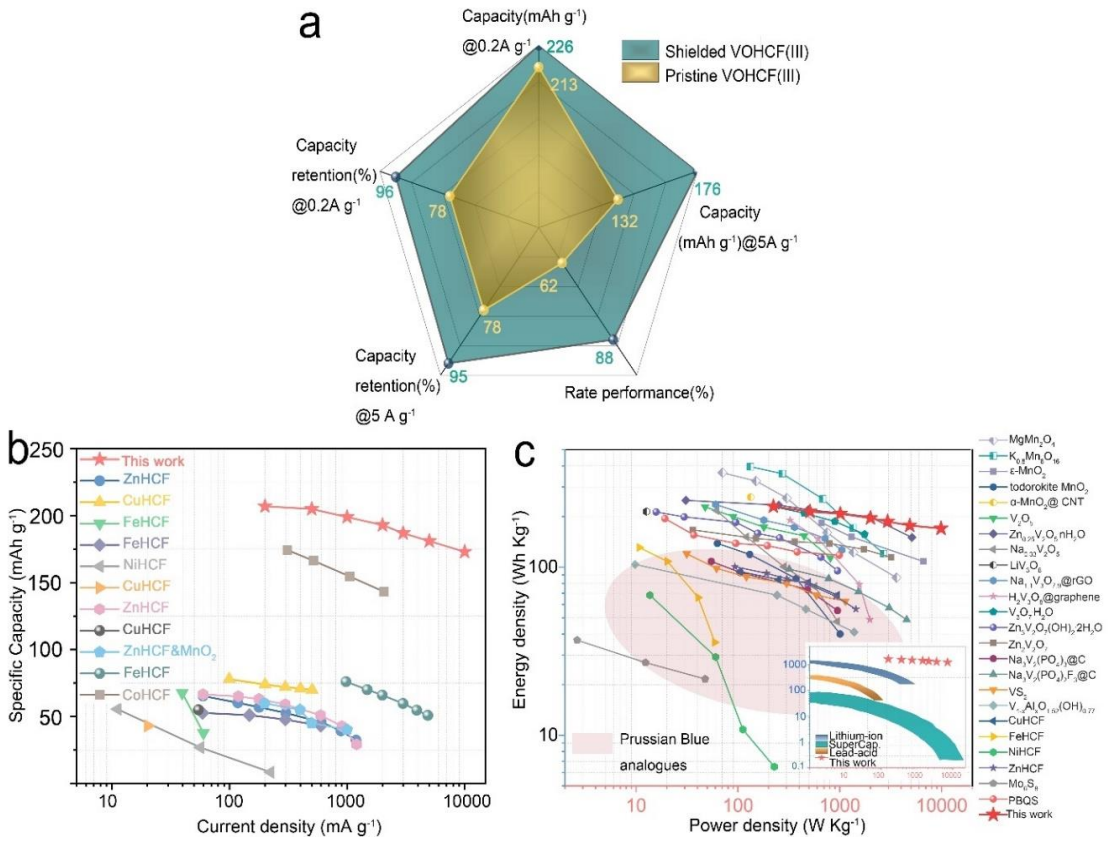

Figure 4.3.10. (a) Radar diagram comparison of the battery performance between alginate treated VOHCF(III) and pristine VOHCF(III) cathodes. (b) Ragone plot of performance comparison on specific capacity and corresponding current density for all

reported Prussian blue analogues cathodes for AZIBs; (c) Ragone plot of specific energy/power comparison between alginate shielded VOHCF(III) and other reported cathodes for AZIBs.

In addition to battery performance evaluation of alginate shielded VOHCF(III), FTIR characterizations were carried out to identify the anchored functional group in as-obtained samples. Figure 4.3.11 illustrates a comparison of FTIR spectra between pristine VOHCF(III), sodium alginate and alginate shielded VOHCF(III) with dwelling time of 1 and 10 minutes during the preparation, respectively. It was observed that the specific features belongs to sodium alginate within sphere of 1000 to 1500 cm^{-1} can be indexed to C=O, C-O and C-C groups,[66] which were also detected in surface shielded VOHCF(III) samples with increased intensity along with build-up treatment time, suggesting functionalized surface with alginate agents. Moreover, there was no obvious shifts of characteristic peaks with regard of vanadyl Prussian blue analogues which indicate few impacts on raw structure of VOHCF(III) after treatment. Figure 4.3.11b shows the TGA analysis of pristine and alginate shielded VOHCF(III) samples to reveal a different mass response during annealing process. It is seen that both of the materials lost nearly half mass at the end of heating treatment of 600 ˚C due to escape of absorbed/crystal water and decomposed HCN component. However, an attenuated downtrend in alginate shielded VOHCF(III) sample compared with untreated VOHCF(III) sample suggests strengthened interaction of crystal water molecule and reinforced framework after hydrogel surface decoration, reflecting a better thermal stability in this case. Additionally, in order to examine the porosity of pristine and alginate shielded VOHCF(III) samples, the BET specific surface area was characterized and corresponding results are exhibited in Figure 4.3.11c, where a notable high specific surface area of 158.3 $m^2\ g^{-1}$ is obtained for pristine VOHCF(III) sample. It should be emphasised that the values of BET specific surface area is almost 3-8 times higher than conventional Prussian analogues (Co, Ni, Mn, Zn, Fe, CuHCF et. al.)[23,33,67] owing to its unique crystal structure with abundant vacancy. Meanwhile, unlike other surface coating strategy, it is also seen that the alginate shielded VOHCF(III) still remains 76.5% specific surface area (121.2 $m^2\ g^{-1}$), indicating that the *in-situ* self-confinement growth alginate hydrogel on VOHCF(III) surface have minor effects on porosity which can ensure the greatest level of surface interaction with aqueous electrolyte without deterioration of interfacial properties. Moreover, the related pore size distributions were

also analysed by DFT method and illustrated in Figure 4.3.11d, in which there is a dominant pore diameter of 4.4 nm existing in pristine VOHCF(III) sample against to a pore diameter of 5.6 nm in alginate shielded VOHCF(III). The slightly large mesopore size could be interpreted as hydrogel induced pore structural changes, but intrinsic micropore is still maintain with the same size (1.8 nm) as before.

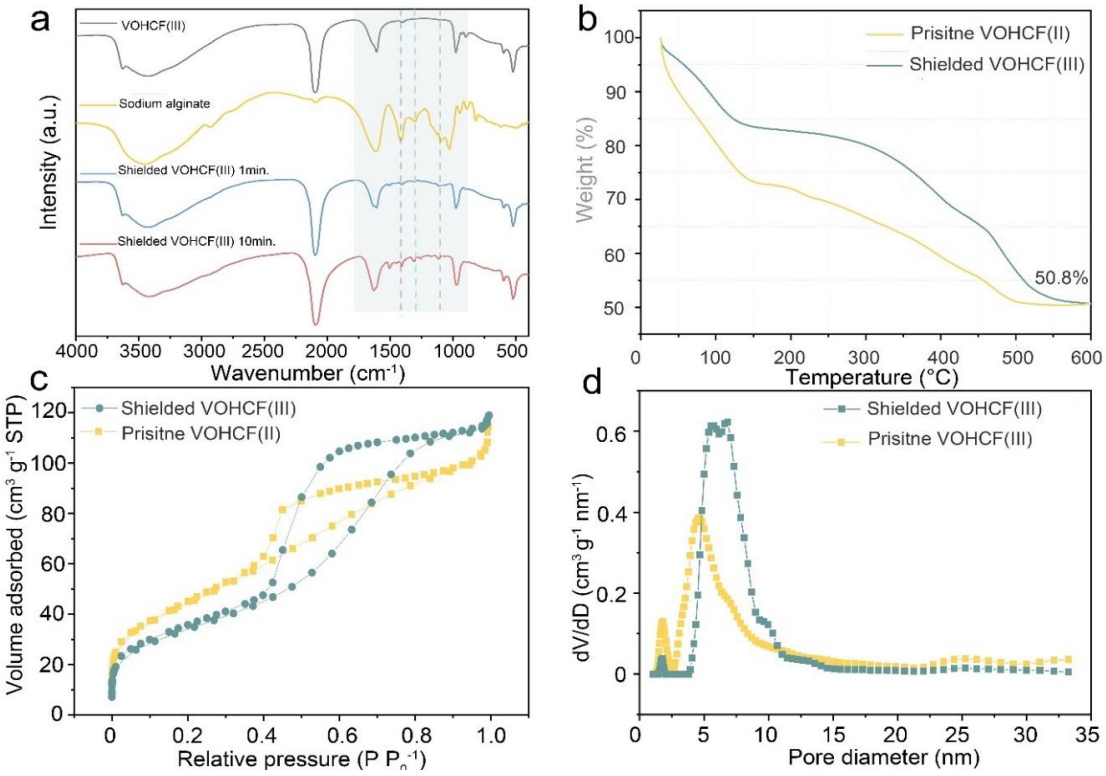

Figure 4.3.11. (a) FTIR spectra of sodium alginate, pristine, alginate shielded VOHCF(III) under different dwelling time of treatment. (b) TGA analysis of pristine and shielded VOHCF(III); (c) N_2 adsorption-desorption isotherm of pristine and alginate shielded VOHCF(III) and their corresponding (d) pore size distribution measurements.

The further characterization of varied interfacial properties was performed by water contact angle which clearly illustrate significant improvement of hydrophilic properties as the alginate hydrogel was adopted, reflecting with the contact angle reduced from 77° to fully infiltrated surface in alginate shielded VOCHF(III) electrode (Figure 4.3.12).

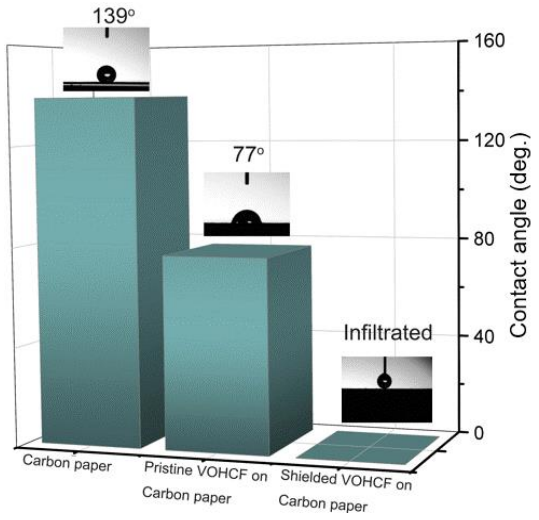

Figure 4.3.12. Water contact angel characterizations on carbon paper (substrate current collector), pristine VOHCF(III) printed carbon paper and alginate shielded VOHCF(III), respectively.

Additionally, the interfacial enhancement in regard of electrochemical properties was clarified by the EIS technique on both pristine and alginate treated VOHCF(III) samples. According to the Nyquist plots of as-obtained samples at initial and cycled states, the fitted equivalent circuit was simulated and exhibited in Figure 4.3.13, and the corresponding resistance parameters were summarized in Table 4.3.2. It is seen that both pristine and alginate treated VOHCF(III) assembled batteries possess very close combined internal resistance ($0.66\ \Omega < Rs < 1.07\ \Omega$) whether at initial state or after cycled GCD treatment, suggesting a very low inherent device resistance beneficial for electronic conductivity. Nevertheless, the interfacial charge transfer resistances (R_{ct}) differ from one to the other samples reflecting as relatively large R_{ct} of 87.53 Ω and 48.72 Ω at initial and cycled pristine VOHCF(III) batteries, respectively, compared with only 29.68 Ω and 24.73 Ω in alginate shielded VOHCF(III) at comparable states. The corresponding results can be explained by surface hydroxylation induced reduced energy barrier for hydrated charge carrier migration and desolvation *via* alginate hydrogel functionality. The similar phenomenon can be also observed at cycled state of pristine sample since the surface was compensated by water or hydroxide radical during the electrochemical reactions within aqueous system.

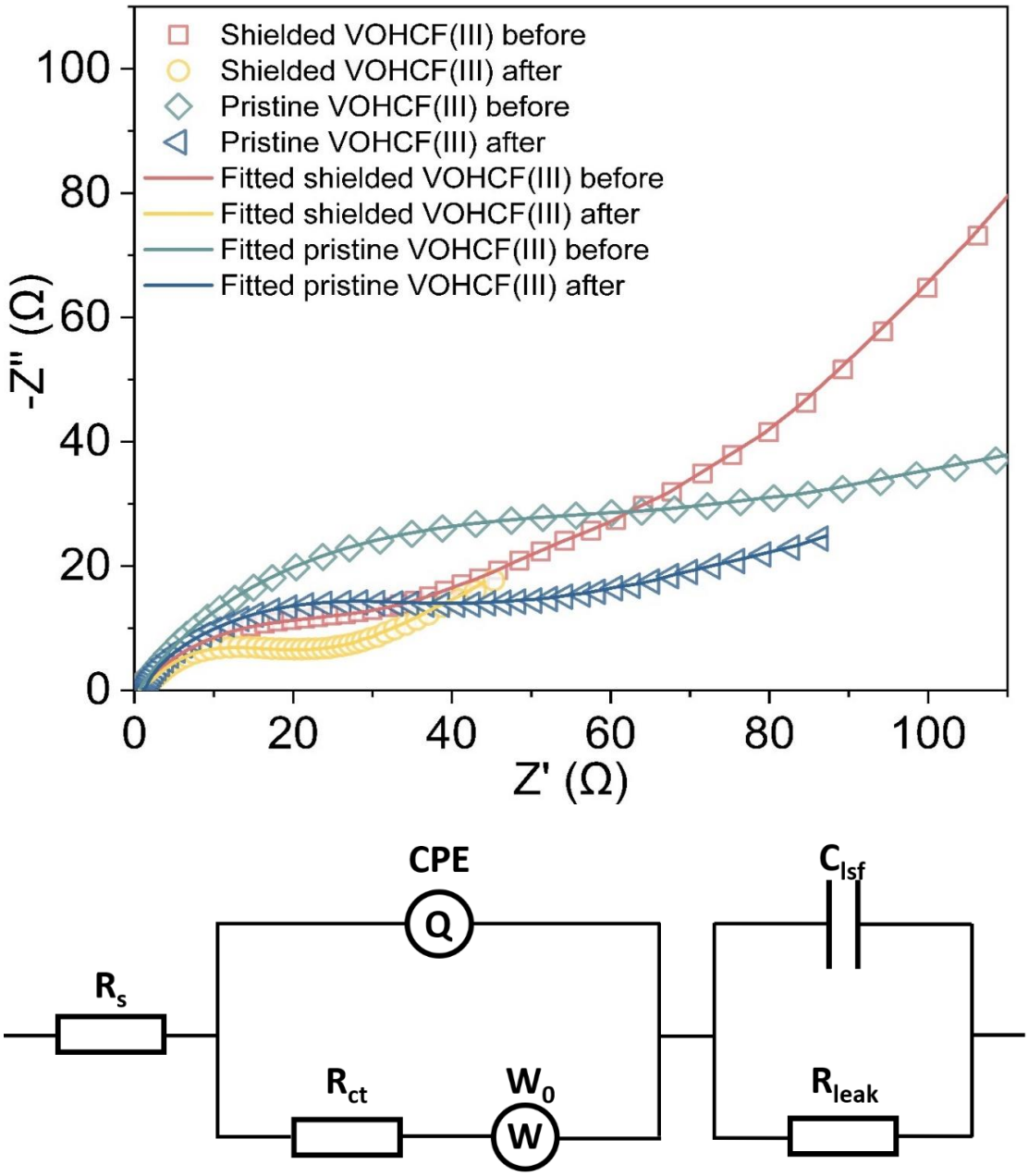

Figure 4.3.13. Equivalent circuit of pristine and alginate shielded VOHCF(III) assembled batteries for EIS fitting.

R_s: Combined internal resistance.

CPE: Constant phase element.

R_{ct}: Interfacial charge transfer resistance.

W_0: Warburg element.

C_{lsf}: Surface capacitance at low-frequency.

R_{leak}: Leakage resistance.

Table 4.3.2 Resistance parameters fitted from equivalent circuit.

Electrode	R_s (Ω)	R_{ct} (Ω)	R_{leak} (Ω)
Shielded VOHCF(III) before	0.70	29.68	91.76
Shielded VOHCF(III) after	0.66	24.73	88.40
Pristine VOHCF(III) before	0.75	87.53	32.82
Pristine VOHCF(III) after	1.07	48.72	24.36

In order to address the flexible capability of as-obtained VOHCF(III) material, the quasi-solid-state AZIB was fabricated by using 4M $Zn(CF_3SO_3)_2$ pre-immersed PAM as hydrogel electrolyte, VOHCF and zinc power printed carbon cloth as cathode and anode, respectively. Figure 4.3.14. demonstrate the flexibility of as-fabricated quasi-solid-state AZIB with stable energy output during the tests regardless of bending, twisting or hitting the battery.

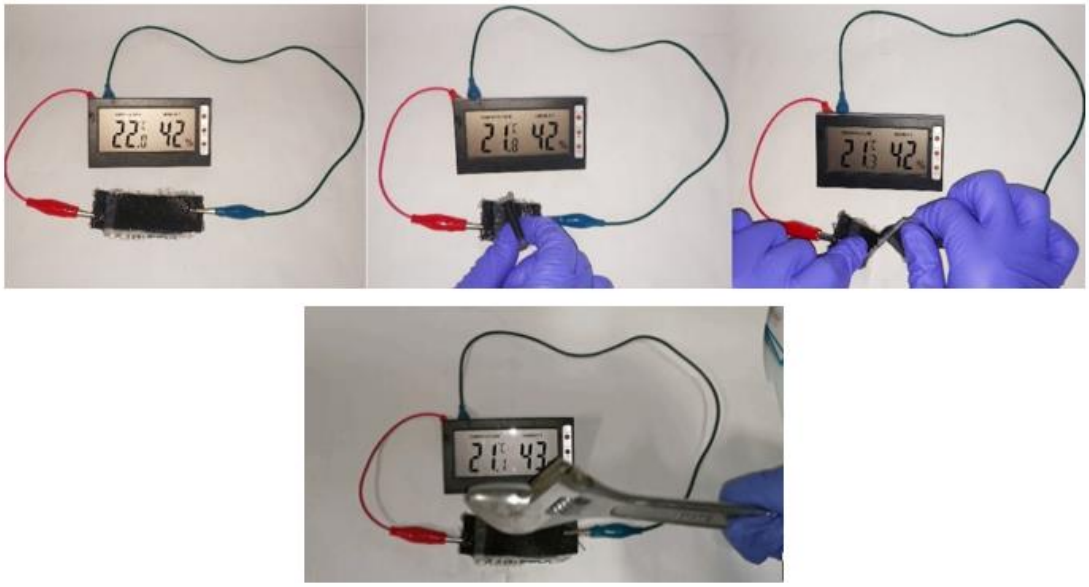

Figure 4.3.14. Demonstration of as-assembled quasi-solid-state VOHCF(III) | PAM(($Zn(CF_3SO_3)_2$) | Zinc

Moreover, the as-fabricated quasi-solid-state AZIB were also comprehensively investigated under GCD measurements to reveal the realized battery performance at this circumstance. Figure 4.3.15a depicts the long-term cycling characterizations of as-fabricated quasi-solid-state batteries based on VOHCF(III) and VOHCF(II) cathodes, respectively. It demonstrates that both of the batteries possess extremely stable charge/discharge reaction behaviour with specific capacity retention of 97% and 90%

(against to the maximum capacity of 203 and 112 mAh g^{-1}), respectively, after 50 cycles at 0.2 A g^{-1} treatment. The following rate capability measurements also verify robust reversible reaction features of both materials in quasi-solid-state AZIB batteries which present 103% recovered capacity of 217 mAh g^{-1} at 91st cycle compared with 204 mAh g^{-1} at initial cycle for VOHCF(III) battery. Similarly, VOHCF(II) battery also present negligible change of capacity after rate cycled tests under varied current density from 0.2 to 5A g^{-1}. However, it is also observed the relatively low rate capability of 50% and 55% for VOHCF(III) and VOHCF(II) quasi-solid-state batteries, respectively, compared with those of previous demonstrated pristine and alginate shielded VOHCF(III) batteries which could be attributed to low intrinsic ionic conductivity in hydrogel electrolyte, resulting relatively sluggish transfer kinetics in flexible batteries. Additionally, the long cycling stability measurement was also conducted under high current density of 5 A g^{-1} for evaluation on reversible feature of VOHCF(III) cathode in flexible battery. Figure 4.3.15c illustrates a remarkable stability of 94.5% (against the maximum capacity of 109 mAh g^{-1}) after 2000 cycles measurement which is superior than all attained results from aqueous electrolyte battery characterizations. Meanwhile, there is an average of 99.6% coulombic efficiency observed during the cycling measurements indicating a highly reversible reaction process upon zinc (de)intercalation.

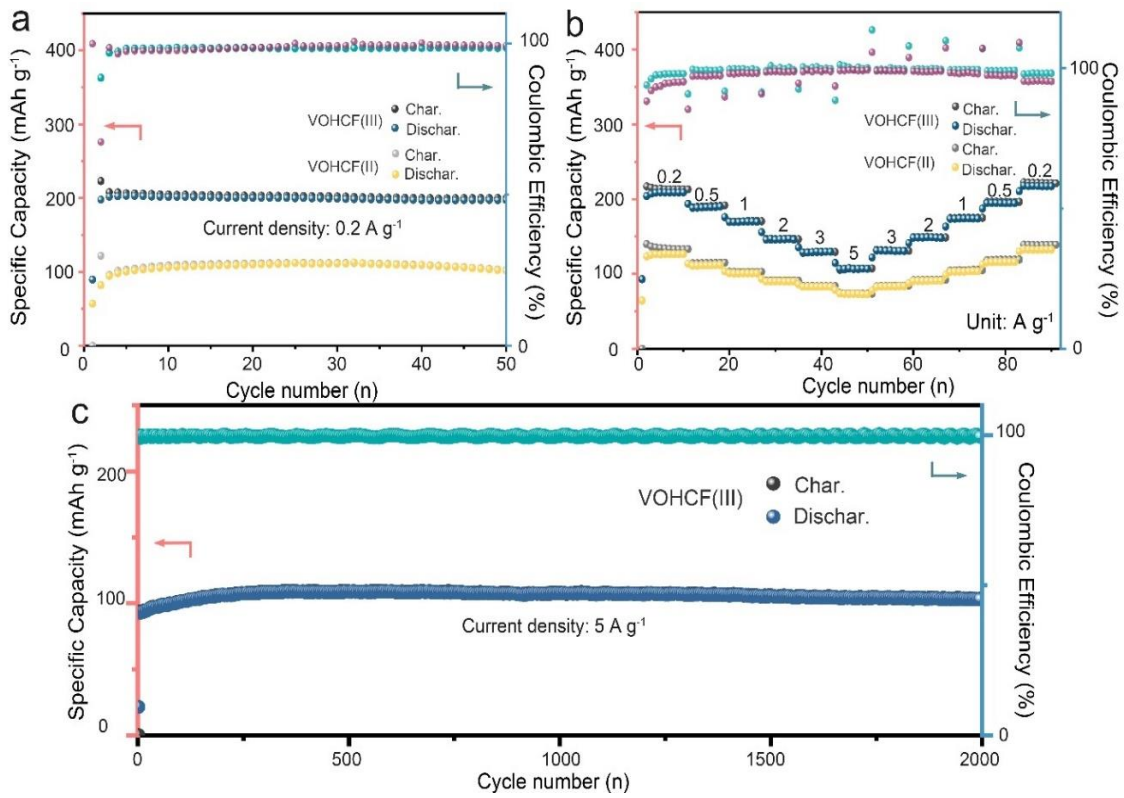

Figure 4.3.15. GCD characterizations of as-prepared quasi-solid-state AZIBs using pristine VOHCF as cathode:(a) long-cycling stability measurement of whole battery (VOHCF(III) and VOHCF(II)) under current density of 0.2 A g-1;(b) rate capability evaluations of quasi-solid-state batteries using VOHCF(III) and VOHCF(II) as cathodes, respectively;(d) long-cycling measurement of whole battery (VOHCF(III)) at 5A g^{-1}.

4.4 Conclusion

The vanadyl hexacyanoferrate and its defective analogue were successfully prepared in this work and demonstrated superior performance among all reported Prussian blue analogues cathodes for AZIBs application since numerous merits of its intrinsic properties derived from not only enriched stable vacancies along with enlarged cavity for charge carrier rapid migration, but also electrochemical redox active vanadyl (III↔V) species contributing to high theoretical capacity. Hence, the corresponding characterizations sufficiently verified the excellent reversibility on both structural and chemical perspectives. In addition, in order to conquer the issues of intrinsic deficiency on developed cathode materials in AZIBs, the *in-situ* self-confinement growth of alginate hydrogel on vanadyl hexacyanoferrate was first proposed in this work, which

critically provides a facile strategy to improve interaction of charge carriers and active material by interfacial functionalisation, and preserve the original microstructures with reinforced gel cross-link shell providing hyper channels for ions transport, that is, an omni-bearing promotion of diffusion kinetics and cycling stability of cathode materials which were effectively verified in this work. Meanwhile, the flexible quasi-solid-state zinc ion batteries were fabricated, suggesting the potential for utilization on practical flexible electronic devices with robust and safe mechanical features. Thereby, this study started with investigation on new competent cathode material which was subsequently decorated by alginate hydrogel shell suggesting attractively promising capability as water-compatible electrodes for AZIBs applications. It is expected that the proposed strategy can offer an avenue to not only elevate the capacity but extend the lifespan of the batteries for sustainable and mighty energy storage systems.

4.5 Reference

1 P. K. Nayak, L. Yang, W. Brehm and P. Adelhelm, *Angew. Chem. Int. Ed.*, **2018**, 57, 102–120.

2 D. Di Lecce, R. Verrelli and D. Di Lecce, *Green Chem.* **2017**, 19, 3442–3467.

3 X. Zhang, A. Wang, X. Liu and J. Luo, *Acc. Chem. Res.*, 2**019**, 52, 3223-3232.

4 L. Suo, O. Borodin, W. Sun, X. Fan, C. Yang, F. Wang, T. Gao, Z. Ma, M. Schroeder, A. Von Cresce, S. M. Russell, M. Armand, A. Angell, K. Xu and C. Wang, *Angew. Chem. Int. Ed.*, **2016**, 128, 7136–7141.

5 M. R. Palacín, A. de Guiber, *Science*, **2016**, 351,2353292

6 B. Tang, L. Shan, S. Liang and J. Zhou, *Energy Environ. Sci.*, **2019**, 12, 3288–3304.

7 G. Li, Z. Yang, Y. Jiang, C. Jin, W. Huang, X. Ding and Y. Huang, *Nano Energy*, **2016**, 25, 211–217.

8 S. Huang, J. Zhu, J. Tian, Z. Niu, *Chem. Eur. J.* **2019**, *25*, 14480.

9 Song, M., Tan, H., Chao, D., Fan, H. J., *Adv. Funct. Mater.* **2018**, 28, 1802564.

10 F. Wang, O. Borodin, T. Gao, X. Fan, W. Sun, F. Han, A. Faraone, J. A. Dura, K. Xu and C. Wang, *Nat. Mater.*, **2018**, 17, 543–549.

11 L. Chen, Q. An and L. Mai, *Adv. Mater. Interfaces*, **2019**, 6, 1–24.

12 L. E. Blanc, D. Kundu and L. F. Nazar, *Joule*, **2020**, 4, 771–799.

13 Z. Liu, Y. Huang, Y. Huang, Q. Yang, X. Li, Z. Huang and C. Zhi, ***Chem. Soc. Rev.***, **2020**, **49**, 180-232.

14 A. Konarov, N. Voronina, J. H. Jo, Z. Bakenov, Y. K. Sun and S. T. Myung, *ACS Energy Lett.*, **2018**, 3, 2620–2640.

15 C. Li, X. Zhang, W. He, G. Xu and R. Sun, *J. Power Sources*, **2020**, 449, 227596.

16 K. Hurlbutt, S. Wheeler, I. Capone and M. Pasta, *Joule*, **2018**, 2, 1950–1960.

17 G. Kasiri, R. Trócoli, A. Bani and F. La, *Electrochim. Acta*, **2016**, 222, 74–83.

18 X. Jia, C. Liu, Z. G. Neale, J. Yang and G. Cao, *Chem. Rev.,* **2020**, 120, 7795–7866.

19 W. Xu and Y. Wang, *Nano-Micro Lett.*, **2019**, 11, 90.

20 J. Ming, J. Guo, C. Xia, W. Wang and H. N. Alshareef, *Materials Science and Engineering: R: Reports*, **2019**, 135, 58-84.

21 P. He, Q. Chen, M. Yan, X. Xu, L. Zhou, L. Mai and C. Nan, *EnergyChem*, **2019**, **1**, 100022.

22 L. Zhang, L. Chen, X. Zhou and Z. Liu, *Adv. Energy Mater.*, **2015**, 5, 1–5.

23 Q. Yang, F. Mo, Z. Liu, L. Ma, X. Li, D. Fang, S. Chen, S. Zhang and C. Zhi, *Adv. Mater.,* **2019**, 31, 1901521.

24 Z. Jia, B. Wang and Y. Wang, *Mater. Chem. Phys.*, **2015**, 149, 601–606.

25 Z. Li, T. Liu, R. Meng, L. Gao, Y. Zou, P. Peng and Y. Shao, *Energy Environ. Mater.,* **2020**, 0, 1–6.

26 L. Ma, S. Chen, C. Long, X. Li, Y. Zhao, Z. Liu, Z. Huang, B. Dong, J. A. Zapien and C. Zhi, *Adv. Energy Mater.* **2019**, 9, 1902446.

27 G. Kasiri, J. Glenneberg, A. Bani, R. Kun and F. La, *Energy Storage Mater.*, **2019**, 19, 360–369.

28 G. Fang, J. Zhou, A. Pan and S. Liang, *ACS Energy Lett.,* **2018**, 3, 2480–2501

29 D. Chen, M. Lu, D. Cai, H. Yang and W. Han, *J. Energy Chem.*, 2021, **54**, 712–727.

30 N. Torres, H. Osiry, A. Rodríguez, L. Martínez-dlcruz and A. A. Lemus-santana, *Z. Anorg. Allg. Chem.,* **2018**, 644, 415–423.

31 J. Yang, H. Wang, L. Lu, W. Shi and H. Zhang, *Crystal Growth & Design,* **2006**, 6, 2438–2440.

32 S. J. Gerber and E. Erasmus, *Mater. Chem. Phys.*, **2018**, 203, 73–81.

33 P. Ge, S. Li, H. Shuai, W. Xu, Y. Tian, L. Yang and G. Zou, *Adv. Mater.* **2019**, 31, 1806092.

34 Y. Liu, B. Shen, X. Liu, Y. Wu, X. He and Q. Li, *Int. J. Electrochem. Sci.*, **2017**, 12, 5483–5491.

35 M. Xue, J. Ge, H. Zhang and J. Shen, *Appl. Catal. A Gen.*, **2007**, 330, 117–126.

36 Y. Xu, H. Dong, M. Zhou, C. Zhang, Y. Wu, W. Li, Y. Dong and Y. Lei, *Small Methods*, **2019**, 3, 1800349.

37 C. Liu, Z. Neale, J. Zheng, X. Jia, J. Huang, M. Yan, M. Tian, M. Wang, J. Yang and G. Cao, *Energy Environ. Sci.*, **2019**, 19–21.

38 G. Moretti and C. Gervais, *J Raman Spectrosc*., **2018**, 49, 1198– 1204.

39 R. Mažeikienė, G. Niaura and A. Malinauskas, *J. Electroanal. Chem.,* **2014**, 719, 60–71.

40 C. Xia, J. Guo, P. Li, X. Zhang and H. N. Alshareef, *Angew. Chem. Int. Ed.*, **2018**, 57, 3943–3948.

41 P. He, G. Zhang, X. Liao, M. Yan, X. Xu, Q. An, J. Liu and L. Mai, *Adv. Energy Mater.*, **2018**, 8, 1–6.

42 F. Wan and Z. Niu, *Angew. Chem. Int. Ed.*, **2019**, 58, 16358–16367.

43 S. Liu, L. Kang, J. M. Kim, Y. T. Chun, J. Zhang and S. C. Jun, *Adv. Energy Mater.,* **2020**, 10, 2000477.

44 F. Ming, H. Liang, Y. Lei, S. Kandambeth, M. Eddaoudi and H. N. Alshareef, *ACS Energy Lett.*, **2018**, 3, 2602–2609.

45 F. Wan, L. Zhang, X. Dai, X. Wang, Z. Niu and J. Chen, *Nat. Commun.*, **2018**, 9, 1–11.

46 Y. Yang, Y. Tang, G. Fang, L. Shan, J. Guo, W. Zhang, C. Wang, L. Wang, J. Zhou and S. Liang, *Energy Environ. Sci.*, **2018**, 11, 3157–3162.

47 L. Shan, Y. Yang, W. Zhang, H. Chen, G. Fang, J. Zhou and S. Liang, *Energy Storage Mater.*, **2019**, 18, 10–14.

48 M. Morcrette, P. Rozier, L. Dupont, E. Mugnier, L. Sannier, J. Galy and J. M. Tarascon, *Nat. Mater.*, **2003**, 2, 755–761.

49 V. Bodenez, L. Dupont, M. Morcrette, C. Surcin, D. W. Murphy and J. M. Tarascon, *Chem. Mater.*, **2006**, 18, 4278–4287.

50 M. Yan, P. He, Y. Chen, S. Wang, Q. Wei, K. Zhao, X. Xu, Q. An, Y. Shuang, Y. Shao, K. T. Mueller, L. Mai, J. Liu and J. Yang, *Adv. Mater.*, **2018**, 30, 1703725.

51 B. Sambandam, V. Soundharrajan, S. Kim, M. H. Alfaruqi, J. Jo, S. Kim, V. Mathew, Y. Sun and J. Kim, *J. Mater. Chem. A*, **2018**, 6, 15530–15539.

52 B. Tang, G. Fang, J. Zhou, L. Wang, Y. Lei, C. Wang, T. Lin, Y. Tang and S. Liang, *Nano Energy*, **2018**, 51, 579–587.

53 Z. Wu, Y. Wang, L. Zhang, L. Jiang, W. Tian, C. Cai, J. Price, Q. Gu and L. Hu, *ACS Appl. Energy Mater.* **2020**, 3, 3919–3927

54 Q. Pang, C. Sun, Y. Yu, K. Zhao, Z. Zhang, P. M. Voyles, G. Chen, Y. Wei and X. Wang, *Adv. Energy Mater.*, **2018**, 8, 1–9.

55 N. Zhang, X. Chen, M. Yu, Z. Niu, F. Chen, J. Chen*, Chem. Soc. Rev.,* **2020**, 49, 4203–4219

56 V. Etacheri, R. Marom, R. Elazari, G. Salitra and D. Aurbach, *Energy Environ. Sci.,* **2011**, 4, 3243

57 M. Winter, B. Barnett and K. Xu, *Chem. Rev.* 2018, **118**, 11433–11456.

58 D. Bin, F. Wang, A. G. Tamirat, L. Suo, Y. Wang, C. Wang and Y. Xia, *Adv. Energy Mater.* 2018, **8**, 1703008.

59 D. Kundu, S. H. Vajargah, L. Wan, B. Adams, D. Prendergast and L. F. Nazar, *Energy Environ. Sci.,* **2018**, 11, 881-892

60 L. Nie, C. Liu, J. Wang, Y. Shuai, X. Cui and L. Liu, *Carbohydr. Polym.*, **2015**, 117, 616–623.

61 L. Iskandar, L. Rojo, L. Di Silvio and S. Deb, *J. Biomater. Appl.,* **2019**, 34, 573-584..

62 Y. Liu, J. Z. C. Zhang, Y. Guo and P. Zhu, *J. Mater. Sci.*, **2016**, 51, 1052–1065.

63 J. Huang, X. Chi, J. Yang and Y. Liu, *ACS Appl. Mater. Interfaces,* **2020**, 12, 17583–17591

64 A. F. Fuzlin and A. S. Samsudin, *Polym. Bull.*, 2020, https://doi.org/10.1007/s00289-020-03207-2.

65 Y. O. Iwaki, M. H. Escalona, J. R. Briones and A. Pawlicka, *Mol. Cryst. Liq. Cryst.,* 2014, 603, 240-247.

66 Z. Li, S. Gadipelli, H. Li, C. A. Howard, D. J. L. Brett, P. R. Shearing, Z. Guo, I. P. Parkin and F. Li, *Nat. Energy*, **2020**, 5, 160–168

67 S. S. Kaye and J. R. Long, *Catal. Today,* **2007**, 120, 311–316.

Chapter 5

Conclusions and outlook

6.1 Conclusions

To fulfil the rigid criteria of energy storage system, this PhD project targeted on developing advanced cathode materials for aqueous zinc ion batteries with detailed analysis of physiochemical properties and critical elucidation of reaction mechanism. Thereby, the project was divided into three perspectives of vanadium based cathode materials in terms of novel nickel/cobalt vanadium bronze, defective ammonium vanadium bronze and vanadyl Prussian blue analog, respectively. Meanwhile, universal strategies were also proposed in this thesis for improving the electrochemical performance in regard of specifically tuned micro-/ electronic-structures, chemical environment and interfacial interactions, which contributed to robust reversibility, high specific capacity and rapid diffusion reaction kinetics. The details of studies on these purpose are summarized as follows:

In Chapter 2, novel nickel/cobalt vanadium bronzes (δ-$Ni(Co)_{0.25}V_2O_5{\cdot}nH_2O$) were successfully fabricated for application in AZIBs. Through comprehensive *ex-situ* examination of their microstructures, chemical states and electronic structure evolutions upon charge/discharge states, it illustrated the varied impacts of atomic level structures on corresponding electrochemical behaviours, suggesting a significance of designing layered vanadium bronze materials on basis of merit-based selection of specific crystal phase of V_2O_5 framework and pre-intercalated cations. Moreover, DFT and 3D-tomography simulation effectively provide deep insight of zinc storage mechanism within the as-design lattice of cathode materials and visual inspection of electrolyte diffusion from device aspect. Hence, the studies sufficiently verified the radical parameters responsible for high performance in AZIBs and depict a whole picture of energy storage process in the elaborately designed experimental investigations of as-obtained cathode materials.

In Chapter 3, there are great interests of investigations on defective vanadium bronze cathode materials so as to further improve the performance in AZIBs applications. Thus, hydrated oxygen defective ammonium vanadium bronzes were prepared to critically discuss the effects of tuned micro/electronic structures on electrochemical reactions. Through finely controlled reduction agent and additive of NH_4F, the resulting sample possessed distinct structural and chemical properties *via* multiple characterization

techniques. As the consequence, the oxygen-defective ammonium vanadium bronzes presented remarkable battery performance in regard of fast ionic diffusion kinetics, elevated electronic conductivity and robust cycling stability compared with untreated control group samples, indicating the essential features of pre-accommodated H_2O molecules and modified localized electronic environment around oxygen point deficiency. Therefore, this study illuminates prospects of two-pronged approaches on optimizing electrochemical properties by introducing lattice water and defects for advanced cathode materials in AZIBs applications.

In Chapter 3, it is first time that a novel Prussian blue analogues was proposed by substitution of electrochemical inert transition metal by redox active vanadyl ions from conventional transition metal hexacyanoferrate framework. Owing to occupation of oxygen species in vanadyl, the corresponding vanadyl hexacyanoferrate spontaneously form thermodynamically stable vacancies in crystallographic structure, offering more assessable channels for charge carriers transports. Accordingly, the resulting battery performance exhibit superior characteristics with highest specific capacity and rate capability among all previous reported Prussian blue analogues cathodes for AZIBs. Moreover, the defective vanadyl hexacyanoferrate was also fabricated to understand the microstructure induced different electrochemical behaviours, indicating that higher crystallinity and dominated concentration of vanadyl are essential for steady and powerful energy storage competence. More importantly, the study also provide a facile strategy of surface modification by capping with *in-situ* generated alginate hydrogel shell by consuming surface escaped vanadyl ions on as-prepared vanadyl Prussian blue analog to address the issues of interfacial incapability and self-dissolution in cathode materials for aqueous rechargeable batteries. It is seen that alginate shielded vanadyl Prussian blue analog exhibited remarkable performance compared with untreated samples and achieved competitive capability as superb energy storage material for practical applications. The corresponding enhancements were not only observed by rapid interfacial transport kinetics of charge carriers, but also significantly stabilized cycling properties via varied characterizations. In the end, the flexible quasi-solid-state zinc ion batteries were fabricated by adopting as-prepared vanadyl Prussian blue analog as cathode, sufficiently confirming the huge potential for utilization of wearable/flexible electronic device in the future. Thereby, this study provides comprehensive research which started with novel cathode material and finished with

optimized properties for practical demonstrations, that is, suggests an open avenue for developing competent cathode materials in the field of AZIBs.

6.2 Outlook

According to the discussion in this thesis, it is understood that vanadium-based materials are the promising candidate for cost-effective and reliable energy storage materials applied in AZIBs. However, it should also be admitted that the development of AZIBs in regard of materials design and reaction mechanism is still in an infancy stage since completed different reaction species and environment compared with conventional alkali metal-ions batteries. Moreover, numerous challenges still remain such as fast degradation under low current density treatments, relatively low working potential (compared with LIBs) and ambiguous energy storage mechanism in the aqueous media system, Thereby, the future studies on advanced vanadium based cathode materials could be carried out from the three aspects which are summarized as follows:

1. Increasing the stability via optimizing microstructures and inhibiting side reactions such as oxygen/hydrogen evolution reactions and irreversible phase transformation under Zn^{2+} (de)intercalation process.
2. Modifying electronic structures for enlarging potential difference by introducing guest species such as polyanions and electrochemical active metal ions ($Co^{2+/3+}$ and $Mn^{3+/4+}$) with low Femi-level redox pairs.
3. Exploring novel characterizations techniques with the rational design of parameters to evaluate veritable reaction behaviour in AZIBs applications. Meanwhile, combinational in-situ experimental approaches can effectively elucidate the dynamic reaction process rather than conventional ex-situ measurements which are severely affected extrinsic factor.

Additionally, the prototype of as-developed AZIBs should also be fabricated to provide authentic assessments not only on practical costs with scalable production routes but also device-level batteries performance, that is, more crucial for commercial applications in the future.

Last but not least, as an integral device, there are more efforts required indeed in terms of electrodes, separator, current collector, cell-package materials and aqueous electrolytes which jointly contribute to the expectation of favourable outcome.

Appendix

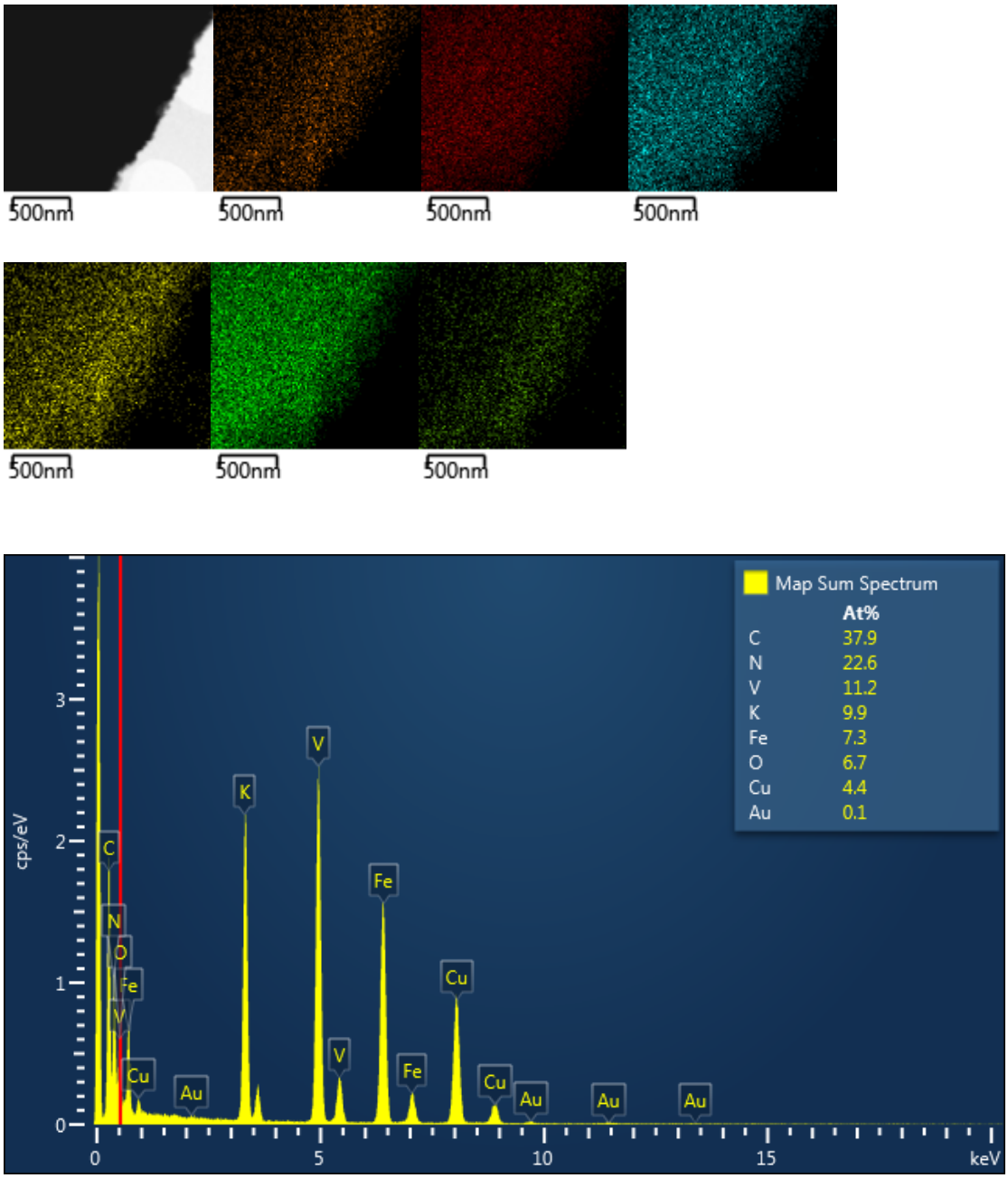

Figure A1. Elemental mapping and analysis of VOHCF(III) achieved by TEM EDS.

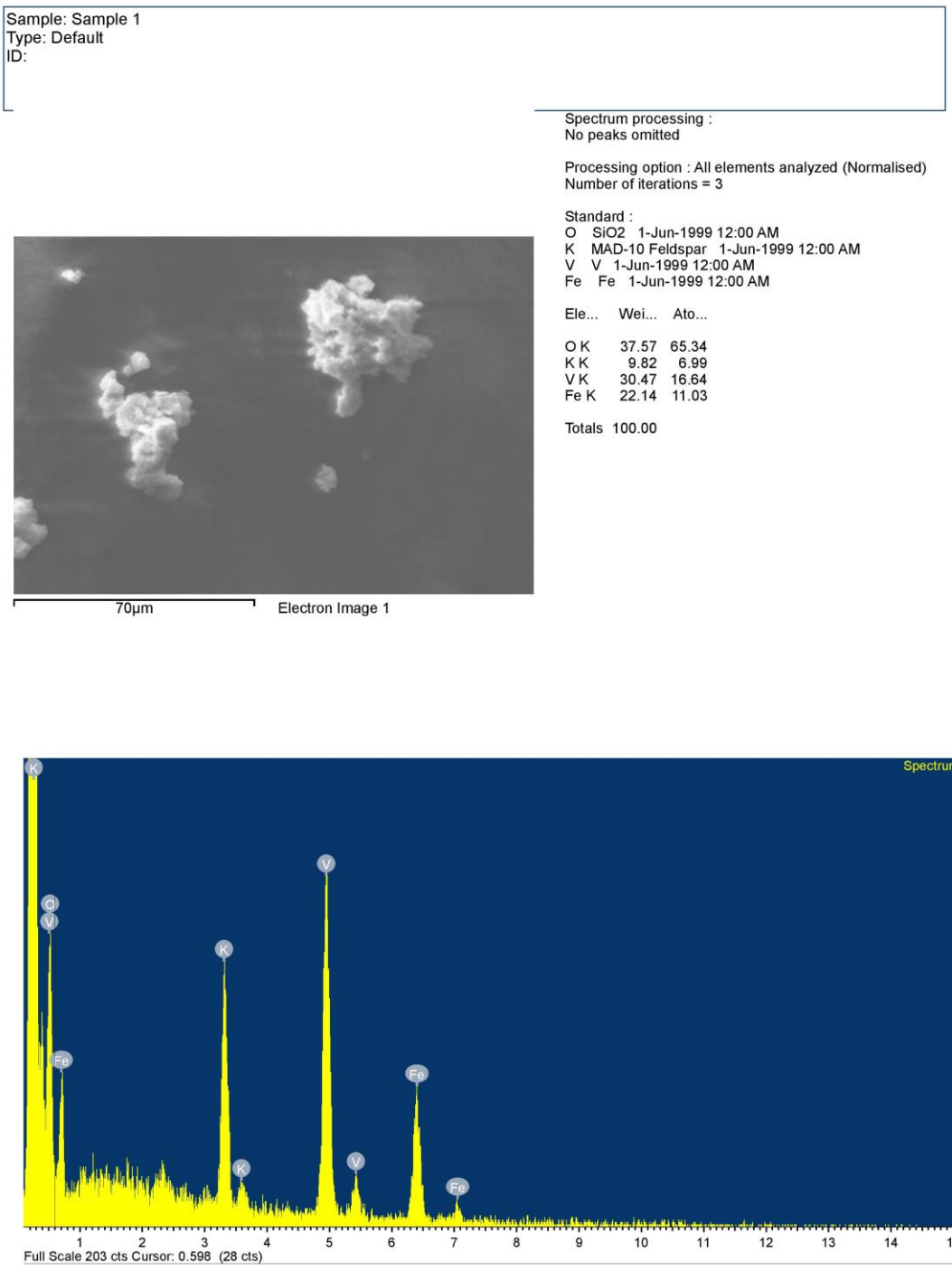

Figure A2. Elemental mapping and analysis of VOHCF(III) achieved by TEM EDS.

Publication List

Publication related to the thesis:

(1) **J. Li**, K. McColl, X. Lu, S. Sathasivam, H. Dong, L. Kang, Z. Li, S. Zhao, A. G. Kafizas, R. Wang, D. J. L. Brett, P. R. Shearing, F. Corà, G. He*, C. J. Carmalt, I. P. Parkin*, Multi-Scale Investigations of δ-$Ni_{0.25}V_2O_5 \cdot nH_2O$ Cathode Materials in Aqueous Zinc-Ion Batteries, ***Adv. Energy Mater.***, 2020, 2000058. **(Frontispiece, Highlighted by Energist News, Nanoer, Clean Energy, Progress in Zn battery)**

(2) **J. Li**, N Luo, F. Wan, S. Zhao, Z. Li, W. Li, J. Guo, P. R. Shearing, D. J.L. Brett, C. J. Carmalt, G. Chai,* G. He*, I. P. Parkin*, Defected vanadium bronzes as improved cathodes in aqueous zinc-ion batteries, ***Nanoscale***, 2020, 10.1039. **(Back cover story)**

Other publications during PhD study:

2020

(3) K. L., Gurunatha, S., Sathasivam, **J. Li,** M., Portnoi, I. P. Parkin*, I., Combined Effect of Temperature Induced Strain and Oxygen Vacancy on Metal-Insulator Transition of VO_2 Colloidal Particles. ***Adv. Funct. Mater***. 2020, 2005311.

(4) S. Zhao, J. Berry-Gair, W. Li, G. Guan, M. Yang, **J. Li**, F. Lai, F. Corà, K. Holt, D. J.L. Brett, G. He* and I P. Parkin*, The Role of Phosphate Group in Doped Cobalt Molybdate: Improved Electrocatalytic Hydrogen Evolution Performance, ***Adv. Sci.,*** 2020, 1903674. **(Frontispiece, Highlighted by Energist News, Nanoer)**

(5) Z., Liu, T., Liu, C. N., Savory, J. P., Jurado, J. S., Reparaz, **J. Li,** L.,Pan, C. F. J., Faul, I. P., Parkin, G., Sankar, S., Matsuishi, M., Campoy-Quiles, D. O., Scanlon, M. A., Zwijnenburg, O., Fenwick, B. C., Schroeder, Controlling the Thermoelectric Properties of Organometallic Coordination Polymers via Ligand Design. ***Adv. Funct. Mater.*** 2020, 30, 2003106

(6) J. Huang, Y. Li*, R. Xie, **J. Li**, Z. Tian, G. Chai, Y. Zhang, F. Lai, G. He, C. Liu, T. Liu and J. L. Dan, Structural Engineering of Cathodes for Improved Zn-ion Batterie. ***J. Energy Chem.,*** DOI:10.1016/j.jechem.2020.09.035.

(7) D. Zhao, S. Sathasivam, **J. Li** and C. J. Carmalt, Transparent and Conductive Molybdenum-Doped ZnO Thin Films via Chemical Vapor Deposition, ***ACS Appl. Electron. Mater.*** 2020, 2, 120−125

(8) H. Dong, **J. Li**, Zhao, S., Zhao, F., Xiong, S., Brett, D., He, G., and Parkin, I.P. An anti-aging polymer electrolyte for flexible rechargeable zinc-ion batteries, ***Journal of Materials Chemistry A*** , 2020, DOI: 10.1039/d0ta07086f

(9) D. Zhao, **J. Li**, Sathasivam, S., & Carmalt, C. J. n-Type conducting P doped ZnO thin films via chemical vapor deposition. ***RSC Advances***, 2020, 10(57), 34527–34533.

2019

(10) Z. Wang, H. Tang, W. Li*, **J. Li**, R. Xu, K. Zhang, **G. He***, P. R. Shearing, D. J. L. Brett*, Core-shell TiO_2@C ultralong nanotubes with enhanced adsorption for antibiotics, ***J. Mater. Chem. A***, 2019, 7, 19081-19086.

(11) Liu, T., Zhao, X., **Li, J.** Z. Liu, F. Liscio, S. Milita, B.C. Schroeder, O. Fenwick. Enhanced control of self-doping in halide perovskites for improved thermoelectric performance. ***Nat Commun.***, 2019, 10, 5750.

(12) P. Promdet, R. Quesada-cabrera, S. Sathasivam, **J. Li**, A. Jiamprasertboon, J. Guo, A. Taylor, C. J. Carmalt and I. P. Parkin, High defect nanoscale ZnO films with polar facets for enhanced photocatalytic performance, ***ACS Appl. Nano Mater.***, 2019, 2, 5, 2881–2889

2018

(13) **J. Li**, S. Sathasivam, A. Taylor and C. J. Carmalt, Single step route to highly transparent, conductive and hazy aluminium doped zinc oxide films, ***RSC Adv.***, 2018, 8, 42300

(14) Y. Tu, **J. Li**, Zhang, D.-W., Briscoe, J., & Krause, S. The Effect of Semiconductor Morphology on the Spatial Resolution of ZnO Based Light-Addressable Potentiometric Sensors. ***Proceedings***, 2018, 2(13), 917.

Manuscript in preparation

J. Li, et, al. Dual-atoms induced spontaneous vacancies in vanadyl Prussian blue analog of ultra-fast kinetics for aqueous zinc ion batteries.

Conference presentations and posters

1. Oral presentation. Multi-Scale Investigations of δ-$Ni_{0.25}V_2O_5 \cdot nH_2O$ Cathode Materials in Aqueous Zinc-Ion Batteries, Johnson Matthey, UK, 2020.
2. Poster. Advanced design of vanadium bronzes for high performance zinc ion batteries, 2019 MRS Fall Meeting, U.S.A, 2019